



**US Army Corps
of Engineers**

Waterways Experiment
Station

Technical Report CHL-97-21
September 1997

Discrete Network Modeling for Field-Scale Flow and Transport Through Porous Media

by *Stacy E. Howington, John F. Peters, WES*
Tissa H. Illangasekare, University of Colorado

DTIC QUALITY INSPECTED 2

Approved For Public Release; Distribution Is Unlimited

DTIC QUALITY INSPECTED 2

19971223 056

Prepared for Discretionary Research Program
U.S. Army Engineer Waterways Experiment Station
and Army Environmental Center, Aberdeen Proving Ground, Maryland

The contents of this report are not to be used for advertising, publication, or promotional purposes. Citation of trade names does not constitute an official endorsement or approval of the use of such commercial products.

The findings of this report are not to be construed as an official Department of the Army position, unless so designated by other authorized documents.



PRINTED ON RECYCLED PAPER

Technical Report CHL-97-21
September 1997

Discrete Network Modeling for Field-Scale Flow and Transport Through Porous Media

by Stacy E. Howington, John F. Peters

U.S. Army Corps of Engineers
Waterways Experiment Station
3909 Halls Ferry Road
Vicksburg, MS 39180-6199

Tissa H. Illangasekare
Department of Civil, Environmental,
and Architectural Engineering
University of Colorado
Boulder, CO 80309

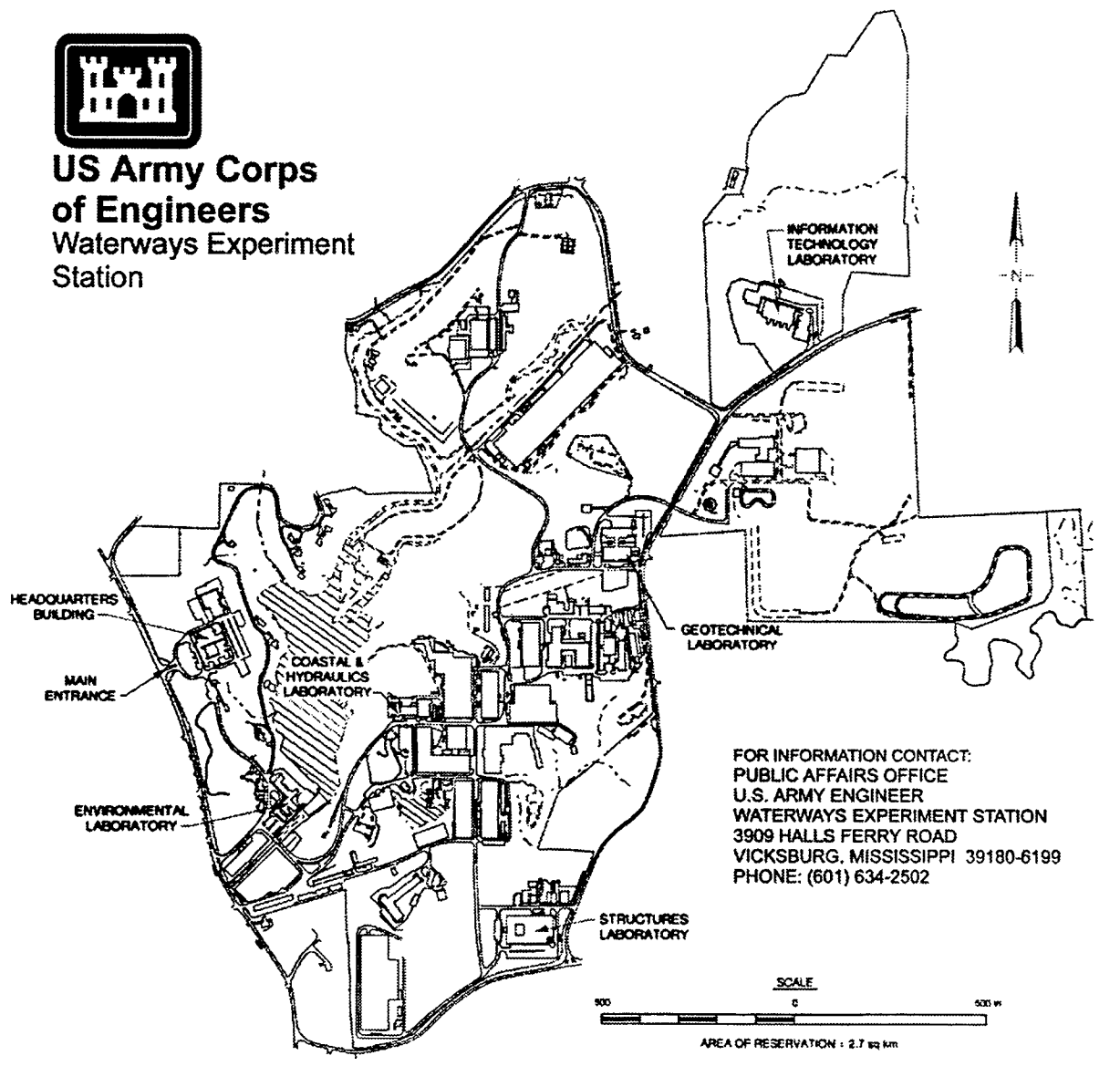
Final report

Approved for public release; distribution is unlimited

Prepared for Discretionary Research Program
 U.S. Army Engineer Waterways Experiment Station
 3909 Halls Ferry Road, Vicksburg, MS 39180-6199
and Army Environmental Center
 Aberdeen Proving Ground, MD 21010



**US Army Corps
of Engineers**
Waterways Experiment
Station



Waterways Experiment Station Cataloging-in-Publication Data

Howington, Stacy E.

Discrete network modeling for field-scale flow and transport through porous media / by Stacy E. Howington, John F. Peters, Tissa H. Illangasekare ; prepared for Discretionary Research Program, U.S. Army Engineer Waterways Experiment Station and Army Environmental Center.

315 p. : ill. ; 28 cm. -- (Technical report ; CHL-97-21)

Includes bibliographic references.

1. Porous materials. 2. Inhomogeneous materials. 3. Transport theory -- Discrete ordinates method -- Mathematical models. I. Peters, John F. II. Illangasekare, T. H. III. United States. Army. Corps of Engineers. IV. U.S. Army Engineer Waterways Experiment Station. V. Coastal and Hydraulics Laboratory (U.S. Army Engineer Waterways Experiment Station) VI. Laboratory Discretionary Research Program (U.S. Army Engineer Waterways Experiment Station) VII. U.S. Army Environmental Center. VIII. Title. IX. Series: Technical report (U.S. Army Engineer Waterways Experiment Station) ; CHL-97-21.

TA7 W34 no.CHL-97-21

Contents

1	Background and Document Format	1
1.1	Groundwater Contamination	1
1.2	Natural Heterogeneity and Scales of Interest	2
1.3	Remediation in Naturally Heterogeneous Media	4
1.3.1	Tools for Assessing Remediation Plans.	4
1.3.2	Practical Problems.	5
1.4	Document Outline	6
2	Continuum Mechanics and Heterogeneous Media	7
2.1	The Representative Elementary Volume	8
2.2	Problems with the Traditional REV Concept	12
2.2.1	Indifference and Invariance.	13
2.2.2	Local Continuum.	13
2.3	The Weight-Function Approach	15
2.4	Consequences of a Continuum Approach in Natural Soils	16
2.4.1	Scale Dependence of Parameters.	16
2.4.2	Inadequate Coupling.	17
2.5	Problem Summary	18
3	Process Descriptions and Problem Definition	19
3.1	Saturated Fluid Flow	19
3.1.1	Flow in a Single Pore.	19
3.1.2	Flow Through a Pore Network.	21
3.1.3	Macroscopic Preferential Flow in Heterogeneous Media.	21
3.2	Conservative Solute Transport	24
3.2.1	Molecular Diffusion.	25
3.2.2	Taylor Dispersion.	25
3.2.3	Pore-Scale Transport Equation.	28
3.2.4	Flow Branching.	28

3.2.5	Path-Dependent Travel Time.	30
3.2.6	Classical Macroscopic Transport Equation.	30
3.2.7	Field-Scale Transport in Heterogeneous Media.	30
3.3	Immiscible Fluid Flow	33
3.3.1	Capillary Barriers.	34
3.3.2	Capillary Entrapment.	34
3.3.3	Capillary Hysteresis.	34
3.3.4	Fingering.	35
3.4	Effects of Heterogeneity	35
3.4.1	Asymptotic Parameters.	36
3.4.2	Pre-Asymptotic Parameters.	36
3.4.3	Breakdown of the Advection-Dispersion Equation.	40
3.4.4	Phase Dispersion in Immiscible Flow.	44
3.4.5	Other Complications.	44
4	Modeling Philosophies and the Proposed Approach	45
4.1	Asymptotic Effective Parameters	48
4.1.1	Asymptotic Effective Conductivity.	48
4.1.2	Asymptotic Macrodispersivity.	49
4.2	Pre-Asymptotic and Non-Asymptotic Coefficients	50
4.3	Discrete Medium Models	53
4.4	Approach Selected for the Present Work	56
5	Discrete Network Modeling for Flow and Conservative Transport Through Porous Media	57
5.1	Background	58
5.1.1	Scale Dependence of Parameters.	58
5.1.2	Non-Fickian Dispersion.	61
5.1.3	Scale Separation.	61
5.1.4	Stochastic Continuum versus Stochastic Discrete Models.	62
5.1.5	Overview of Stochastic Discrete Medium Modeling.	65
5.1.6	Discrete Network Modeling.	66
5.2	Justification of the Network Approach	67
5.2.1	The Network as a Discrete Approximation of Non-local Equations.	68
5.2.2	Comparison to High-Resolution Continuum Models.	70
5.3	Brief Description of the Model	71
5.3.1	Creation of the Network.	71
5.3.2	Governing Equations for Fluid Flow.	73

5.3.3	Conservation of Fluid Mass at the Connections.	76
5.3.4	Remark on Solution Variables.	76
5.3.5	Time Integration.	77
5.3.6	Solution Procedure.	77
5.3.7	Transport.	77
5.3.8	Throat Discretization.	78
5.3.9	Time Advancement.	80
5.3.10	Observation of the Network.	80
5.4	Selected Results from the Network Model	83
5.4.1	Growth of a Plume From an Instantaneous Source.	83
5.4.2	Growth of a Plume From a Continuous Source.	85
5.4.3	Demonstration of Density Dependent Flow.	91
5.5	Parallel Computer Implementation	91
5.5.1	Load Balancing.	91
5.5.2	Performance.	93
5.6	Summary of Findings	94
6	Conditioning Isotropic, Discrete Networks to Match Observed Prop-	
	erties of Flow and Tracer Migration in Porous Media	97
6.1	Structure of the Network	98
6.1.1	Basic Structural Scales.	98
6.1.2	Throat Characteristics.	99
6.1.3	Throat Length Distribution.	99
6.2	Predicting Effective Conductivity	102
6.2.1	Stochastic Theory Predictions.	102
6.2.2	Mapping Throat Conductivities to Connections.	103
6.2.3	Numerical Experimentation for Effective Conductivity.	106
6.2.4	Analysis of Results for Effective Conductivity.	112
6.3	Predicting Apparent Dispersivity	119
6.3.1	Statistics of Dispersion.	119
6.3.2	Numerical Experimentation for Contaminant Transport	124
6.3.3	Analysis of Results for Transport.	135
6.4	Creating Networks to Match Macroscale Observations	145
6.4.1	Network Parameters.	150
6.4.2	Matching Apparent Dispersivity.	150
6.4.3	Matching Effective Conductivity.	154
6.4.4	Matching Porosity.	155
6.4.5	Application of the Conditioning Procedure.	156
6.5	Creating Networks From Laboratory-Scale Observations	158

6.5.1	Hydrogeologic Units.	158
6.5.2	Sub-Unit Statistical Distributions.	159
6.6	Conclusions	162
7	Detailed Analysis of Flow and Transport Behavior in A Macroscopic, Discrete Network Model of Porous Media	163
7.1	Saturated Fluid Flow	164
7.1.1	Analytical Solutions for Steady, Saturated Flow	165
7.1.2	Comparison to Laboratory Measurements of Steady, Saturated Fluid Flow	169
7.1.3	Transient, Saturated Flow :	177
7.2	Conservative Transport in Steady, Saturated Flow	183
7.2.1	Instantaneous Point Source of Tracer.	186
7.2.2	Continuous Point Source of Tracer.	194
7.2.3	Continuous Boundary Source of Tracer.	194
7.2.4	Summary of the Comparisons with Advection-Dispersion Theory.	196
7.2.5	Comparison of the Network Model Against Laboratory Data.	196
7.3	Density-Dependent Flows	209
7.4	Conclusions	209
8	Discrete Network Modeling of Immiscible Flow Through Porous Media	212
8.1	Immiscible Fluid Flow in Heterogeneous Media	213
8.1.1	Capillary Barriers and Capillary Entrapment.	213
8.1.2	Channeling or Fingering.	215
8.2	Modeling Approaches	215
8.2.1	Continuum-Based Flow Equations.	215
8.2.2	Streamtube or Streamline Modeling.	218
8.2.3	Network Modeling.	218
8.3	Discrete Numerical Modeling Philosophy for Immiscible Flow	219
8.4	Numerical Approximation for Immiscible Flow	219
8.4.1	Assigning Throat Properties.	219
8.4.2	Flow Solution in Each Throat.	220
8.4.3	Conservation of Fluid Mass at the Connections.	221
8.5	Results of Network Model Simulation	221
8.5.1	Immiscible Displacement.	223
8.5.2	Spontaneous Imbibition.	223
8.5.3	Primary Drainage.	223

5.1	Observed variation in dispersivity with distance traveled (modified from Anderson [2]).	60
5.2	Hypothetical distribution of characteristic lengths in an idealized medium (above) and a more realistic soil (below).	63
5.3	Schematic of multi-scale heterogeneity in porous media (adapted from Herrmann et al. [65]).	64
5.4	Creating a separation between the scale of averaging and the scale of observation.	69
5.5	A coarse, two-dimensional network with the extent of the simulation domain (in white) lying with the gray bounding box.	72
5.6	Translation of segment boundaries in response to a linear flux profile.	79
5.7	Observation of the actual medium and the network.	81
5.8	A two-dimensional schematic showing the mapping of network data to nodes in the visualization mesh.	82
5.9	Normalized average head, concentration and velocity as a function of averaging area.	84
5.10	Concentration fields from an impulse source of tracer. The field is shown early in its development (top), after 1500 days (middle), and after 2500 days (bottom). Red indicates higher concentration and blue, lower concentration.	86
5.11	A single snapshot of the developed plume shown in successively greater detail. The images show the entire domain (top), the center quarter of the domain (middle), and a very small fraction of the domain at the center (bottom).	87
5.12	The travel distance of the centroid of an instantaneous-source plume versus its rate of growth and an empirical equation by Arya et al. [4].	88
5.13	Contours of the spatially averaged concentration field for the continuous source (red is higher concentration, blue is lower).	89
5.14	Comparison of the network model to the advection dispersion theory for the continuous point source.	90
5.15	Time evolution of the dense wedge. Time sequence is upper left (initial condition), upper right, lower left, lower right.	92
5.16	The number of processors versus the speedup.	95
6.1	Structural hierarchy in the network.	100
6.2	Diagram of a patch of throats.	105

6.3	Histograms of ln throat conductivity for experiment series 2D1. Upper left, 2D1A, upper right, 2D1B, lower left, 2D1C, and lower right, 2D1D. These distributions are virtually identical for all other experiment series.	109
6.4	Histograms of throat length for the two-dimensional networks. Upper left, 2D1, upper right, 2D2, lower left, 2D3, and lower right, 2D4. . .	110
6.5	Histograms of throat length for the three-dimensional networks. Upper, 3D1, and lower, 3D2.	111
6.6	Contours of patch-renormalized ln conductivity (K_{xx}) for experiments 2D3A (top) and 2D3B (bottom). Reds indicate higher conductivity values and blues, lower.	113
6.7	Contours of patch-renormalized ln conductivity (K_{xx}) for experiments 2D3C (top) and 2D3D (bottom). Reds indicate higher conductivity values and blues, lower.	114
6.8	Contours of patch-renormalized ln conductivity (K_{xy}) for experiments 2D3A (top) and 2D3B (bottom).	115
6.9	Contours of patch-renormalized ln conductivity (K_{xy}) for experiments 2D3C (top) and 2D3D (bottom).	116
6.10	Contours of total head for experiments 2D3A (top) and 2D3B (bottom).	117
6.11	Contours of total head for experiments 2D3C (top) and 2D3D (bottom).	118
6.12	Comparison of conductivities from the network, various means, and stochastic theory for experiment series 3D1.	120
6.13	Predicted effective conductivity versus measured effective conductivity for all experiments.	121
6.14	A scale effect in conductivity demonstrated by the network model. .	122
6.15	Contours of tracer concentration for developed plumes in experiments 2D3A (top) and 2D3B (bottom).	126
6.16	Contours of tracer concentration for developed plumes in experiments 2D3C (top) and 2D3D (bottom).	127
6.17	Contours of tracer concentration for developed plumes in experiments 2D1C (top) and 2D2C (bottom).	128
6.18	Contours of tracer concentration for developed plumes in experiments 2D3C (top) and 2D4C (bottom).	129
6.19	Isosurface and contours of tracer concentration for experiment 3D1C. Red indicates lower concentrations, blue, higher.	130
6.20	Apparent longitudinal dispersivity versus centroid travel distance for series 2D3.	131

6.21	Apparent lateral dispersivity versus centroid travel distance for series 2D3.	132
6.22	Apparent longitudinal dispersivity versus plume size for series 2D3.	133
6.23	Apparent lateral dispersivity versus plume size for series 2D3.	134
6.24	Apparent longitudinal dispersivity for ln throat conductivity variance of 4.0 with different throat length distributions.	136
6.25	Apparent lateral dispersivity for ln throat conductivity variance of 4.0 with different throat length distributions.	137
6.26	Transport statistics for experiment 2D3B.	141
6.27	Normalized velocity deviations versus standard deviation in throat conductivity for the two-dimensional experiments.	143
6.28	Normalized velocity deviations versus standard deviation in throat conductivity for the three-dimensional experiments.	144
6.29	Correlation terms versus throat conductivity deviations for a single experiment series (2D2).	146
6.30	Empirical predictions of the correlation term versus network model observations.	147
6.31	Empirical predictions and network observations of apparent longitudinal dispersivity.	148
6.32	Empirical predictions and network observations of apparent lateral dispersivity.	149
6.33	A nomograph for asymptotic, apparent dispersivity in two-dimensional networks.	152
6.34	A nomograph for asymptotic, apparent dispersivity in three-dimensional networks.	153
6.35	An example, exponential semi-variogram for hydraulic conductivity.	160
7.1	Steady flow between two ditches in a confined, homogeneous aquifer. Contours of the piezometric surface (top) and cross-section comparing network results and the analytical solution for Darcy flow (bottom).	166
7.2	Steady flow to a well in a confined, homogeneous aquifer. Contours of the piezometric surface (top) and comparison of network results and analytical solution (bottom).	168
7.3	Diagram of the experimental tank at the University of Colorado (from Illangasekare [70]).	170
7.4	Location and numbering of the sampling ports.	171
7.5	Contours of total head for the experimental tank [51] (top) and the network model (bottom) for HMTE1.	174

7.6	Distribution of materials in the experimental tank. Red indicates #8 sand, orange, # 16 sand, green, #30 sand, blue, #70 sand, and navy, #110 sand.	176
7.7	Ln-transformed, connection-averaged conductivity contours for the network with explicit structure (top) and the network with statistical structure (bottom).	178
7.8	Computed head fields with the heterogeneous packing.	179
7.9	Transient flow to a well in a confined, homogeneous aquifer. Contours of the piezometric surface (top) and comparison of network results and analytical solution (bottom) for an elapsed time of 15 days. . . .	181
7.10	Comparison of network simulation and analytical solution at a fixed position for transient flow to a well in a confined, homogeneous aquifer.	182
7.11	A transient pressure wave moving through a homogeneous porous medium. Contours of the piezometric surface (top) and comparison of network results and analytical solution (bottom) for an elapsed time of 12 days.	184
7.12	A schematic showing dimensions of the domain and the point of injection.	187
7.13	Lateral cross-sections through plumes predicted by the advection dispersion equation and the network model for an instantaneous source of contaminant.	189
7.14	Longitudinal cross-sections through plumes predicted by the advection dispersion equation and the network model for an instantaneous source of contaminant.	190
7.15	Plume characteristics for constant and scale-dependent dispersivities.	192
7.16	Concentration breakthrough curves taken at (1158, 800, 780) for the network plume and two ADE solutions.	193
7.17	ADE and network simulation concentration profiles along the approximate centerline of a plume from a continuous point source injection of tracer.	195
7.18	Dispersivities computed from a moving concentration front and an instantaneous point source of tracer.	197
7.19	Speed of the median concentration for the moving front problem and the speed of the centroid of a plume from an instantaneous injection.	198
7.20	Simulated and measured concentration breakthrough curves for HMTE7.	200
7.21	The sample domain, the computational subdomain, and contours of concentration for HMTE1.	202

7.22	Simulated and measured concentration breakthrough curves for HMTE1 (Port 13).	203
7.23	Simulated and measured concentration breakthrough curves for HMTE1 (Port 12).	204
7.24	Interconnection spacing versus peak concentration at port 13.	205
7.25	Concentration plumes for the network with explicit structure (above) and statistical structure (below) HTTE4.	206
7.26	Simulated and measured concentration breakthrough curves for HTTE4 with explicit structure.	207
7.27	Simulated and measured concentration breakthrough curves for HTTE4 with statistical structure.	208
7.28	Time series of the overturning of an unstable density configuration. Elapsed time increases from upper left (initial condition), to upper right (6000 s), to lower left (14000 s), to lower right (20000 s). Red indicates higher concentration and blue indicates lower concentration.	210
7.29	Alternative contouring for an elapsed time of 14000 s in the overturning problem. Red indicates relative concentration greater than 0.25 and blue indicates relative concentration smaller than 0.25.	211
8.1	Experimental observation of a capillary barrier caused by a fine grain lens and capillary entrapment in a coarse-grain lens (from Illangasekare et al. [71]).	214
8.2	Observed distribution of non-aqueous contaminant showing macroscale entrapment and evidence of macroporous breakthrough [22].	216
8.3	Procedure for filling voids in the throats.	222
8.4	Contours of apparent saturation for fine observation of immiscible displacement.	224
8.5	Contours of apparent saturation for coarse observation of immiscible displacement.	225
8.6	Contours of spatially-averaged entry head for the two-dimensional porous slab.	226
8.7	Contours of apparent saturation for imbibition in the network.	227
8.8	Contours of apparent saturation for gravity drainage in the network.	229
8.9	Capillary pressure versus wetting-fluid saturation for drainage and imbibition.	230
8.10	Diagram of the material types used to simulate a capillary barrier. The green material around the exterior defines a bounding box used only for network generation.	232
8.11	Contours of entry head for the capillary barrier problem.	233

8.12	Contours of apparent saturation for the capillary barrier problem. .	234
8.13	Contours of apparent saturation showing localized breakdown of the capillary barrier problem.	235
9.1	Histogram of concentration within a single observational-averaging volume.	241

List of Tables

1.1	General length scale categories for heterogeneity.	3
6.1	Numerical Experiment Matrix	107
6.2	Basic properties of the networks in the experiment matrices.	108
6.3	Results from Flow and Transport Simulations.	138
6.4	Examples of conditioned networks.	157
7.1	Network Properties.	186

Preface

This report is a dissertation in partial fulfillment of the requirements for the degree of Doctor of Philosophy from the University of Colorado at Boulder. This study was supported by the Laboratory Discretionary Research Program at the U.S. Army Engineer Waterways Experiment Station (WES), the Army Environmental Center, and the Strategic Environmental Research and Development Program.

This report is being published by the WES Coastal and Hydraulics Laboratory (CHL). The CHL was formed in October 1996 with the merger of the WES Coastal Engineering Research Center and Hydraulics Laboratory. Dr. James R. Houston is the Director of the CHL, and Messrs. Richard A. Sager and Charles C. Calhoun, Jr., are Assistant Directors. Dr. Jeffery P. Holland directs the Groundwater Modeling Program.

This report was written by Stacy E. Howington. Dr. Tissa H. Illangasekare (University of Colorado) served as thesis director. Dr. John F. Peters (WES) served as technical advisor and thesis reader. Dr. Robert S. Maier (Army High-Performance Computing Research Center) guided the parallelization of the numerical model. Ms. Donna C. Barnard and Ms. Tamara L. Butler generated many figures in this report. Dr. Jane M. Smith reviewed a portion of the draft text. Mr. Joseph H. Schmidt provided an iterative matrix solver subroutine. Dr. Illangasekare provided data sets from ongoing laboratory experiments at the University of Colorado.

At the time of publication of this report, Director of WES was Dr. Robert W. Whalin.

The contents of this report are not to be used for advertising, publication, or promotional purposes. Citation of trade names does not constitute an official endorsement or approval for the use of such commercial products.

Chapter 1

Background and Document Format

An adequate supply of clean, drinkable water is plainly one of our most basic needs. The earth's subsurface provides thirty-five percent of the total municipal water supply and most rural drinking water in this country [145]. Contamination of this important resource poses serious health concerns and is forcing our society to weigh public safety against the cost of cleanup. Cleaning up contaminated groundwater resources requires an in-depth understanding of fluid flow and constituent transport and transformation processes.

The goal of this research is to improve our ability to predict groundwater flow and contaminant transport behavior in heterogeneous media to support remediation design and decision making. Toward that end, this work shows that macroscopic, stochastic, discrete-network modeling is an effective tool for predicting flow and transport behavior in porous media. This first chapter provides a foundation for the work that follows by establishing the importance of numerical modeling in groundwater remediation and by discussing problems encountered by practicing engineers and scientists using current techniques.

1.1 Groundwater Contamination

Leaking underground storage tanks, uncontained surface spills, and inadequate refuse disposal have caused widespread contamination of our subsurface water resources, a problem that represents an enormous future burden to our society. For example, contamination at Department of Defense (DoD) facilities is a major obstacle to military base closure plans and the return of these lands to public use. Thanks to the earth's resilience, pollution at some sites can be remedied by extract-

ing any persisting sources of contaminant and allowing natural processes to degrade or dilute the remaining contaminant. However, at many sites, natural attenuation is not sufficient and we must remove the offending substances. Unfortunately, efforts beyond natural attenuation are costly and their effectiveness is uncertain. Using current remediation practices, estimates for cleanup costs at DoD sites are near 30 billion dollars [104]. The potential for sizable cost savings, both within and outside the government, is fueling much research in groundwater remediation technology.

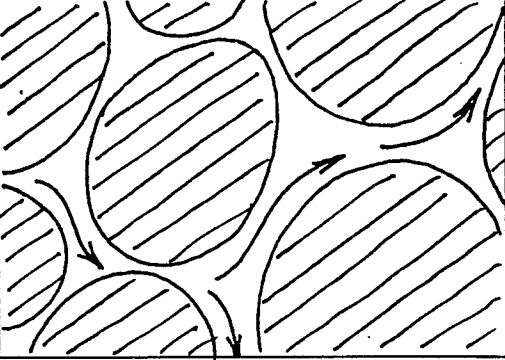
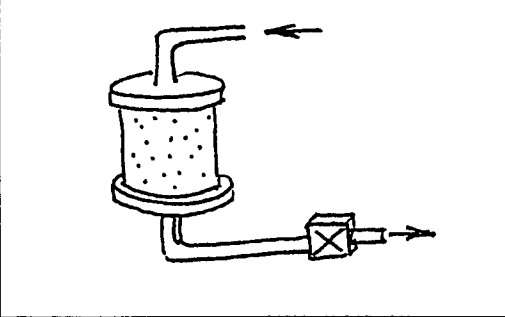
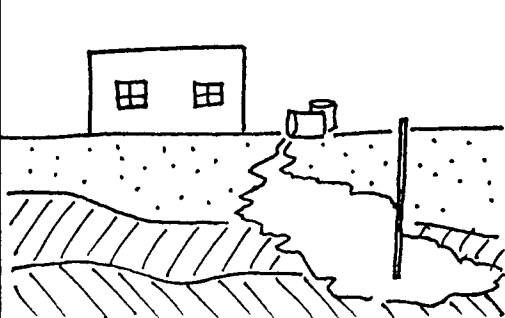
No two remediation problems are identical, greatly complicating the task of developing clean-up strategies. The soil's physical, chemical, and biological fabric vary from site to site. Further, detailed fluid flow patterns and the composition of contaminants are unique to each site. For these reasons, we cannot rely on historical performance of a remediation strategy to predict its utility at another site. Each contaminated site must be considered individually.

1.2 Natural Heterogeneity and Scales of Interest

Any mention of 'homogeneous' media implies averaging over a spectrum of scales. Porous media consist of soil particles and voids and, therefore, are heterogeneous at the scale of individual particles. Natural sediments are also heterogeneous at larger scales because the soil particles' shapes and sizes and the depositional processes that placed them are not uniform. The resulting spatial variability in physical structure causes a great assortment of characteristic length and time scales in flow and transport behavior. Table 1.1 shows geological features of interest occurring from the size of individual pores to the scale of the basin and defines spatial scale labels that are adopted in this work. These definitions do not imply a discrete hierarchy of scales of heterogeneity, as porous media may display a continuous spectrum of characteristic lengths [26].

In the past, heterogeneity beneath the aquifer unit has been neglected. This is so because regional-scale water supply analyses seek composite fluxes at the tens-of-meters scale and smaller-scale variations in the flow field are inconsequential. However, when considering transport through porous media, the range of spatial and temporal scales of importance increases substantially. For systems containing hydrologic and chemical processes, the range of significant length scales extends over 15 orders of magnitude and the time scale over 17 orders of magnitude [37]. The implications of such a wide range of scales of interest are significant and will be discussed in the chapters that follow.

Table 1.1: General length scale categories for heterogeneity.

<p>pore scale (less than 1 mm)</p>	
<p>laboratory or small scale (1 cm to 1 m)</p>	
<p>macroscopic or engineering or field scale (10 m to 10 km)</p>	
<p>basin scale (greater than 1 km)</p>	

1.3 Remediation in Naturally Heterogeneous Media

Early remediation attempts conceptualized geologic media too simply. Within a stratum defining an aquifer unit, soils normally were assumed uniform, largely because data were not available to characterize strata in more detail. The groundwater remediation community is coming to realize that multi-scale physical, chemical, and biological heterogeneity in porous media render traditional remediation technologies uncertain, if not altogether ineffective [105]. Consequently, few sites can be declared clean, despite the billions of dollars that have been spent on groundwater remediation [16, 147]. Today, the effects of heterogeneity are appreciated, if not well understood, and remediation schemes are being designed accordingly. For example, simple pump-and-treat methods are being abandoned as stand-alone solutions. When evaluated in homogeneous laboratory samples and with numerical models of homogeneous media, pump-and-treat methods seemed appropriate. However, when installed in naturally heterogeneous soils, these schemes have required an intolerable amount of time to 'sweep' contaminants from the medium. On closer inspection, the role of heterogeneity becomes clear. Contaminants in higher permeability regions are removed readily by the passing water but those in lower permeability regions are effectively trapped by the absence of local fluid flow. In extreme cases, contaminant in low permeability regions may move only by molecular diffusion. Innovative schemes are emerging to remediate contaminants in low permeability zones. However, additional physical and chemical processes associated with these schemes dramatically increase the complexity of these systems. Without effective tools to anticipate performance of these methods in real media, costly, long-term, site-specific, field-scale remediation trials will be needed.

1.3.1 Tools for Assessing Remediation Plans.

Often, careful consideration must be given to several candidate remediation strategies before one or more is selected for a particular site. The high cost of field construction and project operation requires well-planned remediation schemes whose effectiveness is judged before field work begins. Constructing a full-scale or pilot-scale remediation scheme to evaluate its abilities is seldom practical. Analytical evaluations are limited to gross simplifications of the field setting and normally are only useful for preliminary screening of alternatives or simple numerical model testing. Thus, by elimination, numerical simulation is a primary tool for remedial scheme assessment.

Remediation plans must be assessed at the engineering or macroscopic scale as defined in Table 1.1. Even with recent and anticipated computing advances, pore

scale simulations are impossible even for moderately-sized laboratory samples. We are resigned to analyses performed at time and length scales much coarser than the scales of the smallest and quickest processes, meaning that we must be content to substitute constitutive parameters for indescribable detail [37].

1.3.2 Practical Problems.

Laboratory testing and numerical modeling suffer important weaknesses in heterogeneous media. Problems encountered by practitioners in this field include:

- *Laboratory-derived parameters may not apply at the field scale.* Laboratory testing is useful only if the parameters that result are applicable at the scale of the remedial project analysis. Field testing yields parameters that may be orders-of-magnitude different than those obtained by laboratory evaluation of a core from the same site [53]. Because these parameters should be medium/fluid properties, this dependence on scale implies a breakdown in the description of the physics. That is, scale dependence is not only a problem of measurement technique. It is a limitation of the theory that produced the effective, laboratory- or macroscopic-scale parameters we are trying to measure.
- *Interpretation of field and laboratory measurements is difficult.* An instrument does not measure quantities at a mathematical point in space and time. Rather, an instrument provides an average measure over an observation window for a finite duration [24]. The size and shape of this window are usually unknown. Further, variability at many scales implies that a measurement at one location may be significantly different than one taken very nearby. A measurement taken in the same location with a different instrument (and different averaging window) may produce a different result. Also, to ‘measure’ a property, other properties must be known. For example, to estimate sorption behavior from a breakthrough test, the dispersivity must be known. Thus, a problem with understanding one process may impede observing another, even if the second process is adequately understood.
- *Parameters in the governing equations lose their physical significance.* The parameters used in the governing equations depend on how and at-what-scale measurements are made. Therefore, in practice, these ‘properties’ become calibration knobs used to match available observations. The resulting quasi-empirical equations match field behavior in the limited range of conditions for which they were calibrated, but can be poor predictors when conditions change. Lack of precedence in applying a particular scheme at a particular site requires that predictive methods not depend solely on empirical relationships.

In summary, to make measurements and calculations practical, it is necessary to deal with media consisting of several scales that are lumped, for analysis purposes, into regions of homogenized material. The central problem is performing practical measurements and computations at the engineering scale without including the nearly unlimited number of variables necessary to define the medium completely.

1.4 Document Outline

The work described here is the development and testing of an alternative, macroscopic, application-oriented numerical simulation approach that helps assuage some of these practical concerns. The document detailing this work is divided into three major parts with a total of nine chapters. Part I contains four chapters providing the background, problem description, and rationale for the approach chosen. Part II contains four draft journal articles describing the present work. Part III contains a single, brief chapter summarizing this work and suggesting future efforts. An outline of the structure follows, with a brief description of the subject covered within each chapter:

- PART I: Introduction
 - Chapter 1 justifies the need for this work in practical terms.
 - Chapter 2 identifies problems with continuum-mechanical methods.
 - Chapter 3 details the processes to be studied.
 - Chapter 4 rationalizes the approach taken.
- PART II: The Present Work
 - Chapter 5 describes the numerical model for flow and tracer transport.
 - Chapter 6 discusses network creation to match observations.
 - Chapter 7 explores network behavior in more detail.
 - Chapter 8 describes a field-scale network model for immiscible flow.
- PART III: Summary
 - Chapter 9 summarizes this effort and proposes future work.

Because the chapters in Part II are drafts of journal articles and must be understandable as separate documents, the reader must endure some redundancy.

Chapter 2

Continuum Mechanics and Heterogeneous Media

Nature's intricacy confounds attempts to describe its structure and behavior in detail. Historically, scientists and engineers have relied on the continuum hypothesis to permit description of natural processes at a manageable scale [40]. A continuum is a purely mathematical concept valid for describing perfectly continuous bodies. In a mathematical continuum, each point within the material domain is occupied, permitting definition of extensive properties for the medium. Real materials are, of course, discrete and the continuum concept never strictly applies. We must speak in terms of equivalent continuous media that behave the same as real media in some averaged sense. Therefore, the process of constructing a continuum theory involves redistributing discrete data to infinitely many mathematical points within the material domain. Then, well-established techniques of numerical analysis may be applied to reduce the number of degrees of freedom to a manageable level.

This chapter is devoted to application of the continuum hypothesis to porous media. Its purpose is to establish theoretical causes for practical problems described in the preceding chapter (laboratory derived parameters that do not apply at the field scale, difficulty in interpreting lab and field data, and macroscale parameters that have lost their physical significance). This chapter is purposely general because the basic problems are common to many discrete materials. The following chapter will address these same issues for a few specific processes.

A continuum representation for porous media replaces indescribably-fine-scale data with their spatial and temporal averages. This permits us to construct equations and interpret measurements with the averaged variables that are valid at the coarser scale. A simple example using void fraction is shown in Figure 2.1. In the figure, pore scale values for void fraction are binary (0 or 1), but their continuum

representation is a smoothly varying quantity lying somewhere between 0 and 1. Note that the averaging shown in the figure does not reveal any boundary effects, because the averaging window was modified near boundaries to include only the interior of the domain.

According to Baveye and Sposito [7], the classical macroscopic, local continuum view in porous media has rested on two fundamental assumptions:

- The physical properties of the medium are associated with field variables defined at the centroids of representative elementary volumes (REVs).
- The time and space dependence of these field variables can be described with differential balance equations for mass, momentum, and energy.

2.1 The Representative Elementary Volume

Consider the hypothesized variation in an averaged property value with changes in averaging volume. Figure 2.2 shows a hypothetical, porous medium and the cross sections of several, spherical, averaging volumes. Figure 2.3 shows the postulated relationship between averaging volume and an average property value, volumetric porosity.

The shape of the curve in Figure 2.3 has important ramifications and deserves further discussion. Although not the first work to propose the existence of an REV, Bear's exposition [10] may be the most frequently cited in the context of groundwater. Parallel concepts, such as the sensitive volume in fluid mechanics [6], exist in other fields. The following rationale for the REV parallels that of Bear. The property chosen for examination is volumetric porosity, defined as

$$\phi_i(V_i) = \frac{(V_v)_i}{V_i} \quad (2.1)$$

where $(V_v)_i$ is the volume of void space within V_i .

Bear begins with a very large volume V_i centered around a mathematical point Z (as in Figure 2.2). As this volume is decreased, Bear describes the three regimes encountered. For large values of V_i , gradual variations in ϕ_i are observed (as in Figure 2.3). These are caused by macroscopic, stratigraphic layering in the medium. At some scale, depending on the distance from Z to a layer boundary, these fluctuations diminish. Only small amplitude fluctuations in the porosity are observed due to spatial distributions in pore and grain sizes. As the volume declines beneath V_0 and approaches the dimensions of a single pore, observations of porosity vary substantially. As the volume approaches zero, the porosity becomes zero or one, depending on whether Z is located in a void or in a solid. This process could continue

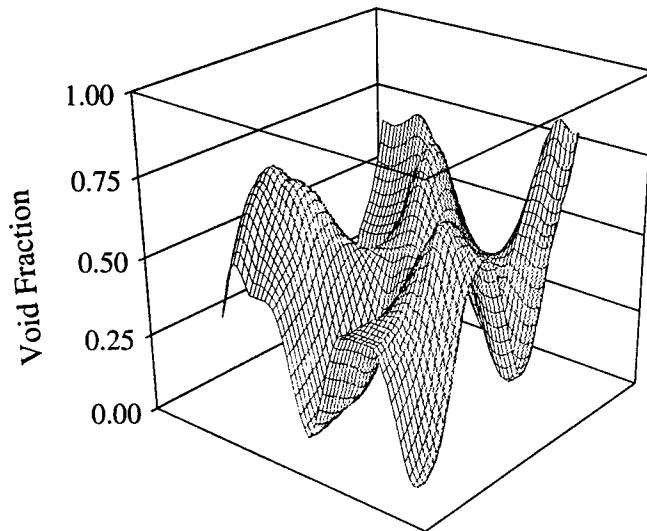
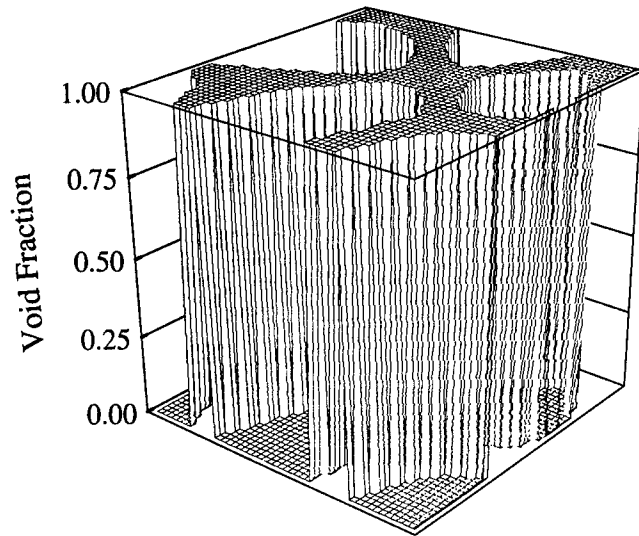


Figure 2.1: Schematic showing maps of local (above) and areally-averaged (below) void fraction.

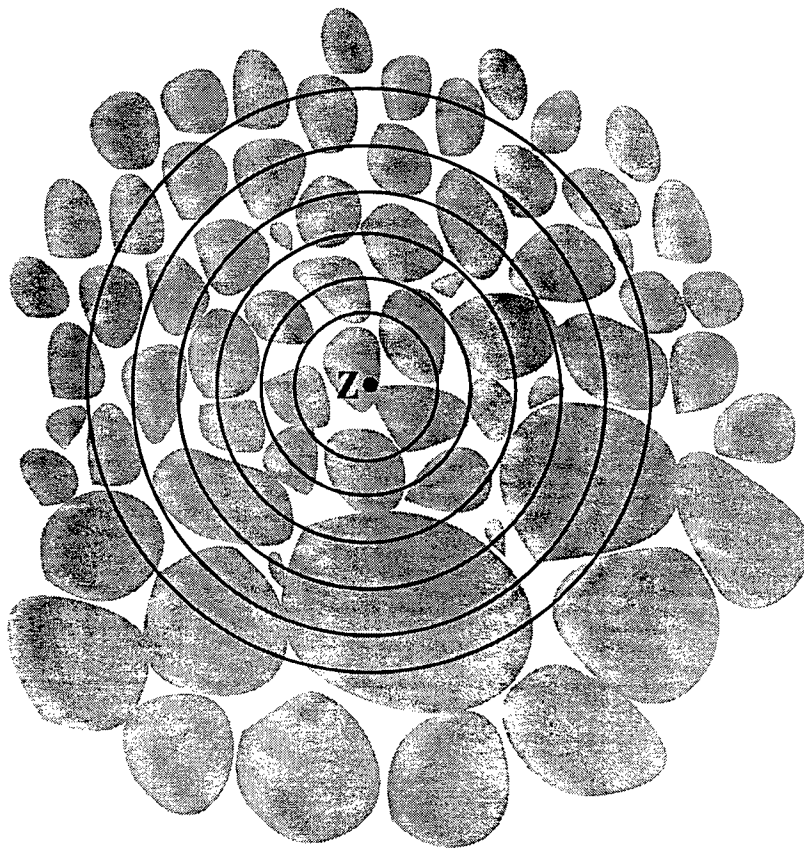


Figure 2.2: Schematic of a porous medium and cross sections through several spherical averaging volumes.

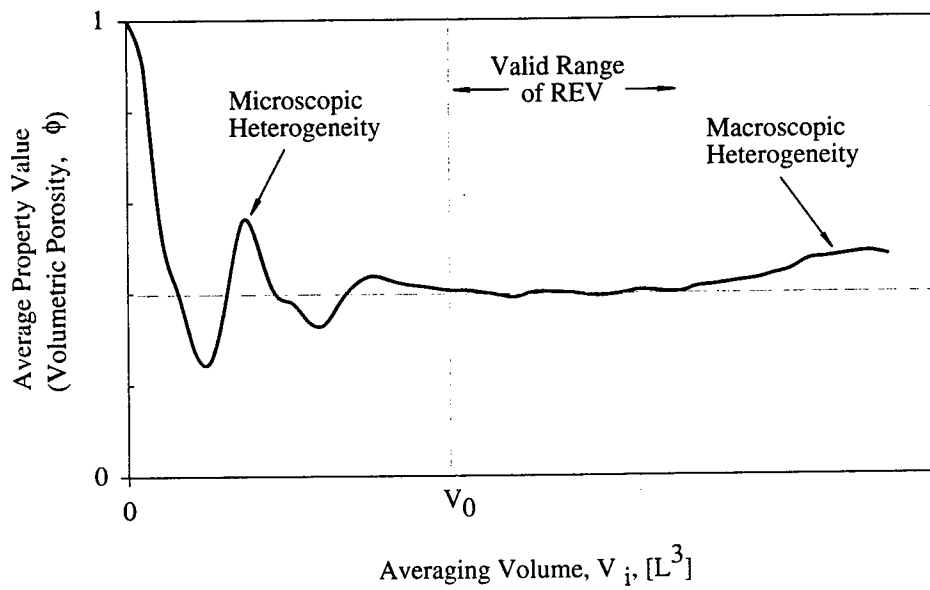


Figure 2.3: Hypothetical volumetric porosity versus the volume of the averaging region (similar to Bear [10], Baye and Sposito [7] and Batchelor [6]).

beneath the fluid continuum or solid continuum to the molecular scale and below. The porosity is defined as

$$\phi(Z) = \lim_{V_i \rightarrow V_0} \frac{(V_v)_i(Z)}{V_i}. \quad (2.2)$$

The volumes V_i and V_v are assumed to vary smoothly which implies that ϕ is a continuous function. The volume V_0 is the REV.

Seeking an ‘unambiguous’ value for the averaged quantity (mass density in his paper), Hubbert [67] extrapolated the plateau in Figure 2.3 toward zero averaging volume and assigned the plateau value to a point in the medium [7]. Marle [90] (as cited in [7]) asserted that the length scale for averaging should correspond to the plateau region in Figure 2.3, so the averaged value will be independent of the averaging region length scale (REV dimension). Bear [10] proposed that the lower limit of this plateau region is the threshold between the microscopic and macroscopic domains and labeled that averaging volume with characteristic length V_0 to be the REV.

The REV dimension is based on the following criteria [11].

- Average values should be independent of the size and shape of the REV.
- Average values should be continuous and infinitely differentiable.
- The linear dimension (D) of the REV should be much greater than the characteristic length of the soil grains (d) and much less than the macroscopic characteristic length over which significant changes in average macroscopic quantities of interest occur (L) [144, 60]. The plateau in Figure 2.3 corresponds to the range of D , such that $d \ll D \ll L$.

Armed with these assumptions, differential conservation equations in terms of the averaged properties can be constructed that are valid in the range of D .

2.2 Problems with the Traditional REV Concept

Although the traditional REV concept has been in use for years in the study of groundwater, it is considered to be too restrictive and theoretically unverifiable in porous media [7, 23]. Whitaker concluded that the REV idea implies a linear variation in the macroscopic variable over the dimension of the REV [144]. Therefore, the continuum approach, in this form, is not applicable for resolving detail beneath the REV scale (e.g., wave propagation with wavelengths shorter than the lower bound of the REV size or a solute plume smaller than the lower bound of the REV [5]).

Baveye and Sposito [7] suggest that the plateau required for the REV definition may not exist. This is supported by Cushman and others [24, 101] who argue that real media possess structure at all scales (so-called 'evolving' heterogeneity) which precludes the existence of an REV.

In heterogeneous media, if a plateau exists for which the average value is insensitive to the averaging volume, the corresponding averaging volume may be large. REV theory asserts that measurement beneath that scale is invalid. By one estimate, the REV for contaminant transport at a particular field site would exceed 100 km in one dimension [97]. Measurements and computations cannot be restricted to such large scales, and must be performed at scales beneath the REV size.

2.2.1 Indifference and Invariance.

The classical REV concept requires that the REV dimension exhibit invariance and indifference [7]. Invariance means that it retains the same geometric character regardless of the time or its spatial position. This requirement was weakened by Cushman [23] so that the REV could deform smoothly in space and time, permitting the study of materials with gradual spatial variation in properties. Indifference means that the REV retains the same configuration regardless of the field variable being averaged. Further, for multiple state variables, a single, common REV must be found for all variables being averaged [5]. Bear and Braester recognized that the REV could be different sizes for different physical properties (Figure 2.4) [12] and that the valid range of the composite REV is the intersection of the individual property ranges.

2.2.2 Local Continuum.

In practice, measurement and computation are made without regard to the size of the representative elementary volume. Even if the dimensions of the REV were computed or estimated (which they are not), nowhere in the usual theory can that size be used. It does not enter into the mathematical description. The tacit assumption is that the REV is small compared to the measurement or computation scale, thus implying a 'local' continuum in the sense of Edelin [39]. Using local continuum mechanics, differential balance laws written for a body of finite dimensions are assumed to apply at a mathematical point as the control volume for which these balances were constructed tends to zero. By definition, the local continuum is defined in terms of infinitesimal elements which can contain no information about the characteristic lengths of the medium. In a local continuum, response depends on properties and state at a point, not on surrounding points.

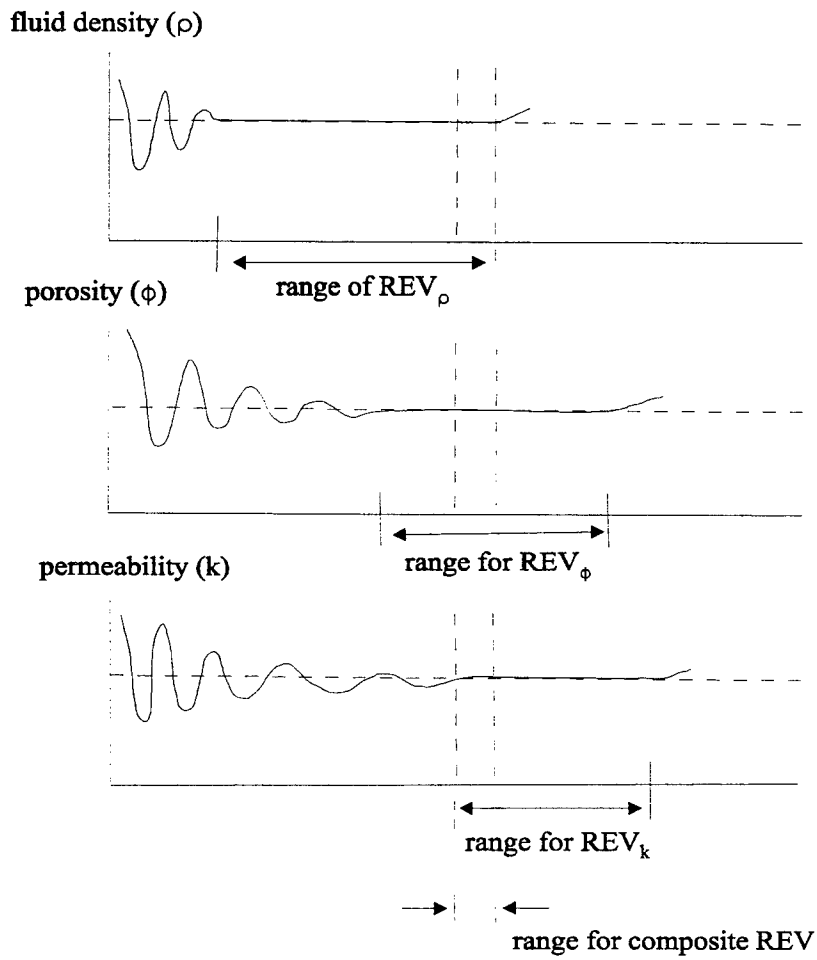


Figure 2.4: Different REV sizes for different properties (modified from Bear and Braester [12]).

Real porous media often are observably not continuous. Variation from the soil grains and pores themselves through depositional layering is often plainly visible with the human eye. These media defy accurate representation with a local continuum approach because the scale of heterogeneity is finite. Thus, properties at a ‘point’ are actually averages of surrounding points. Heterogeneous media are more suited to description with non-local continuum mechanics as in Eringen [41]. Improperly treating the medium as a local continuum is responsible for much of the difficulty with measurement and simulation identified at the end of the last chapter.

2.3 The Weight-Function Approach

The weight function approach was first advocated by Matheron [91] and continued by Marle [90] (cited by [24]) and Baveye and Sposito [7]. This approach includes the REV concept as a special case. In this so-called ‘relativist’ approach, macroscopic variables are defined as convolution products of their microscopic counterparts. For example, the property A would be averaged

$$A_m(x, t) \equiv \int_V A(x - \xi, t) w(\xi, x, t) dV \quad (2.3)$$

where V = averaging volume, $[L^3]$,
 x = position vector, $[L]$,
 ξ = dummy variable of integration, $[L]$,
 t = time, $[T]$, and
 w = weight function.

The weight function is defined such that

$$\int_V w(\xi, x, t) dV \equiv 1. \quad (2.4)$$

The weight function approach to averaging does not assume indifference or invariance and, thus, is more flexible than the REV concept. For a constant w equal to the inverse of the volume, the local volume average (REV) is returned.

Baveye and Sposito [7] suggested that the weight function in the convolution should correspond to the instrument used to measure the property. This approach allows us to resolve differences in measurements taken with different instruments. Baveye and Sposito [7] derived macroscopic balance laws for fluid flow and transport using the convolved average quantities. In theory, these equations are valid at any scale if all measurement and interpretation are performed with the same averaging function. However, this approach assumes that averages are taken in an infinite domain. For now, this approach does not account for the boundaries imposed by measurement practices.

2.4 Consequences of a Continuum Approach in Natural Soils

The continuum approach tries to replace a heterogeneous medium with a homogeneous continuum. When concepts from local continuum mechanics are applied to describe heterogeneous media, several problems arise, including:

- scale dependence of parameters, and
- inadequate description of coupled processes.

2.4.1 Scale Dependence of Parameters.

At the laboratory scale, where most processes are investigated, macroscopic variations cannot be observed. Given enough samples, an estimate of field-scale *variability* may be surmised. Spatial *continuity* or *correlation* of properties, which defines the larger characteristic lengths, is more difficult to extract from spot measurements. Thus, behavior measured at the laboratory-scale must be synthesized to estimate effective behavior at the engineering scale. Processes with characteristic length scales or time scales larger than the scales of measurement exhibit an apparent size or time dependence. Observations made at scales beneath the REV size *must* vary with the scale of observation, a fact that arises from the very definition of an REV. The apparent scale effect explains laboratory-measured values that do not resemble field-scale observations. It also accounts for difficulty in interpreting laboratory and field observations. Even if one adopts the weight function approach, the apparent scale effect will persist because boundary conditions have not been considered. If a boundary lies within the integral-averaging region defined by the weight function, a scale effect in property measurement will emerge.

In heterogeneous porous media, we lack a separation between the processes' characteristic scales and the scale of observation. If a clear scale separation exists, we may use traditional, local-continuum-mechanical ideas to interpret measurements and perform simulations. The following cases are presented using saturated fluid flow as the example process and hydraulic conductivity as the averaged parameter.

- *Process scale* \ll *observation scale*. For this case, we may often average effectively to the observation scale. For example, in a uniform homogeneous porous medium, a rational, constant saturated hydraulic conductivity parameter can be determined to represent the macroscopic effect of pore-scale flow.
- *Process scale* \gg *observation scale*. In this situation, we can resolve the process discretely, including as much detail as is necessary and practical. For

highly resolved pore-scale models, saturated conductivity may be determined simply by accumulating the observation-scale flows and averaging afterward.

- *Fine process scale* \ll *observation scale* \ll *coarse process scale*. Here we may average the fine-scale process and resolve the coarse-scale process. This corresponds to a porous medium composed of several distinct, homogeneous units. Conductivities may be determined at the observation scale and the layering (coarse process scale) may be resolved discretely by spatial variability in the observation-scale parameters. This condition is normally assumed in remediation modeling.

When the characteristic length for a process and the observation scale are similar, this traditional philosophy breaks down. Unfortunately, in natural soils, this condition may very common.

2.4.2 Inadequate Coupling.

When volume averaging is performed, information about variability beneath the size of the averaging volume is lost. If a mean value is sought, the lost information may not be important. However, if two properties in a coupled process are averaged to the macroscopic scale before they are coupled (e.g., multiplied), the result may be different than would be obtained by performing the averaging after coupling. That is, the average of products may not equal the product of averages. For example, let A and B be properties to be averaged. Express these quantities as mean values (denoted by the overlines) plus zero-mean perturbations (indicated with primes),

$$\begin{aligned} A &= \bar{A} + A', \\ B &= \bar{B} + B'. \end{aligned}$$

The averages of A and B are, obviously, \bar{A} and \bar{B} , and the product of their averages is $\bar{A} \cdot \bar{B}$. If we take the mean of the product of A and B , we have

$$\overline{A \cdot B} = \overline{(\bar{A} + A') \cdot (\bar{B} + B')} = \bar{A} \cdot \bar{B} + \overline{A' \cdot B'}. \quad (2.5)$$

The right side of this equation contains the product of the averages and an average of the product of the perturbations. If A and B are uncorrelated and the sample population is sufficiently large, the average of the product of perturbations will be zero. However, if A and B are correlated, it follows that the discrepancy will grow as the variance in the distributions of A and B increase. When averaging heterogeneous properties, structure and variability may be lost over a wide range of scales. Often, constitutive laws are simply attempts to recover the macroscopic effects of this lost microscopic information ($\overline{A' \cdot B'}$).

In the context of groundwater, consider the coupling between conductivity (K) and head (H) in steady flow through a one-dimensional, heterogeneous medium [10].

$$\frac{\partial}{\partial x} K \frac{\partial H}{\partial x} = K \frac{\partial^2 H}{\partial x^2} + \frac{\partial K}{\partial x} \frac{\partial H}{\partial x} = 0. \quad (2.6)$$

When we homogenize this medium by seeking a composite, constant conductivity, we replace this equation with

$$K_e \frac{\partial^2 H}{\partial x^2} = 0 \quad (2.7)$$

where K_e is the effective conductivity. However, unless K is spatially uniform or the spatial derivatives of K and H are random and uncorrelated, Equation 2.6 does not *behave* like Equation 2.7. This problem does not arise because our statistical sample size is inadequate. There is no single value for K_e that captures the behavior of both terms in Equation 2.6. This problem may manifest itself as an apparent scale effect.

Constitutive theories are required to ‘close’ the system of equations produced by balance laws. These constitutive theories necessarily are quasi-empirical in their origins and are ‘proven’ by their ability to reproduce a few, specific behaviors. If the observations used to ‘prove’ the constitutive theory are from a limiting case, such as long-time behavior, the theory may not be universally valid. In this regard, observation-scale heterogeneity has caused time-tested methods from homogeneous analyses to fail in some cases. In these cases, parameters become the calibration knobs discussed in the prior chapter. Again, a pertinent example is conservative transport. In a particular soil, a plume’s growth rate due to dispersion may become nearly constant after travelling several thousand meters and its growth beyond that point will be described well by traditional, asymptotic theory. However, if the questions being asked are on the tens or hundreds of meters scale, the asymptotic transport equation is not useful.

2.5 Problem Summary

There are two key problems that hinder our description of heterogeneous materials. First, there may be finite-size structures in the material. Second, fine-scale variables may not be independent random distributions and macroscopic effects of their correlation may be significant and difficult to capture.

Chapter 3

Process Descriptions and Problem Definition

Before complex chemical and biological processes in porous media may be studied effectively, the basics of fluid flow and conservative transport must be mastered. The processes chosen for detailed study in this work are:

- saturated, Darcian fluid flow,
- advection-dominated, conservative transport, and
- flow of multiple, immiscible fluids.

Although the volume of literature on these subjects is daunting, unresolved problems persist. To be valid in multi-scale heterogeneous media, solutions to these problems should be process oriented and not macroscopic, empirical descriptions. For this reason, a detailed review of the physical processes and the classical governing equations at both the microscopic and macroscopic scales is warranted. This chapter concludes by describing the difficulties encountered by the present methods when confronted with heterogeneity.

3.1 Saturated Fluid Flow

3.1.1 Flow in a Single Pore.

At the scale of a pore (still large enough for the assumption of a fluid continuum to be valid) the Navier-Stokes equations describe fluid motion [13]. For incompressible flow (constant fluid density, ρ_f), the equation of fluid flow is

$$\frac{\partial \mathbf{u}}{\partial t} + \mathbf{u} \cdot \nabla \mathbf{u} = -\frac{1}{\rho_f} \nabla P + \nu \nabla^2 \mathbf{u} + \mathbf{g} \quad (3.1)$$

where \mathbf{u} = fluid velocity, $[LT^{-1}]$,
 t = time, $[T]$,
 ρ_f = fluid density, $[ML^{-3}]$,
 P = fluid pressure, $[ML^{-1}T^{-2}]$,
 ν = kinematic viscosity of the fluid, $[L^2T^{-1}]$, and
 \mathbf{g} = gravitational acceleration, $[LT^{-2}]$.

Bold variables indicate vector quantities. Square brackets contain the fundamental dimensions of each variable in mass (M), length (L), and time (T) units.

The momentum transport equation (Equation 3.1) may be recast in non-dimensional form [82], and rearranged to give,

$$\frac{a^2}{\nu T} \frac{\partial \mathbf{u}^*}{\partial t^*} + Re \mathbf{u}^* \cdot \nabla^* \mathbf{u}^* = -\frac{aP_0}{U\nu\rho_f} \nabla^* P^* + \nabla^{*2} \mathbf{u}^* + \frac{a^2 \mathbf{g}}{U\nu} g^* \quad (3.2)$$

where $Re = aU/\nu$, the Reynolds number, $[-]$,
 a = characteristic length (perhaps the radius of the pore), $[L]$,
 T = characteristic time, $[T]$,
 P_0 = reference pressure, $[ML^{-1}T^{-2}]$,
 U = maximum fluid velocity magnitude in the pore, $[LT^{-1}]$,
 \mathbf{g} = magnitude of the gravitational acceleration, $[LT^{-2}]$.

The variables are non-dimensionalized by physical quantities relevant to the problem,

$$\begin{aligned} \mathbf{u}^* &= \frac{\mathbf{u}}{U} \\ P^* &= \frac{P}{P_0} \\ t^* &= \frac{t}{T}, \\ \nabla^* &= \nabla a, \\ g^* &= \frac{g}{g}. \end{aligned}$$

If the Reynolds number is very small compared to the coefficients preceding each of the other terms,

$$Re \ll \frac{a^2}{\nu T} \Rightarrow U \ll \frac{a}{T},$$

$$\begin{aligned}
Re \ll \frac{P_0 a}{\rho_f U \nu} &\Rightarrow U \ll \sqrt{\frac{P_0}{\rho_f}}, \\
Re \ll 1 &\Rightarrow U \ll \frac{\nu}{a}, \\
Re \ll \frac{a^2 g}{U \nu} &\Rightarrow U \ll \sqrt{g a},
\end{aligned} \tag{3.3}$$

the inertial term is negligible and the creeping flow approximation is valid [13]. In steady, creeping flow (large T), the fluid seeks an equilibrium between the gradient in potential and the viscous diffusion of momentum. Returning to dimensional form and expressing gravitational term as hydrostatic pressure potential, these conditions reduce Equation 3.1 to

$$\nabla(P + \rho g z) = \rho_f \nu \nabla^2 u. \tag{3.4}$$

where z is the position above a datum, $[L]$.

Within a single pore, fluid velocity magnitudes near the pore walls are small compared to those near the center of the pore. If the pore is conceptualized as a straight cylinder and fully-developed laminar flow exists, the velocity magnitude distribution within the pore is parabolic (Figure 3.1) with zero velocity at the pore walls (Poiseuille flow). The fully-developed velocity profile in a horizontal tube is

$$u_l = \frac{1}{4\rho\nu} \frac{dP}{dl} (a^2 - a_0^2) \tag{3.5}$$

where u_l = velocity magnitude along the pore, $[LT^{-1}]$,
 l = position along the pore, $[L]$,
 a = lateral distance from the pore centerline, $[L]$, and
 a_0 = pore radius, $[L]$.

3.1.2 Flow Through a Pore Network.

As additional, interconnected pores are included, the problem becomes equivalent to a complex pipe network. At a pore junction, ignoring inertia, fluid flow will subdivide in accordance with the resistance provided by each pore and the potential gradient along the pores.

3.1.3 Macroscopic Preferential Flow in Heterogeneous Media.

Likewise, macroscopic flow through heterogeneous media can be similar to flow through a network of pipes. Fluid will bypass regions of low permeability in favor of easier paths. Because the contrast in permeability can be high, the medium may resemble voids and solids at any scale (Figure 3.2).

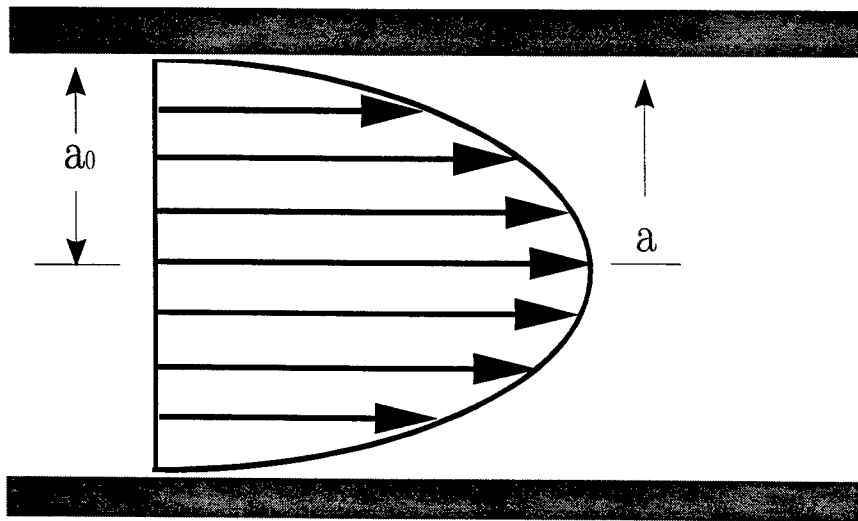


Figure 3.1: Poiseuille flow in a cylindrical pore.



Figure 3.2: Preferential flow in a macroscopically heterogeneous medium.

At the macroscopic scale, the classical flow equations may be derived by invoking the continuum assumption. The equations are assumed to be valid in a weighted-average (e.g., REV) sense as described in the previous chapter. Beginning with conservation of mass of the fluid, these equations are

$$\frac{\partial}{\partial t} (\rho_f \phi) = -\nabla \cdot (\rho_f \mathbf{q}) + q_s \quad (3.6)$$

where ϕ = volume-averaged porosity of the material, $[-]$,
 \mathbf{q} = Darcy flux, $[LT^{-1}]$ and
 q_s = source or sink of fluid mass, $[ML^{-3}T^{-1}]$.

Darcy flux is simply the volume of fluid passing through a unit cross-sectional area of porous medium per unit time. Equation 3.4 may be simplified (e.g., [33]) to produce a differential equation that reflects Darcy's law for flow through porous media

$$\mathbf{q} = -\frac{k}{\mu} (\nabla P + \rho_c g \nabla z), \quad (3.7)$$

where k = intrinsic permeability of the material, $[L^2]$,
 μ = dynamic viscosity of the fluid, $[ML^{-1}T^{-1}]$,
 ρ_c = composite fluid/constituent density, $[ML^{-3}]$, and
 z = vertical position above a datum, $[L]$.

Combining these, we arrive at the macroscopic, saturated flow equation

$$\frac{\partial}{\partial t} (\phi \rho_f) = \nabla \cdot \left[\frac{\rho_f k}{\mu} (\nabla P + \rho_c g \nabla z) \right] + q_s. \quad (3.8)$$

3.2 Conservative Solute Transport

Historically, solute transport has been divided into a translational component (advection) and a spreading component (dispersion). Advection is caused by the bulk (average) fluid motion carrying the solute particles along. Dispersion covers all solute motion not described by advection. In practice, dispersion is an amalgamation of several distinct processes that operate in very different manners. Dispersion consists of

- molecular diffusion,
- Taylor dispersion,
- flow branching, and
- path-dependent travel time.

Each components of dispersion will be analyzed separately and in an stationary reference frame.

3.2.1 Molecular Diffusion.

Molecular diffusion is the net movement of species from higher concentration to lower concentration due to Brownian motion of the individual molecules [13]. This process is depicted in Figure 3.3 and diffusive flux is described accurately by Fick's law of molecular diffusion [13]

$$J_x = -D_m \frac{dc}{dx} \quad (3.9)$$

where J_x = mass flux in the x direction due to molecular diffusion, $[MT^{-1}]$,
 D_m = coefficient of molecular diffusion, $[L^2T^{-1}]$, and
 c = concentration, $[ML^{-3}]$.

Molecular diffusion is present regardless of the fluid velocity, but represents only a small contribution to total dispersion at the REV scale, except in nearly stagnant fluid. For this reason, molecular diffusion is neglected in many numerical models. The speed at which contaminants diffuse depends on the structure of the pore space. Contaminants migrating by diffusion must follow tortuous paths created by the existence and nonuniform distribution of soil grains. Thus, a diffusion coefficient from a water-only batch experiment will overestimate the rate of diffusion in the pore space of a porous medium.

3.2.2 Taylor Dispersion.

Recall the description of Poiseuille flow in a single, straight pore. When a solute is introduced, variation in velocity magnitude across the pore's width contributes to spreading of the solute. Travel time for a solute particle in the pore depends on the fraction of time it spends in the low velocity region near the pore wall and the fraction it spends in the higher velocity region near the center. Molecular diffusion, which acts in all directions, causes solute particles to move among the streamlines and experience a variety of velocity magnitudes during their trek along the pore [17]. This effect is termed Taylor dispersion [134] or Taylor-Aris dispersion [3] and is diagramed in Figure 3.4.

If the travel time along the pore is large compared to the time for diffusion across the pore (t large and a small), such that $tD_m/a^2 \gg 1$, the dispersive behavior obeys Fick's law of diffusion with an exaggerated coefficient. Using moment analysis, Aris [3] confirmed the coefficient rigorously and determined that the spreading reaches this asymptotic condition exponentially in time. In a macroscopic medium, Taylor dispersion in a pore is generally a small contributor to the total dispersive flux. It is overwhelmed by the large-scale dispersive effects to be discussed in the coming paragraphs.

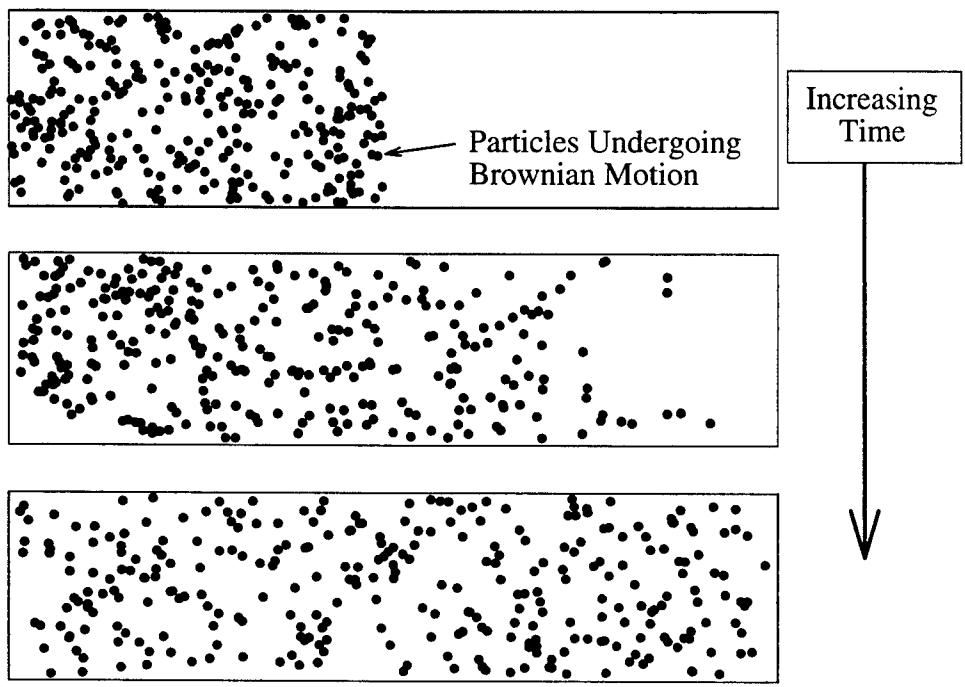


Figure 3.3: Schematic of the molecular diffusion process showing the time evolution of the position of Brownian particles in a box.

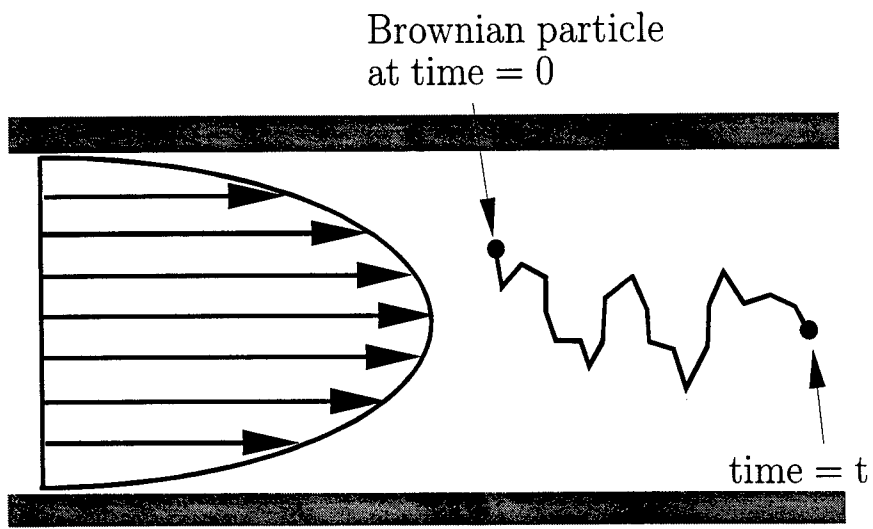


Figure 3.4: Schematic of Taylor dispersion.

3.2.3 Pore-Scale Transport Equation.

Within a pore, transport is normally described by a one-dimensional advection-dispersion equation (ADE).

$$\frac{\partial c}{\partial t} = -\frac{\partial(u_l c)}{\partial l} + \frac{\partial}{\partial l}\left(D\frac{\partial c}{\partial l}\right). \quad (3.10)$$

D is a scalar dispersion coefficient that contains a Taylor dispersion component and a molecular diffusion component,

$$D = \frac{a^2 \bar{u}^2}{48 D_m} + D_m, \quad (3.11)$$

where \bar{u} = average velocity magnitude in x , $[L/T]$, and
 a = pore radius, $[L]$.

3.2.4 Flow Branching.

Consider a slightly larger sample that contains several interconnected pores. For fluid to pass through an interconnected porous medium, it must frequently subdivide itself among the pores and rejoin at pore intersections [115]. If the fluid contains solute, this branching effect causes a spreading of the solute mass. This particular phenomenon is not caused by variation in the velocity magnitude. It is present even if the average pore velocities along each of the paths are identical (as in Figure 3.5). In this case, flow branching causes no dispersion in the direction of flow, only perpendicular to it. Neglecting small travel time differences caused by molecular diffusion and Taylor dispersion, all particles will arrive at the downstream boundary at the same instant. This hypothesis is supported by Sahimi's finding [120] that, in a numerical model consisting of a regular, rectangular network of tubes oriented at 45 degree angles to the direction of flow, a solute spreads only laterally, not in the direction of flow.

Although molecular diffusion is a small contributor to dispersion, without it, flow branching would not spread the constituent. Molecular diffusion causes mixing and permits molecules to move among streamlines. Without molecular diffusion, all molecules beginning on a streamline stay on that streamline through branch points, thus following the same path through the medium.

The dispersive effect caused purely by flow branching may be isolated by considering a classical demonstration of the Gaussian distribution (Figure 3.6). Releasing many balls in the same location over an array of equally-spaced, offset nails and collecting them in bins beneath demonstrates spreading caused by the ability to choose alternate paths. This process is a function of the number of rows of nails,

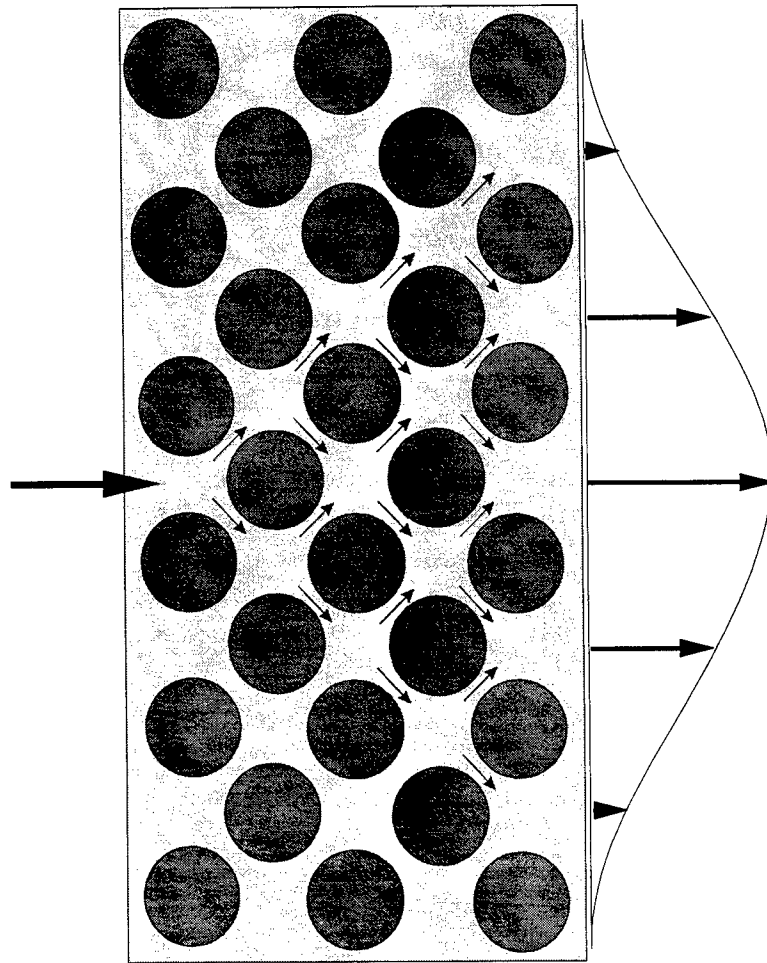


Figure 3.5: Flow branching at the pore scale in a discrete medium.

but is scale independent. In other words, if the geometric configuration is retained, the same distribution results, regardless of scale. This mechanism causes the dispersion coefficient to be a tensor. That is, macroscopic flow in x produces spreading in y and in z , even in a medium with no inherent orientation. This spreading is a consequence of the material's discreteness.

3.2.5 Path-Dependent Travel Time.

The final component of dispersion is path-dependent travel time. If the mean velocities in two parallel pores are different, travel times along these pores will differ. When several, interconnected pores are involved, the variety in paths and, therefore, travel times increases (Figure 3.7). Path-dependent travel time normally constitutes the majority of dispersion in the direction of flow, with the rate of dispersion depending on the distribution of travel times.

3.2.6 Classical Macroscopic Transport Equation.

Plumb and Whitaker [110] use volume averaging to show that if the ADE (Equation 3.10) is valid for a solute migrating through a pore, and if the macroscopic scale is large compared to the small-scale (pore-scale) variability, an ADE with modified coefficients may be applied at the macroscopic scale. The traditional macroscopic equation for conservation of mass for dilute concentrations of a conservative, miscible contaminant is

$$\frac{\partial c}{\partial t} = -\nabla \cdot (uc) + \nabla \cdot (D\nabla c) \quad (3.12)$$

with u being the seepage velocity. The dispersion coefficient in Equation (3.12) is normally prescribed by

$$D_{ij} = (\alpha_L - \alpha_T) \frac{u_i u_j}{\bar{u}} + \alpha_T \bar{u} \delta_{ij} + D_m \delta_{ij} \quad (3.13)$$

where α_L = longitudinal dispersivity, $[L]$,
 α_T = transverse dispersivity, $[L]$,
 δ_{ij} = Kronecker delta, $[-]$, and
 D_m = molecular diffusion coefficient. $[L^2/T]$.

3.2.7 Field-Scale Transport in Heterogeneous Media.

One can imagine that the processes comprising dispersion at the field scale are similar to those described for a network of pores. Preferential flow at the macroscopic scale, described earlier, is a large-scale equivalent to flow branching. Obstacles to be avoided may be large, causing considerable spreading perpendicular to the

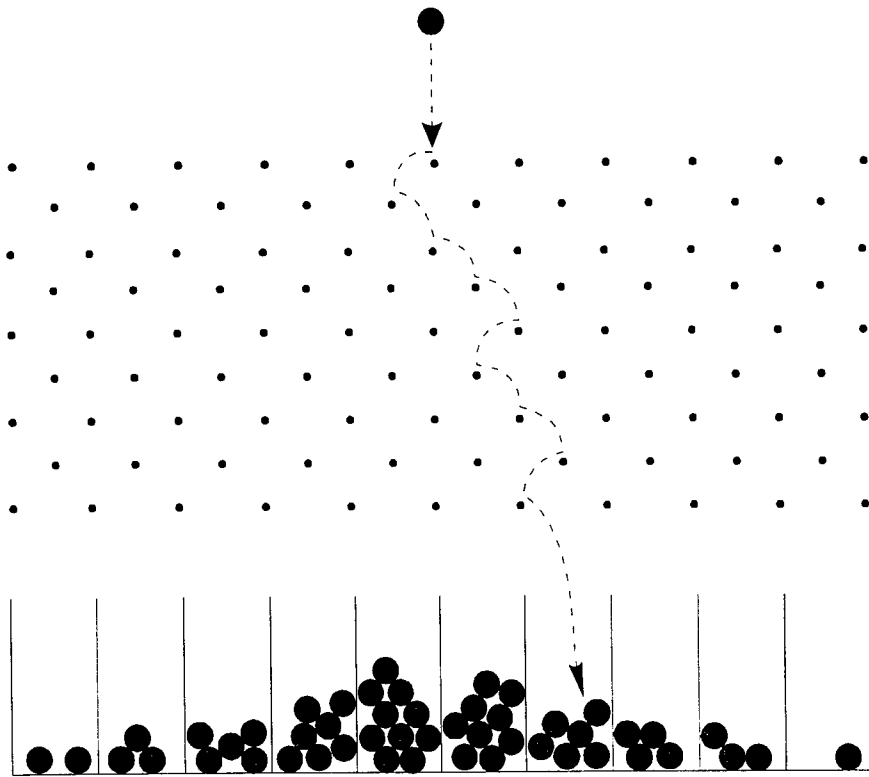


Figure 3.6: Balls and nails analogy for dispersion by multiple paths.

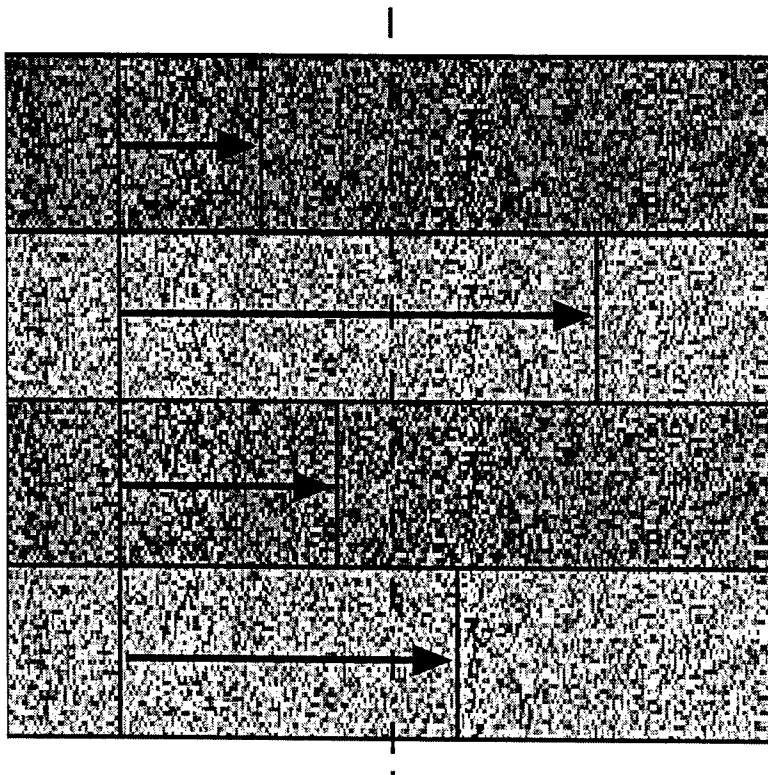


Figure 3.7: Path-dependent travel time. Each layer has a different seepage velocity with the average displacement indicated by the dashed line.

macroscopic flow path. Further, because these paths are of unequal lengths and conductivities, each path will have a different travel time. These two effects cause the majority of dispersion at the field scale. Mass that chooses higher conductivity paths will emerge first, while mass that must pass through lower conductivity regions will emerge later.

In summary, dispersion is not a monolithic process. It is composed of several very different sub-processes. More importantly, dispersion is not diffusion, although it is usually modeled as a diffusion process with the ADE. In a field setting with a natural spectrum of heterogeneities, dispersion will be dominated by differential advection at spatial scales much larger than the pore scale. The only truly diffusive component in total dispersion is molecular diffusion. Taylor dispersion in the pores and molecular diffusion may be ignored in many practical applications with little consequence. There are exceptions, generally in cases with regions of very low velocity, for which the inclusion of molecular diffusion may be crucial.

3.3 Immiscible Fluid Flow

The theory of immiscible flow through porous media is important because it describes two physical systems that are encountered often in the assessment of remediation plans; air and water flow in the unsaturated zone, and the motion of non-aqueous phase liquid (NAPL) contaminants. Drinking water standards for these organic contaminants are usually very stringent, and their solubilities, although small, usually exceed these standards by orders of magnitude. Their relatively low solubilities permit the immiscible fluid to act as long-term, continuous sources of dissolved contaminant to passing groundwater.

The physics of immiscible flow have been studied in a variety of disciplines including petroleum engineering, chemical engineering, and, more recently, water resources engineering. The following paragraphs briefly describe a few key processes relevant to the work that will follow:

- capillary barriers,
- capillary entrapment,
- capillary hysteresis, and
- fingering.

At the pore scale, flow of immiscible fluids is identical to single fluid flow with one exception, surface tension. Intermolecular attraction prevents some fluid pairs from mixing with each other, causing the formation of fluid-fluid interfaces. When

the surface of the soil grains shows a preference for one of the fluids, the presence of interfaces causes a capillary force. The Young-Laplace equation [38] describes the resulting pressure difference across the fluid-fluid interface as a function of the surface tension and the radius of the interface

$$P_c = \frac{2\sigma \cos \theta}{r_m} \quad (3.14)$$

where P_c = capillary pressure, $[ML^{-1}T^{-2}]$,
 σ = surface tension, $[MT^{-2}]$,
 θ = contact angle, $[-]$, and
 r_m = mean radius of curvature of the interface, $[L]$.

Because a soil's pore radii are normally small (on the order of microns), the capillary pressure may be large. Further, spatial variability in material type and pore size cause dramatic differences in capillary pressure resulting in well-defined preferential flow patterns.

3.3.1 Capillary Barriers.

When a pore's radius is sufficiently small, the capillary pressure resisting invasion of the non-wetting fluid may exceed the driving pressure gradient, and the non-wetting fluid will not invade this pore. When this effect occurs for all pores at a material interface, an entire invading fluid front may be arrested by capillary force. This effect is labeled a capillary barrier. Highly heterogeneous soils often contain dramatic variations in physical properties, permitting formation of capillary barriers [71].

3.3.2 Capillary Entrapment.

Once non-wetting fluid has entered a medium, bubbles or ganglia (larger, connected blobs) of this fluid may become surrounded by the wetting fluid and immobilized. This effect is pore-scale capillary entrapment. Using analytical calculations, Hunt et al. [68] proposed that DNAPL ganglia in homogeneous media may be large and the amount of trapped fluid significant. In heterogeneous media, entrapment may occur in pockets or layers of coarser material surrounded by fine grain material. This macroscopic entrapment may result in large quantities of immobile contaminant [71].

3.3.3 Capillary Hysteresis.

Entrapment is also important in describing the macroscopic capillary-pressure-versus-saturation function. Because of entrapment, capillary-pressure-versus-saturation

curves for drainage will be different than those for imbibition. Therefore, knowing the saturation is not sufficient to predict the capillary pressure. Capillary pressure is a function of the pore-scale state of the fluids in the medium. To know the capillary pressure at the macroscopic scale, we must know the history of saturation. This effect is capillary or saturation hysteresis and reflects a poor macroscopic description of the pore-scale process. Hassanizadeh and Gray have proposed macroscopic capillary pressure versus saturation relationships that include fluid-fluid interfacial surface area to lessen the memory effect [62].

3.3.4 Fingering.

When one fluid displaces another, it may do so as a non-uniform front. The term fingering is used loosely to describe such nonuniform displacement. Two phenomena are credited with creating this nonuniformity

- viscous or gravitational instability, and
- heterogeneity-driven preferential flow.

Glass et al. [56] have studied the occurrence and description of fingering in a water-air system in layered soils. In their experiments they were careful to ensure homogeneity within each layer. Even so, heterogeneity is credited with causing irregular finger spacing and merging of fingers.

Kueper and Frind [83] provide an overview of immiscible fingering in porous media in which they state that 'natural porous media contain heterogeneities at a fine enough scale such that no distinction need be made between stable and unstable displacements.' They suggest that true instability is an academic question when considering real soils. They also propose that non-uniform flow be termed channeling rather than fingering to distinguish it from unstable displacement. This implies that, if one can describe preferential flow due to heterogeneity, true instability is not a concern. But, the same processes that give rise to instabilities may enhance the tendency for immiscible flow to flow through channels.

3.4 Effects of Heterogeneity

The classical equations derived for flow and transport through macroscopically *homogeneous* media have been applied in macroscopically *heterogeneous* media with mixed success. Problems will be discussed in three groups; asymptotic parameters, pre-asymptotic parameters, and breakdown of the governing equations.

3.4.1 Asymptotic Parameters.

As has been stated repeatedly, the classical flow and transport equations were founded on the premise that the scale of observation is significantly larger than the characteristic length of heterogeneity (asymptotic conditions). Because the asymptotic scale in heterogeneous media may be very large, macroscale constitutive variables must replace information lost over a wide range of scales. Characteristic length of the process is unimportant at the asymptotic scale and determining these macroscopic constitutive variables relies solely on capturing the proper coupling.

The correct macroscopic effective conductivity results from a coupling between the local conductivity and the macroscopic pressure gradient. If the pressure gradient were constant over the entire field, the effective conductivity would equal the arithmetic average of the small-scale conductivities. On the other hand, if the velocity were constant over the field, the effective conductivity would approach the harmonic mean of the small-scale sample values. In reality, the effective conductivity lies between these two extremes and is a function of the statistical distribution of the small-scale conductivities.

Asymptotic macrodispersion is the coupling of the ‘mean-removed’ velocity and concentration. Small-perturbation methods have been used successfully to compute this coupling for small variance in velocity (conductivity) and for certain statistical distributions of velocity and concentration [53].

3.4.2 Pre-Asymptotic Parameters.

Because the problem scale necessary to achieve asymptotic conditions may be large or infinite, pre-asymptotic behavior is very important. For example, measured conductivity changes with changes to the screened interval in a well [30]. Tests performed on a well with a very small screened interval may measure a relatively local conductivity, but when a well’s screen intercepts several layers, the value produced is a composite. Field data collected by Molz et al. [96] and Rovey and Cherkaur [69] demonstrate a scale dependence in hydraulic conductivity. In Rovey and Cherkaur’s data, the natural logarithm of the hydraulic conductivity measurements increased linearly with the logarithm of the test radius until an asymptote was reached between 20 and 200 meters. Döll and Schneider [36] attributed an observed scale dependence of hydraulic conductivity to the existence of macropores. Figure 3.8 shows averaged observations of hydraulic conductivity versus measurement volume for three carbonate units and a general form of the scale dependence of conductivity from Shulze-Makuch and Cherkaur [124].

As for solute transport, consider the well-studied problem of a plume resulting

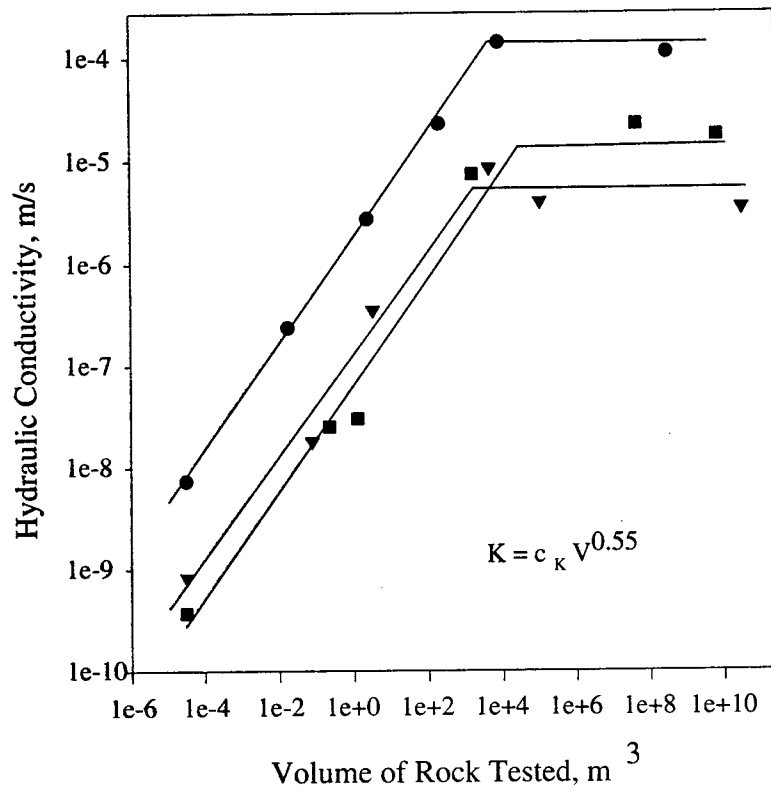


Figure 3.8: Scale effect of hydraulic conductivity (after Schulze-Makuch and Cherkaur [124]).

from an instantaneous point injection. This discussion follows closely that given by Peters and Howington [109]. Under asymptotic conditions, Equations (3.12) and (3.13) predict the resulting plume spreads at a constant rate longitudinally with the dispersivity described by

$$\alpha_x = \alpha_L = \frac{1}{2} \frac{d\sigma_x^2}{d\bar{x}} \quad (3.15)$$

where for a plume with total mass c_0 , the travel distance of the plume centroid, \bar{x} , is given by

$$\bar{x} = \frac{1}{c_0} \int_{-\infty}^{\infty} xc(x)dx \quad (3.16)$$

and

$$\sigma_x^2 = \frac{1}{c_0} \int_{-\infty}^{\infty} x^2 c(x)dx. \quad (3.17)$$

For a constant dispersivity, Equation (3.15) implies that the size of the plume, as measured by σ , increases as the square root of the distance it travels ($\sigma \propto \sqrt{\bar{x}}$). For a uniform mean flow, the plume's centroid position and its travel time are related by the constant velocity, which means that $\sigma \propto \sqrt{t}$.

Laboratory and field observations of the apparent dispersivity of a conservative solute plume indicate a strong correlation with the scale of observation [47, 2, 52, 100]. Figure 3.9 shows field observations discussed by Anderson [2]. This scale dependence occurs primarily because the plume encounters increasingly large structures in the heterogeneity [125]. These observations of actual plume growth show that the rate of plume spreading increases nearly linearly with travel distance ($\sigma \propto \bar{x}$). From Figure 3.9 it is apparent that an REV for the dispersivity parameter may be very large for natural soils. Similar observations of scale dependence in apparent dispersivity are presented by Gelhar et al. [55] and by Schulze-Makuch and Cherkauer [124].

A plume's growth rate can be described by

$$\alpha_x = p\sigma_x^b. \quad (3.18)$$

where p and b are empirical parameters. Plume growth consists of two distinct phases. In the first phase, the rate of plume growth increases linearly with plume size (b is almost universally observed to be close to one). In the second phase, after the plume becomes large, b tends to zero, α becomes constant, and the plume grows in accordance with the Fickian model in the traditional advection-dispersion equation. A transition region exists as b decreases from near one to near zero and α becomes a constant equal to p .

Gelhar [53] and Matheron and de Marsily [92] discuss a stratified flow model that displays plume growth during the pre-asymptotic phase. In this model, flow

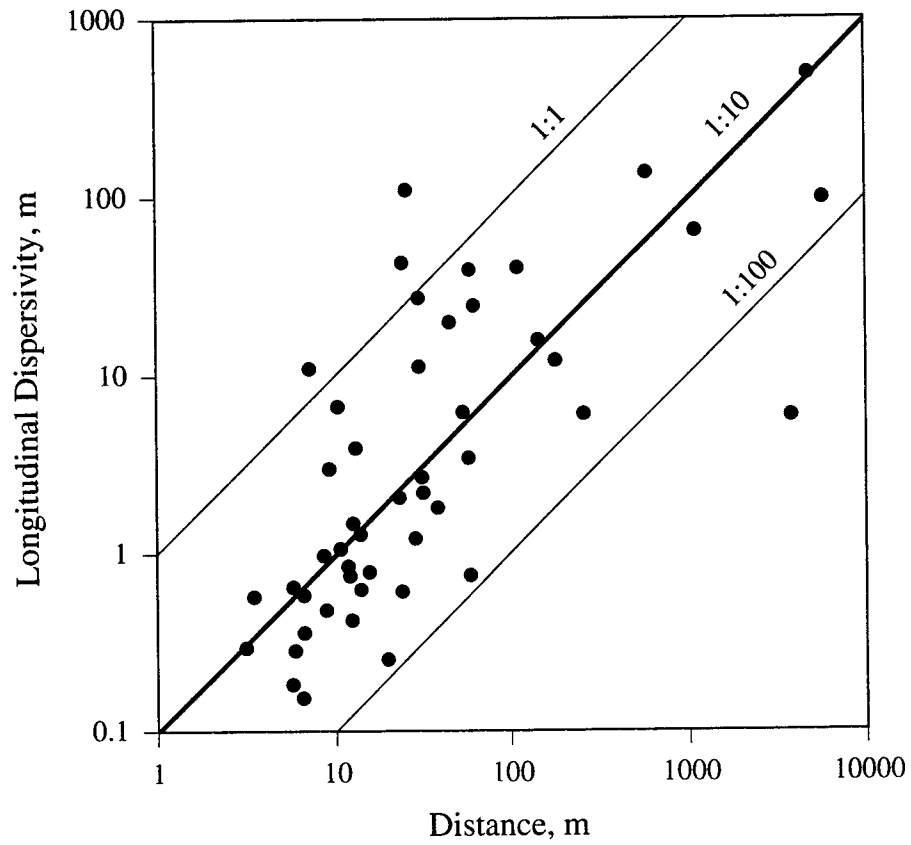


Figure 3.9: Scale effect of apparent longitudinal dispersivity (modified from Anderson [2]).

is parallel to the bedding and each stratum may have a different fluid velocity. Transport in the stratified flow model is similar to a horse race (Figure 3.10) which is a simple analogy to Figure 3.7. Each horse in this model has its own constant speed. Therefore, at any instant, the speed of each horse is perfectly correlated with its speed at any prior or future time. As a result of this perfect velocity correlation, the pack of horses will separate at a rate much faster than predicted by a diffusion model, implying uncorrelated velocities.

In fact, this situation corresponds to a value of b equal to one in Equation 3.18. Spreading of the plume about its center of mass due to the different velocities is given by:

$$\alpha_x = \frac{\sigma_k^2}{\bar{K}^2} \bar{x} = \sigma_x^2 \bar{x}. \quad (3.19)$$

where \bar{K} is the mean hydraulic conductivity. This equation may be recast in the form of Equation (3.18) to give

$$\alpha_x = \frac{\sigma_k}{\bar{K}} \sigma_x = \frac{\sigma_u}{\bar{u}} \sigma_x \quad (3.20)$$

where \bar{u} and σ_u are the mean and variance, respectively, of seepage velocity in the layers.

Comparison of Equations (3.18) and (3.20) reveals that $p = \sigma_u/\bar{u}$ and b is one for this stratified aquifer. Velocity magnitudes of each solute ‘particle’ are constant, leading to a perfect correlation between the distance of the particle from the plume centroid and the particle velocity. Similarly, during pre-asymptotic growth of a plume from an instantaneous source, solute velocities are correlated with distance from the plume’s centroid. Asymptotic behavior develops as the correlation is lost. Empirical fits have produced b values ranging from 0.755 (field data) to 1.13 (all data) [4], 0.83 (scale > 100 m) to 1.53 (scale < 100 m) [100], and 1.07 [124] for observations spanning several orders of magnitude in length.

3.4.3 Breakdown of the Advection-Dispersion Equation.

Dispersion is conceptualized as a Fickian process almost without exception for practical analyses. Therefore, it is assumed to behave like molecular diffusion even though Dagan [30] reported that “there is no *a priori* reason to believe that the diffusion type equation is valid at all.” Sposito et al. [132] say that the question as to the validity of the Fickian assumption is “tantamount to asking for what broad classes of spatially varying coefficients in a laboratory scale CDE [convection-dispersion equation] can its fundamental solution be approximated asymptotically by a Gaussian density function.” Dagan [30] states that “the problem of transport

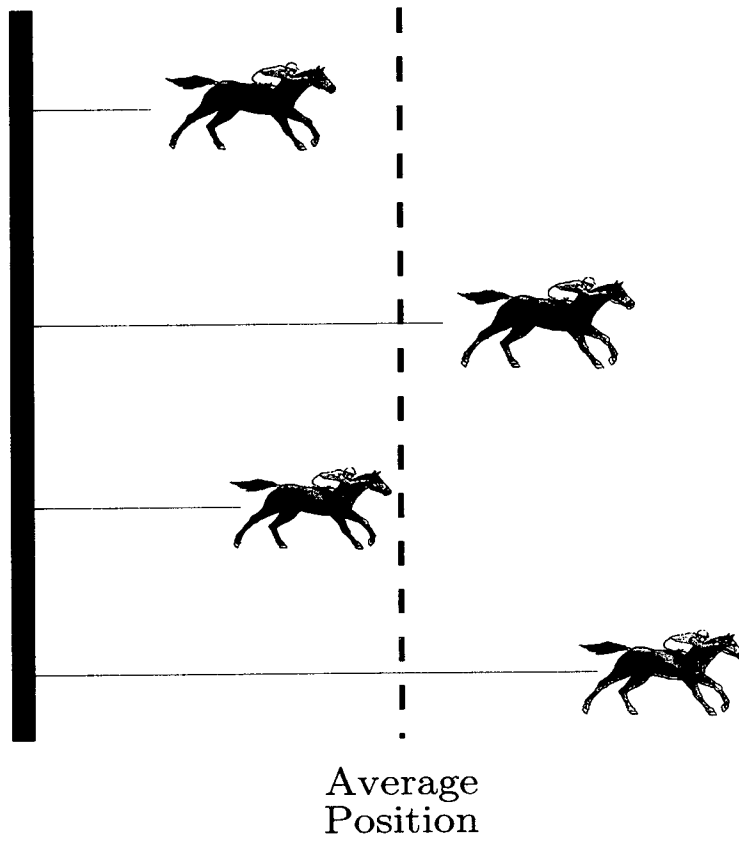


Figure 3.10: The horse-race model for perfectly correlated transport.

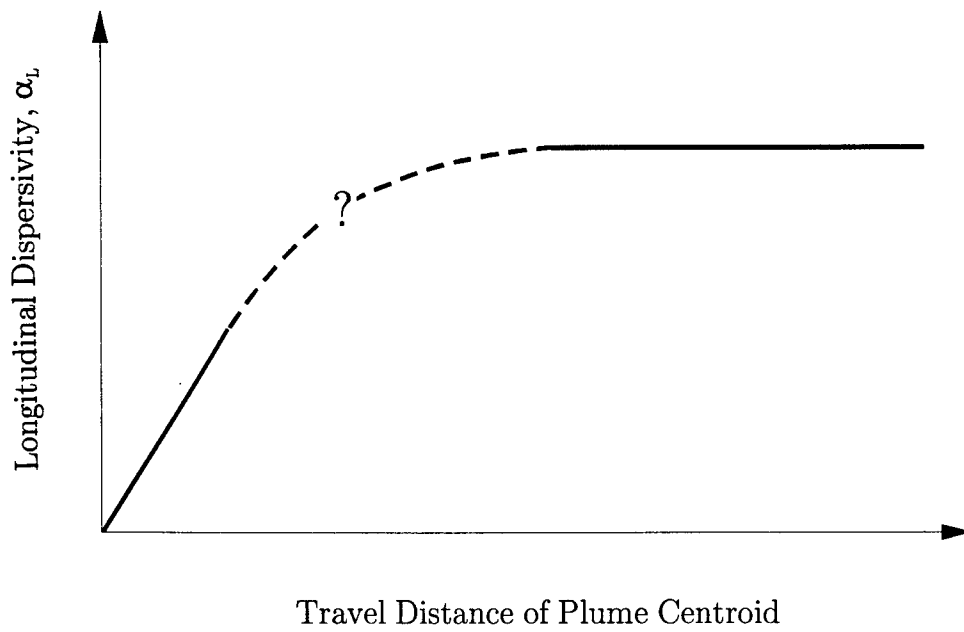


Figure 3.11: Dispersivity as a function of displacement distance (modified from Gelhar [53]).

by convective motion differs essentially from that of molecular transport.” The traditional dispersion model assumes these two processes have the same fundamental form and behavior. Defense of these equations is largely founded on their performance in controlled laboratory experiments on homogeneous soil columns [10]. Taylor [133, 134] has been credited [2] with first proposing a Fickian law for dispersion and early experimental work supported this contention [9]. Some researchers have questioned the applicability of a Fickian model [2, 138, 61] on the basis of the observed scale dependence. Hassanizadeh [61] further objected to the implied infinite propagation speed of solutes in the Fickian model of dispersion.

Supporters of the Fickian model recognize that this model is valid only after a sufficient length of time for process development, but contend that it is valid in the asymptotic condition [53]. This is often justified using a moving-observer argument for one of two very common problems,

- evolution of an impulse point source of solute, and
- spreading of a moving front created by a continuous source of contaminant at an inflow boundary.

For a developing plume from a point source, the observer is made to move with the centroid of the plume. If the mean advection is removed, the remaining velocities (and, corresponding mass flux) may be represented by a zero-mean random perturbation. If the correlation structure in these perturbations are negligible (asymptotic limit), this process is analogous to Brownian motion at the molecular scale which drives diffusion. The asymptotic condition is reached quickly in homogeneous media, explaining how the Fickian model was originally adopted. Most early theory and experiments were performed with homogeneous media. However, in heterogeneous media, the velocity field has structure and the motions will not be random.

Some physical situations simply are not amenable to representation by a Fickian model with macroscopic coefficients. Among these are:

- evolution of a continuous point source,
- transport in media with heterogeneity at all scales (fractal or evolving heterogeneity), and
- transport in flow that is parallel to the bedding in a stratified aquifer [92].

For an instantaneous point source, the centroid location, plume size, and travel time are related and interchangeable as independent variables (assuming the velocity of the plume centroid is a constant). This is not true for the continuous point source. To match growth of a plume from a continuous injection, dispersivity would

need to vary with distance from the source. In essence, each Lagrangian point would need a time-dependent dispersivity. In an Eulerian approach, dispersivity would depend on the local definition of plume size which would make the equations nonlocal. Using a single value for macroscopic dispersivity to describe the growth of a plume from a continuous source is not possible. The diffusive Fickian model predicts omnidirectional spreading, unlike the small scale advection it represents. With a large diffusive effect, non-physical upstream transport of contaminant is predicted. With a small diffusion coefficient, the upstream migration is limited, but downstream spreading is underestimated.

3.4.4 Phase Dispersion in Immiscible Flow.

When observed from a distance, spreading of an immiscible fluid can resemble the spreading of a conservative tracer in single-phase flow. For this reason, some have advocated immiscible flow with a Fickian dispersion term to account for nonuniformity of the displacement (e.g., [111, 85]). There are serious problems with this approach. First, the process is not diffusion. At the pore scale, the fluids do not mix. Partial saturation is a macroscopic quantity that only exists upon spatial averaging. Spreading is caused by small-scale fingering and by the same processes that spread a miscible plume. Second, capillary barriers are discontinuities that are difficult to represent with parabolic flow equations. Numerical smearing at the capillary barrier may cause non-physical migration of the non-wetting phase (NAPL) across the barrier. Once the barrier is broken, the relative conductivity across the barrier is non-zero and the model will predict migration of the non-wetting phase. Numerical spreading across capillary barriers will be even more difficult to avoid with the inclusion of phase dispersion, and a numerically predicted immiscible contaminant plume may be vastly different than that observed in a heterogeneous medium.

3.4.5 Other Complications.

In some instances, the dispersion term has been modified to incorporate simple chemistry [50]. Because we extract coefficients from bulk testing (for example, breakthrough curves from column tests), it is difficult to isolate individual process parameters. The implication is that dispersivity (as it is used) is not a medium property [101], but a function of the constituents, fluid, and medium. Dispersivity has also displayed a mild dependence on velocity, indicating a non-linear relationship between dispersion coefficient and velocity [10, 120, 61], and on concentration gradient [61], making the dispersion coefficient even more ambiguous.

Chapter 4

Modeling Philosophies and the Proposed Approach

All modeling represents a compromise among the realism of the model, resources available to gather data, and resources available to represent that data. The art of modeling lies in devising the optimal strategy for capturing the most significant information with the fewest degrees of freedom and, to the greatest extent possible, discarding only that information that is redundant or represents 'higher-order' variation.

Modeling philosophies may be categorized by the level of discrete structure included explicitly, and that which is left for the constitutive parameters (Figure 4.1). At one end of the spectrum, the medium is treated as a homogeneous material. All variability is included statistically in the form of macroscopic effective parameters. This is the approach adopted in the macrodispersion work of Gelhar [53], Dagan [30], and others. At the other extreme, discrete-medium models attempt to resolve structure and variability explicitly. This approach is represented by pore-scale models that describe fluid flow and transport in the interstices of a medium. Most practical groundwater model applications rest in the middle; large-scale stratigraphy is described explicitly and sub-formation-scale heterogeneity is handled through macroscopic parameters. Present alternatives for addressing the problems with traditional groundwater flow and transport theory in heterogeneous media tend toward one or the other extreme in Figure 4.1. For the following discussion, these two approaches are labeled effective-parameter approaches and discrete-medium modeling approaches.

Because we can never know the spatial details of a medium's heterogeneity in a natural field setting, their effects are often included in a stochastic rather than deterministic fashion. As Gelhar points out [53], the question as to a medium's het-

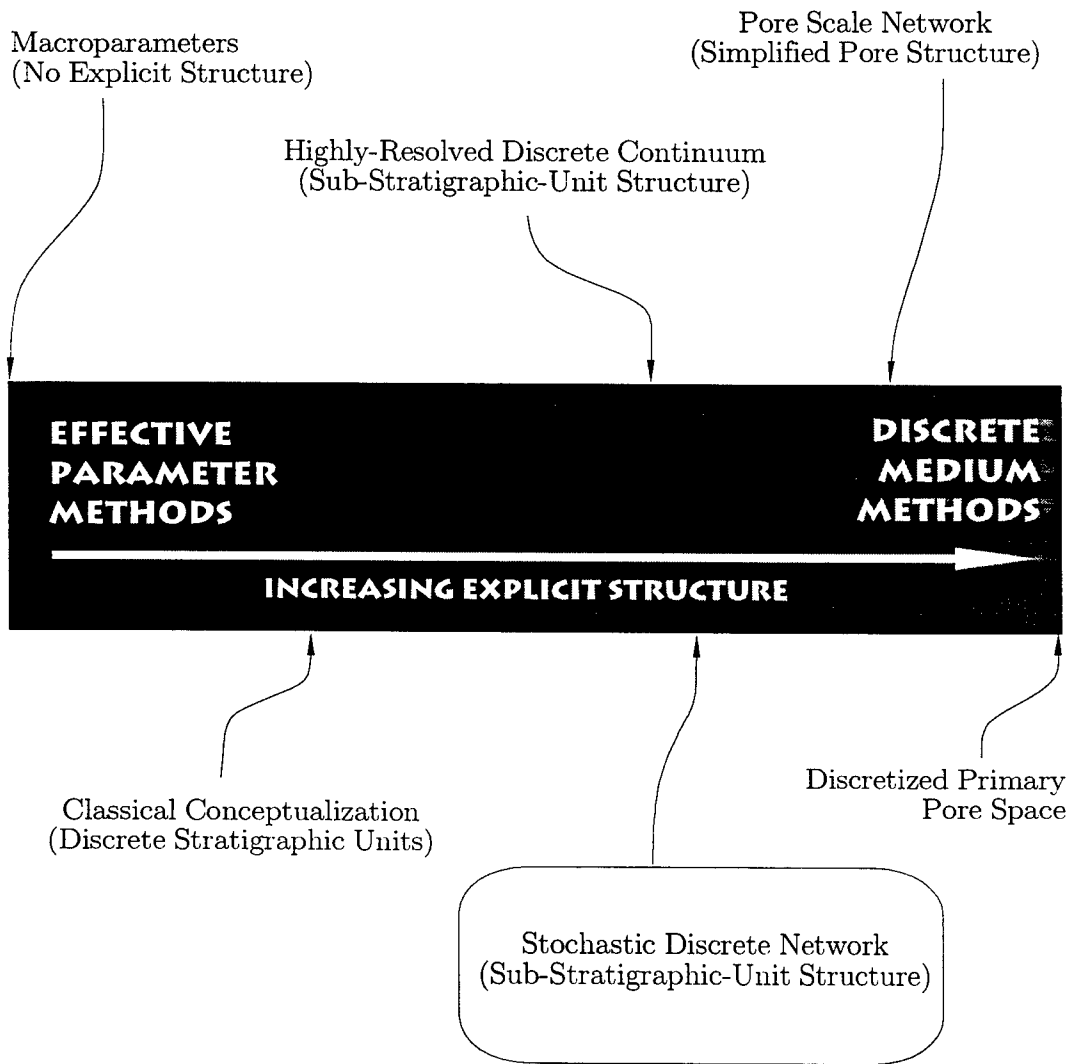


Figure 4.1: Modeling philosophies categorized by level of discretization.

erogeneity being stochastic or deterministic is an academic one. The actual medium is not random. It is a deterministic, normally static, geologic structure through which fluids and constituents move. A stochastic representation is convenient and permits us to quantify our inadequate knowledge of the spatial structure of the medium.

The two modeling philosophies include uncertainty at different points in the modeling process. Effective-parameter (or stochastic-continuum) approaches account for variability within the governing equation formulation. The solution consists of a mean and variance in the solution variable, providing a direct estimate of uncertainty in the solution. In the stochastic, discrete-medium approach, observations are coupled with a statistical description of the medium to generate informed guesses (realizations) about the details of the true medium. Flow and transport through each realization of the medium is modeled deterministically. This approach relies on simulating multiple realizations and post processing of results to assess uncertainty. Averaging of the solution variables is delayed until after simulation, preserving proper coupling, but often at great computational expense.

Effective properties and ensemble-average solutions enjoy some important advantages over discrete-medium modeling, but they also suffer some weaknesses. On their behalf, they provide direct estimates of mean concentration fields and of uncertainty without performing simulations on many realizations. The most important detraction from effective-parameter approaches is that solutions to the stochastic governing equations are possible only for a few situations. Macro-parameters for dispersion in converging or unsteady flows and for unsaturated or multiphase flows are still under study. The variance in lognormal hydraulic conductivity in real porous media may easily violate the limits imposed by the small-perturbation assumption that the variance in lognormal conductivity is much less than one. Further, statistical homogeneity assumed by many of these approaches is not always appropriate.

The following review is intended to be a discussion of modeling philosophy. As such, not every work in a particular area is included. A few, representative articles are provided as examples of each approach. The discussion is divided into three areas:

1. asymptotic effective parameters
2. pre-asymptotic and non-asymptotic effective parameters, and
3. discrete medium modeling.

This brief review is followed by a rationale for the path chosen in this effort.

4.1 Asymptotic Effective Parameters

Asymptotic parameters are those that have ceased to display scale dependence and are nearly constant. These macroscopic parameters must maintain consistency with the small-scale physics being averaged to be applicable for a wide range of hydrologic conditions and contaminant configurations. Derivation of asymptotic parameters is possible only under certain conditions. Gelhar [53] states that parameters derived from statistical analyses of single realizations will be valid, ensemble coefficients only if the overall length of the sample is larger than the scale of heterogeneity by at least an order of magnitude.

4.1.1 Asymptotic Effective Conductivity.

Using a perturbation technique, Gutjahr et al. [57] derived effective conductivity for an n -dimensional, isotropic medium ($n = 1, 2, 3$). Their approach assumes that

- the REV concept and the continuum equations are valid,
- the problem is large compared to the correlation scale of the medium properties (implying ergodicity), and
- perturbations about the mean are small so that the first-order perturbation equations are accurate.

Ergodicity means that spatial averaging of a single realization (or the experience of a single tracer particle) is equivalent to averaging over an ensemble of realizations.

The procedure used by Gutjahr et al. [57] to derive the effective conductivity parameter is

1. employ a local Darcian flow equation,
2. decompose the head and conductivity into mean and perturbation terms,
3. discard second-order and higher perturbation terms, and
4. relate the spectrum of head to the spectrum of conductivity and compute an expected value for effective conductivity.

The expression that resulted from their work is

$$K_e = K_g \left[1 + \left(\frac{1}{2} - \frac{1}{n} \right) \sigma_f^2 \right], \quad (4.1)$$

where K_e = effective conductivity, $[LT^{-1}]$,
 K_g = geometric mean conductivity, $[LT^{-1}]$,
 n = dimension of the medium, $[-]$,
 σ_f^2 = variance in lognormal conductivity, $[-]$.

Using a 'self-consistent' approach, Dagan [28] also found that the effective conductivity is the geometric mean of the small-scale values for a two-dimensional medium. Gelhar and Axness [54] extended this result to anisotropic media (Appendix A). They also postulated that, for perturbations larger than first order, the effective conductivity may be given by

$$K_e = K_g \exp \left[\left(\frac{1}{2} - \frac{1}{n} \right) \sigma_f^2 \right] \quad (4.2)$$

a result that was also found by Dagan [30].

Another approach to computing effective conductivity is real-space renormalization [79]. In this method, fine-scale realizations of the hydraulic conductivity are generated using observations and statistical descriptions. Then, beginning at the small scale and working upward, the effective conductivity is computed on a group of cells. For saturated flow and simple cell groups (2×2 in 2D, or $2 \times 2 \times 2$ in 3D), the calculations may be performed analytically. This process continues on successively coarser grids until the desired computational resolution is achieved. To compute the local conductivity on the group of cells, one must assume boundary conditions. Typically, to compute the K_{xx} component of effective conductivity in a two-dimensional problem, specified pressure conditions are applied in the x direction and no-flow boundaries are applied in y . To compute the K_{yy} component, the boundary conditions are swapped. This restriction causes some inaccuracy, especially for anisotropic systems with strong off-diagonal components of conductivity.

4.1.2 Asymptotic Macrodispersivity.

Applying stochastic theories for conservative transport in porous media consists of three basic steps [113]

1. approximating hydraulic conductivity as a spatially random field,
2. relating velocity variations to variations in conductivity, and
3. computing macrodispersivities from the predicted velocity spectrum.

By replacing the concentration and velocity variables of the traditional transport equation with their respective means and perturbations, mean and perturbed

transport equations may be derived. Appendix B relates the spectrum of fluxes ($S_{q_i q_j}$) to the spectrum of lognormal conductivities (S_{ff}) in Fourier space

$$S_{q_i q_j}(k) = K_g^2 J_m J_n \left(\delta_{im} - \frac{k_i k_m}{k^2} \right) \left(\delta_{jn} - \frac{k_j k_n}{k^2} \right) S_{ff}(k) \quad (4.3)$$

where k = the wave number vector, [-],
 J_m = the mean head gradient in direction m , [-],
 J_n = the mean head gradient in direction n , [-].

For a three-dimensional, statistically isotropic medium with an exponential covariance model for the conductivity, it may be shown [53] that

$$\begin{aligned} A_{ij} &= 0, i \neq j \\ A_{11} &= \frac{\sigma_f^2 \lambda}{\gamma^2} \\ A_{22} = A_{33} &= \frac{\sigma_f^2 \alpha_L}{15\gamma} \left(1 + \frac{4\alpha_T}{\alpha_L} \right) \end{aligned} \quad (4.4)$$

where A_{ij} = macrodispersivity tensor components, [L],
 γ = flow factor, [-],
 λ = correlation length, [L], and
 α_T = transverse dispersivity, [L].

Others have presented similar forms for asymptotic macrodispersivities, including Dagan [30], and Neuman [103]. This same approach permits the prediction of concentration variance as a function of the lognormal variance in hydraulic conductivity, the macroscopic concentration gradients, and lateral dispersivity.

4.2 Pre-Asymptotic and Non-Asymptotic Coefficients

By using non-constant constitutive parameters, some aspects of pre-asymptotic behavior may be reproduced. For example, Dagan suggests that the dispersivity is a function of time in the pre-asymptotic regime [30]

$$D(t) = \frac{1}{2} \frac{dX_{11}}{dt} \quad (4.5)$$

where X_{11} is the displacement covariance tensor defined by

$$X_{11}(t) = 2\sigma_f^2 \left[t - \frac{8}{3} + \frac{4}{t} - \frac{8}{t^3} + \frac{8}{t^2} \left(1 + \frac{1}{t} \right) e^{-t} \right]. \quad (4.6)$$

Rajaram and Gelhar [113] proposed a plume-scale-dependent dispersivity. Only those velocity correlations with length scales smaller than the dimension of the plume

contribute to dispersion. Velocity structures larger than the plume that cause it to meander are excluded from the dispersivity computation. This is accomplished by a low-wave-number filter on the velocity correlation spectrum [113]. This remedies the problem of overestimating growth rate of individual plumes when using macrodispersivities derived from ensemble-average equations [112]. If the meandering effect is not removed, plumes with different centers of mass are averaged directly. The second moment of the ensemble average of the concentration field is given by

$$M_{ij}(t) = \sum_{ij} (t) + E [(\bar{x}_i(t) - \hat{x}_i(t))(\bar{x}_j(t) - \hat{x}_j(t))] \quad (4.7)$$

where

$$\sum_{ij} (t) = E \left[\frac{n}{m} \int_{-\infty}^{\infty} (x_i - \bar{x}_i(t))(x_j - \bar{x}_j(t))c(x, t)dx \right], i, j = 1, 2, 3. \quad (4.8)$$

The second term in Equation 4.7 represents this variation in the position of the plume's center of mass. The first term represents the desired dispersion term which is the rate of spreading about a plume's center of mass. By averaging multiple realizations, these two effects are not discriminated. A plume-scale-dependent relative dispersivity is given as

$$A_{ij}^r(\hat{x}_1, \sum_{ij}) = \frac{1}{2} \frac{d \sum_{ij}}{d \hat{x}_1} = \frac{1}{\hat{u}^2} \int_0^{\hat{x}_1} \int_{-\infty}^{+\infty} e^{(ik_1 - \alpha k^2)\xi} \left[1 - e^{k_i k_j \sum_{ij}(\hat{x}_1)} \right] S_{u_i u_j}(k) dk d\xi \quad (4.9)$$

where $S_{u_i u_j}$ is the velocity spectrum. This approach predicts a finite asymptotic dispersivity in fractional Gaussian conductivity fields, depending on the initial plume configuration [113].

Other attempts to account for the scale effect of dispersivity include the work of Wheatcraft and Tyler [143] and Neuman [100]. Wheatcraft and Tyler fit a fractal streamtube model to match the trend in observed dispersivity provided in Figure 3.9. This model predicts a continuous increase in dispersivity for a fractional Gaussian medium. Neuman [100] analyzed field observations to determine that the spatial correlation of hydraulic conductivity scales with the fractal dimension $D \approx E + 0.75$, where E is the topological dimension, [-]. This analysis assumes that the conductivity fluctuations at different scales are statistically independent, even though there is no proof that this is a valid assumption [142].

As discussed earlier, all physical systems are discrete at some scale and representation of these systems as local continua is valid only under certain conditions. Eringen [41] states that

“All bodies are nonlocal in character, and the locality represents approximations valid for only a certain limited class of physical phenomena in which the interaction of distant subbodies are unimportant.”

Non-local theories have been used in such areas as turbulent flow [93], crack tip propagation [41], and wave propagation [41, 77, 48]. Koch and Brady [80] were the first to apply non-local theory to advection-diffusion problems.

“Generally, any problem that requires the solution of integrodifferential equations with spatial integrals can be said to be nonlocal in character.” [41]

Koch and Brady [80] began by stating that

“When the length scales and time scales on which a transport process occur are not much larger than the scales of variations in the velocity field experienced by a tracer particle, a description of the transport in terms of a local, average macroscale version of Fick’s law is not applicable.”

With that motivation, they derived a non-local description of transport, beginning with a local transport equation

$$\frac{\partial c}{\partial t} + \nabla \cdot q = S \quad (4.10)$$

where q includes the convective and diffusive flux.

$$q = uc - D_m \nabla c \quad (4.11)$$

Expanding the velocity and concentration in terms of expected values (denoted in angle brackets), and perturbations (denoted with primes)

$$u' \equiv u - \langle u \rangle \quad (4.12)$$

$$c' \equiv c - \langle c \rangle \quad (4.13)$$

Substituting these terms in equation 4.10 and removing the mean equation gives

$$\frac{dc'}{dt} + \nabla \cdot (uc' - D_m \nabla c' + u'c') = -u' \cdot \nabla \langle c \rangle + \nabla \cdot \langle u'c' \rangle. \quad (4.14)$$

Neglecting products of perturbations, this equation is solved to obtain

$$c' = \int_0^t \int_x P(x - x_1, t - t_1) u'(x_1) \cdot \nabla_1 \langle c \rangle dx_1 dt_1 \quad (4.15)$$

where the transition probability P is the probability of finding a constituent particle at (x, t) given that it was at (x_1, t_1) . P satisfies the following equation

$$\frac{\partial P}{\partial t} + \nabla \cdot (uP - Dm \cdot \nabla P) = \delta(x - x_1)\delta(t - t_1). \quad (4.16)$$

With some assumptions, the concentration perturbation solution may be used to compute a non-local dispersion coefficient

$$D = D_m \delta(x - x_1)\delta(t - t_1) + \langle u'(x)P(x - x_1, t - t_1)u'(x_1) \rangle. \quad (4.17)$$

Koch and Brady [81, 80] show good agreement between local and non-local theory for times greater than about 10 advective timescales (\sqrt{k}/U , where k is the intrinsic permeability and U is the mean tracer velocity magnitude). The non-local dispersion coefficient is said to be valid at all times and give a full concentration profile. The effective diffusivity is equal to the molecular diffusivity in the limit of short distances and early time.

One may arrive at a non-local form of the governing equations by several methods. Cushman and Ginn [26] show that a non-local equation for transport may be obtained by derivation from statistical mechanics, building on fundamental molecular hydrodynamics theories derived by Boon and Yip [15]. Cushman and Hu [27] provide a summary of non-local theories for transport in porous media including the effects of diffusion, dispersion, and sources. Lenormand [86] proposed the use of non-integer spatial derivatives of concentration to describe the scale dependence of dispersivity. Because a non-integer derivative is expressed as a convolution integral, it is simply a particular form of a non-local model with a fractal basis (see [89]).

4.3 Discrete Medium Models

Discrete models are those that attempt to resolve the important scales of variability explicitly, rather than through constitutive parameters. There are two distinct types of discrete medium models. In the first type, each component in the discrete model corresponds to a physically tangible piece of the actual medium. Examples include pore-scale fluid flow simulations using a network [43] and molecular dynamics [1]. Each throat in the network model has a one-to-one correspondence with a pore in the medium. Likewise, molecules and their interactions are simulated individually in molecular dynamics. This type of discrete model is not practical for this work because we cannot hope to include every molecule or every pore in a macroscopic simulation.

When a physical system contains more detail than can be included practically, a different sort of discrete model may be constructed. In this, the second-type

discrete model, the individual elements obey rules from which the realistic large-scale behavior emerges, even though each component in the discrete model may have no correspondence to a particular element in the physical system. Lattice gas and lattice Boltzmann methods are commonly used examples of this type of discrete model [49]. These techniques do not presume to capture the physics of molecular motion. Instead, they use packets of mass and momentum that obey prescribed collision rules. These rules are constructed to enforce large-scale mass conservation and momentum transport behavior. If enough detail is included in these models, the averaged behavior is not distinguishable from averages taken on the actual system.

A heterogeneous porous medium may be approximated by subdividing a fictitious continuum into small gridblocks with properties taken from a statistically-generated random field. This work was pioneered by Warren and Skiba [141] who simulated miscible displacement through a three-dimensional, rectangular array of homogeneous blocks with block conductivities taken from a lognormal distribution. The block-to-block conductivities were uncorrelated, but they did observe an increase in dispersion with block size. Smith and Freeze [129] and Smith and Schwartz [130] extended this work by including correlation structure larger than the gridblock. For each set of parameters, deterministic governing equations were approximated numerically. By doing this for a wide range of input parameters and statistically analyzing model output, an assessment of uncertainty may be made. This is generally recognized as the Monte Carlo approach for assessing uncertainty and is gaining popularity with increasing computer power and availability.

In practice, realizations of the medium properties are generated in detail that is limited only by the capacity of the available computer resources. Random field generators are used to create media that have the same character of the field setting under study. Such character is represented by the mean, variability, and spatial persistence of a medium property. Figure 4.2 shows a traditional geological characterization and a high-resolution characterization of a Lawrence Livermore National Laboratory (LLNL) site [84].

Discrete medium modeling is consistent with the ideas of Molz et al. [95]

“In modeling dispersion phenomena, it appears that more emphasis should be placed on ... the accurate determination of hydraulic conductivity variations ... and less on incorporating somewhat arbitrary dispersion coefficients into complex mathematical models.”

Discrete models are desirable because they are not subject to the limitations of effective-parameter theories when confronted with porous media containing large conductivity variance or long-range correlation structure. Availability of computer resources defines a lower limit on the size of the computational elements. Only those

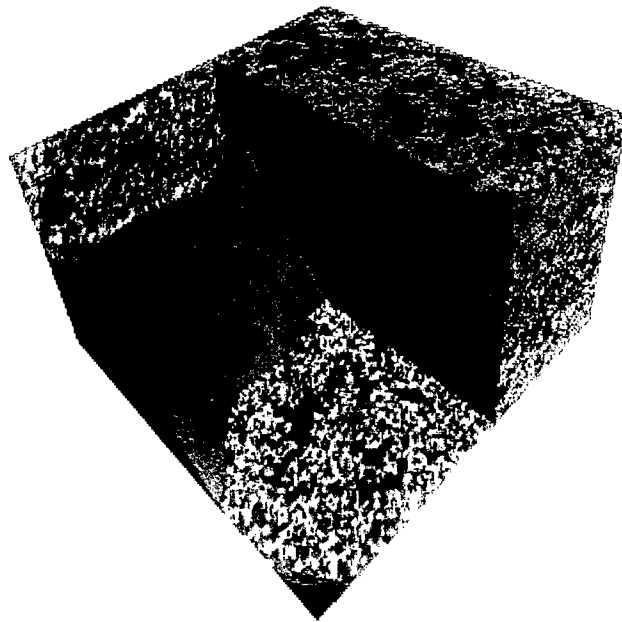
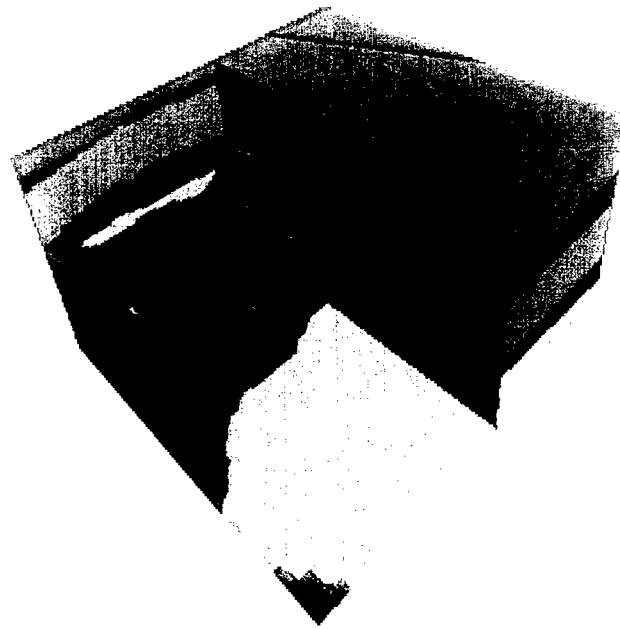


Figure 4.2: A coarse, layered realization (top) and a high-resolution realization (bottom) of the LLNL site (from the LLNL website [84]).

scales between this minimum size and the upper limit defined by the simulation domain may be represented. This is restricted to, at most, a few of orders of magnitude variation in the scales of structure represented. The disadvantage of discrete models is computational expense [118].

Another approach to high-resolution modeling is the random walk method for simulating transport. Pure random-walk modeling is like Brownian motion and, thus, represents Fickian dispersion well. Scheidegger [123] proposed that transport in media with correlation is like a random walk with some memory. Scheibe [122] used a correlated random-walk model to capture the velocity correlation structure and pre-asymptotic dispersion.

4.4 Approach Selected for the Present Work

The goal in simulating remediation schemes is to determine whether the scheme proposed has a reasonable chance of success in cleaning up the site under study. An effective-parameter (stochastic-continuum) model generates an ensemble mean concentration field (average plume). The ensemble mean concentration field is an overly-smoothed representation that may lead to optimistic cleanup-time estimates. A stochastic discrete-medium model produces a single, potential plume (typical plume) with the same basic character and complexity as the contaminated site under study. A scheme's performance in the field is better judged by its ability to remediate several typical plumes than an average plume. Both schemes offer estimates of local concentration variance which may be useful in evaluating threshold reactions or competitive sorption.

Based on these considerations and an interest in modeling for remediation design and operation, a discrete-medium modeling approach is chosen for this work. The particular type of model chosen is a discrete-network model applicable at the field scale and consistent with the non-local vision of porous media. This model qualifies as a discrete model of the second type discussed earlier. The individual throats of this model do not correspond to pores in the medium, nor do they map directly to a particular piece of the porous medium. These throats represent potential avenues for fluid and constituent to travel from one point to another within the medium. It will be shown in the following chapter that this model is consistent with non-local transport theories.

Chapter 5

Discrete Network Modeling for Flow and Conservative Transport Through Porous Media

Abstract

A macroscopic, stochastic, discrete network modeling approach is presented to describe transient or steady, variable-density fluid flow and conservative transport through heterogeneous porous media. This model addresses the issues of scale dependence of constitutive parameters (conductivity and dispersivity) and generally non-Fickian dispersive transport at the scale of remedial-action design (tens or hundreds of meters). These problems arise because heterogeneous media resist description by simple, continuum-based, differential governing equations. Stochastic discrete-medium models like this one are contrasted with stochastic continuum methods that produce modified constitutive parameters. This approach is shown to be consistent with discretizing non-local governing equations.

Flow and transport are solved in deterministic networks that are individual realizations of the poorly-known medium. The network consists of one-dimensional throats and volumeless connections. Flow through the throats is modeled as if each throat contains a uniform, homogeneous material. Pressures are determined that enforce continuity at the throat connections. Transport is modeled as pure advection in each throat with perfect mixing of constituents at the connections. The network permits

higher resolution in the velocity and concentration fields than in pressure.

The network produces pressure solutions that are comparable to standard discretization techniques (for example, continuous finite elements). Transport in the network is mass-conservative and process-correct, and is shown to capture pre-asymptotic and asymptotic growth rates of a tracer plume. The model also correctly predicts the plume formed by a continuous point source to be wholly downstream in the absence of diffusion. A demonstration calculation is provided for density-dependent flow and transport. Observation of the discrete network is possible by spatial averaging. Early results from implementation of the model on parallel computer architectures indicate significant potential.

5.1 Background

At many sites with contaminated groundwater, active remediation is unavoidable and we must choose from a long and growing list of remediation schemes. Ideally, candidate schemes are compared before construction begins. To make credible comparisons in natural soils, our ability to measure and simulate remediation processes must not be compromised by the existence of multi-scale heterogeneity. Historically, we have relied on local continuum mechanical descriptions, meaning that we replace the discontinuous, discrete medium with one containing smooth, continuous, local properties. This permits the construction of local differential balance laws on which our numerical modeling and measurement interpretation are presently based. These equations represent an attempt to fit real media into a mathematical continuum and have proven sufficient when the characteristic size of the heterogeneity structure is negligibly small.

5.1.1 Scale Dependence of Parameters.

Observations in discrete media are made as averages in space and time. When the maximum characteristic length of heterogeneity is small compared to the scale of averaging or observation (measuring instrument window or discrete numerical element), the local continuum assumption is appropriate and we may average effectively. However, when characteristic lengths of heterogeneity are not small, problems arise. A primary symptom of heterogeneity is apparent scale dependence of parameters in the governing equations.

The most celebrated example of scale dependence in the groundwater community is the dispersivity parameter. Dispersivity measured for a laboratory specimen may

be several orders of magnitude smaller than one measured for a fully-developed plume in the field [2, 55] (Figure 5.1). This effect was noted many years ago by de Josselin de Jong [32], who found that the apparent diffusion coefficient was a function of travel distance. The rate of change of concentration of a conservative solute is given by

$$\frac{\partial c}{\partial t} = -\nabla \cdot (uc) + \nabla \cdot (D\nabla c) \quad (5.1)$$

where c = concentration of solute, $[M/L^3]$,
 t = time, $[T]$,
 u = seepage velocity from a decoupled flow solution, $[L/T]$, and
 D = dispersion coefficient tensor, $[L^2/T]$.

The dispersion coefficient is composed of a hydrodynamic dispersion term and a molecular diffusion term

$$D_{ij} = D_{ij}^d + D^m \delta_{ij} = (\alpha_L - \alpha_T) \frac{u_i u_j}{u} + \alpha_T u \delta_{ij} + D^m \delta_{ij} \quad (5.2)$$

where D^d = hydrodynamic dispersion coefficient, $[L^2/T]$,
 δ_{ij} = Kronecker delta, $[-]$,
 D^m = molecular diffusion coefficient, $[L^2/T]$,
 α_L = longitudinal dispersivity, $[L]$,
 α_T = transverse dispersivity, $[L]$,
 u_i, u_j = velocity magnitudes in the i and j directions, $[LT^{-1}]$, and
 u = mean fluid velocity magnitude, $[LT^{-1}]$.

Hydrodynamic dispersion typically is much larger than molecular diffusion. Equation 5.1 predicts that a solute plume resulting from an instantaneous point source of solute spreads longitudinally (the x direction in this case) at a constant rate described by

$$\alpha_L = \alpha_x = \frac{1}{2} \frac{d\sigma_x^2}{d\bar{x}} \quad (5.3)$$

where for a plume with total mass c_0 , the first spatial moment in x is

$$\bar{x} = \frac{1}{c_0} \int_{-\infty}^{\infty} xc(x)dx \quad (5.4)$$

and the second spatial moment in x is

$$\sigma_x^2 = \frac{1}{c_0} \int_{-\infty}^{\infty} x^2 c(x) dx. \quad (5.5)$$

Equation 5.1 predicts that the size of the plume, as measured by σ_x , increases as the square root of the distance it travels ($\sigma_x \propto \sqrt{\bar{x}}$). For a uniform mean flow the

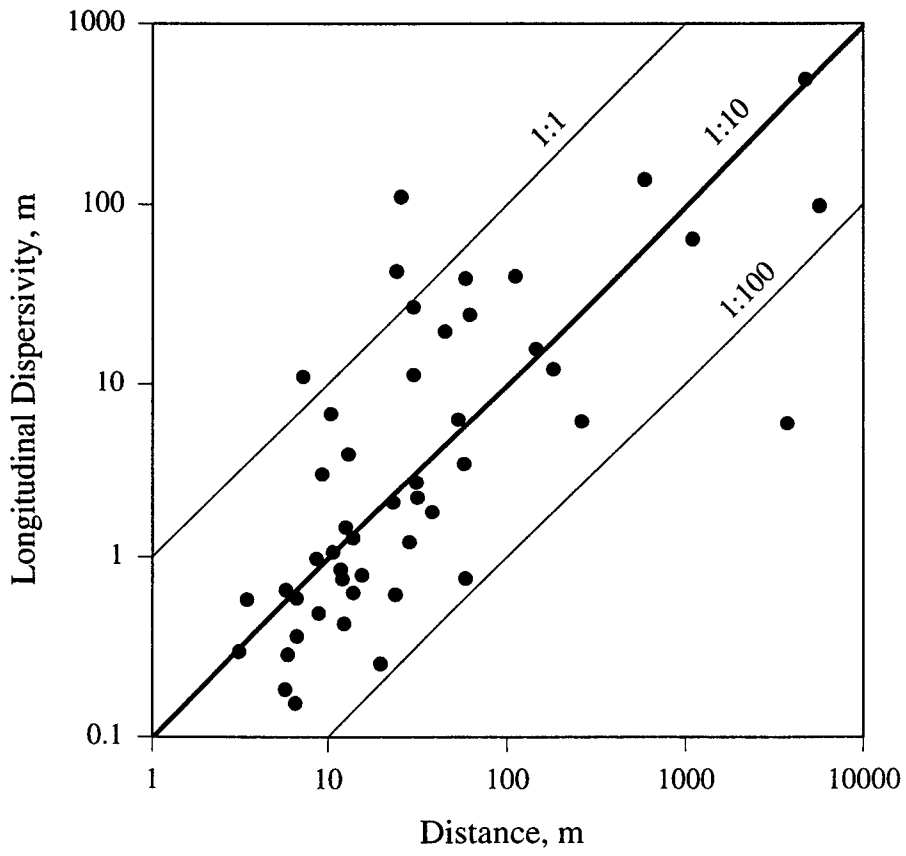


Figure 5.1: Observed variation in dispersivity with distance traveled (modified from Anderson [2]).

plume centroid and travel time are related by the fluid velocity. Thus, $\sigma_x \propto \sqrt{t}$. Observation of actual plume growth shows that the rate of plume spreading increases nearly linearly with travel distance ($\sigma_x \propto \bar{x}$) [53].

5.1.2 Non-Fickian Dispersion.

The existence of finite-scale heterogeneities has another important consequence. Non-negligible heterogeneity exposes inconsistencies in the governing equations. Dispersion is not diffusion, even though the traditional model used to describe dispersion is Fick's law of molecular diffusion with an exaggerated coefficient, e.g. [38]. A diffusion model describes dispersion well under some conditions. Fick's law applies when the principal mode of dispersive transport is by random, Brownian-like motions. This mode is possible for problems that exhibit symmetrical behavior about the mean motion of the contaminant. For example, if an observer travels with the mean speed of a plume evolving from an impulse point source, the plume seems to spread nearly symmetrically. When this plume is large compared to the size of the heterogeneities, each contaminant particle's motion appears random. The position of a particle of contaminant relative to the plume centroid indicates nothing about its relative speed. In other words, the particle's velocity is uncorrelated in time. This is analogous to Brownian motion, explaining why a diffusion model predicts asymptotic plume growth rates. This situation also applies to breakthrough curves from column experiments. However, the mechanisms for dispersion are not those for diffusion, and Fick's law is justified only as an approximation in the asymptotic limit.

When a medium's characteristic length scales are finite, a different picture emerges. A particle leading the plume's centroid is probably traveling faster than the centroid, and vice versa. Therefore, a contaminant particle's present velocity, relative to the plume speed, is an indication of its future relative speed. A positive velocity correlation exists in time, and the Fickian model does not apply. Further, for problems that do not satisfy the symmetry requirements, a Fickian model for dispersion will never model the behavior correctly. For example, with a continuous injection of tracer, one cannot easily remove the mean motion of the plume. Tracer particles near the source of injection will exhibit correlated motions that will decay as the particles move downstream.

5.1.3 Scale Separation.

A fundamental issue here is a lack of separation between the observation and averaging scale and the characteristic length for a process.

“In general, events distinguished by a great disparity in size have little influence on one another; they do not communicate, and so the phenomena associated with each scale can be treated independently.”
[146]

Most effective averaging theories assume that the underlying structure is small compared to the averaging volume and this required separation exists. This conforms to the idealized conceptual model of porous media that has prevailed for the last several decades. Porous media have been assumed heterogeneous at the pore scale and the formation scale (Figure 5.2). Each formation was assumed to be composed of a single, homogeneous porous material. That is, the formation size was conceived as being so much larger that the grain size, heterogeneity at the pore scale was ‘averaged’ away. This averaging was formalized in the definition of the REV [10]. Formation-scale heterogeneity has been modeled explicitly in numerical simulations.

Unfortunately, conceptual models that assume structure exists only at the pore and aquifer scales are often inaccurate for natural porous media (Figure 5.3). Natural soils contain heterogeneity with an entire spectrum of characteristic lengths, with limited scale separation as illustrated in Figure 5.2 adapted from Herrmann et al. [65]. With a continuum of scales present, it is difficult to model all scales explicitly and, in practice, one must attempt to capture representative scales.

5.1.4 Stochastic Continuum versus Stochastic Discrete Models.

Models that account for uncertain heterogeneity in the medium may be categorized as stochastic-continuum models or stochastic-discrete models [118]. Stochastic continuum models produce effective parameters that include the effects of variability in medium properties. In their simplest form, effective parameters are constants or are some function of a global property such as plume age, size, or distance traveled. Examples of effective parameter modeling in heterogeneous media include the macrodispersion work of Gelhar [53], Dagan [29], and Neuman [103] and the effective conductivity work of King [78], Dagan [28], and Gelhar [53]. Much work continues toward solving stochastic-continuum equations, but solutions still are possible for only a few idealized conditions. Converging flows and unsaturated or multiphase flows are still under study. Many stochastic theories neglect second-order and higher terms in the perturbation expansion. Variance in lognormal hydraulic conductivity in real porous media may easily violate the limits imposed by the small perturbation assumption that the variance in log hydraulic conductivity is small ($\sigma_f \ll 1$). Further, long-range correlation structure violates the premise that the medium is a statistically-homogeneous random field.

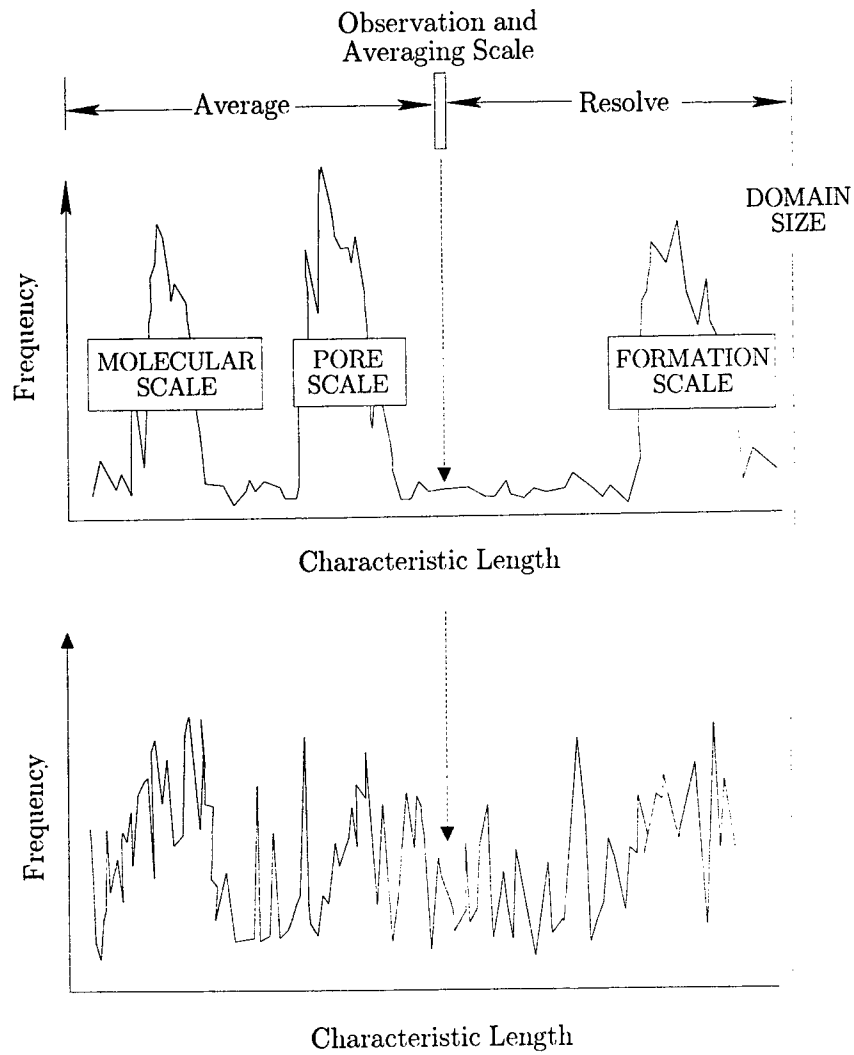


Figure 5.2: Hypothetical distribution of characteristic lengths in an idealized medium (above) and a more realistic soil (below).

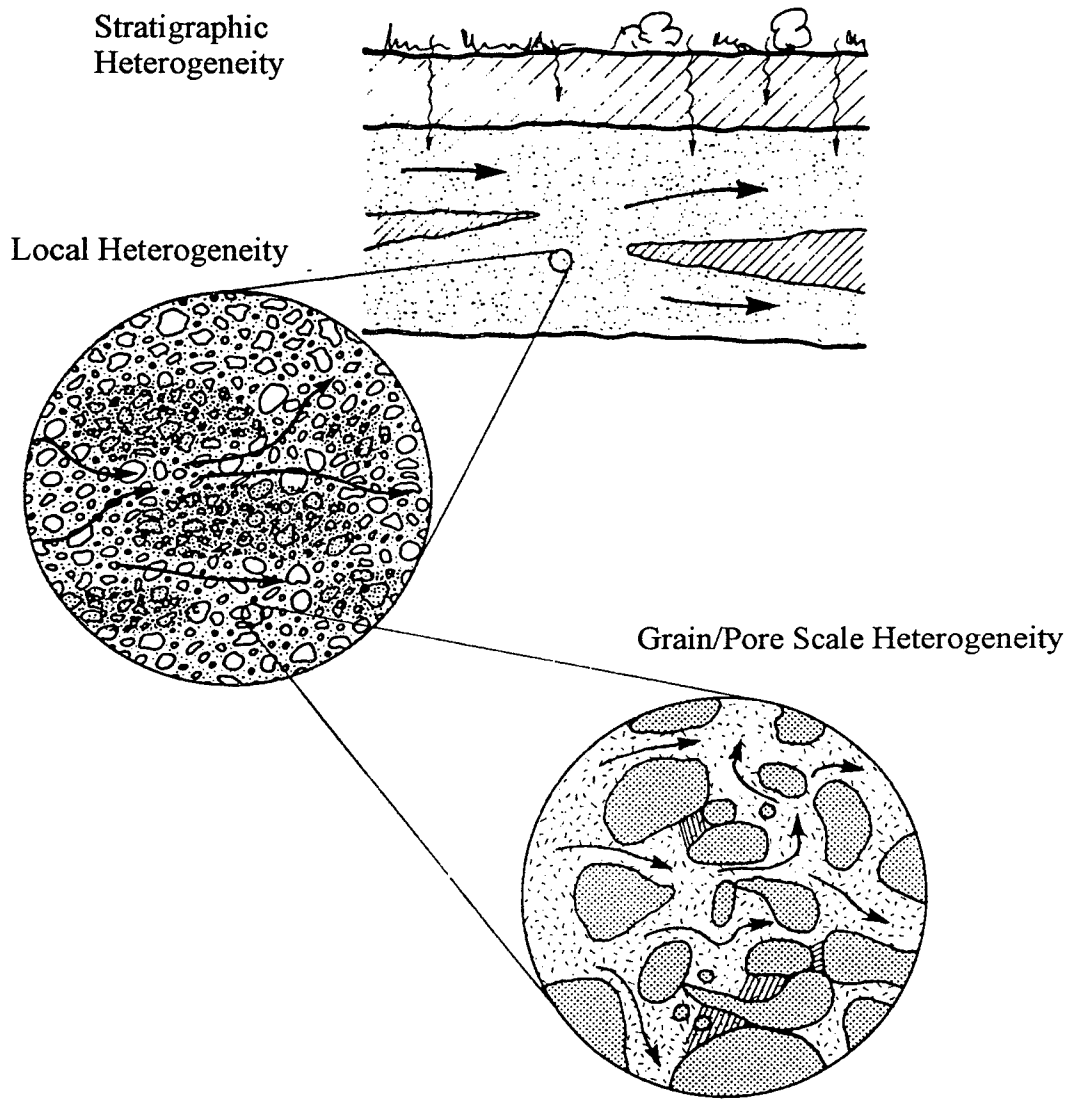


Figure 5.3: Schematic of multi-scale heterogeneity in porous media (adapted from Herrmann et al. [65]).

Stochastic discrete models solve simplified forms of the governing equations in detailed, statistically-generated, deterministic media. This type of model attempts to resolve many scales of variability explicitly, rather than through macroscopic constitutive parameters. Stochastic-discrete models are desirable because they are not limited by the assumption of small variance in property values and are capable of simulating many processes for which no solution to the stochastic equations is yet possible. Discrete medium models are capable of handling large conductivity variance and long-range correlation. However, discrete-medium models may only resolve detailed structure within a limited range of scales and any measure of uncertainty in the results must be addressed through multiple-realization, Monte-Carlo simulations. With these considerations, the primary disadvantage of discrete models is generally computational expense [118].

The goal in practical remediation modeling is decision support. We must choose and defend the most cost-effective remediation strategy that will clean up a site. Modeling must predict a scheme's likelihood of success for the particular site under study. A stochastic-continuum model generates an ensemble mean concentration field (average plume) and a concentration variance field. An ensemble concentration field is an average of the plumes that would result from simulating transport through all possible statistical realizations of the medium. This plume is effectively a probability map for transport. It gives the probability of finding a tracer particle at a particular location, given that it was introduced at the injection point at time 0. A stochastic discrete-medium model produces a single, potential plume (typical plume) that has the same large-scale character as the problem under study. A scheme's performance cleaning up this typical plume is probably a better indicator of performance in the actual soil than its ability to remediate an ensemble-average plume. For this reason and our desire to evaluate remedial scheme performance, a stochastic discrete medium modeling approach is proposed to simulate flow and transport through heterogeneous media.

5.1.5 Overview of Stochastic Discrete Medium Modeling.

There are two basic types of discrete-medium models. In the first type, each component in the discrete model corresponds to a piece of the actual medium. An example is pore-scale fluid flow simulation with a network. Each throat in the network model has, in theory, a one-to-one correspondence with a pore in the medium. These models are not of practical interest for this work because we cannot hope to include every pore in a macroscopic simulation.

A heterogeneous medium may be approximated by subdividing the domain into small gridblocks with properties taken from a statistically generated random field.

This work was pioneered by Warren and Skiba [141] and Heller [64]. In their work, block property assignments were made independently. Smith and Freeze [129] and Smith and Schwartz [130] extended this work by including correlation structure larger than the gridblock. For each set of parameters, deterministic governing equations were approximated numerically.

In practice, realizations of the medium properties are generated in detail that is limited only by the capacity of the available computer resources. Random field generators are used to create media that have the same structural character of the field setting under study [137].

When a physical system contains more detail than can be included practically, a different sort of discrete model may be constructed. In this, the second-type discrete model, the components represent only the larger scales of structure and behavior. Each component in the discrete model may not correspond to a particular structure in the physical system. Lattice gas and lattice Boltzmann methods are common examples of this type of discrete model [49]. These techniques do not presume to capture the physics of molecular motion. Instead, they use packets of mass and momentum that obey prescribed collision rules. These rules are constructed to enforce large-scale mass conservation and momentum-transport behavior. If enough detail is included in these models, the averaged behavior is not distinguishable from averages taken on the real system.

This document describes a discrete network model for field-scale simulation of saturated flow and conservative transport through heterogeneous porous media. The model falls into the second type of discrete-medium models. Each throat represents a potential path from one location in the domain to another.

5.1.6 Discrete Network Modeling.

Network representation of the pore space dates back to the work of Bjerrum and Manegold [14] (cited in [118]) for single-phase flow and, for two-phase flow, Fatt [43]. De Josselin de Jong [32] performed calculations in a pore-scale network to examine dispersion. Bear [8] proposed a series of mixing cells connected by channels to describe tracer transport through soil pores. Perfect mixing was assumed in the cells and perfect translation in the channels. This model is equivalent to a network with nodal storage. Sahimi et al. [119] used network-computed fluid velocities to drive particle transport. Sahimi and Imdakm [121] added molecular diffusion to this network.

Network modeling of flow and transport through fractured media has been practiced for several years including Schwartz et al. [126] and Tsang et al. [139]. However, network model representations of macroscopic porous media are uncommon.

Ewing and Gupta [42] present a domain network approach to simulate quasi-static drainage and imbibition. In this approach, the domain is divided into equal-size subdomains. Within each subdomain, all pores are assumed to have the same radii, and there may be many pores within a single subdomain. Communication among subdomains is performed only at the subdomain interfaces. Sahimi [116] suggested that a percolation network could be constructed in which each bond of the network could represent a homogeneous region of the medium. Mukhopadhyay [98] extended these ideas by constructing a correlated percolation network model to represent media with infinite-length correlation structure. Yortsos et al. [148] apply percolation theory to macroscopic, heterogeneous media in the context of immiscible flow.

The popularity of network-like discretization approaches is increasing in other fields as well. For example, in network thermodynamics [106], a discrete network is considered an expression of combinatorial topology rather than the point-set topology that leads to partial differential field equations. Thus, the network graph contains information on system structure that is not available in bare differential equations [106]. This approach has been used to exploit similarities between electrical networks and coupled flows with driving forces [66]. The fluid flow problem is discretized in space, but not in time, producing a network structure that may be evaluated with well-developed methods from circuit analysis [66]. Likewise, network discretizations (or network-like, edge-based finite elements) are offered as complementary decomposition alternatives to finite difference or finite element representations of the domain for fluid dynamics computations [58, 107]. These network discretizations are valued for low storage needs and computational efficiency with accuracy comparable to traditional discretizations [107].

5.2 Justification of the Network Approach

Because there have been few network models designed to represent the field scale, some justification of the network approach is appropriate. The network is an appealing conceptual model because of its structural and functional similarity with the pore scale. Further, it is a reasonable conceptual model at the macroscopic scale. Heterogeneity creates preferential flow paths at all scales. Flow subdivides and bypasses lower permeability regions creating an interconnected network of flow paths. This and many other approaches may be shown to be valid representations of the porous medium because they honor the fluid balance law and may be shown to obey a macroscopic Darcy's law [108].

As with a real porous medium, the network is viewed through an averaging filter (i.e., a measuring instrument) for comparison to observations. Averaging removes

degrees of freedom by imposing smoothness. Therefore, there are an infinite number of detailed images that will produce the same average image. If enough of the ‘right’ kind of sub-observation detail is included, images averaged from the network simulation and from observation of the real medium cannot be distinguished. The network is simply a coarsened discrete system that is a lower-order approximation of the actual, detailed medium.

In high-resolution discrete-medium modeling, we impose a separation between the scale of observation and the scale of effective parameter averaging (Figure 5.4). We install reasonable, deterministic structure beneath the observation scale to create this separation. Because we cannot resolve all scales, we must use averaged effective parameters at some scale. This approach simply removes some of the burden from the constitutive parameters, placing it on computation.

5.2.1 The Network as a Discrete Approximation of Non-local Equations.

In addition to its functional similarity to the pore scale and its simplicity, a network may be shown to be consistent with non-local descriptions for flow and transport [81, 25, 102]. We begin with a convolution integral equation describing non-local advection

$$\frac{\partial c(x, t)}{\partial t} = \int_0^t \int_{-\infty}^{\infty} \Psi(x - x', t - t') \frac{\partial c}{\partial x'} dx' dt' \quad (5.6)$$

If we assume the kernel (Ψ) is a smooth, differentiable function, we may use integration by parts to move the spatial derivative of concentration onto the kernel function. This produces an integral involving concentrations, boundary conditions at infinity, and initial conditions involving concentration.

$$\begin{aligned} \frac{\partial c(x, t)}{\partial t} &= \int_0^t \int_{-\infty}^{\infty} \frac{\partial \Psi(x - x', t - t')}{\partial x'} c(x', t') dx' dt' \\ &+ \int_0^t [\Psi(x - x', t - t') c(x', t')]_{-\infty}^{\infty} dt' \end{aligned} \quad (5.7)$$

We define points in space and time that might correspond to nodes in a numerical approximation. Assuming that the concentration field is a smoothly varying function, we may express the concentration anywhere in the field as a linear combination of the concentrations at these nodes

$$c(x, t) = \sum N_i c_i = \{N\}^T \{c\} \quad (5.8)$$

where N_i defines values of the averaging or interpolating function at node i . The advection equation becomes

$$\frac{\partial c(x, t)}{\partial t} = \int_0^t \int_{-\infty}^{\infty} \frac{\partial \Psi(x - x', t - t')}{\partial x'} \{N\}^T dx' dt' \{c\} + B \quad (5.9)$$

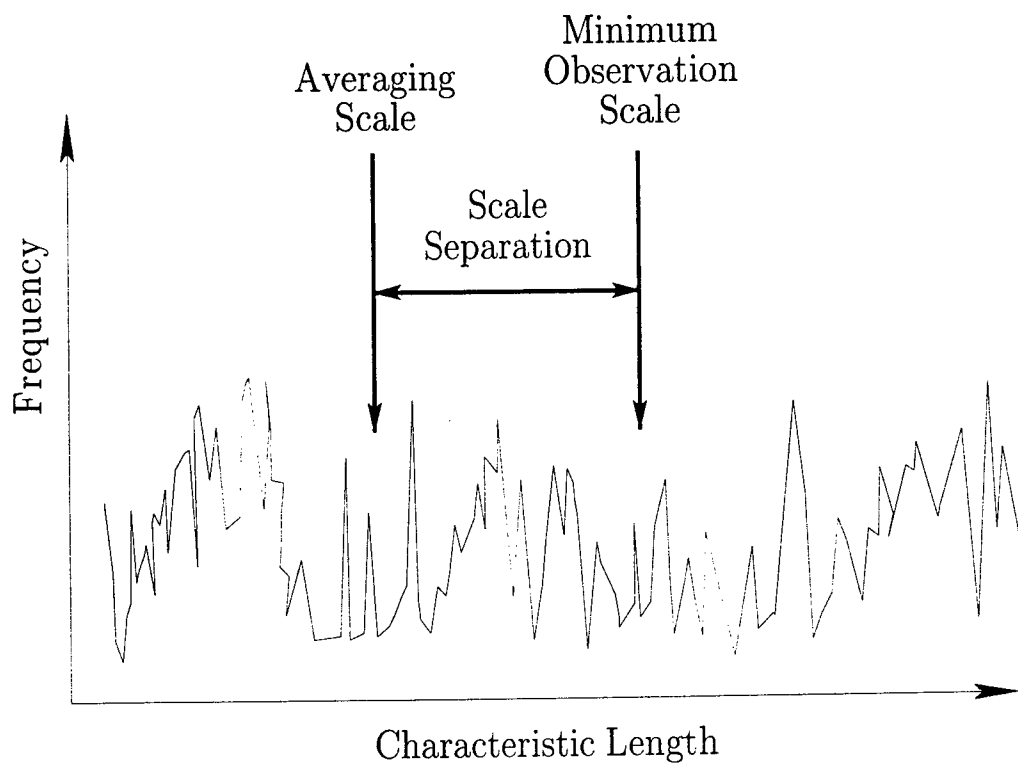


Figure 5.4: Creating a separation between the scale of averaging and the scale of observation.

where B represents the boundary terms. The change in concentration with respect to time at any location in the domain becomes a weighted summation of the concentrations at the nodes

$$\frac{\partial c(x, t)}{\partial t} = \sum_i \left(\int_0^t \int_{-\infty}^{\infty} \frac{\partial \Psi(x - x', t - t')}{\partial x'} N_i dx' dt' + B_i \right) c_i \quad (5.10)$$

Choosing different functions to apply these weightings leads to different numerical approximations. Presenting this in a simpler form,

$$\frac{\partial c(x, t)}{\partial t} = \sum_i (F_i(x, t) + B_i) c_i. \quad (5.11)$$

By evaluating the rate of change of concentration at each node, a system of equations is retrieved.

$$\frac{\partial c_i}{\partial t} = \sum_j (F_{ij} + B_j) c_j. \quad (5.12)$$

where $F_{ij} = F_i([x, t]_j)$ with $[x, t]_j$ being the x - t pair at the j space-time node.

This process has reduced the convolution integral to a potentially complex finite-difference stamp in space and time. At time t , the rate of change in concentration is a weighted sum of all previous times for all ‘upstream’ nodes. Advection through a network produces exactly the same form of difference equations. If the spacing of the nodes in the numerical grid exceeds the range of the convolution integral’s kernel function, the numerical approximation appears to be that of a local problem. Only the nearest neighbors and the most recent time period will contribute. In fact, when the kernel function is a Dirac delta operator, local advection is retrieved. However, when the numerical grid spacing is less than the range of the kernel function, the difference stamp may become quite complicated, involving points far removed in space and time. In either case, this stamp may be replaced, without loss of information, by a network through which there is pure advection. A network is a graphical interpretation of the system of equations 5.12. This network may have coordination numbers much larger than those common to classical network models and may have ‘non-local’ connectivity absent in the physical pore-scale network. The key to the approach taken here is that it is more straightforward to calibrate the network directly than it is to determine the kernel function in the non-local equation.

5.2.2 Comparison to High-Resolution Continuum Models.

Although their origins differ, the network model and the finely-discretized continuum [137, 136] are very similar in application. Both rely on the adequate resolution of the velocity variation and small-scale coupling with concentration to reproduce dispersion. Both rely on geostatistical methods to create realizations of the medium. Both

have the same general modeling philosophy, which is to embed the salient features of the geological medium, the correlation structure, the macroscopic permeability, and anisotropy directly into the computational model.

Although not as widely used, the network approach may enjoy a few advantages compared to high-resolution continuum models. For example, the network permits us to partially separate the resolution in pressure from that in velocity, because pressure is computed at the connections and velocity is computed in the throats. We may increase or decrease the relative resolution associated with these two variables by altering the coordination number. The network permits us to install throats with a length distribution that honors the spatial correlation structure and anisotropy in the medium. The equations solved in the throat are one dimensional, making the addition of processes simpler than in a multidimensional framework. Lastly, the fact that the network decomposes so cleanly into many one-dimensional problems makes it a strong candidate for parallel computer processing.

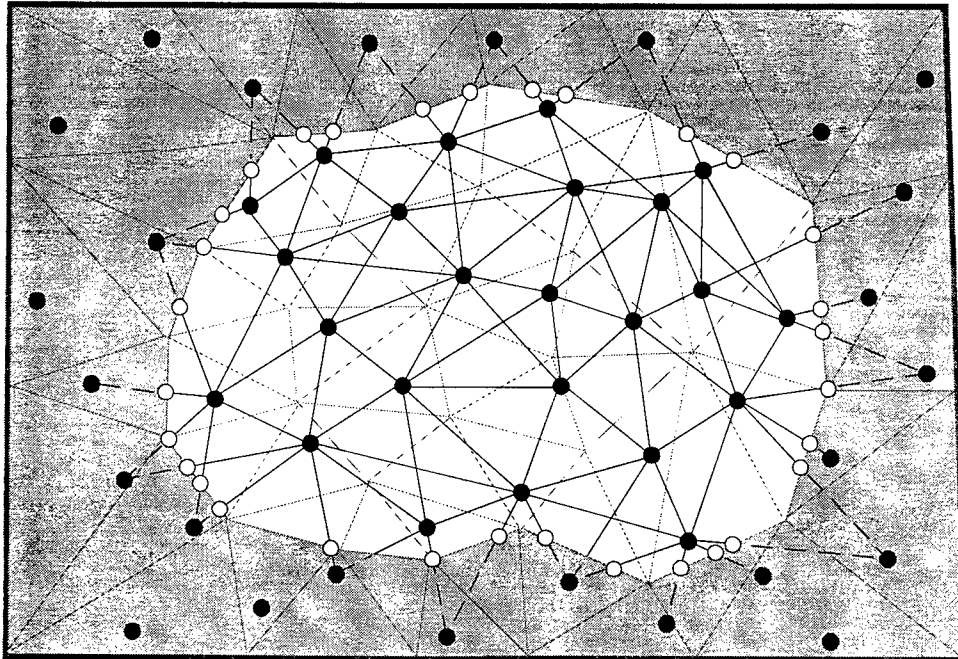
5.3 Brief Description of the Model

Applying the stochastic discrete-network model developed in this work consists of three major exercises: (1.) creating the network, (2.) simulating flow and transport, and (3.) visualizing the results.

5.3.1 Creation of the Network.

The network consists of throats of arbitrary cross section that meet at zero-volume connections. To avoid boundary effects, the desired simulation domain is situated within a larger bounding box. Connection positions are established randomly within this bounding box. The number of connections created is determined by the desired average connection spacing. A minimum connection spacing is enforced to prevent the creation of very short throats for which the computational time step may be impractically small. Throats are created to join the connections in accordance with a probability function that decays with inter-point spacing. That is, the odds of two connections being joined by a throat decrease as the connections are farther apart. After throats have been created, the region between the simulation domain and the bounding box is discarded. Throats that cross the boundaries of the simulation domain are truncated at the boundaries. Boundary conditions are applied to these truncated throats during flow and transport simulation. A coarse network, the simulation domain, and the bounding box are shown in Figure 5.5.

Throat properties are assigned from statistical distributions. The network may be constructed in a fashion to honor macroscopic measurements such as porosity,



- Active Throats
- - - Truncated Throats
- Connections
- Boundary Connections

Figure 5.5: A coarse, two-dimensional network with the extent of the simulation domain (in white) lying with the gray bounding box.

conductivity, and dispersivity. The process for accomplishing this is described in Chapter 6. The network embodies all the geologic character of the medium, including flow and transport properties.

5.3.2 Governing Equations for Fluid Flow.

By conservation of fluid mass in a control volume, the change in storage is balanced by the net flux through the surface and the internal sources,

$$\frac{1}{V} \frac{\Delta M}{\Delta t} = -\frac{\Delta(\rho_f q)_x}{\Delta x} - \frac{\Delta(\rho_f q)_y}{\Delta y} - \frac{\Delta(\rho_f q)_z}{\Delta z} + \frac{\rho_f Q_s}{V} \quad (5.13)$$

where V = size of the control volume, $[L^3]$,
 M = mass of fluid in the control volume, $[M]$,
 t = time, $[T]$,
 ρ_f = fluid density, $[ML^{-3}]$,
 q = fluid flux through the face, $[LT^{-1}]$, and
 Q_s = source of fluid, $[L^3T^{-1}]$.

The change in storage occurs through rearrangement of soil grains and compression of the fluid. The volume of solids is assumed to be invariant. The change in storage is

$$\frac{1}{V} \frac{\Delta M}{\Delta t} = \frac{\partial}{\partial t}(\phi \rho_f) = \phi \frac{\partial \rho_f}{\partial t} + \rho_f \frac{\partial \phi}{\partial t} \quad (5.14)$$

where ϕ is the porosity. The porosity is assumed to be constant for simplicity and to permit the straightforward tracking of all fluid mass. All compressive storage is lumped into the fluid part of the total compression,

$$\frac{1}{V} \frac{\Delta M}{\Delta t} = \phi \frac{\partial \rho_f}{\partial t}. \quad (5.15)$$

The flow equation (5.13) becomes

$$\phi \frac{\partial \rho_f}{\partial t} = -\nabla \cdot (\rho_f q) + \frac{\rho_f Q_s}{V} \quad (5.16)$$

When this is applied in one dimension along the throat with no internal sources of fluid, we have

$$\phi \frac{\partial \rho_f}{\partial t} + \frac{\partial}{\partial l}(\rho_f q) = 0 \quad (5.17)$$

where l is the position along the throat, $[L]$. The variational statement for this equation is

$$\int_0^L w \left(\phi \frac{\partial \rho_f}{\partial t} + \frac{\partial}{\partial l}(\rho_f q) \right) dl = 0 \quad (5.18)$$

where w is a weight function, $[-]$, and L is the throat length, $[L]$. Separating these terms and performing integration by parts on the second term gives

$$\int_0^L w \phi \frac{\partial \rho_f}{\partial t} dl - \int_0^L \frac{\partial w}{\partial l} (\rho_f q) dl - [w \rho_f q]_0^L = 0 \quad (5.19)$$

Swapping the order of integration and differentiation in the first term gives

$$\phi \frac{\partial}{\partial t} \left(\int_0^L w \rho_f dl \right) - \int_0^L \frac{\partial w}{\partial l} (\rho_f q) dl - [w \rho_f q]_0^L = 0 \quad (5.20)$$

Here we elect to enforce the variational statement with a constant weight function. This serves two purposes. First, it keeps the flow solution as simple as possible. Second, it keeps the problem symmetric in the presence of density variability, an important feature for numerical implementation. This choice leads to

$$\phi \frac{\partial}{\partial t} \left(\int_0^L \rho_f dl \right) - [\rho_f q]_0^L = 0 \quad (5.21)$$

Because the throat is effectively the control volume under these conditions, the flow equation is trivial. It simply states that the rate of change of mass in the throat is the difference in mass flux through the two ends.

The total mass of fluid must be conserved at each junction of the throats (connection) for each time step. Therefore, we must determine the fluid mass flux at each end of the throat. The total flux along the throat (q_T) is the sum of fluxes due to total potential (q_D) and to compression (q_C).

$$q_T = q_D + q_C \quad (5.22)$$

Darcy's law for exchange of momentum relates the difference in potential to the fluid flux [10]

$$q_D = -\frac{k}{\mu} (\nabla P + \rho_C g \nabla z) \quad (5.23)$$

where k = intrinsic permeability of the medium, $[L^2]$,
 μ = dynamic fluid viscosity, $[ML^{-1}T^{-1}]$,
 P = fluid pressure, $[ML^{-1}T^{-2}]$,
 ρ_C = density of the fluid/constituent mixture, $[ML^{-3}]$, and
 g = gravitational acceleration, $[LT^{-2}]$.

Expressing the pressure in terms of an equivalent, fresh-water pressure head,

$$q_D = -\frac{k}{\mu} (\nabla(\rho_0 g h_0) + \rho_C g \nabla z). \quad (5.24)$$

The fresh-water density and the gravitational acceleration may be extracted to produce

$$q_D = -\frac{k\rho_0g}{\mu} \left(\nabla h_0 + \frac{\rho_C}{\rho_0} \nabla z \right). \quad (5.25)$$

Recasting in terms of total, fresh-water head (H_0), the potential flux is

$$q_D = -K_0 \frac{\mu_0}{\mu} \left(\nabla H_0 + \left(\frac{\rho_C}{\rho_0} - 1 \right) g \nabla z \right) \quad (5.26)$$

where K_0 is the saturated hydraulic conductivity of the medium, μ_0 is the dynamic viscosity of fresh water, and ρ_0 is the density of fresh water. The total compression is

$$Q_C = \frac{\Delta V}{\Delta t} = \frac{c_p V \Delta P}{\Delta t} \quad (5.27)$$

where c_p is the fluid compressibility. Recasting pressure as pressure head (h_0),

$$Q_C = \frac{c_p V \Delta(\rho_0 g h_0)}{\Delta t} \approx c_p V \rho_0 g \frac{\partial h_0}{\partial t}. \quad (5.28)$$

The time derivative of the pressure head is equal to the time derivative of the total head. After dividing by the volume, we have the compressive flux per unit volume of fluid.

$$q_C = c_p \rho_0 g \frac{\partial H_0}{\partial t}. \quad (5.29)$$

The total flux is

$$q_T = -K_0 \frac{\mu_0}{\mu} \left(\nabla H_0 + \left(\frac{\rho_C}{\rho_0} - 1 \right) g \nabla z \right) + c_p \rho_0 g \frac{\partial H_0}{\partial t}. \quad (5.30)$$

In one dimension along the throat,

$$q_T = -K_0 \frac{\mu_0}{\mu} \left(\frac{\partial H_0}{\partial l} + \left(\frac{\rho_C}{\rho_0} - 1 \right) g \frac{\partial z}{\partial l} \right) + c_p \rho_0 g \frac{\partial H_0}{\partial t} \quad (5.31)$$

To solve the pressure problem, we need only know the end fluxes for each throat. By continuity in a one-dimensional throat, without fluid compression, the flux at every position along the throat must be constant. Because conductivity may vary with density and viscosity, the conductivity may not be constant along the throat. The effective conductivity for the one-dimensional throat is the harmonic mean of the variable conductivity. The composite density and compressibility are computed as a volume averages over the throat. Then, the compression term is compiled at the ends of the throats. This effectively assigns one-half the total throat compressibility to each end of the throat, thus producing a diagonal matrix in the time term. Lumping slightly reduces the spatial accuracy of the solution [20], but simplifies the solution process. With compression, the flux profile along the throat is linear.

The discrete equation for flux in the throat is

$$\begin{aligned} \{q_T\} &= \frac{K_h}{L} \begin{bmatrix} 1 & -1 \\ -1 & 1 \end{bmatrix} \{H_0\} - \frac{1}{L} \int_0^L \left(\frac{\rho_C}{\rho_0} - 1 \right) dl \begin{bmatrix} 1 & -1 \\ -1 & 1 \end{bmatrix} \{z\} \\ &+ \frac{1}{2L} \int_0^L c_p \rho_0 g dl \begin{bmatrix} 1 & 0 \\ 0 & 1 \end{bmatrix} \{\dot{H}_0\}. \end{aligned} \quad (5.32)$$

where K_h is the effective, saturated hydraulic conductivity in the throat and the dotted quantity indicates a temporal derivative.

5.3.3 Conservation of Fluid Mass at the Connections.

We wish to enforce conservation of fluid mass at each connection and for each time step. Because all throats have the same cross-sectional area, we may write the fluid-mass conservation statement as

$$\sum_{n=1}^{nt} \rho_f q_n = \frac{S_f}{A_t} \quad (5.33)$$

where S_f is the source of fluid mass per unit time, $[MT^{-1}]$ and A_t is the cross sectional area of the throats, $[L^2]$. We may replace this conservation of mass statement with a fluid volume balance because there is no storage at the connections themselves.

$$\sum_{n=1}^{nt} q_n = -\frac{\partial H_0}{\partial t} \sum_{n=1}^{nt} \frac{1}{2} \rho_0 c_p g. \quad (5.34)$$

When the coefficient of compressibility is non-zero and the head at a connection is changing with time, fluid will be entering or leaving 'storage'. At each connection, the inbound and outbound fluid volumes may differ, but the inbound and outbound fluid masses will balance. Further, the inbound constituent masses are distributed within each time step at each connection. Thus, densities and concentrations are affected by the fluid compressibility. The throat-level flux equations are assembled into a global problem using Equation 5.34, permitting the computation of total fresh-water head at the connections.

5.3.4 Remark on Solution Variables.

The choice of solution variable may have dramatic consequences for numerical accuracy. For example, in a gram-centimeter-second system, reasonable values for permeability may be $10^{-12} cm$ while 100 m of water represents a pressure of $10^7 g\text{-}cm^{-1}\text{-}s^{-2}$. This range of values is difficult to manipulate numerically. By using total fresh-water head, saturated hydraulic conductivity, specific gravity, and specific viscosity, and by specifying gravitational acceleration times compressibility as

a single value, we take advantage of as much cancellation as possible. This keeps solution values in a reasonable range and minimizes potentially serious numerical problems associated with finite precision.

5.3.5 Time Integration.

A first-order, backward Euler scheme is used to advance the solution in time. To further simplify the process, the buoyancy force (the C matrix in Equation 5.35) is lagged a time step, making the flow and transport equations weakly coupled and iteration is avoided. The method is unconditionally stable, but lagging the buoyancy effect limits the practical length of a time step for the flow computation to maintain accuracy. In matrix form, the equation solved is

$$([M] + \Delta t [B]) \{H_0\}^{n+1} = [M] \{H_0\}^n + \Delta t [C] \{z\} + \Delta t \{q_s\}. \quad (5.35)$$

where

$$[M] = \frac{K_h}{L} \begin{bmatrix} 1 & -1 \\ -1 & 1 \end{bmatrix}, \quad (5.36)$$

$$[B] = \frac{1}{2L} \int_0^L c \rho_0 g dl \begin{bmatrix} 1 & 0 \\ 0 & 1 \end{bmatrix}, \quad (5.37)$$

$$[C] = \frac{1}{L} \int_0^L \left(\frac{\rho_C}{\rho_0} - 1 \right) dl \begin{bmatrix} 1 & -1 \\ -1 & 1 \end{bmatrix}. \quad (5.38)$$

5.3.6 Solution Procedure.

A diagonally-preconditioned, conjugate-gradient, iterative solution scheme was used to solve the linear system of equations for total head. Because the network may be well connected, the bandwidth on the matrix may be large compared to traditional simulation methods. To avoid forming this potentially large matrix, a matrix-free solution scheme was adopted. The matrix-vector product, $([M] + \Delta t [B]) \{H_0\}$, is computed by compiling the contributions from each throat at the connections. This process requires more operations than multiplying a pre-formed matrix with a vector, but saves considerable memory. The pressure solution is found simply by enforcing continuity at the connections. The total volume imbalance accumulated at each connection is used as the residual for the iterative solution scheme.

5.3.7 Transport.

Conservative transport in the network assumes perfect mixing at the connections and perfect advection along each throat, which is functionally similar to the pore-scale transport model advanced by Bear [8]. Throat end fluxes corresponding to

the converged head solution are used to drive transport. Equation 5.32 is consistent with a linear flux distribution in the throat when compression is present, and a constant flux when the fluid is incompressible. The linear velocity profile is used to solve the pure advection problem in each throat

$$\frac{\partial c}{\partial t} = -u(l)\frac{\partial c}{\partial l}. \quad (5.39)$$

where $u(l)$ is the linear seepage velocity along the throat. The seepage velocity is related to the flux through the porosity (ϕ), $u = q/\phi$. The porosity is constant within each throat, but need not be constant over the entire domain.

5.3.8 Throat Discretization.

To maintain high resolution and minimize numerical dissipation in the constituent concentrations, each throat is discretized into segments. Each segment has a length, a fluid mass, and a mass for each constituent. Because the transport equation is pure advection, the segments may be moved intact with the seepage velocity in the throat (Figure 5.6). To include the effects of compression, the segment interfaces move with the velocity as follows

$$S_b = u_i \Delta t + S_b \frac{\left(1 + \frac{\Delta t}{2} \frac{du}{dl}\right)}{\left(1 - \frac{\Delta t}{2} \frac{du}{dl}\right)} \quad (5.40)$$

where S_b = position of the segment interface, $[L]$,
 u_i = velocity at the i end of the throat, $[LT^{-1}]$,
 Δt = time step size, $[T]$,
 du/dl = slope of the velocity profile along the throat, $[T^{-1}]$.

This scheme preserves the total flux at each end of the throat prescribed by the flow solution while preventing segment boundaries from overlapping.

Segments may be created or deleted as fluid enters and leaves the throat. A segment is only created if there is a measureable difference between the concentration in the throat and that in the inbound fluid. Once a preset ceiling has been reached in the number of segments in an individual throat, some of the segments are merged. Neighboring segments with similar concentrations are merged first to minimize smearing of concentration fronts. Segments are stored in a common 'circular' array, permitting resolution to be allocated wherever needed. Thus, transport computations in the network are made with an adaptive computational mesh capable of adding and removing resolution as needed.

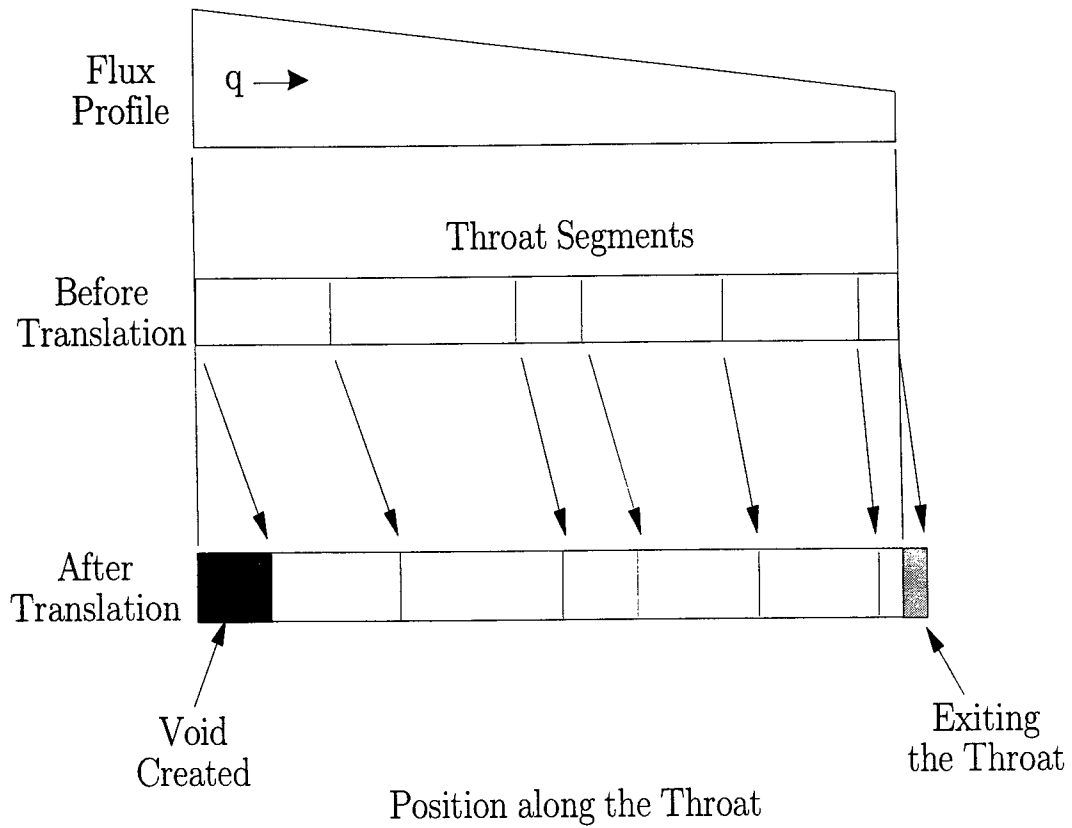


Figure 5.6: Translation of segment boundaries in response to a linear flux profile.

5.3.9 Time Advancement.

The transport solution is explicit in time. Therefore, a Courant condition defines the maximum time step size. The time step limit is the minimum travel time for any throat in the domain.

$$\Delta t \leq \left(\frac{L}{v} \right)_{min}. \quad (5.41)$$

Using an explicit scheme decouples the transport solution into many, independent one-dimensional problems. Because there is no storage at the connections, a two-step process is needed. During the first step, at each connection, inbound fluid and contaminant are collected. In outbound throats, voids are created by translating the segment boundaries. The accumulated fluid and constituents are mixed fully at each connection. During the second step, the voids are filled with the mixed fluids and constituents. There is an implied volume at each connection that is set by the amount of fluid accumulated over a time step. This volume does not affect the rate of transport, but does affect the amount of mixing. Therefore, the time step controls the resolution of concentration in the transported quantities. Complete mixing at the connections also implies a local dispersion that will be discussed in Chapter 6.

5.3.10 Observation of the Network.

Observation of the network is central to the applicability of the network model itself. Figure 5.7 shows how visualization is equivalent to applying a filter to the results. Before filtering, the network and the actual medium are structurally similar, but their scales are distinctly different. After averaging to the same resolution, detail beneath that scale is removed, and the two solutions contain the same amount of information. If enough detail is included in the network, the two average solutions may be virtually identical.

A post-processing visualization program was written to compute spatial averages of the network results for interpretation. Fluid masses and constituent masses in the network are distributed to uniformly spaced nodes in a visualization mesh (Figure 5.8). Trilinear interpolation is used to accumulate the quantities. If all nodes in the visualization mesh contain mass, all nodes are retained and a visualization mesh composed entirely of hexahedra is written to file for viewing. If all nodes do not contain mass, only those containing mass are retained and a mesh composed entirely of tetrahedra is constructed. This capability permits viewing of individual throats if desired, an ability especially useful when checking the correctness of code changes. In keeping with the theory behind the network, observation should be made at scales larger than the average length of a throat in the network. Therefore, the desired

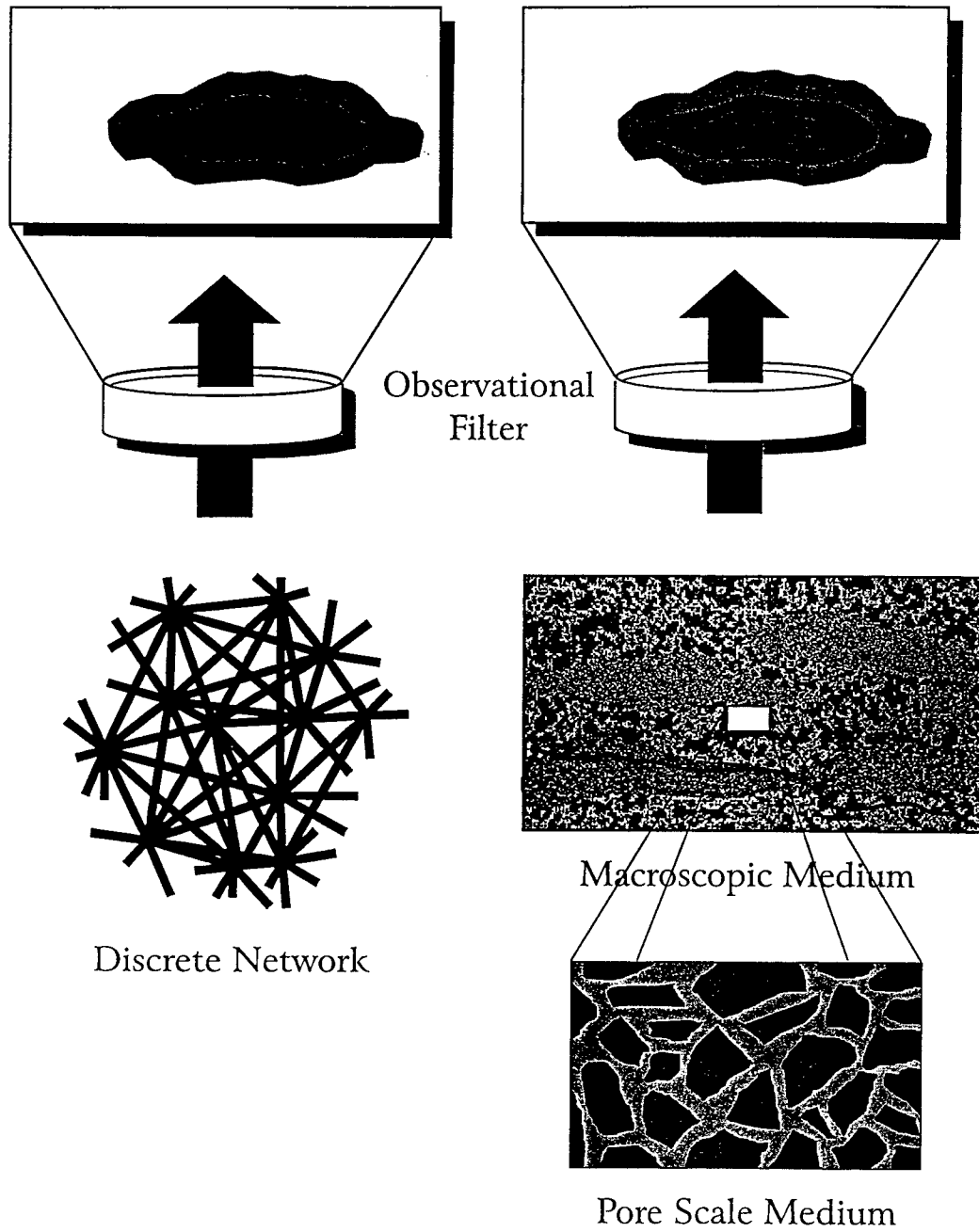


Figure 5.7: Observation of the actual medium and the network.

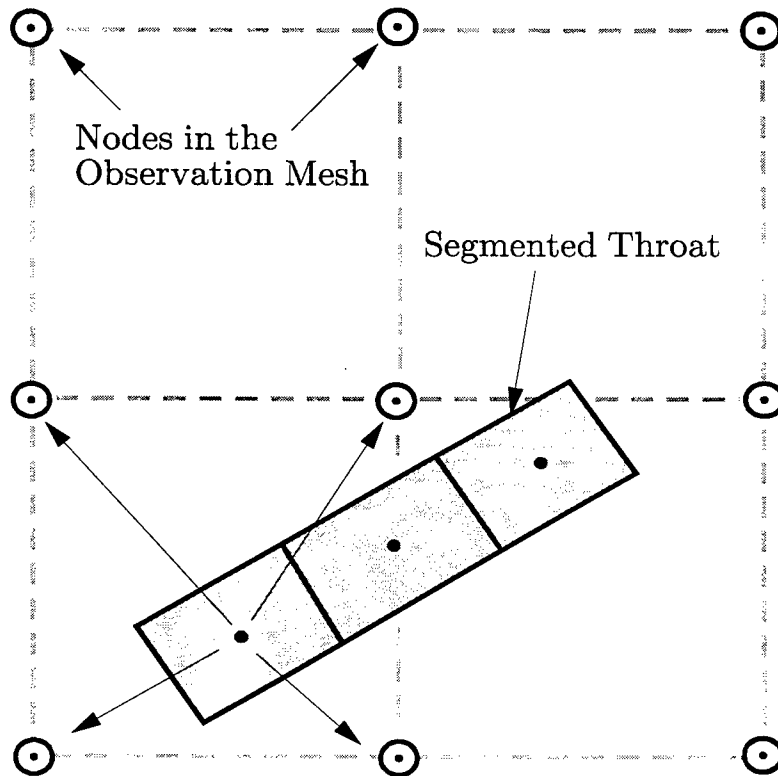


Figure 5.8: A two-dimensional schematic showing the mapping of network data to nodes in the visualization mesh.

resolution in observation sets the maximum inter-connection spacing for network creation.

The network is a discrete medium. Therefore, plots of average quantity versus averaging volume may be created to estimate the existence and size of representative elementary volumes. Figure 5.9 shows the spatially averaged velocity and concentration with change in averaging volume. These plots show that the pressure observation reaches a stable value for very small averaging area. The velocity requires a larger averaging volume to become stable. The average concentration does not reach a stable observation because there are large-scale trends in the data. For these applied boundary conditions, the head field is nearly a planar function. Thus, increases in averaging area incorporate compensating values making the observations very stable. Because velocity is a derivative of the pressure, it is expected to be more variable than pressure in heterogeneous media. Observation of the velocity field become stable once the averaging area includes a sufficient statistical sample. Logically, the REV for velocity will be similar to the the REV for conductivity. For this reason, the averaging area for velocity may need to be larger than the medium's correlation length that defines the size of physical heterogeneities. The concentration field is far from a statistically random distribution. As averaging area increases, it includes more of the plume's mass, causing the average concentration value to increase. Once the majority of the plume has been included, additional increases simply add zero-concentration fluid to the average, causing a continuous decrease in the average concentration. Therefore, no REV for concentration can be found.

5.4 Selected Results from the Network Model

The network model was run for a few, select problems. Some of these results parallel those given in a recent paper by Peters and Howington [109].

5.4.1 Growth of a Plume From an Instantaneous Source.

Flow and transport were computed through a porous slab. Twenty thousand connections were placed randomly in a two-dimensional domain 2500 m long and 1000 m wide. These connections were joined with 50,000 throats laid out isotropically with a maximum throat length of 30 m and a minimum throat length of 8 m . Conductivities in the throats were drawn randomly from a lognormal distribution with a lognormal mean of 0.0 m/d and a lognormal variance of 1.0. Fluid flow through the throats was simulated as incompressible to achieve steady flow immediately. Total freshwater head was prescribed at each end of the rectangle and the sides were

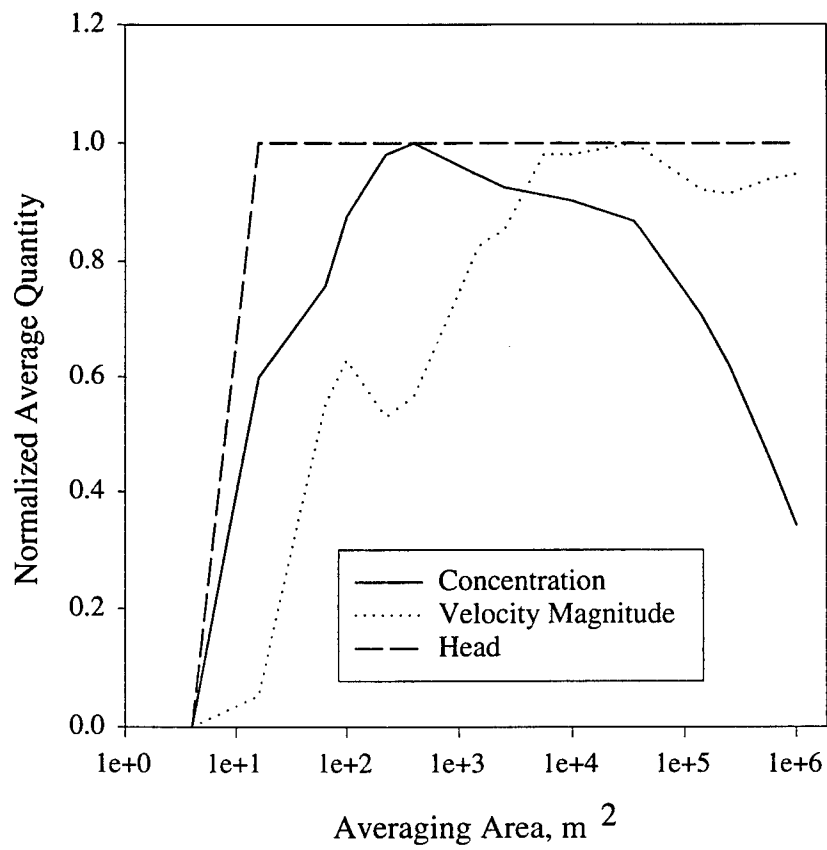


Figure 5.9: Normalized average head, concentration and velocity as a function of averaging area.

declared to be solid boundaries. Five kilograms of constituent were introduced in the first two days of the simulation at a single connection located near the upstream boundary and at mid-width. Figure 5.10, shows the plume's development in time. Figure 5.11 contains a sequence of images centered at the midpoint of the domain. The first image shows the entire domain. The second shows about half the domain in each direction. The third shows a closeup of the throats in the network. Near the center of each image, there is a high concentration value that may be used for orientation when comparing images.

The rate of plume growth, reflected by the apparent dispersivity, is shown in Figure 5.12. Apparent dispersivity values were computed using the first and second spatial moments of the modeled plume. The model output displays a linear growth rate for the plume with travel distance over the entire simulation and closely matches the solid line showing the trend in measured field data proposed by Arya [4]. An asymptotic state, characterized by a constant apparent dispersivity, is not reached for this problem. The apparent dispersivity is highly variable when the plume is small, but the trends in spatial moments stabilize as the plume size approaches four times the largest throat length. Growth of a plume at a rate faster than is predicted by a Fickian model (with a local coefficient) is consistent with the findings of Sahimi [117] in well connected networks.

5.4.2 Growth of a Plume From a Continuous Source.

Figure 5.13 shows the model-computed concentration field near steady state for another problem of practical interest, the continuous point source. These calculations were made with the same network used for the instantaneous source. Apparent dispersivity near the source will be small, but that farther downstream may be much larger. This poses significant problems when trying to use effective coefficients in a Fickian model for dispersion. For this problem, there is no asymptotic state for which a Fickian model with effective coefficients will provide satisfactory results. If an effective coefficient is used, the analytical solution for Equation (3.12) predicts substantial upstream migration of the solute. This non-physical diffusion is shown in Figure 5.14 which compares longitudinal cross sections through plumes predicted by the advection-dispersion equation (ADE) and the network model. The meandering nature of the plume in the network model makes it difficult to define a representative concentration profile. Because there is no dispersion coefficient in the network model, a common ground on which to make comparisons was needed. Results from the instantaneous point source problem (Figure 5.12) were used to estimate an effective, macroscopic dispersion coefficient for use in the ADE. Using this effective dispersion coefficient in the ADE produces substantial upstream spreading

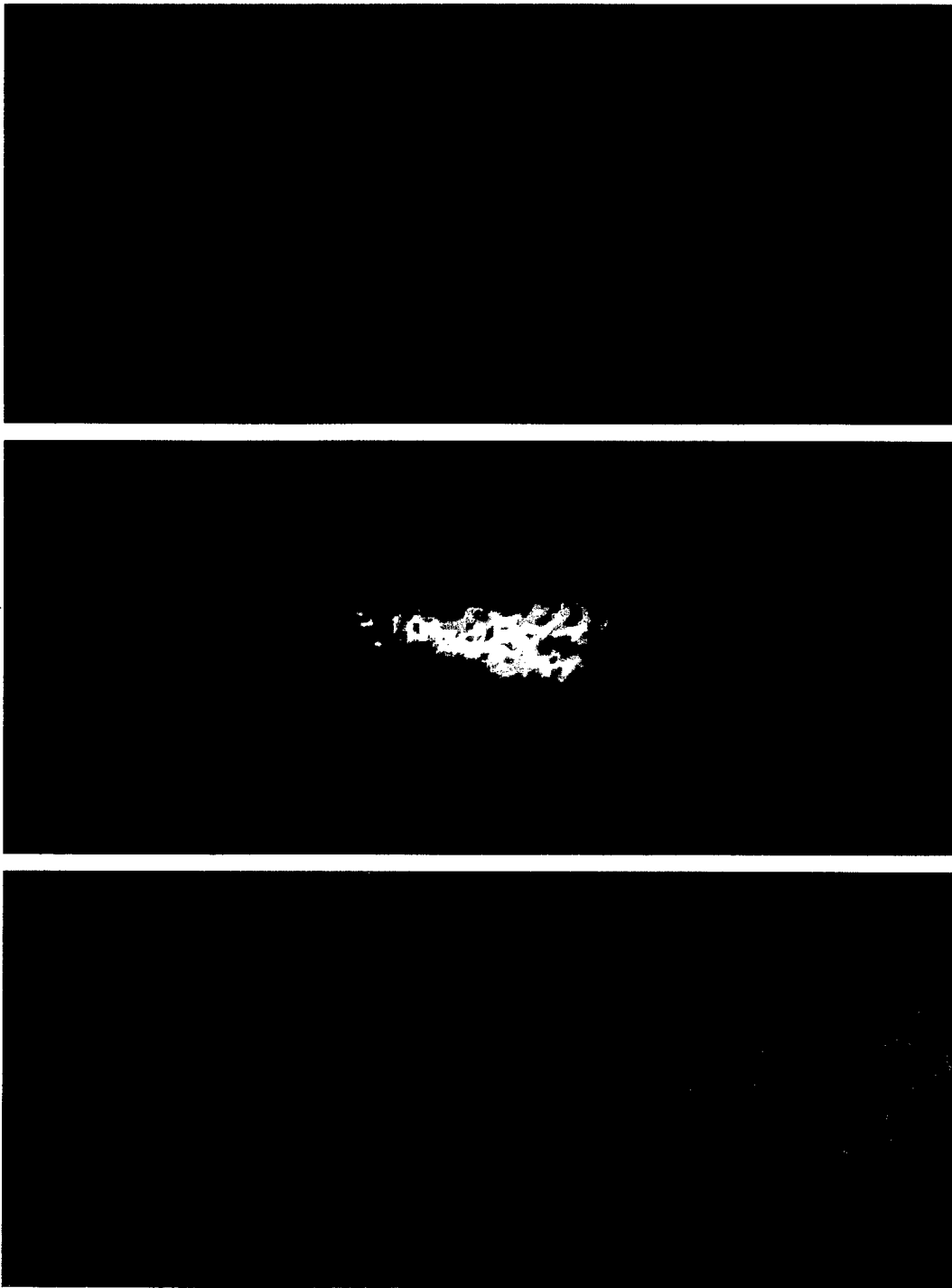


Figure 5.10: Concentration fields from an impulse source of tracer. The field is shown early in its development (top), after 1500 days (middle), and after 2500 days (bottom). Red indicates higher concentration and blue, lower concentration.

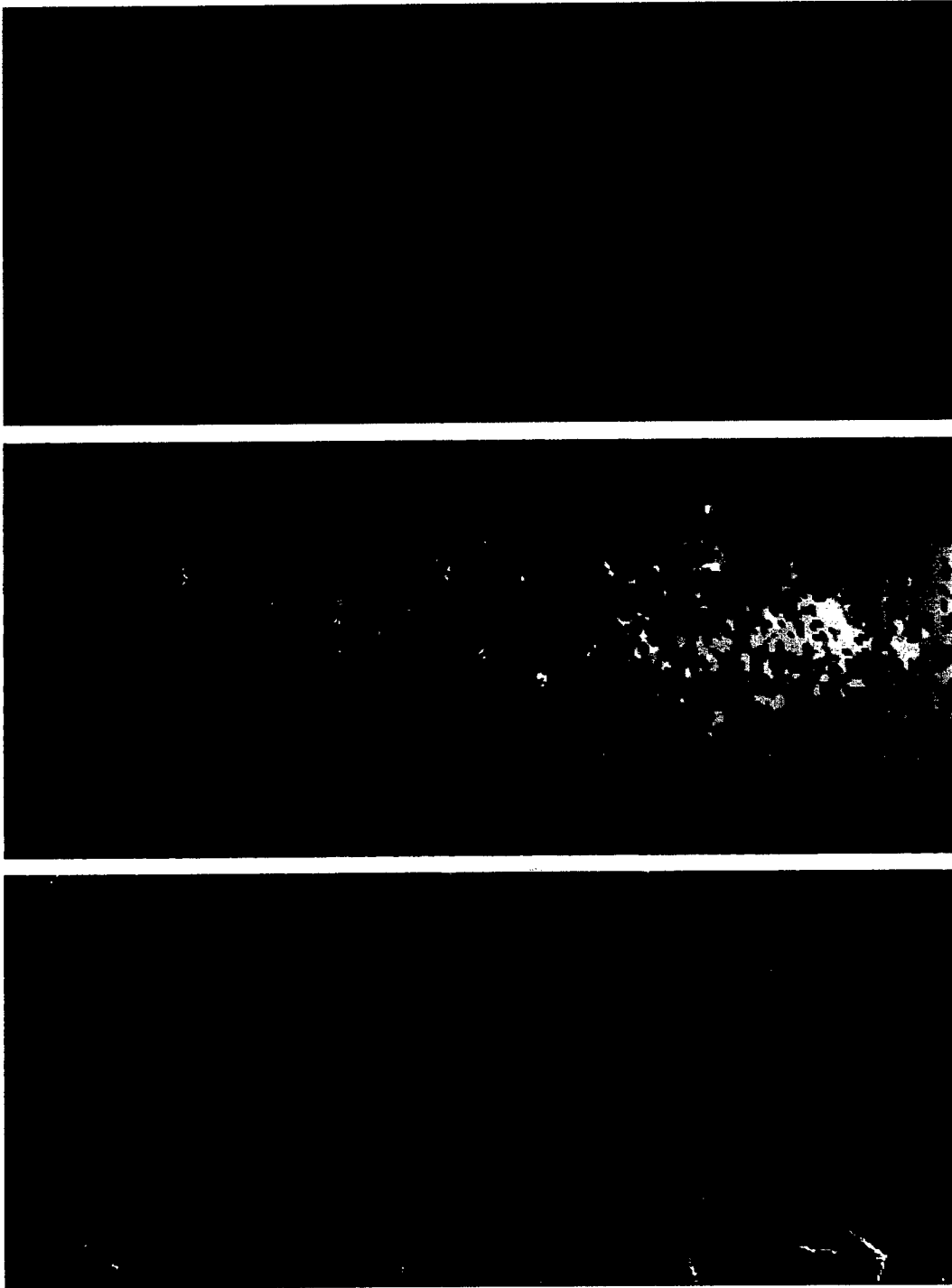


Figure 5.11: A single snapshot of the developed plume shown in successively greater detail. The images show the entire domain (top), the center quarter of the domain (middle), and a very small fraction of the domain at the center (bottom).

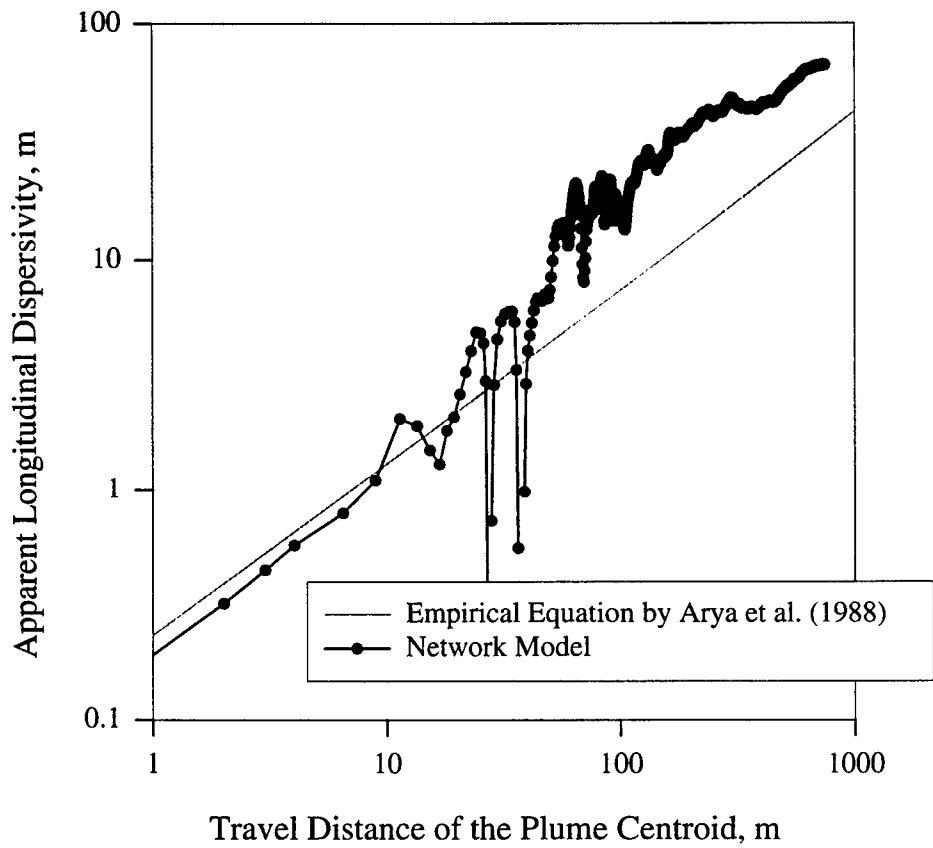


Figure 5.12: The travel distance of the centroid of an instantaneous-source plume versus its rate of growth and an empirical equation by Arya et al. [4].

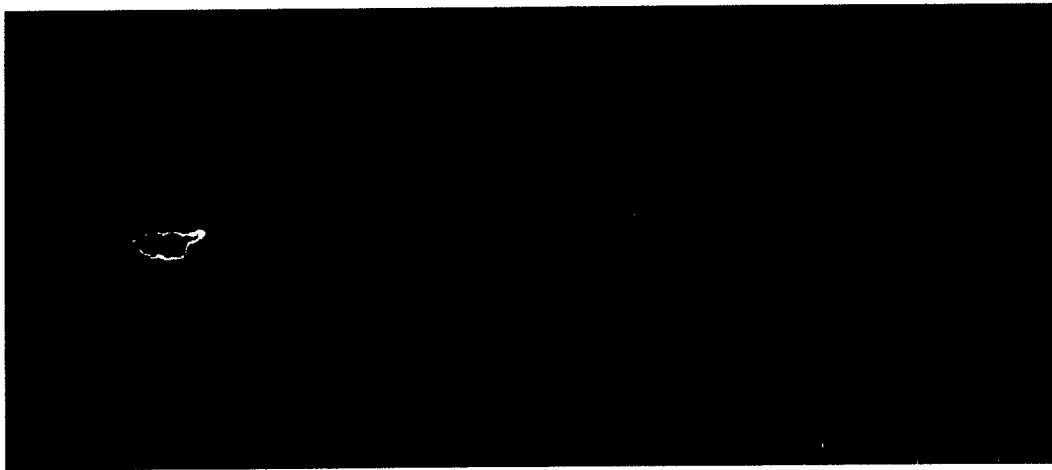


Figure 5.13: Contours of the spatially averaged concentration field for the continuous source (red is higher concentration, blue is lower).

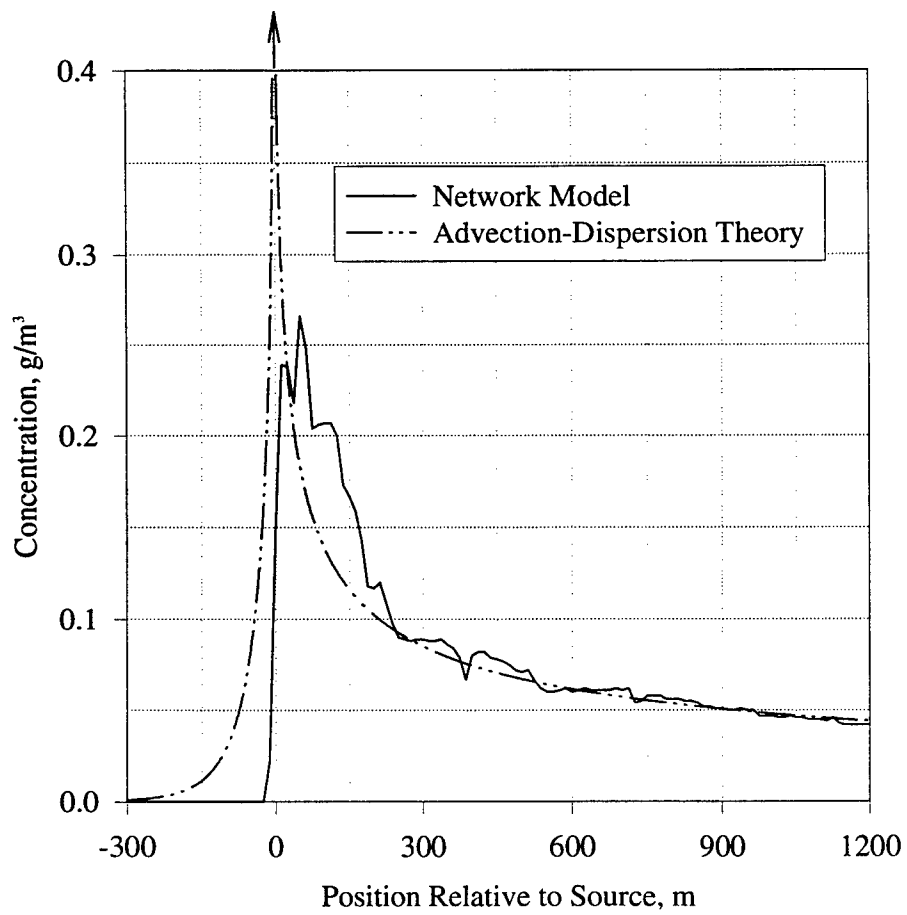


Figure 5.14: Comparison of the network model to the advection dispersion theory for the continuous point source.

of the solute (Figure 5.14). The effect becomes negligible at an upstream distance equal to about five times the assumed dispersivity ($5\alpha_x$). Downstream, but near the source, the network model produces concentrations slightly higher than those from advection-dispersion theory. Farther downstream of the source, the two approaches agree very closely.

5.4.3 Demonstration of Density Dependent Flow.

The network was also used to demonstrate density-dependent flow. Two columns of water were positioned side-by-side in a thin, vertical slab that is 100 *m* on a side by 10 *m* thick. All boundaries on the slab are defined as solid. One of the columns contained fresh water while the other contained a dense constituent. The presence of this constituent at a concentration of 1.0 *g/g* produced a fluid/constituent mixture with a specific gravity of 1.5. The fluid containing the dense contaminant pushed its way to the bottom of the container. Figure 5.15 shows four images in the time evolution of the dense wedge. This is noteworthy because it shows that the network model is capable of simulating salt-water intrusion and other density-dependent flow problems.

5.5 Parallel Computer Implementation

Because the network model decomposes an *n*-dimensional physical problem into many one-dimensional numerical problems, it is well suited for implementation on a parallel computer architecture (single instruction, multiple data). The machine chosen for the parallel work is a Cray T3D with 256 processors. Each processor in the T3D is a Digital Equipment Corporation Alpha processor with 8 megawords of random access memory. The machine used is located at the Minnesota Supercomputer Center. As a first step, vendor-specific Fortran compiler directives were added to the code to distribute the data storage and the workload requirements among the processors.

5.5.1 Load Balancing.

The most common method for distributing work to processors is geographically. The domain is subdivided to distribute the work approximately evenly. This type of distribution has the advantage of minimizing communication requirements among the processors. For example, with a simple structured numerical mesh and a discrete numerical approximation that relies only on nearest neighbor information, only those elements that border the subdomain boundary will require information from another processor to perform its duties. However, if the discretization changes

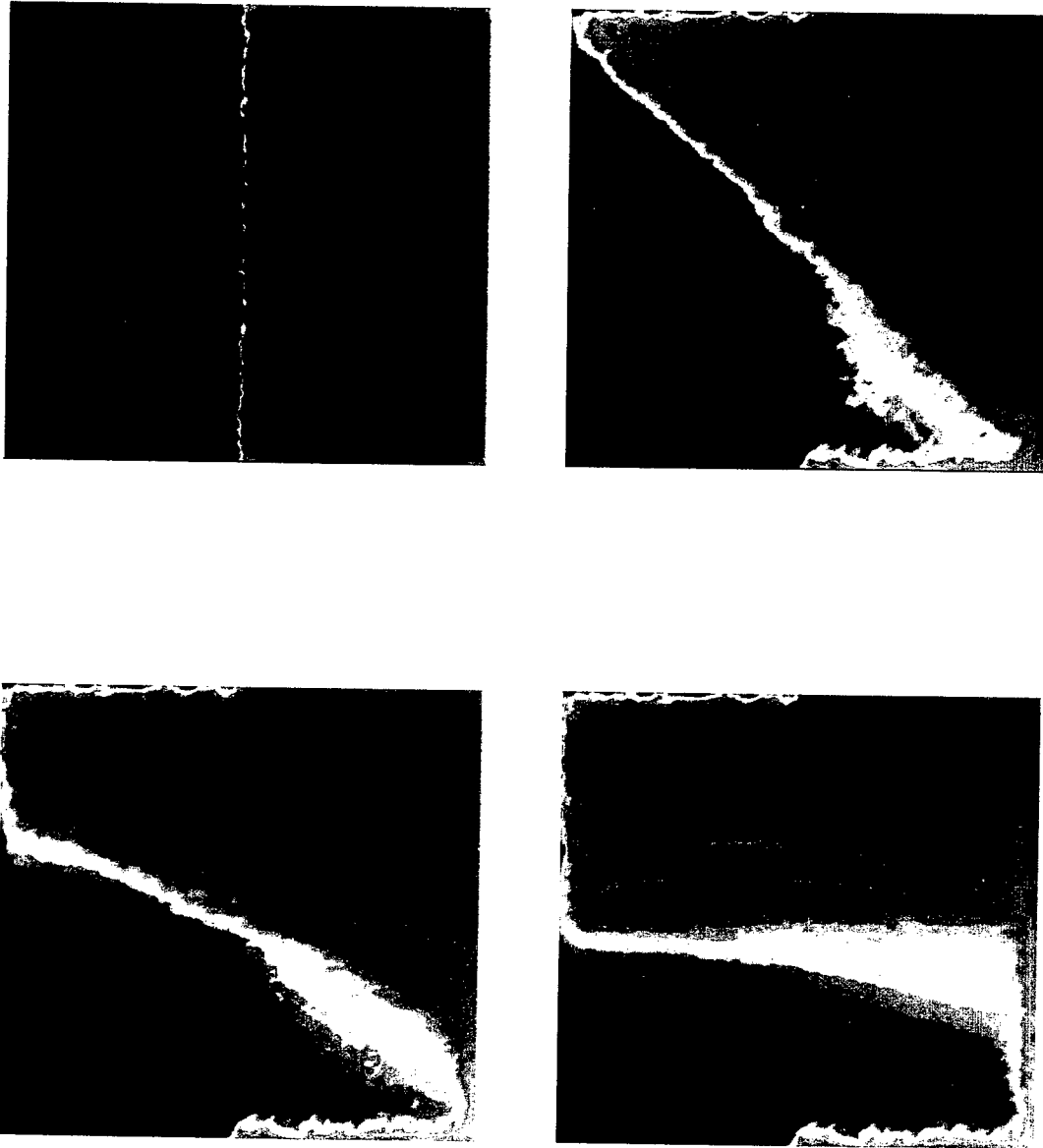


Figure 5.15: Time evolution of the dense wedge. Time sequence is upper left (initial condition), upper right, lower left, lower right.

as the problem evolves, as with an adaptive mesh, the amount of work associated with each geographic region is not constant. This leads to an imbalance of work among the processors. Some processors will finish their work long before others. At synchronization points, the processors must wait until all are finished before proceeding. Partitioning algorithms to address these issues are the subject of present research (e.g., Karypis [76]). A trade-off exists between the amount of time required to repartition the problem to the processors versus the time lost to a poorly balanced workload.

Because the throats are discretized adaptively in the network model, partitioning problems arise. A single, geographical distribution of throats to processors will not produce a balanced workload for a moving concentration plume. This problem was addressed by adopting a cyclical distribution of the throats to the processors. The throats are distributed randomly in space and the first throat is assigned to the first processor, the second throat to the second processor, and the $(N + 1)$ th throat is assigned to the first processor (where N is the number of processors being used), etc. This approach relies on the fact that there will be many more throats than processors. With enough throats, each processor will have approximately the same total amount of work to do, because, on average, all processors will have the same percentage of throats within the plume. The disadvantage of this is that interprocessor communication is maximized. A future effort will examine the potential benefits of using alternative partitioning techniques with an optimal mix of geographical and cyclic partitioning.

5.5.2 Performance.

To evaluate the degree to which the code and the problem are 'parallel', a speedup curve normally is created. The particular speedup measure chosen (Figure 5.16) shows normalized run times for the code for a fixed problem size. In an ideal 'parallel' code, there is no overhead or latency, and running on N processors causes the code to run N times faster. This idea may be expressed with the following equation for speedup

$$\frac{t_1}{t_N} = \frac{N}{1 + N \frac{t_l(N)}{t_1}} \quad (5.42)$$

where t_1 , t_N , and $t_l(N)$ are the time for a single processor, time for N processors, and the latency time, respectively. Assuming that the latency time does not depend on the number of processors chosen, it is apparent that the speedup will approach a constant value as N approaches infinity. That constant value is the ratio of the single processor run time to the latency. Further, if we assume that latency is additive, we

may examine latency by individual subroutine to determine the best place to focus optimization resources.

A few simulations were conducted with an early version of the discrete network model. The test problem contained about 20,000 connections and about 50,000 throats. A steady flow field was computed and transport was simulated for about 700 time steps. This problem represents a relatively small problem and a very short simulation time. For this problem, the model achieves about 60 percent of ideal speedup for 8 processors and only 25 percent of ideal for 32 processors. The asymptotic speedup is estimated to be about 12, regardless of the number of processors used. This implies that about 9 percent of the single processor run-time is consumed by computations that are inherently serial. However, the subroutines that perform the implicit head computations and the transport through the throats show about 75 percent of ideal for 32 processors. Much of the large latency is created by input and output which presently are handled by a single processor. To investigate this, a single simulation was made with 32 processors for which each processor wrote to an individual file. This improved the speedup at 32 processors from 25 percent to 31 percent. These results are promising for more computationally intensive problems requiring less input and output and additional computations at the throat level. Further, adding physical and chemical processes will likely increase the fraction of work being done at the throat level, which is highly parallel. Work is underway to convert this code to a more portable parallel format and to improve the input/output procedure.

5.6 Summary of Findings

The stochastic discrete-network model for flow and transport through porous media has proven to be a viable alternative to traditional discretization and simulation methods. The network is an efficient and intuitive method for including the effects of finite-size heterogeneity. The network is a simple, easily-implemented, discrete approximation of formal non-local theories for flow and transport.

The network reproduces the observed scale dependence of the apparent dispersivity, regardless of the choice of boundary conditions. Further, the network produces physically-correct, wholly downstream contaminant spreading in the absence of diffusion.

The network offers some computational advantages not realized with other high-resolution simulation approaches. First, the network permits partial decoupling of the resolution in the pressure and velocity solutions, improving computational efficiency. Further, by mapping the multi-dimensional porous medium to a network its

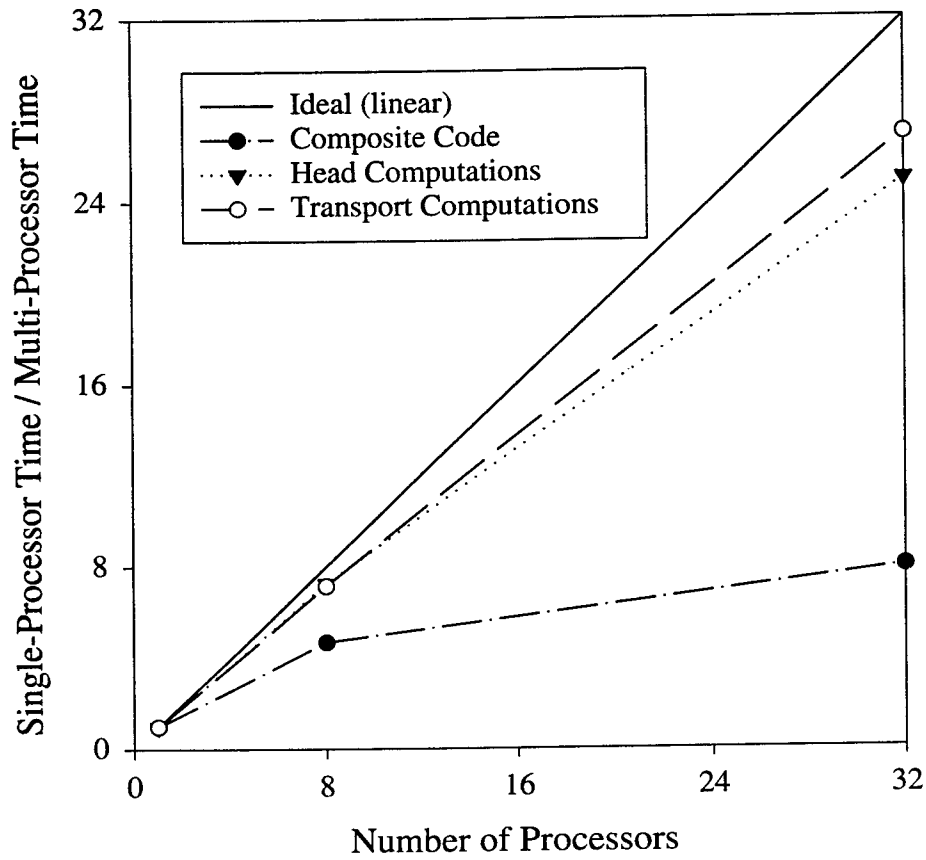


Figure 5.16: The number of processors versus the speedup.

computational dimensionality is reduced to one. Therefore, the network's structure is well-suited for parallel computer architectures.

Chapter 6

Conditioning Isotropic, Discrete Networks to Match Observed Properties of Flow and Tracer Migration in Porous Media

Abstract

Macroscopic, stochastic discrete network modeling of flow and transport through porous media is a rational alternative to traditional numerical approximation techniques that discretize the domain into a continuous field of finite elements or finite volumes (Chapter 5). The network model offers comparable definition in the pressure field and a more refined velocity field to drive transport. This approach displays reasonable flow and transport behavior for both asymptotic and non-asymptotic conditions.

For this approach to be useful for practical remediation modeling, we must be able to construct networks that accurately represent the soils at individual remediation sites. Therefore, these networks must match common field and laboratory observations for that site. Toward that goal, this paper addresses two issues: (1.) anticipating macroscopic flow and transport behavior prior to simulation, and (2.) selecting network construction parameters that produce desired behavior. By combining a local renormalization of conductivity for each patch of throats with existing stochastic theory, the effective conductivity of a particular network may be estimated, even for large variance in local conductivity. Empirical relationships are derived to compute normalized velocity deviation

and position-velocity correlation as functions of the problem dimension, the correlation length, and the installed throat conductivity variance. When combined, these relationships predict asymptotic longitudinal and lateral apparent dispersivities. A step-by-step procedure for constructing isotropic networks to approximately match observed flow and conservative transport properties is presented. Where asymptotic property measurements are not available, the network may be constructed using statistical descriptions of ‘point’ observations.

A stochastic discrete network has been presented as an intuitive conceptual model for macroscopic, heterogeneous porous media in Chapter 5. Flow and conservative transport through these discrete networks appear physically reasonable and are process-consistent with flow and transport in the actual medium. Further, it has been shown that a network model emerges naturally from non-local governing equations. The network has demonstrated an ability to reproduce asymptotic and pre-asymptotic plume growth, matching observed trends in scale-dependent apparent dispersivity from Chapter 5. However, if the network model cannot be conditioned to match site-specific observed information, it is of little practical value.

This chapter provides a plan for endowing the network with the measurable properties of a particular medium. It begins by critically evaluating our ability to solve the ‘forward’ problem. That is, can macroscopic flow and transport properties of a particular network be predicted prior to simulation? Specifically, can macroscopic effective conductivity and apparent dispersivities be anticipated? This evaluation is followed by a heuristic procedure for addressing the ‘inverse’ problem — constructing finely-resolved networks to match desired macroscopic properties.

6.1 Structure of the Network

The structure of these macroscopic-scale networks differs fundamentally from traditional discretization approaches. This network implementation consists of throats with arbitrary cross-sectional shape that meet at volumeless connections. Connections are placed randomly throughout the domain, while maintaining a minimum inter-connection spacing. Throats bridge between these connections to define flow paths.

6.1.1 Basic Structural Scales.

The network model consists of three basic structural scales: (1.) an individual throat or tube, (2.) a patch of throats with a common connection, and (3.) the macroscopic scale containing many patches (Figure 6.1). Individual throats are

sub-observation or 'subgrid' components. Throat information must be averaged to the patch scale for spatial interpretation. The patch represents the minimum scale at which a 'continuum' could be imagined and, thus, is the smallest meaningful observational scale. Bulk properties such as effective conductivity from a pump test or dispersivity from a tracer test must be compared at the macroscopic scale which includes many patches.

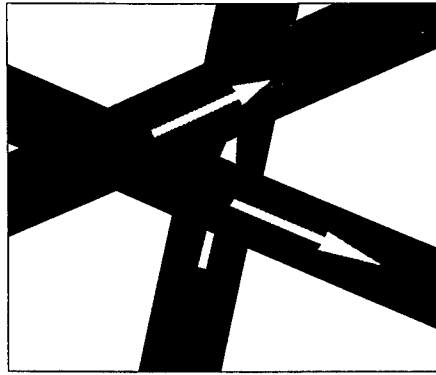
6.1.2 Throat Characteristics.

Throats are treated as though they contain porous material. The conductivity of this material may vary substantially from throat to throat, but is assumed homogeneous within a single throat. Darcy's law is assumed to predict fluid flux in response to gradients in potential. This is in contrast to the common assumption of Poiseuille flow through open, cylindrical pores in many pore-scale network models.throats are considered three-dimensional objects, although they may be arranged in a plane to produce a two-dimensional approximation, or along a line to provide a one-dimensional model. Further, because each throat is internally uniform and boundary conditions are confined to the ends of the throats, flow and transport solutions within each throat reduce to one dimension.

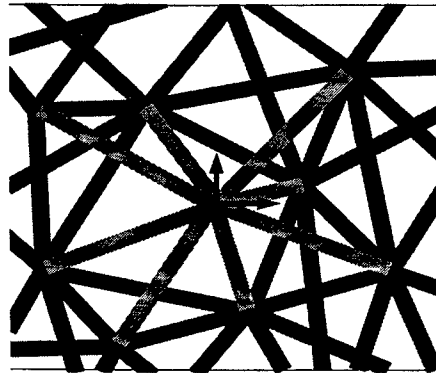
If the network is interpreted as an approximation to a non-local flow and transport problem (see Chapter 5), the throats simply represent vehicles for transporting information among connections. Throats enforce appropriate transit times for fluid and constituent masses traveling between connections. In the present model, transport along throats is by pure advection. There is no molecular diffusion or dispersion in the throat transport equation. Thus, each throat contains a discrete history of concentration at the upstream connection. Conceptualization of a throat as a straight cylinder, or any other geometrical shape, is simply for convenience. Throats are not required to be straight or cylindrical. Therefore, any mathematical intersection among throats in the space between connections is neglected. Throats are permitted to exchange mass only by mixing at the connections.

6.1.3 Throat Length Distribution.

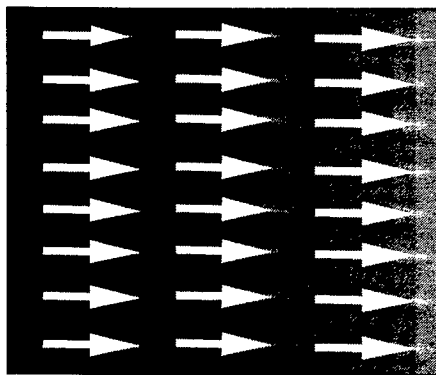
This network's topology is not restricted to a 'nearest-neighbor' connectivity as it is for most networks. In theory, any two connections in the domain may be joined by a throat. Each pair of connections is visited and a probability function is applied to determine whether a throat should exist between these connections. A uniform random number between 0 and 1 is chosen and compared to the probability function value. If the probability function value exceeds the random number, the throat is added to a pool from which the desired number of throats will be drawn. The



Throat Scale



Patch or Darcy Scale



Macroscopic Scale

Figure 6.1: Structural hierarchy in the network.

probability function consists of three regimes,

$$P(\xi) = \begin{cases} 1.0, & 0.0 < \xi < s, \\ \frac{\exp\left(\frac{s-\xi}{a}\right)}{(s/\xi)^{n-1}}, & s \leq \xi \leq \xi_{max}, \\ 0.0, & \xi_{max} < \xi. \end{cases} \quad (6.1)$$

where P = probability function, [-],
 ξ = separation distance, [L],
 s = average connection spacing, [L],
 a = probability decay coefficient, [L], and
 ξ_{max} = maximum throat length, [L].

This form of probability function strongly encourages local connectivity in the network. For a separation distance (ξ) less than the average spacing (s), the probability of throat creation is 1.0 and these throats are always added to the pool. For spacing greater than some prescribed maximum (ξ_{max}), the probability of throat creation is 0.0 and these throats are excluded. Between these bounds, the probability decays exponentially with separation distance. The decay variable, a , determines the rate of probability decay with separation distance. Large values of a result in very slow decay in probability with increasing separation distance, while small a values cause more rapid decay.

The denominator in Equation 6.1 adjusts the function to simulate a constant number of 'chances' with separation distance. In multiple dimensions, there are many more point comparisons to be made at a separation distance of 2ξ than at ξ . Therefore, given the same probability of throat creation at these two separation distances, more throats 2ξ in length would be created. Dividing by the denominator reduces probability with separation distance to offset the increase in the number of point pairs. This achieves a throat-length distribution that is independent of the problem dimension. Thus, the distribution of throat lengths in the medium will match the exponential decay function prescribed by the numerator.

Because each throat acts like a lens of homogeneous material, the distribution of throat lengths corresponds to the distribution of structural sizes in the medium. Therefore, the throat probability function describes the spatial correlation of conductivity in the medium. Correlation structure is often quantified by a correlation length. In geostatistics, the principal correlation length or range is taken to be the separation distance that contains about 95 percent of the structural sizes present in the medium [35]. Using this definition, the correlation length for Equation 6.1 lies between $3a$ and $s + 3a$. In a structured network, the average connection spacing and the minimum connection spacing are the same value. Thus, no throats shorter

than the average connection spacing (except truncated boundary throats) will exist. In this case, the correlation length, λ , is $s + 3a$. When connections are placed randomly, throats longer than the minimum connection spacing, but shorter than the average connection spacing, will exist. Their existence reduces the number of throats in the region between s and ξ_{max} , thereby reducing the correlation length. As an approximation, the correlation length will be taken to be

$$\lambda = \min(\xi_{max}, 3a) \quad (6.2)$$

6.2 Predicting Effective Conductivity

The problem of predicting the effective conductivity of a heterogeneous medium has been studied extensively by the oil production industry and, more recently, by the water resources community. Two of the more common approaches for computing effective conductivity are upscaling by renormalization (e.g., [78]) and estimation by stochastic theory (e.g., [28]). Renormalization computes an estimate of effective conductivity by solving a simple flow problem on successively larger subdomains until the subdomain size becomes the desired measurement size. Stochastic theories estimate the effective conductivity by solving small-perturbation approximations to stochastic flow equations. We will use a combination of these two approaches to estimate effective conductivity in the network.

6.2.1 Stochastic Theory Predictions.

Gutjahr et al. [57], Gelhar [53], and Dagan [28], among others, have presented theoretical estimates for effective conductivity. Gutjahr et al. [57] derived effective conductivity for an n -dimensional, isotropic medium ($n = 1, 2, 3$).

Within the limitations of the small perturbation assumption and assuming that the REV and continuum concepts apply, the effective conductivity for an isotropic, randomly heterogeneous medium is

$$K_e = K_g \left[1 + \left(\frac{1}{2} - \frac{1}{n} \right) \sigma_f^2 \right], \quad (6.3)$$

where K_e = the effective conductivity, $[LT^{-1}]$,
 K_g = the geometric mean conductivity, $[LT^{-1}]$,
 n = the dimension of the medium, $[-]$,
 σ_f^2 = the variance in lognormal conductivity, $[-]$.

This indicates that in two-dimensions, the predicted effective conductivity is the geometric mean of the individual values,

$$K_e = K_g. \quad (6.4)$$

This relationship was determined theoretically by Dagan [28], Gutjahr et al. [57], and Gelhar and Axness [54] and confirmed numerically by Follin [45] as cited in [114]. Follin found this expression to hold for large variance (σ_f^2 as large as 16). Gelhar and Axness [54] extended this result to anisotropic media (Appendix C). They also conjectured that, for large perturbations ($\sigma_f^2 > 1$), the effective conductivity may be given by

$$K_e = K_g \exp \left[\left(\frac{1}{2} - \frac{1}{n} \right) \sigma_f^2 \right]. \quad (6.5)$$

The validity of this equation was analyzed by Desbarats [34]. Further, an equation consistent with Equation 6.5 was also proposed by Dagan [31].

6.2.2 Mapping Throat Conductivities to Connections.

Because throat conductivities are scalar quantities with orientation imposed by throat direction, the throats represent a level of structure not found in spatially continuous discretizations. Thus, some preprocessing of the network data must be performed before stochastic theories for effective conductivity may be tested. We must convert scalar throat conductivity values to multidimensional, tensor conductivities that represent a prescribed volume of the medium. Two procedures are presented for mapping the throat conductivities to the connections for interpretation or comparison to measurement:

- patch volume averaging, and
- patch renormalization.

Volume averaging is simply arithmetic averaging of the values weighted by the volumes of material or fluid they represent. The volume average is the sum of the individual throat contributions for the patch, accounting for orientation

$$K_{ij} = \frac{\sum_{t=1}^{CN} n_i n_j V_t K_t}{\sum_{t=1}^{CN} V_t}, \quad (6.6)$$

$$n_i = \cos \beta,$$

$$n_j = \cos \gamma$$

where K_{ij} = components in the patch conductivity tensor, $[LT^{-1}]$,
 CN = coordination number for this patch (the number of throats that are attached at the connection), $[-]$,
 β = angle between the throat vector and the flow direction, $[-]$,
 γ = angle between the throat vector and applied head gradient, $[-]$,
 V_t = throat volume, $[L^3]$,
 K_t = individual throat conductivity scalar, $[LT^{-1}]$.

Arithmetic averaging of this sort implies that every throat in the domain experiences a common, macroscopic head gradient. Therefore, flow through each throat is determined entirely by the throat's orientation and conductivity and is not affected by local variability in head gradient. If this assumed unit head gradient were applied to each throat in a patch and the resulting throat fluxes computed, there is no expectation that fluid conservation would be enforced at the center connection.

An alternative approach for computing patch or connection-scale conductivity will be called patch renormalization. This approach considers each patch of throats that share a common connection to be a separate test specimen. A macroscopic unit head gradient prescribes the heads on the periphery of the patch. Head at the center connection is computed to enforce conservation of fluid mass at that connection (Figure 6.2). Conservation of fluid at the center connection requires that the individual, outbound throat fluxes, q_t , sum to zero

$$\sum_{t=1}^{CN} q_t \frac{n_i}{|n_i|} = 0. \quad (6.7)$$

By Darcy's law, in the one-dimensional throats, the flux is linearly proportional to the gradient in head

$$q_t = -K_t \frac{\Delta H}{\Delta l} = -K_t \frac{H_t - H_c}{L_t} \quad (6.8)$$

where H is the total head, $[L]$, and l is the position along the throat, $[L]$. Combining these two equations, we may solve for the head at the center connection, H_c , in terms of the heads on the periphery of the patch, H_t , the throat conductivities, K_t , and the throat lengths, L_t .

$$H_c = \frac{\sum_{t=1}^{CN} \frac{K_t H_t}{L_t}}{\sum_{t=1}^{CN} \frac{K_t}{L_t}}. \quad (6.9)$$

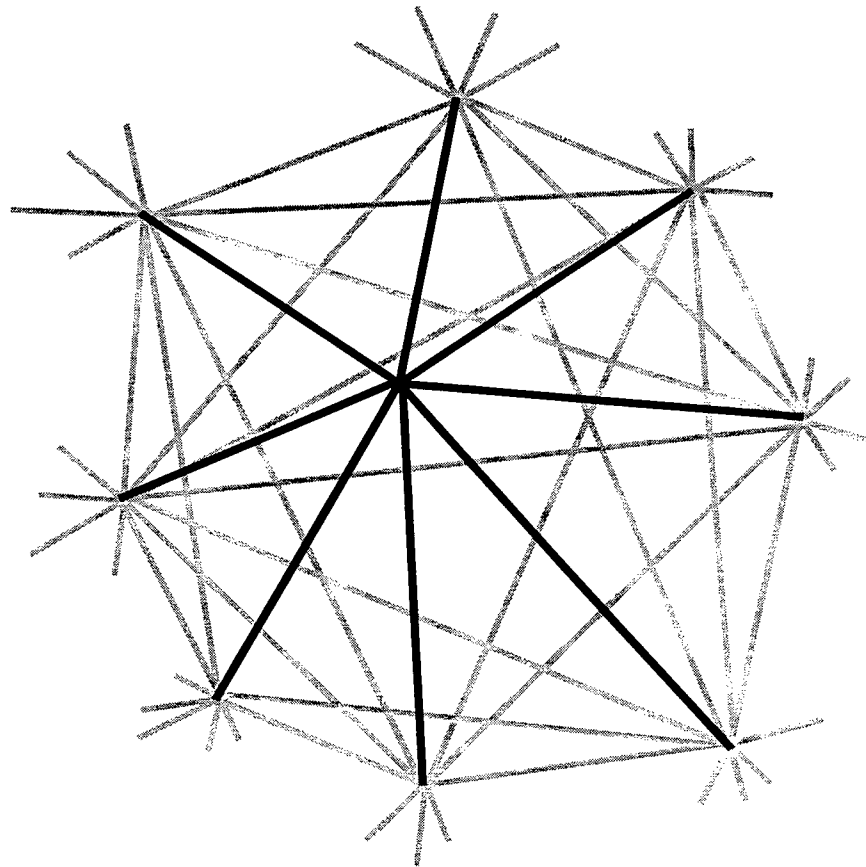


Figure 6.2: Diagram of a patch of throats.

Using the position of the center connection as a reference and defining heads relative to that position, a unit gradient in the j direction produces

$$H_t = -n_j L_t \quad (6.10)$$

at the connections on the exterior of the patch. The equation for head at the center connection becomes

$$H_c = \frac{\sum_{t=1}^{CN} K_t n_j}{\sum_{t=1}^{CN} \frac{K_t}{L_t}}. \quad (6.11)$$

Flux through each throat in the patch may be determined using this head. Then, by summing the directional contributions of each throat, a net directional flux through the connection may be computed. Because we assumed a unit head gradient, the resulting flux is a component of the connection conductivity tensor. The conductivity in the i direction caused by a unit gradient in the j direction is

$$K_{ij} = Q_{ij} = \frac{1}{2} \sum_{t=1}^{CN} n_i q_t = \frac{1}{2} \sum_{t=1}^{CN} n_i \frac{K_t}{L_t} (H_c - n_j L_t). \quad (6.12)$$

By applying a unit head gradient in three orthogonal directions, all nine components of the full patch conductivity tensor may be computed. The matrix is symmetric, including only six distinct values. The resulting patch or connection-level conductivity tensors are comparable to the element-level conductivity tensors in a continuum model formulation.

6.2.3 Numerical Experimentation for Effective Conductivity.

A series of numerical experiments were conducted with the network to test the applicability of the effective conductivity equations. The experiment matrix, detailed in Table 6.1, was designed to explore the effects of throat length distribution and throat conductivity variance on the effective conductivity. The first digit in the experiment label indicates the dimensionality of the network. Probability decay in the table shows the values used for a in Equation 6.1.

Many properties of the networks were held constant among the experiments. These constants are given in Table 6.2. The coordination number is the average number of throats meeting at a connection. Enforcing a minimum spacing is necessary to maintain a reasonable time step size for the explicit transport solutions. Because the same seed is used for the random number generator in each of the

Table 6.1: Numerical Experiment Matrix

Experiment Label	Maximum Throat Length (m)	Probability Decay (m)	Variance of Ln Throat Conductivity
2D1A	36.	9999.	0.0
2D1B	36.	9999.	1.0
2D1C	36.	9999.	2.0
2D1D	36.	9999.	3.0
2D2A	60.	9999.	0.0
2D2B	60.	9999.	1.0
2D2C	60.	9999.	2.0
2D2D	60.	9999.	3.0
2D3A	60.	22.	0.0
2D3B	60.	22.	1.0
2D3C	60.	22.	2.0
2D3D	60.	22.	3.0
2D4A	250.	22.	0.0
2D4B	250.	22.	1.0
2D4C	250.	22.	2.0
2D4D	250.	22.	3.0
3D1A	100.	9999.	0.0
3D1B	100.	9999.	1.0
3D1C	100.	9999.	2.0
3D1D	100.	9999.	3.0
3D2A	200.	60.	0.0
3D2B	200.	60.	1.0
3D2C	200.	60.	2.0
3D2D	200.	60.	3.0

Table 6.2: Basic properties of the networks in the experiment matrices.

Property	2-D Networks	3-D Networks
Average Coordination Number	8.6	11.7
Domain Length (x)	2500 m	2500 m
Domain Width (y)	1500 m	1500 m
Domain Thickness (z)	10 m	1500 m
Average Connection Spacing	18.	60.
Minimum Connection Spacing	11.	35.
Approximate Number of Connections	11000	25000
Mean ln Throat Conductivity	0.0	0.0
Approximate Number of Throats	50000	150000

two-dimensional experiments, the position of the connections will be identical in the networks. The same holds true for all the three-dimensional experiments.

A pool of potential throats is created for each experiment according to the probability function (Equation 6.1). The desired number of throats is then selected from this pool. Conductivities are assigned randomly from the lognormal distribution as the throats are selected. The throat conductivity distributions are shown in Figure 6.3. These distributions are from experiment series 2D1, but, because we are working with such large statistical samples (50,000 throats or more), the distribution is virtually identical to the other experiment series, both two- and three-dimensional. Figure 6.4 shows the length distribution for each two-dimensional experiment series. Within a experiment series, the networks are topologically identical. Only the conductivity distribution changes. Figure 6.5 provides length distributions for a three-dimensional experiment series (3D1). To create these contoured images, the fluid and constituent masses moving through the network were averaged to a 125 x 75 x 1 structured observation grid. The resolution of the observation grid (20 m) was chosen to be not less than the average connection spacing (18 m). If a finer grid is chosen, holes in the contoured image begin to appear.

Experiment series 2D1 minimizes throat-length variability and the network is well connected locally. In series 2D2, some longer throats are permitted, but the throat-length frequency is held nearly constant. Experiment series 2D3 has the same range of throat lengths as series 2D2, but the distribution in series 2D3 is biased toward shorter throat lengths. Series 2D4 permits a few throats that are much longer than the other series. In series 2D1, 2D2, and 2D3, the principal correlation length is set by the maximum throat length. In 2D4, the probability decay function controls the correlation length.

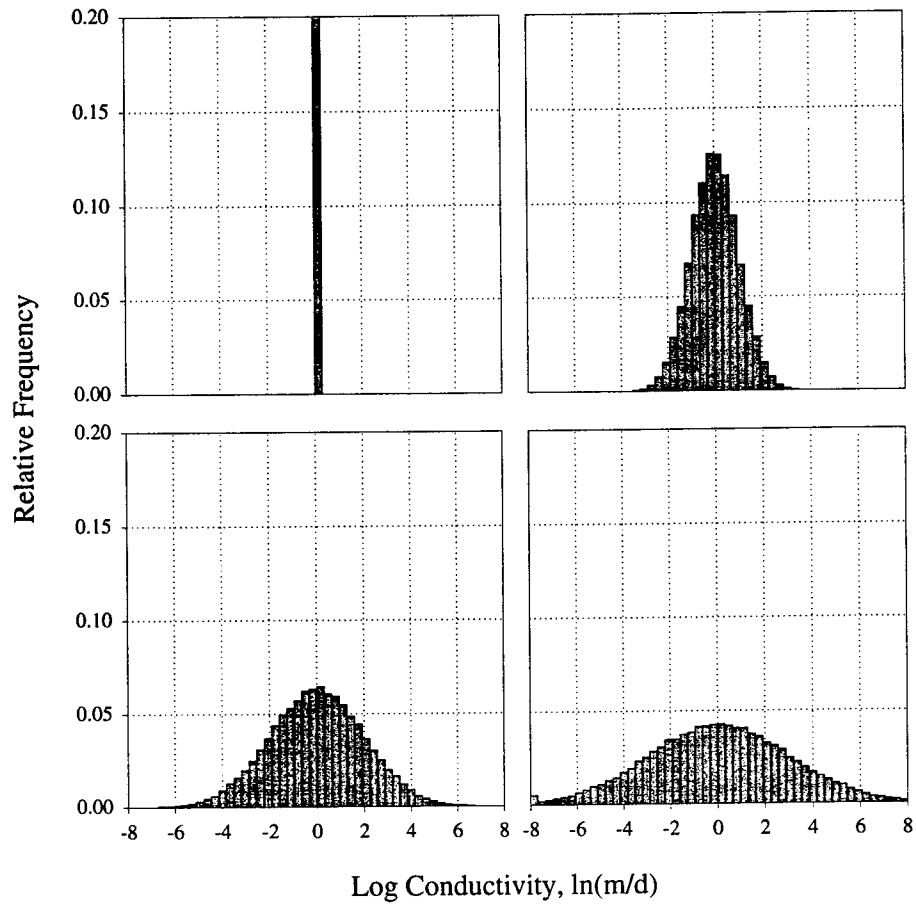


Figure 6.3: Histograms of \ln throat conductivity for experiment series 2D1. Upper left, 2D1A, upper right, 2D1B, lower left, 2D1C, and lower right, 2D1D. These distributions are virtually identical for all other experiment series.

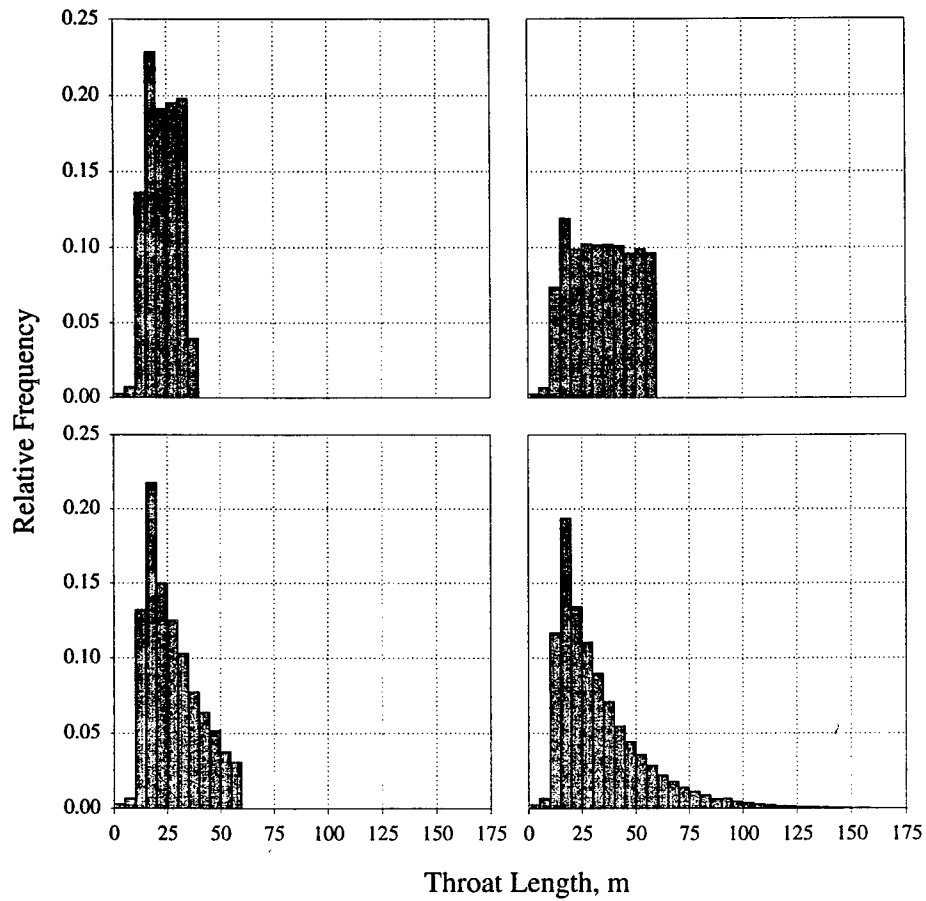


Figure 6.4: Histograms of throat length for the two-dimensional networks. Upper left, 2D1, upper right, 2D2, lower left, 2D3, and lower right, 2D4.

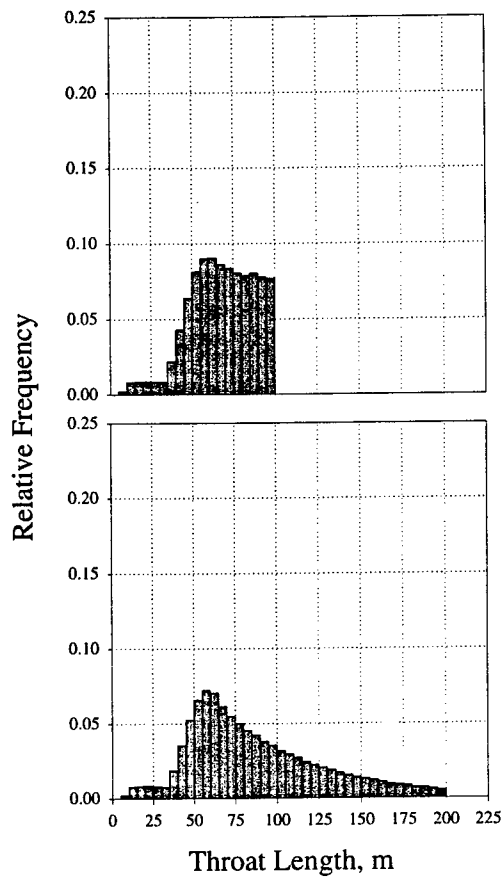


Figure 6.5: Histograms of throat length for the three-dimensional networks. Upper, 3D1, and lower, 3D2.

Figures 6.6 and 6.7 show contours of the x -direction, \ln -transformed, patch-renormalized conductivity for an applied gradient in the x direction ($\ln K_{pxx}$) for series 2D3. Figures 6.8 and 6.9 show the same plots for the y direction with an applied gradient in the x direction ($\ln K_{pxy}$). Figures 6.10 and 6.11 show the corresponding contours of total head for series 2D3 when a macroscopic, unit gradient in total head is applied to the boundaries in the x direction. As variance in throat conductivity increases from experiments 2D3A to 2D3D, irregularities in the head field increase. However, even with a variance in \ln throat conductivity of 9.0, the head field only deviates slightly from the planar solution for homogeneous media. This supports the idea that the pressure field is relatively insensitive to underlying variability in velocity.

6.2.4 Analysis of Results for Effective Conductivity.

Steady fluxes were computed through the downstream boundaries for each of these experiments. The observed macroscopic effective conductivities computed from these fluxes were compared against predictions from stochastic theory. Patch conductivities were computed using the renormalization procedure in Equation 6.12. The arithmetic, geometric and harmonic means of these patch conductivities were computed for comparison. The arithmetic mean, K_a is simply

$$K_a = \frac{1}{np} \sum_{p=1}^{np} K_p \quad (6.13)$$

where np is the number of patches and K_p is the patch conductivity tensor [LT^{-1}]. The geometric mean of the patch conductivities, K_g , is computed by

$$K_g = e^{\overline{\ln K_p}} = \exp \left(\frac{1}{np} \sum_{p=1}^{np} \ln(K_p) \right), \quad (6.14)$$

and the harmonic mean of the patch conductivities, K_h , is given as

$$K_h = \frac{np}{\sum_{p=1}^{np} \frac{1}{K_p}}. \quad (6.15)$$

Patch conductivities are tensors and matrix manipulation rules apply. To perform objective exponentiation or inversion, each patch tensor must be rotated to its principal orientation such that the eigenvalues of the matrix lie along the diagonal. Then, the operation may be performed on the diagonals and the rotation reversed to produce the tensor expanded.

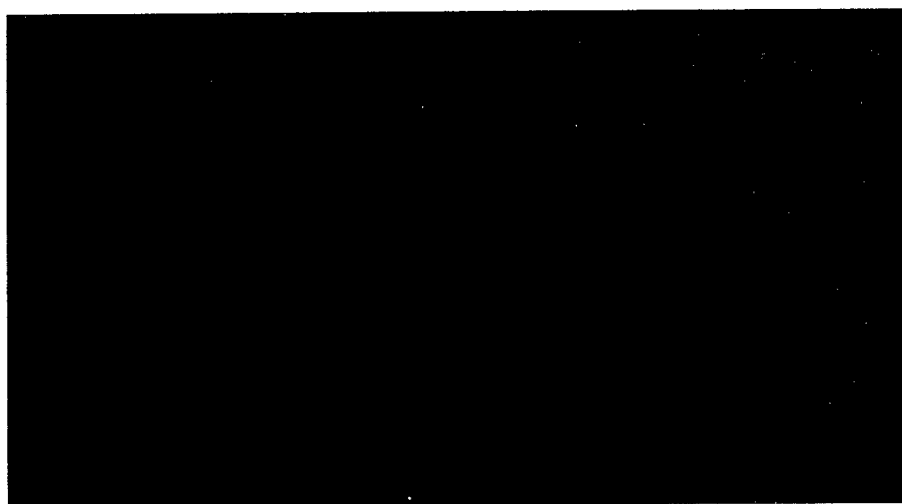
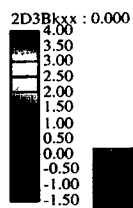
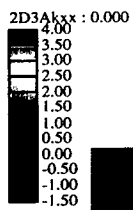


Figure 6.6: Contours of patch-renormalized \ln conductivity (K_{xx}) for experiments 2D3A (top) and 2D3B (bottom). Reds indicate higher conductivity values and blues, lower.

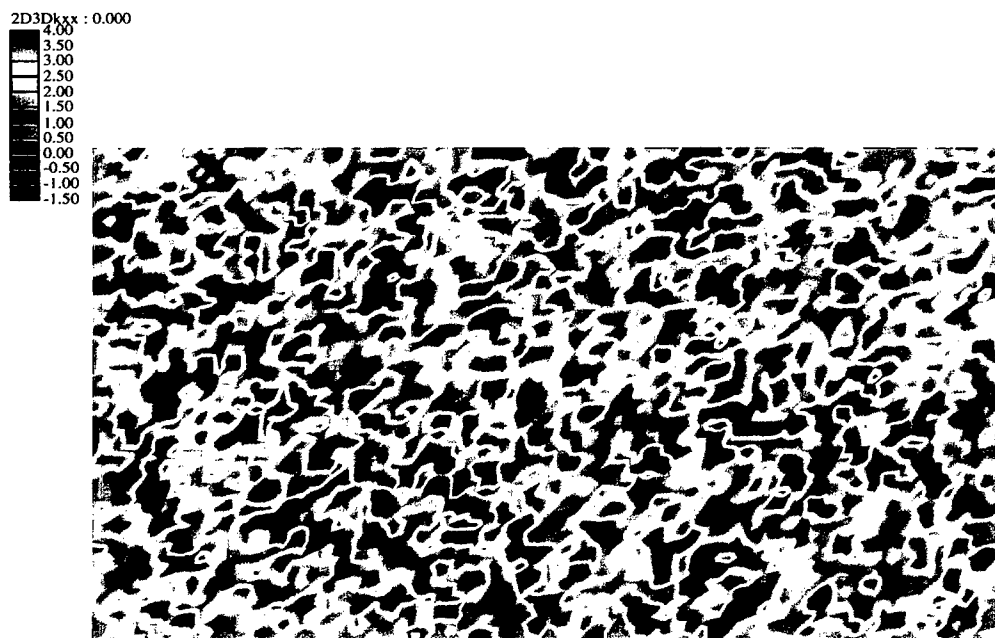
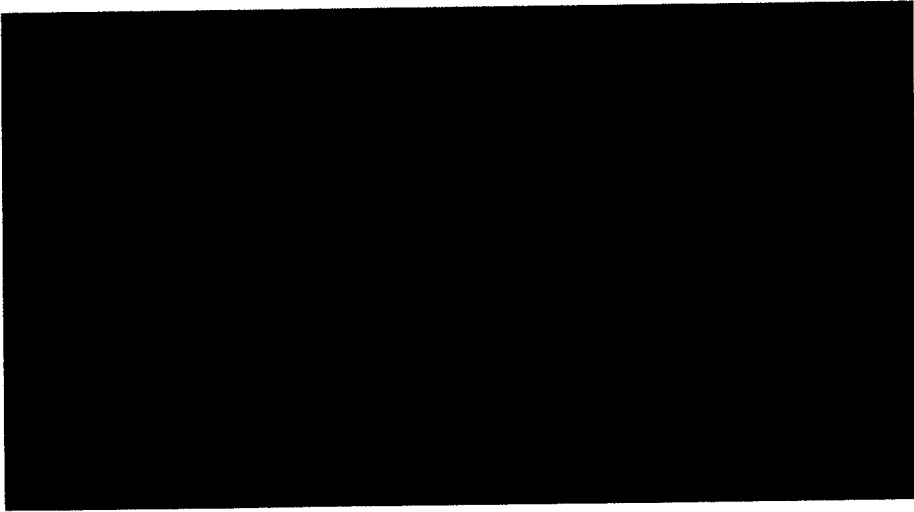
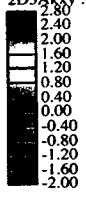


Figure 6.7: Contours of patch-normalized \ln conductivity (K_{xx}) for experiments 2D3C (top) and 2D3D (bottom). Reds indicate higher conductivity values and blues, lower.

2D3A K_{xy} : 0.000



2D3B K_{xy} : 0.000

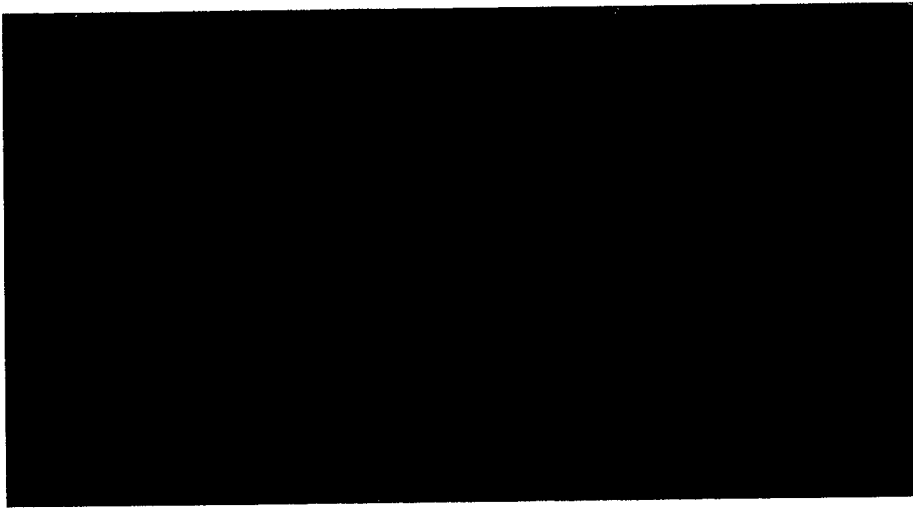
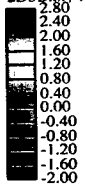


Figure 6.8: Contours of patch-renormalized \ln conductivity (K_{xy}) for experiments 2D3A (top) and 2D3B (bottom).

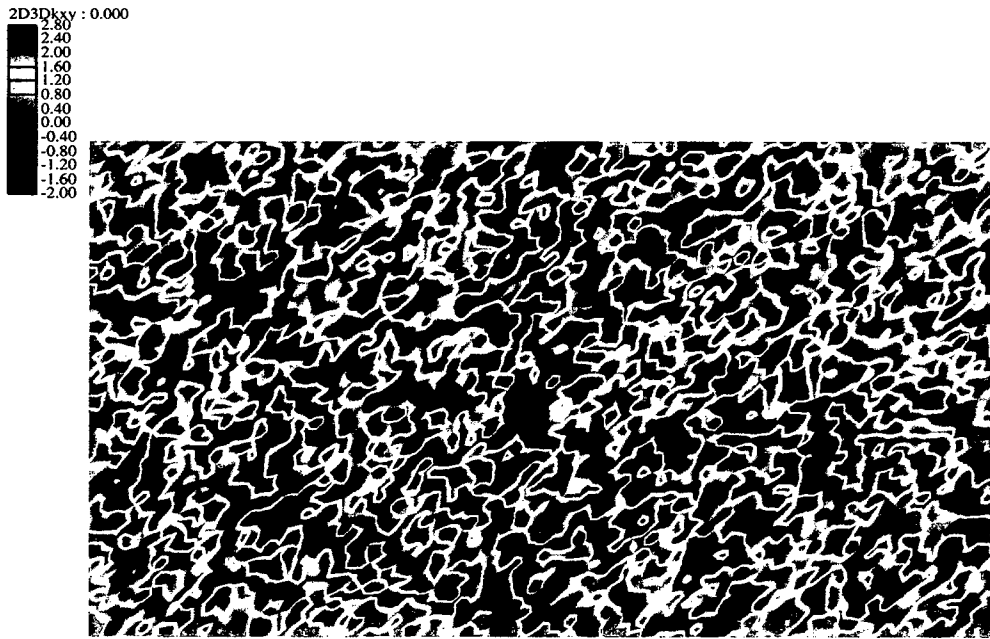
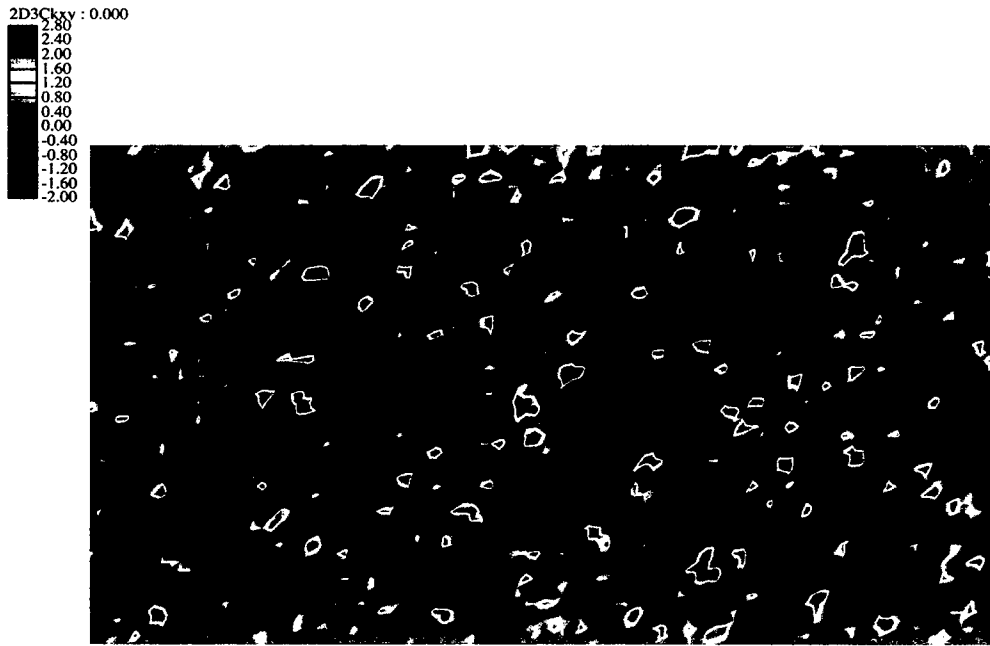
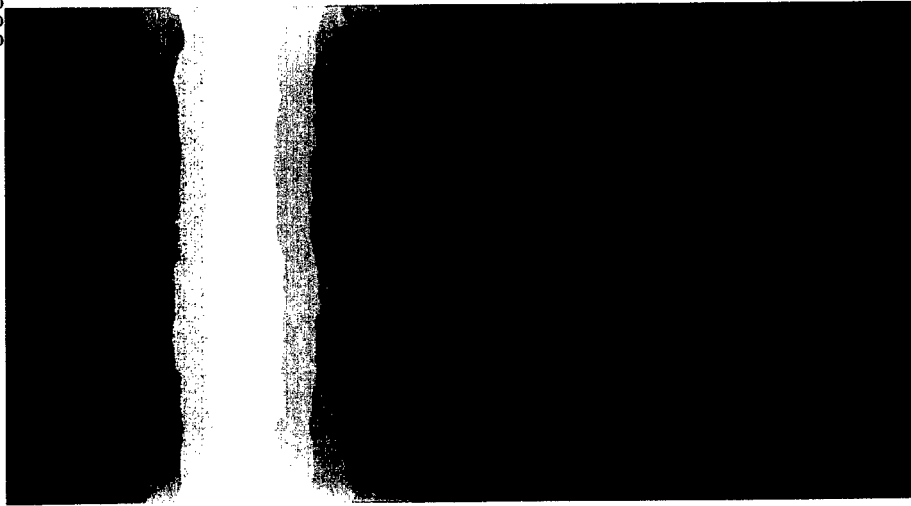


Figure 6.9: Contours of patch-normalized \ln conductivity (K_{xy}) for experiments 2D3C (top) and 2D3D (bottom).

2D3A : 5,000
3600.0
3300.0
3000.0
2700.0
2400.0
2100.0
1800.0
1500.0
1200.0
900.0



2D3B : 5,000
3600.0
3300.0
3000.0
2700.0
2400.0
2100.0
1800.0
1500.0
1200.0
900.0

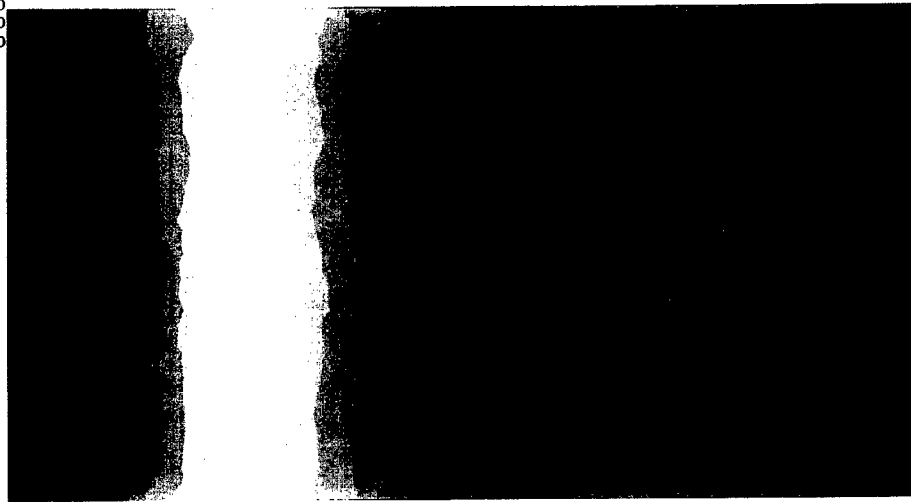


Figure 6.10: Contours of total head for experiments 2D3A (top) and 2D3B (bottom).

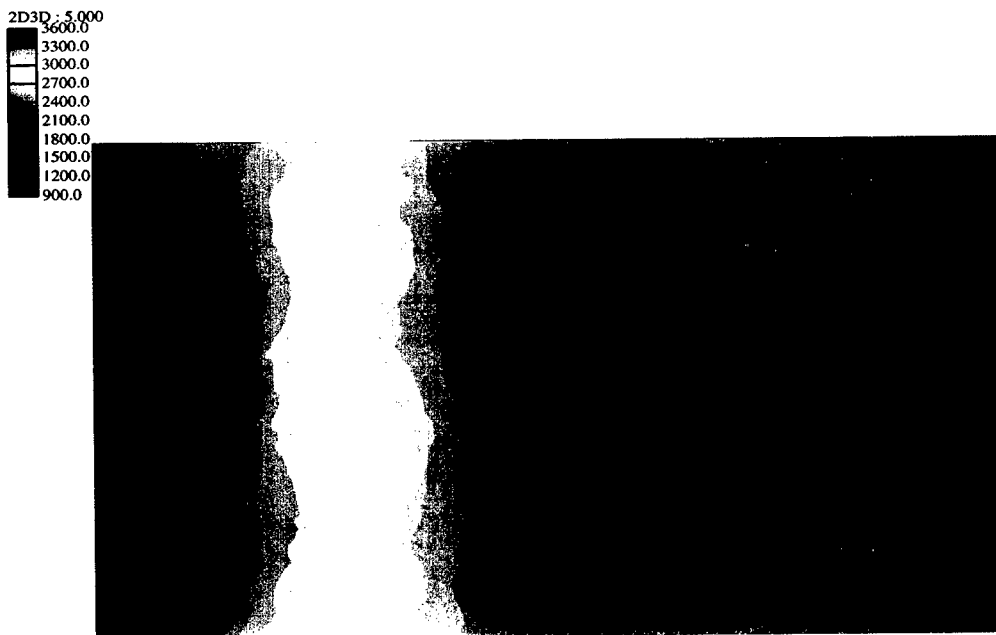
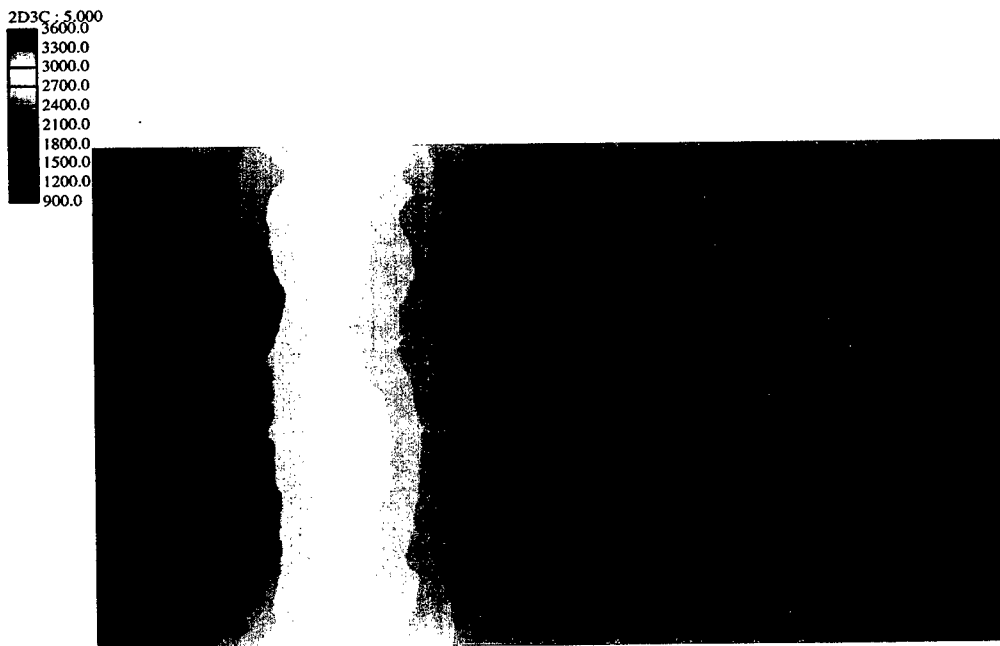


Figure 6.11: Contours of total head for experiments 2D3C (top) and 2D3D (bottom).

Figure 6.12 shows the arithmetic mean, the geometric mean, the harmonic mean, Equations 6.3 and 6.5, and network results for experiment series 3D1. Gelhar's small-perturbation theory [53] (Equation 6.3) appears to provide an acceptable estimate for effective network conductivity in the figure. Equation 6.3 is compared against all observations (two and three dimensional) in Figure 6.13. The agreement is generally very good. But, for large patch variance in two dimensions, the predictions and measurements begin to diverge. The geometric mean tends to underpredict the effective conductivity of a set of tensors with large variance and variable orientation. This effect may be attributed to local anisotropy in the patch conductivity tensor. Two factors control the local anisotropy, coordination number and throat conductivity variance. For random network layout, all patches will be anisotropic. However, for coordination numbers less than about 6 in two dimensions or about 10 in three dimensions, the local anisotropy becomes much stronger. As throat conductivity variance increases, local isotropy is lost, regardless of the coordination number. Perhaps this effect was not observed in three-dimensions because the coordination number is higher and there are more paths around low conductivity regions.

Stochastic theory assumes that the observation scale is large compared to the size of heterogeneities in the medium (represented by the correlation length). To examine the consequences of non-negligible correlation length on the effective conductivity, a simple experiment was conducted. A network was created to represent a column of porous material and its effective conductivity determined. The column was successively shortened and effective conductivity measured. The results of this experiment, shown in Figure 6.14, indicate that, with all throats in the network having the same throat conductivity, no measureable difference in conductivity is noticed. However, when the throat conductivities are not uniform, the correlation length may influence the effective conductivity. Conductivity is shown to be nearly constant for domains larger than 3 times the correlation length. Beneath that size, the effective conductivity increases as the domain size decreases. Thus, the REV for conductivity is approximately 3 times the correlation length for this example.

6.3 Predicting Apparent Dispersivity

6.3.1 Statistics of Dispersion.

Transport character is embodied by the rates of translation and spreading of a conservative tracer. These rates may be measured conveniently using the rates of change of spatial moments of a plume developing from an instantaneous point source of tracer. Gelhar [53] defines the dispersivity as one half the ratio of growth of the

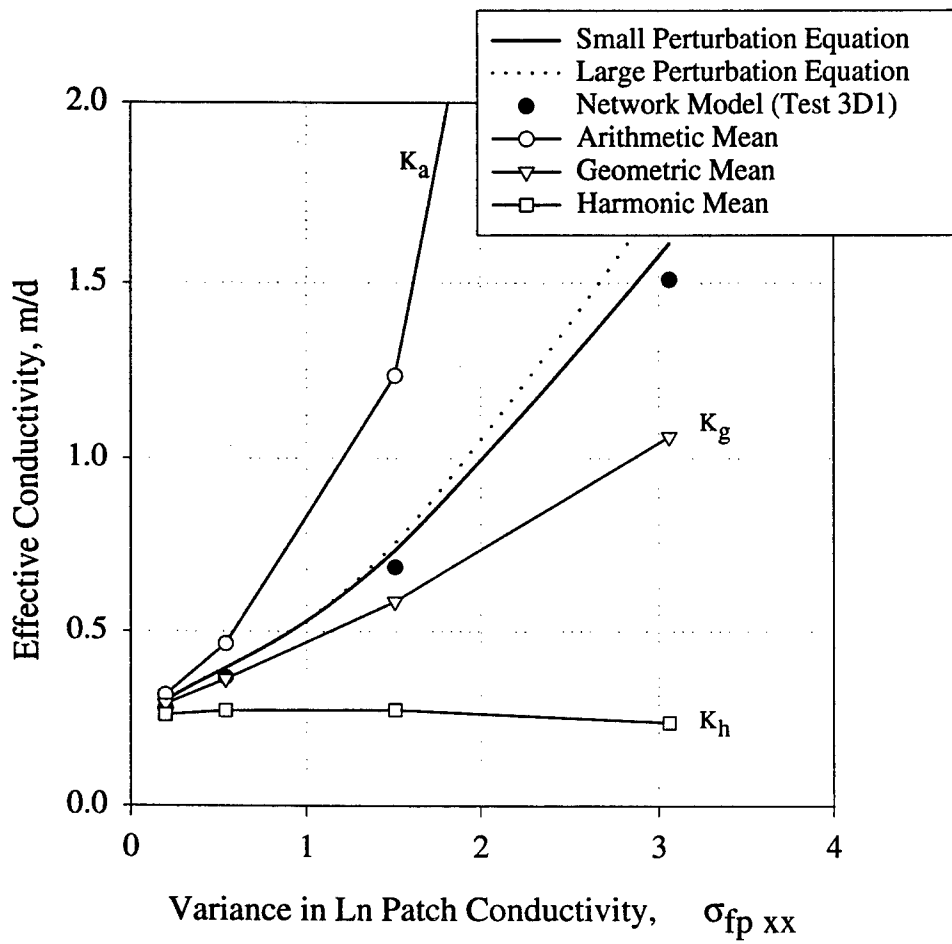


Figure 6.12: Comparison of conductivities from the network, various means, and stochastic theory for experiment series 3D1.

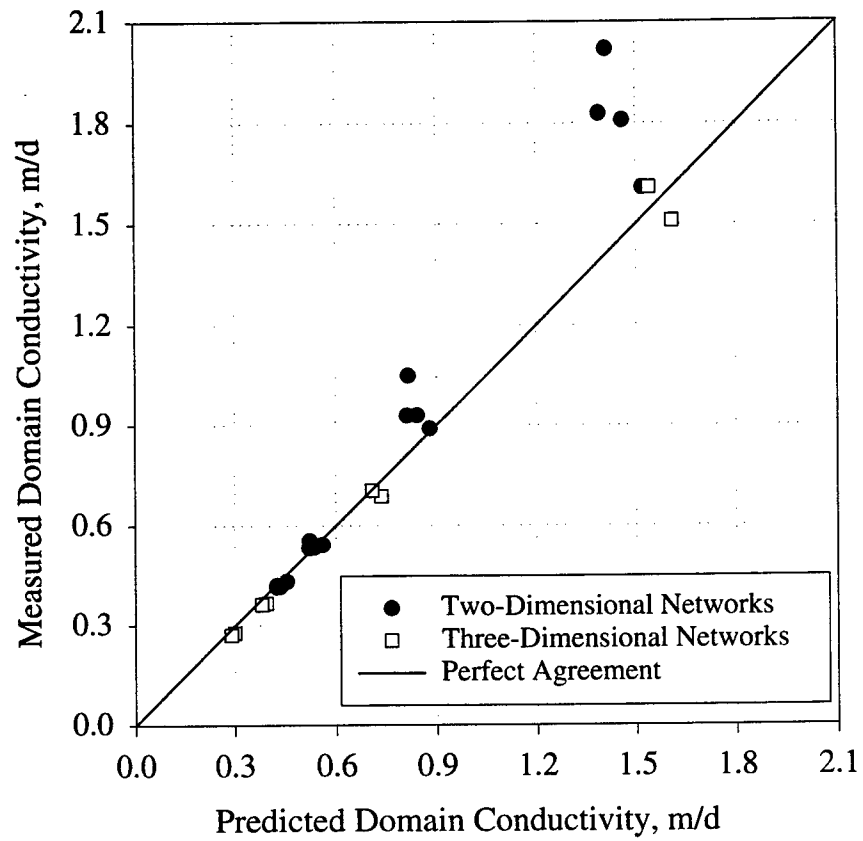


Figure 6.13: Predicted effective conductivity versus measured effective conductivity for all experiments.

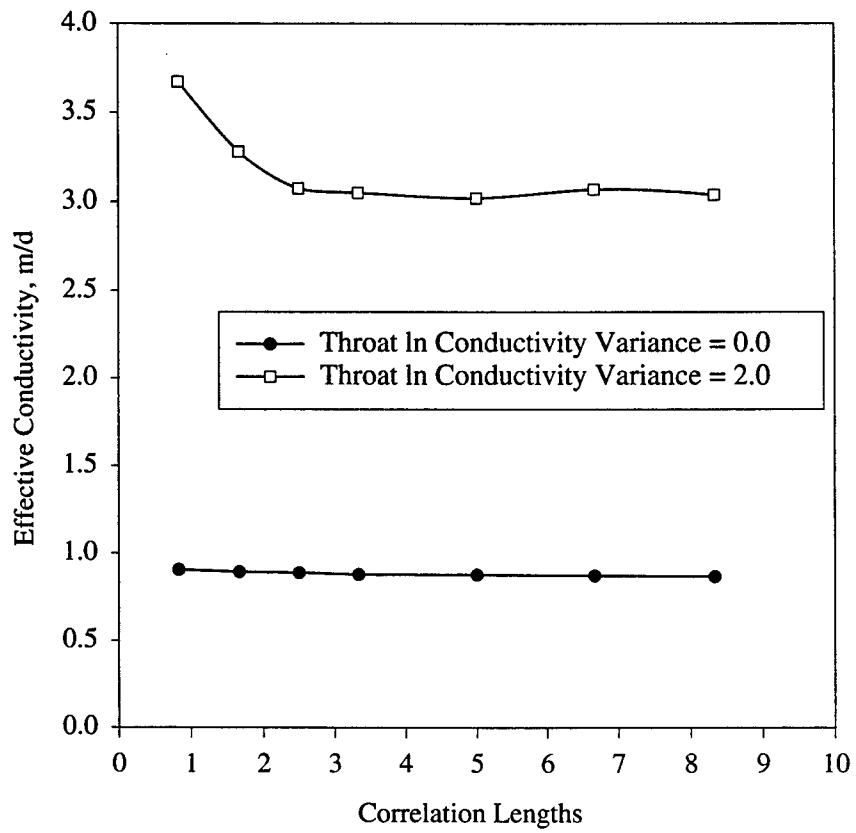


Figure 6.14: A scale effect in conductivity demonstrated by the network model.

second spatial moment with respect to the first spatial moment of the tracer. With macroscopic flow in the x direction, the dispersivity in the longitudinal direction is

$$\alpha_x = \alpha_L = \frac{1}{2} \frac{\frac{d\sigma_x^2}{dt}}{\frac{d\bar{x}}{dt}} = \frac{1}{2} \frac{d\sigma_x^2}{d\bar{x}} \quad (6.16)$$

where for a plume with total mass c_0

$$\bar{x} = \frac{1}{c_0} \int_{-\infty}^{\infty} xc(x)dx \quad (6.17)$$

and

$$\sigma_x^2 = \frac{1}{c_0} \int_{-\infty}^{\infty} x^2c(x)dx. \quad (6.18)$$

The fundamental relationship 6.16 may be explored in more detail. To simplify this analysis, the plume is assumed to consist of N neutrally-buoyant contaminant particles that are transported with the local advective velocity. Again, the growth of an instantaneous point source of tracer is examined. At any time after the placement of the particles the second moment of the mass about the centroid of the plume is

$$\sigma_x^2 = \frac{1}{N} \sum_{i=1}^N (x_i - \bar{x})^2 \quad (6.19)$$

where without loss of generality each particle is assumed to have a unit mass. The centroid \bar{x} is

$$\bar{x} = \frac{1}{N} \sum_{i=1}^N x_i. \quad (6.20)$$

The rate of change of the second moment is obtained by a straightforward time differentiation of Equation (6.20)

$$\frac{d\sigma_x^2}{dt} = \frac{2}{N} \sum_{i=1}^N (x_i - \bar{x})(\dot{x}_i - \dot{\bar{x}}) \quad (6.21)$$

Equation (6.21) can be rewritten in terms of the particle velocities $u_i = \dot{x}_i$ and the centroid velocity $\bar{u} = \dot{\bar{x}}$ as

$$\frac{d\sigma_x^2}{dt} = \frac{2}{N} \sum_{i=1}^N (x_i - \bar{x})(u_i - \bar{u}). \quad (6.22)$$

The right hand side of Equation (6.22) is twice the covariance of particle position and its velocity, S_{xu} . The covariance can be expressed in terms of the variance of

the two quantities and their coefficient of correlation ρ_{xu} , where $-1 \leq \rho_{xu} \leq 1$. Thus,

$$\frac{d\sigma_x^2}{dt} = 2\sigma_x\sigma_u\rho_{xu}. \quad (6.23)$$

The rate of spreading of a plume is often quantified by the apparent dispersivity back-calculated from observed data using Equation (6.16). Combining Equations (6.23) and (6.16), the apparent dispersivity is related to plume statistics by

$$\alpha_x = \frac{\sigma_x\sigma_u\rho_{xu}}{\bar{u}}. \quad (6.24)$$

Regrouping, we have

$$\alpha_x = (\sigma_x\rho_{xu}) \left(\frac{\sigma_u}{\bar{u}} \right). \quad (6.25)$$

A similar procedure may be used to examine lateral dispersivity. The lateral equivalent of Equation 6.22 is

$$\frac{d\sigma_x^2}{dt} = \frac{2}{N} \sum_{i=1}^N (x_i - \bar{x})(v_i - \bar{v}). \quad (6.26)$$

where \bar{v} is 0.0. Ultimately, we have an expression for lateral dispersivity

$$\alpha_y = (\sigma_y\rho_{yv}) \left(\frac{\sigma_v}{\bar{u}} \right). \quad (6.27)$$

6.3.2 Numerical Experimentation for Contaminant Transport

To explore the relationship between network structure and apparent dispersivity, transport was simulated through the experimental networks described in Table 6.1. A conservative tracer was injected at a position one tenth of the domain length from the left boundary and centered laterally and vertically. The tracer was injected at a rate of 1000 g/d for a period of 5 days. Figures 6.15 and 6.16 show plumes for series 2D3. Again, each experiment series corresponds to a fixed network topology with throat conductivity variance increasing from experiments *A* to *D*. Because effective conductivity increases substantially with increasing variance, the plumes travel at much different rates. The figures compare plumes at different times for which the developmental stages are similar. From these images, it is apparent that increases in conductivity variance increase longitudinal dispersion. However, the lateral growth of the plumes appears much less sensitive to changes in conductivity variance. Figures 6.17 and 6.18 show plumes for experiments 2D1C, 2D2C, 2D3C, and 2D4C. These experiments maintain the same variance while the throat-length distribution changes. Again, these are shown at different simulation times to permit well-developed plumes to be shown for each experiment. Lateral plume growth is

seen to increase somewhat with increasing throat length. Figure 6.19 shows an isosurface and contours of concentration for a three-dimensional series (3D1C). The isosurface value is 10^{-7} times the initial injection concentration. These experiments show an elongation of the plume as throat conductivity variance increases.

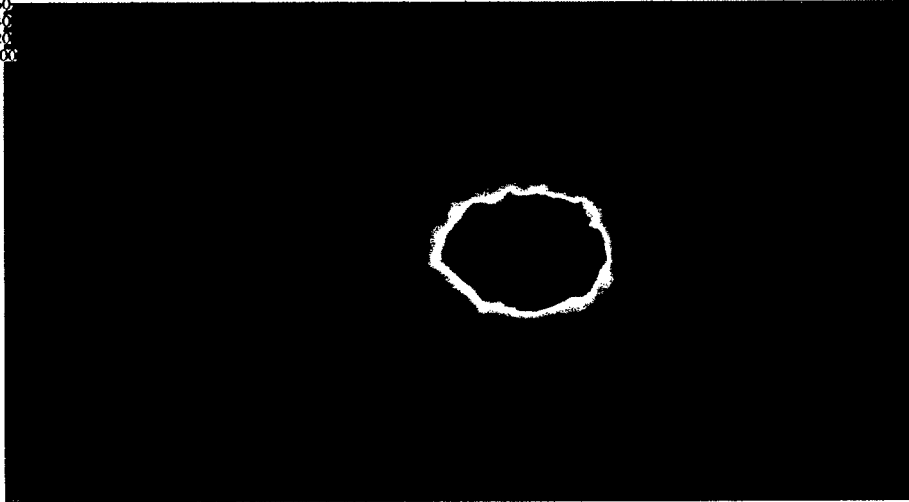
Even though the network model includes no dispersion term in the transport equation it solves, it is convenient to measure plume growth in terms of an equivalent, apparent dispersivity derived from observed spatial moments of the tracer concentration field. Apparent longitudinal dispersivity is plotted against travel distance for series 2D3 in Figure 6.20. Figure 6.21 shows the same plots for lateral dispersivity. These curves show definite growth of the apparent dispersivity with travel distance or measurement size; the so-called 'scale effect'. Although the behavior of the dispersivity measure is erratic until the plumes reach an adequate size, the curves follow the same general growth trend observed by Anderson [2] and Arya et al. [4]. At some large travel distance, the curves break away from this trend and approach a constant value for dispersivity. Networks with smaller throat variance are shown to reach asymptotic conditions (nearly constant dispersivity) for shorter travel distances than networks with larger variance.

Figures 6.20 and 6.21 also confirm the prior observation that longitudinal dispersivity is more sensitive than lateral dispersivity to changes in throat conductivity variance. Note that asymptotic lateral dispersivity is not zero as is predicted by some stochastic continuum theories [30]. The network contains an implied local dispersion caused by complete mixing of masses at the connections, resulting in non-zero asymptotic, apparent lateral dispersivity values.

Asymptotic dispersion behavior is achieved when a plume becomes sufficiently large compared to the size of the velocity structures [113]. However, travel distance is not always a good measure of plume size. Plots similar to Figures 6.20 and 6.21 are given in Figures 6.22 and 6.23 wherein the dispersivity is plotted as a function of the plume size measured by σ_x . These plots show slightly less dependence on throat conductivity variance in the pre-asymptotic region, demonstrating that plume size is a better predictor of a plume's dispersivity than travel distance.

Often, dispersivity is compared to travel time. This convention stems from pure diffusion where spreading rates reveal dispersivity proportional to the square root of time ($\alpha \propto t^w, w = 1/2$). Ideally, travel time and plume centroid position are related by a constant which is the seepage velocity. However, travel distance of the plume centroid and travel time are not interchangeable until the plume centroid's speed stabilizes. In heterogeneous media, this asymptotic condition is not reached quickly. Evaluating dispersivity as a function of travel time leads to the ideas of subdiffusive transport ($w < 1/2$) and superdiffusive transport ($w > 1/2$) [118].

2D3A2 : 2705.000
0.00200
0.00180
0.00160
0.00140
0.00120
0.00100
0.00080
0.00060
0.00040
0.00020
-0.00000



2D3B2 : 1805.000
0.00200
0.00180
0.00160
0.00140
0.00120
0.00100
0.00080
0.00060
0.00040
0.00020
-0.00000

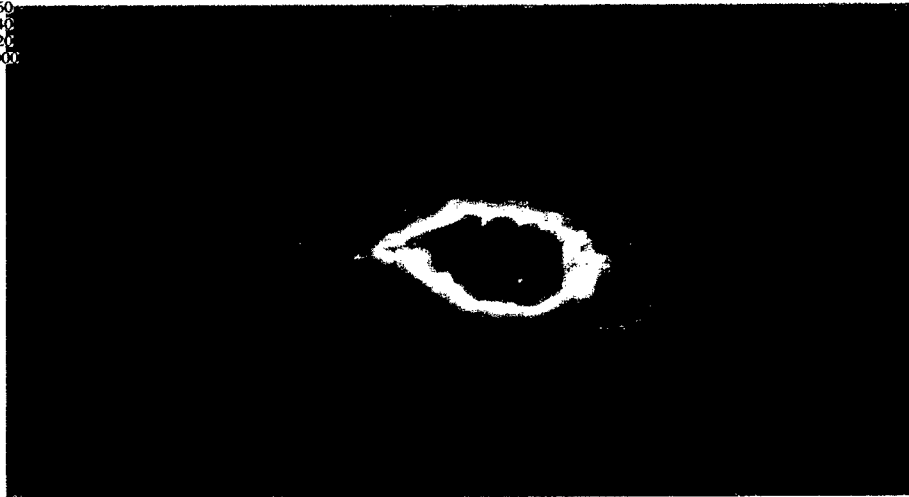
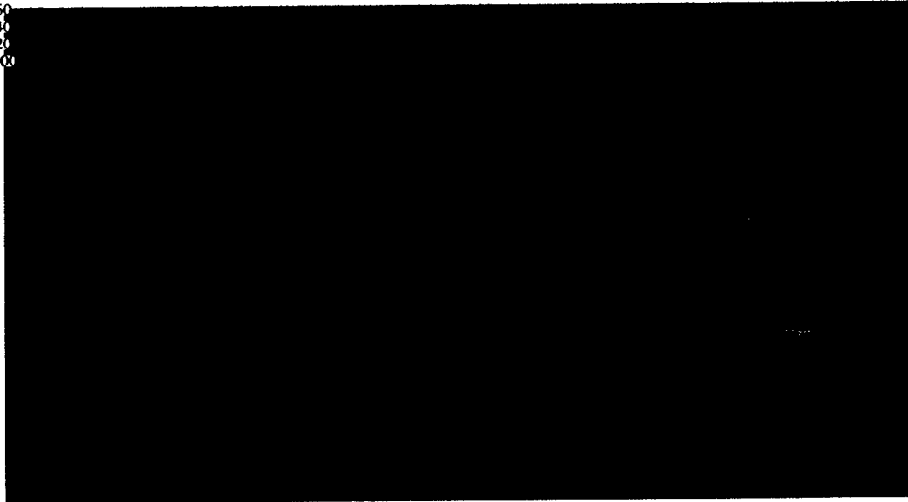


Figure 6.15: Contours of tracer concentration for developed plumes in experiments 2D3A (top) and 2D3B (bottom).

2D3C : 1505,000
0.00200
0.00180
0.00160
0.00140
0.00120
0.00100
0.00080
0.00060
0.00040
0.00020
-0.00000



2D3D : 605,000
0.00200
0.00180
0.00160
0.00140
0.00120
0.00100
0.00080
0.00060
0.00040
0.00020
-0.00000

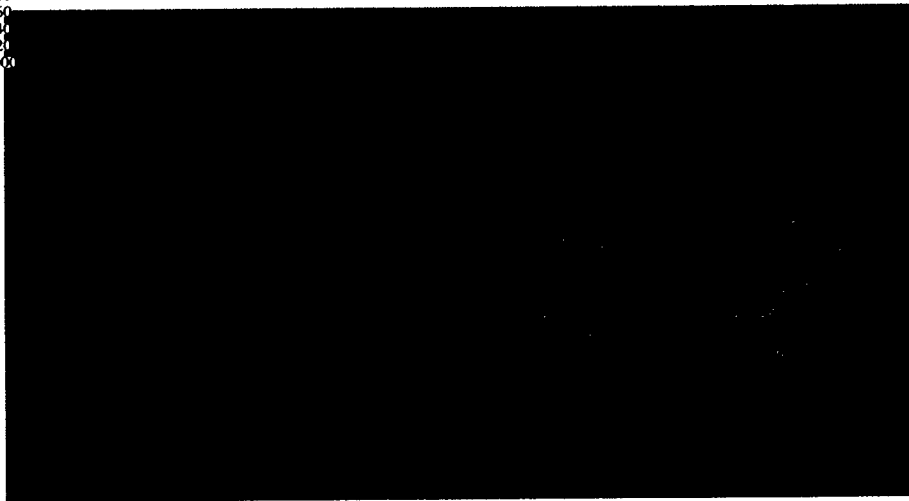
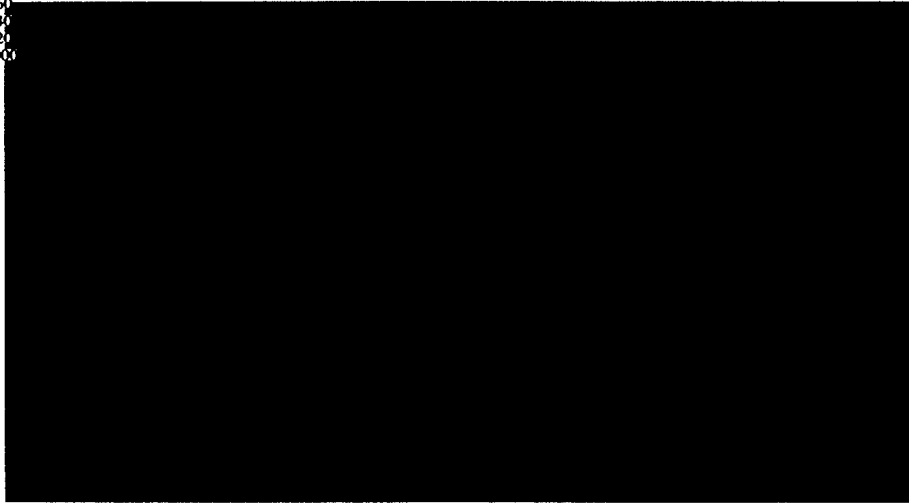


Figure 6.16: Contours of tracer concentration for developed plumes in experiments 2D3C (top) and 2D3D (bottom).

2D1C : 1505.000
0.00200
0.00180
0.00160
0.00140
0.00120
0.00100
0.00080
0.00060
0.00040
0.00020
-0.00000



2D2C : 1505.000
0.00200
0.00180
0.00160
0.00140
0.00120
0.00100
0.00080
0.00060
0.00040
0.00020
-0.00000

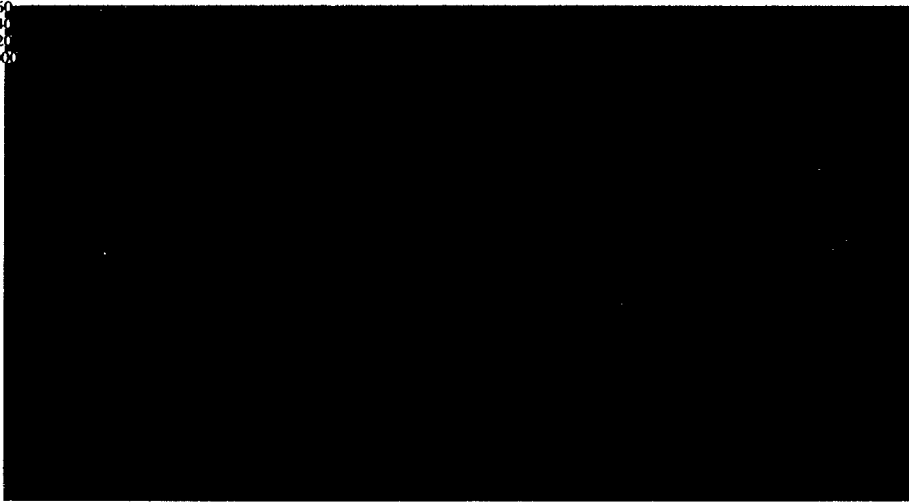


Figure 6.17: Contours of tracer concentration for developed plumes in experiments 2D1C (top) and 2D2C (bottom).

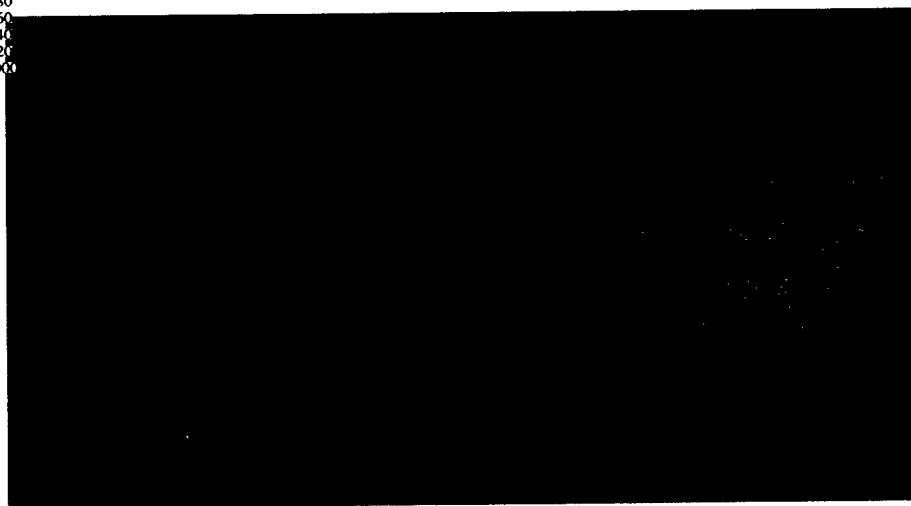
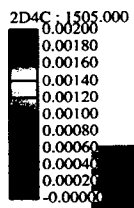
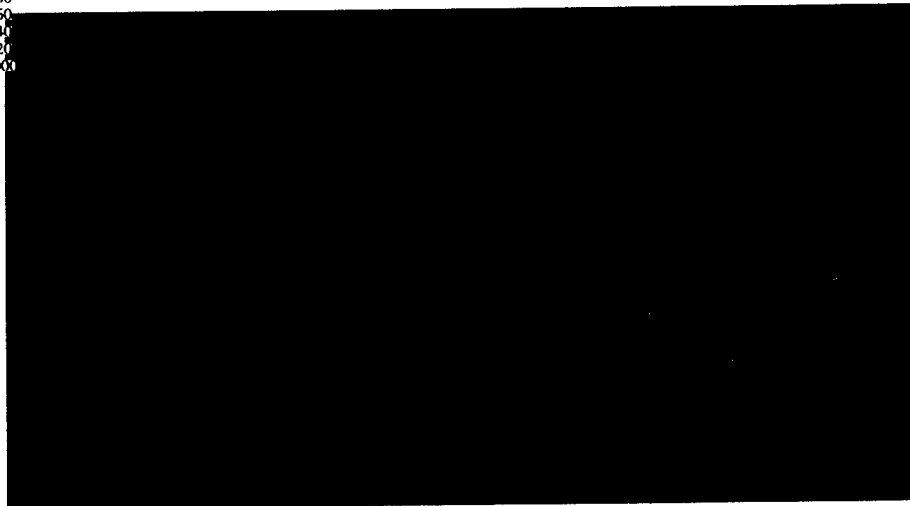
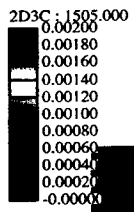


Figure 6.18: Contours of tracer concentration for developed plumes in experiments 2D3C (top) and 2D4C (bottom).

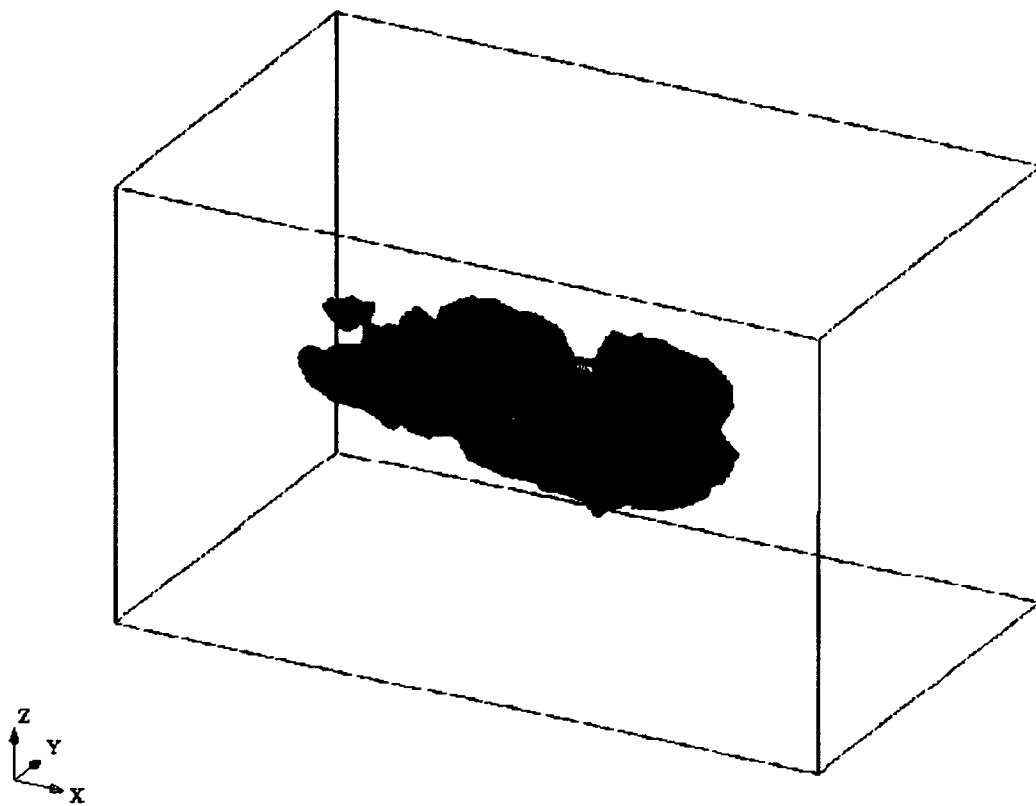


Figure 6.19: Isosurface and contours of tracer concentration for experiment 3D1C. Red indicates lower concentrations, blue, higher.

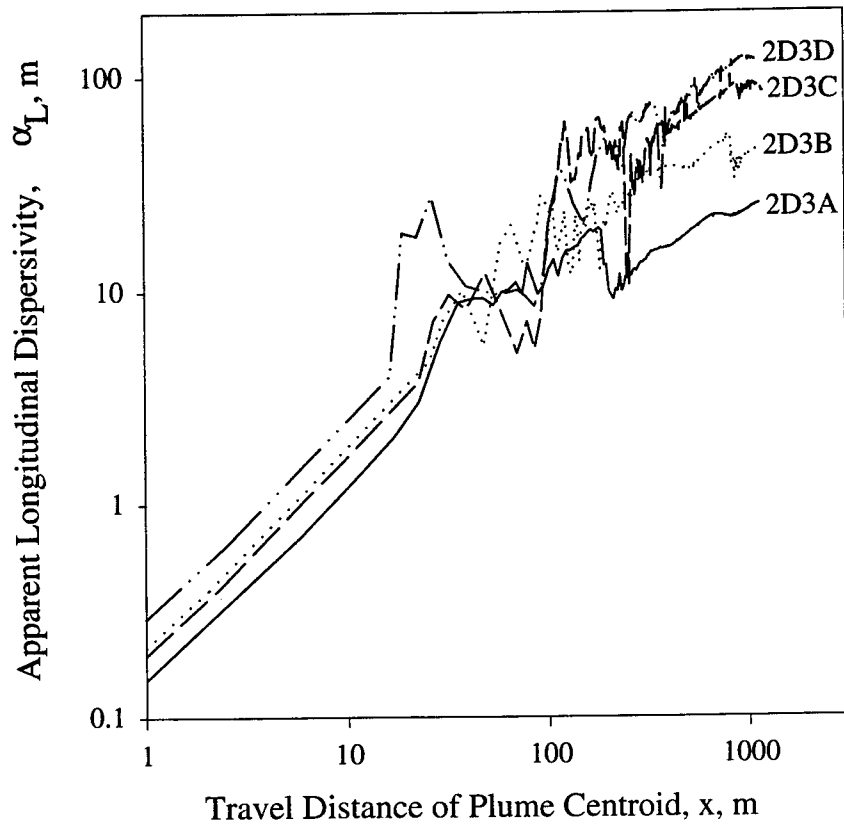


Figure 6.20: Apparent longitudinal dispersivity versus centroid travel distance for series 2D3.

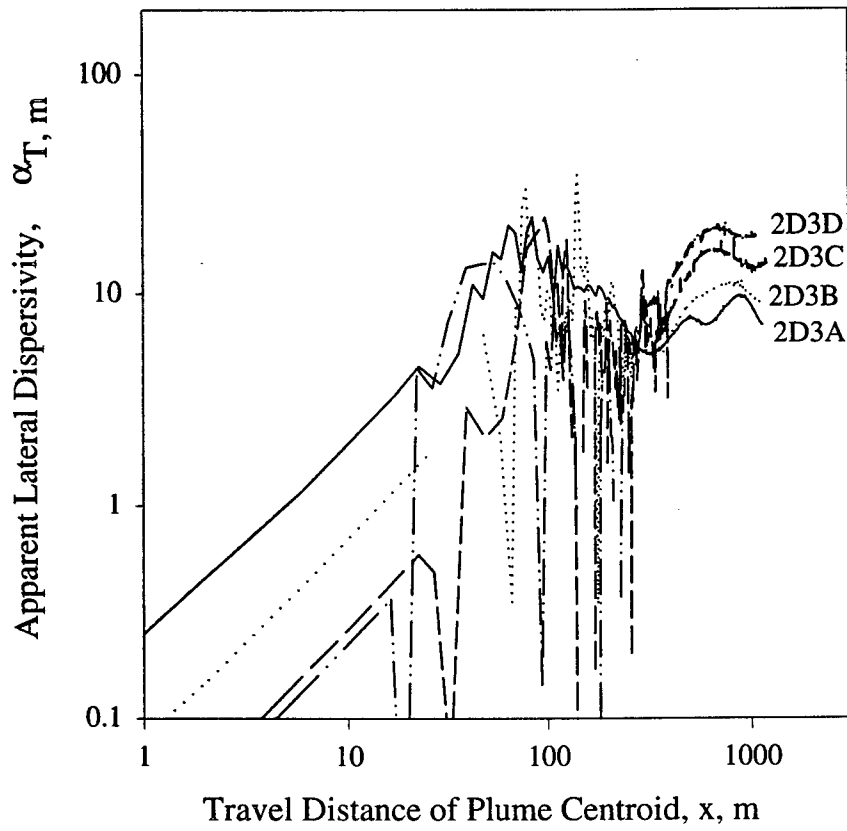


Figure 6.21: Apparent lateral dispersivity versus centroid travel distance for series 2D3.

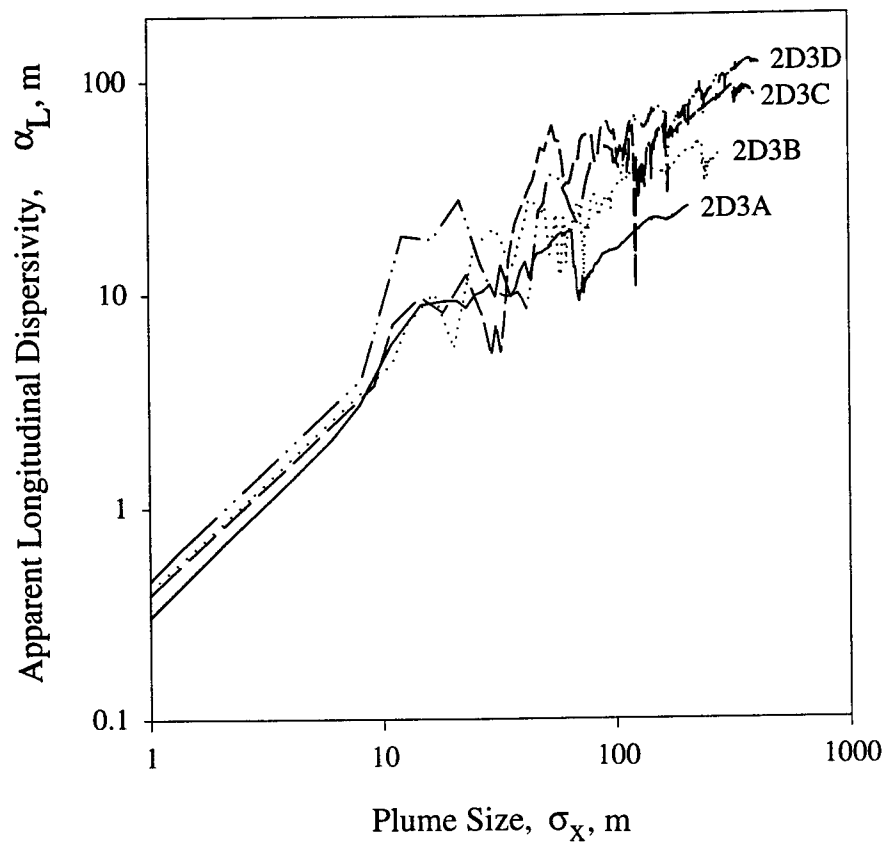


Figure 6.22: Apparent longitudinal dispersivity versus plume size for series 2D3.

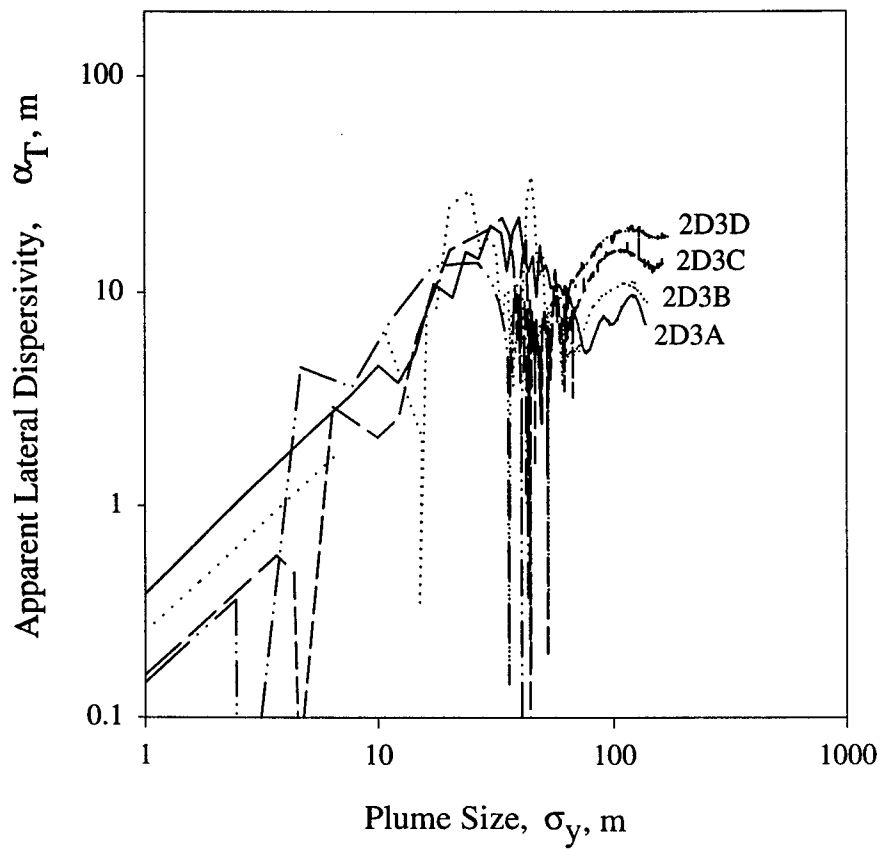


Figure 6.23: Apparent lateral dispersivity versus plume size for series 2D3.

These distinctions are not necessary. In porous media, subdiffusive transport should occur only when the plume is small and confined to a relatively low permeability region. In this case, the plume speed is small compared to the mean fluid velocity in the medium and \sqrt{t} overestimates the rate of plume growth. Measuring dispersivity as a function of plume size takes these differences into account automatically.

Figures 6.24 and 6.25 show the longitudinal and lateral dispersivities for experiment *C* in each of the 4 two-dimensional series. The structure of the network seems to have little effect on the apparent longitudinal dispersivity, but substantial effect on the apparent lateral dispersivity. Table 6.3 summarizes many of the results from these experiments. In the table, q is the Darcy flux, $[LT^{-1}]$, \bar{u}_L is the longitudinal, mass-averaged velocity, $[LT^{-1}]$, λ is the correlation length in the network, $[L]$, α_i are the apparent dispersivities, $[L]$, $\rho_{x_i u_i} \sigma_{x_i}$ are the position-velocity correlation terms, $[L]$, σ_{u_i}/u_L are the normalized velocity deviations, $[-]$, and i is the direction index (L, T_H, T_V), $[-]$. Time-dependent statistical measurements were taken at a consistent travel distance of the plume centroid of 1100 m. For the three dimensional 'C' and 'D' experiments, the leading edge of the plume exited the downstream boundary before the centroid traveled 1100 m, and measurements were made for travel distances between 850 and 1000 m. This was necessary because mass exiting the boundary greatly affected the plume statistics, invalidating further apparent dispersivity measurements.

6.3.3 Analysis of Results for Transport.

As a tracer plume becomes large compared to the velocity structures in the medium, the mass-averaged tracer velocity will approach the medium's mass-averaged fluid velocity. The mass-averaged fluid velocity, also known as the seepage or linear pore velocity, is computed by

$$v_s = q/\phi_e \quad (6.28)$$

where v_s is the seepage velocity and ϕ_e is the effective areal porosity (or simply the effective porosity). Effective porosity describes the fraction of the domain containing 'mobile' fluid [33]. The effective porosity permits us to include the effect of low- or zero-permeability regions in the medium on the seepage velocity. In the absence of 'immobile' fluid, the volumetric porosity and the effective porosity will be equal (assuming equality of areal porosity and volumetric porosity). The volumetric porosity for these numerical experiments was arbitrarily set to 1.0. Therefore, the difference between the Darcy velocity and the asymptotic, mass-averaged transport velocity in Table 6.3 reveals the effective porosity. For zero variance in the throat conductivities, the effective porosity and volumetric porosity are virtually equal.

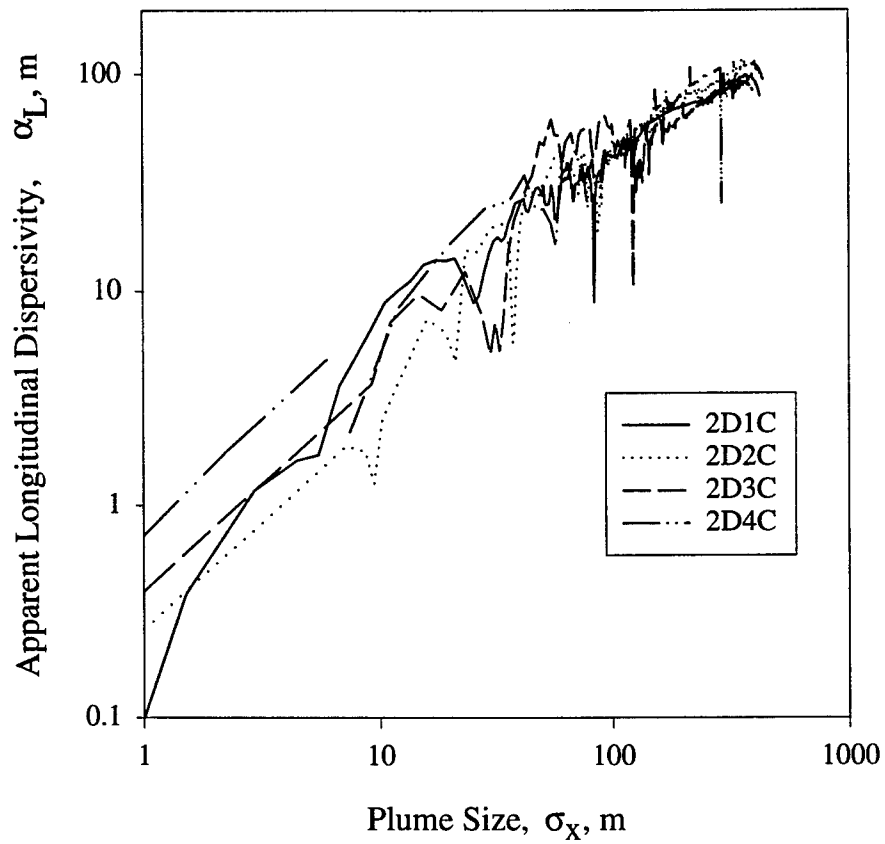


Figure 6.24: Apparent longitudinal dispersivity for ln throat conductivity variance of 4.0 with different throat length distributions.

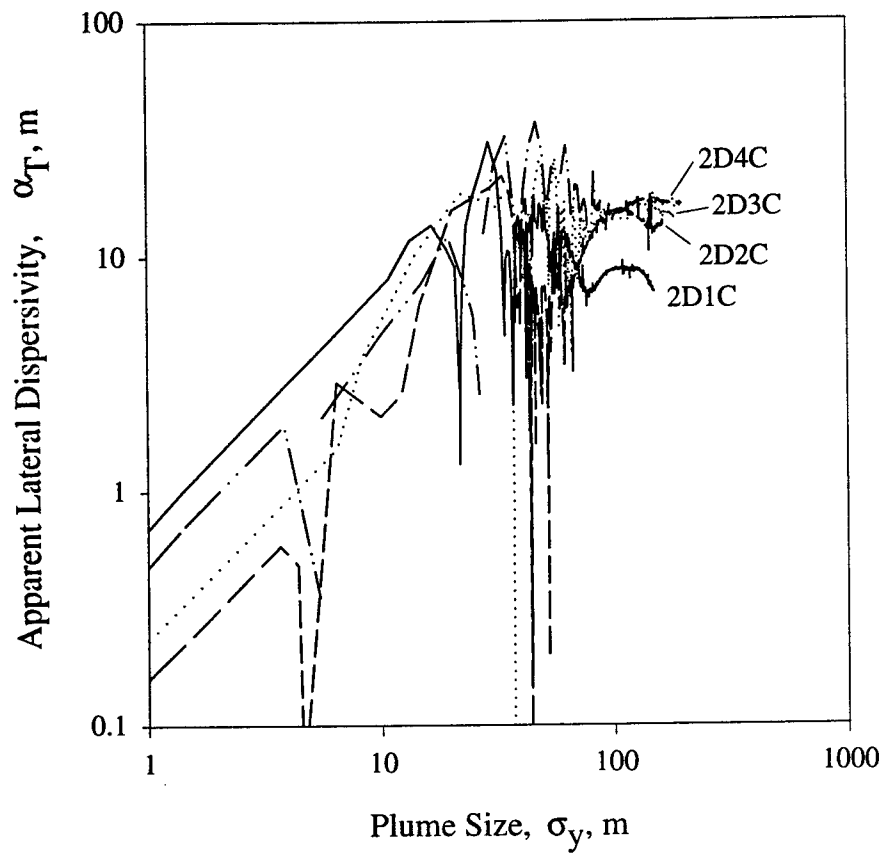


Figure 6.25: Apparent lateral dispersivity for \ln throat conductivity variance of 4.0 with different throat length distributions.

Table 6.3: Results from Flow and Transport Simulations.

Exp. Label	q (m/d)	\bar{u}_L (m/d)	λ (m)	$\rho_{x_i u_i} \sigma_{x_i}$ (m)	σ_{u_i} / u_L (m)	α_i (m)
2D1A	.43	.44	36	24 / 8.4	.81 / .77	20 / 6.4
2D1B	.54	.55	36	29 / 6.6	1.3 / 1.1	38 / 7.1
2D1C	.89	.93	36	49 / 5.0	2.0 / 1.6	100 / 8.2
2D1D	1.6	1.7	36	63 / 4.2	2.8 / 2.3	177 / 9.9
2D2A	.42	.42	60	33 / 13	.82 / .82	27 / 11
2D2B	.53	.54	60	37 / 11	1.4 / 1.1	50 / 12
2D2C	.93	.94	60	58 / 8.7	2.2 / 1.8	125 / 16
2D2D	1.8	1.9	60	67 / 7.9	3.0 / 2.6	201 / 21
2D3A	.42	.42	60	29 / 9.1	.83 / .82	24 / 7.4
2D3B	.54	.55	60	32 / 8.0	1.4 / 1.1	44 / 9.1
2D3C	.93	1.0	60	44 / 7.6	2.1 / 1.7	93 / 13
2D3D	1.8	2.3	60	49 / 8.1	2.7 / 2.3	134 / 19
2D4A	.42	.42	66	39 / 14	.82 / .80	32 / 11
2D4B	.56	.56	66	42 / 11	1.4 / 1.1	56 / 13
2D4C	1.0	1.0	66	57 / 9.4	2.3 / 1.8	130 / 17
2D4D	2.0	2.3	66	67 / 9.0	3.1 / 2.6	206 / 23
3D1A	.28	.28	100	50 / 20 / 21	1.0 / .86 / .86	51 / 17 / 18
3D1B	.37	.38	100	49 / 16 / 16	1.6 / 1.2 / 1.2	77 / 19 / 19
3D1C	.69	.81	100	60 / 12 / 12	2.4 / 1.9 / 1.9	143 / 23 / 22
3D1D	1.5	2.4	100	61 / 11 / 11	2.8 / 2.3 / 2.3	170 / 26 / 25
3D1A	.27	.29	180	67 / 28 / 28	1.1 / .91 / .91	70 / 25 / 25
3D1B	.36	.37	180	75 / 21 / 21	1.6 / 1.2 / 1.2	119 / 26 / 26
3D1C	.71	.80	180	87 / 16 / 16	2.4 / 1.9 / 1.9	206 / 30 / 30
3D1D	1.6	2.2	180	92 / 13 / 14	3.0 / 2.4 / 2.5	278 / 32 / 36

However, as the variance in throat conductivity increases, the transport velocity becomes increasingly larger than the Darcy flux, indicating a decrease in the effective porosity. It is logical that effective porosity should be a function of the variability in the throat conductivities. As variance increases, the degree of preferential flow through the network increases and more near-zero permeability regions are created. Simple regression of the data suggests the following empirical equation

$$\phi_e = \phi \left(1 - \frac{(n-1)^2}{100} \sigma_{ft}^2 \right). \quad (6.29)$$

We know that asymptotic behavior (nearly constant dispersivity) occurs when the size of the plume is sufficiently large. A rule of thumb (for example, [53]) is that the plume must travel about 10 correlation lengths before becoming asymptotic. This has been supported by laboratory observations of Irwin et al. [72] who found that dispersion of a front in a one-dimensional packed column became asymptotic after traveling about 20-30 correlation lengths. However, plots showing travel distance of a plume versus apparent dispersivity (for example, Figure 6.20) and those showing plume size versus apparent dispersivity (for example, Figure 6.22) expose a problem. These plots show that networks with the same correlation length may reach asymptotic conditions at much different travel distances or plume sizes. This implies that an expression defining the travel distance or plume size necessary to reach an asymptotic state should include conductivity variance.

Determining the travel distance or plume size at which plume growth becomes asymptotic is difficult because the transition to a constant dispersivity is a gradual one and there is much short-time variability in the observations. However, the asymptotic dispersivity may be estimated with some precision and the pre-asymptotic trend in the observations is known. Assume that the asymptotic state begins at the intersection of the constant dispersivity line and the pre-asymptotic trend. This is a measurable quantity. The pre-asymptotic trend is followed more closely when apparent dispersivity is plotted against plume size rather than travel distance. Therefore, an empirical equation describing the pre-asymptotic trends in dispersivity as a function of plume size was determined from network observations to be

$$\alpha_L \approx \frac{\sigma_{xL}}{2} \quad (6.30)$$

for two and three dimensions. Using this expression and the nearly asymptotic dispersivities listed in Table 6.3, we may estimate the relationship among plume size, correlation length, and conductivity variance. Empirical relationships derived from these limited data indicate a significant dependence on the conductivity variance. The following relationships define the longitudinal plume size for which asymptotic

dispersivity conditions may be expected, in two and three dimensions, respectively.

$$\sigma_{x_L} > \lambda \left(\sigma_{ft} + \frac{1}{1 + \sigma_{ft}} + \frac{4}{10} \sigma_{ft}^2 \right) \quad (6.31)$$

$$\sigma_{x_L} > \lambda \left(\sigma_{ft} + \frac{1}{1 + \sigma_{ft}} \right) \quad (6.32)$$

These are coarse approximations designed to show interdependence for the data collected and should not be taken as universal. They show a marked increase in the plume size required for asymptotic conditions as the variance in conductivity increases. These and other data may be used in the future to examine the idea of an apparent correlation length that includes the conductivity variance. This implies that, as conductivity variance increases, the size or relative importance of the high-conductivity structures increases.

Equation 6.25 is the fundamental relationship between plume size and the statistical properties of the network. Figure 6.26 shows plume size, correlation coefficient, velocity variance, and the product of plume size and correlation coefficient for a single test. For large plumes, the term σ_{u_i}/\bar{u}_L can be taken as a constant that is a network property. Therefore, for α_{x_i} to become constant at the asymptotic limit, the product $\sigma_{x_i}\rho_{x_i u_i}$ must become constant. That is, $\rho_{x_i u_i}$ must become very small as the plume grows in size. This situation is fully consistent with the idea that there is a transition from an initially well-correlated plume to an ultimate condition of Brownian motion. For if the particle's velocity is perfectly correlated to its position relative to the centroid, $\rho_{x_i u_i}$ is 1.0. If the particle's position and velocity are not correlated (i.e. $\rho_{x_i u_i} \rightarrow 0$, with $\sigma_{x_i}\rho_{x_i u_i} \neq 0$), the particles are essentially undergoing random motion that can be described as a Brownian process. Evidently, the growth of α_{x_i} results from the relationship between plume size, σ_{x_i} , and correlation, $\rho_{x_i u_i}$.

The two components of asymptotic dispersion ($\rho_{x_i u_i}/u_L$ and $\sigma_{x_i}\rho_{x_i u_i}$) were analyzed separately. Non-linear regression of the observed, normalized velocity deviations (σ_{u_i}/\bar{u}_L , $i = L, T_H, T_V$) were performed. The resulting empirical equations are

$$\begin{aligned} \frac{\sigma_{u_L}}{\bar{u}_L} &= \left(\frac{3+n}{6} \right) + \left(\frac{4+3n}{20} \right) \sigma_{ft} + \left(\frac{3-n}{15} \right) \sigma_{ft}^2, \quad n = 2, 3 \\ \frac{\sigma_{u_T}}{\bar{u}_L} &= \left(\frac{6+n}{10} \right) + \left(\frac{n}{7} \right) \sigma_{ft} + \left(\frac{7-2n}{30} \right) \sigma_{ft}^2, \quad n = 2, 3, \end{aligned} \quad (6.33)$$

where n is the dimension of the problem. These asymptotic, normalized, velocity deviation terms proved to be insensitive to the different network topologies and correlation lengths used in these experiments. Figure 6.27 shows network observations and these empirical equations for longitudinal and lateral velocity deviation

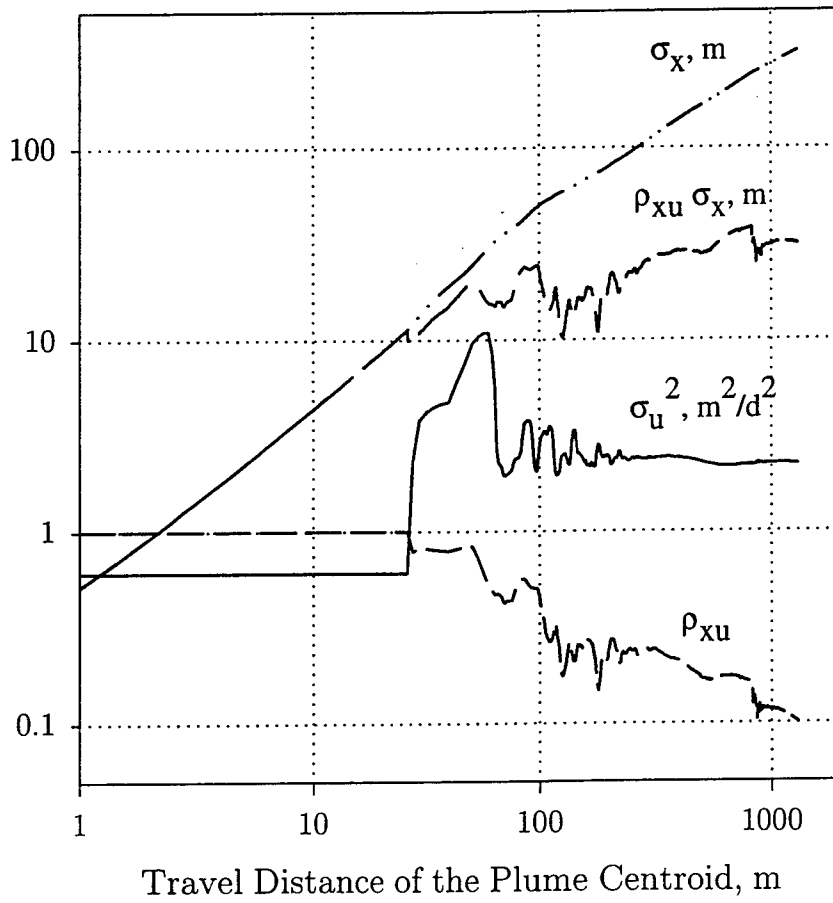


Figure 6.26: Transport statistics for experiment 2D3B.

for the two-dimensional experiments. These data show a small quadratic trend with increasing throat conductivity variance. The intercepts describe velocity variation due to the network topology when all throats have the same conductivity value. In two dimensions, the longitudinal and lateral values for this intercept are about 0.80. This intercept value may be estimated analytically by assuming an infinite coordination number and perfect isotropy. Each throat's velocity magnitude in the direction of the applied pressure gradient is $\cos^2 \theta$. Flow perpendicular to the direction of applied gradient is $\sin \theta \cos \theta$. By integrating over all possible angles, the mean velocity magnitude is computed to be $1/2 v_t$ and the variance in velocity is $1/8 v_t$, where v_t is the velocity magnitude in a throat parallel to the applied gradient. Thus, the normalized deviations in velocity should be $1/\sqrt{2}$ (or 0.7071) in both the longitudinal and lateral directions. This is close to the observed value of 0.8. The difference may be due to less-than-infinite coordination number.

Figure 6.28 shows trends in normalized velocity deviations versus increase in throat conductivity variation for the three-dimensional tests. The three-dimensional results show nearly linear behavior.

Gelhar [53] offers a relationship between the velocity variance and the conductivity variance for isotropic, statistically homogeneous media. These equations are only valid in the ergodic limit and for small velocity variance. In three dimensions,

$$\sigma_u^2 = \frac{8 \sigma_f^2 J^2}{15 K_g^2} \quad (6.34)$$

$$\sigma_v^2 = \frac{1 \sigma_f^2 J^2}{15 K_g^2} \quad (6.35)$$

where J is the head gradient in the longitudinal direction. These equations suggest a constant ratio of longitudinal to lateral velocity variance of 8. In two dimensions,

$$\sigma_u^2 = \frac{3}{8} \sigma_f^2 \bar{v}^2 \quad (6.36)$$

$$\sigma_v^2 = \frac{1}{8} \sigma_f^2 \bar{v}^2 \quad (6.37)$$

and the same ratio is 3. These indicate that there should be a constant ratio between σ_{u_L}/\bar{u}_L and σ_{u_T}/\bar{u}_L that is $\sqrt{8}$ in three dimensions and $\sqrt{3}$ in two dimensions. The network observations produce a nearly constant ratio of 1.2 for all observations except two-dimensional networks with zero throat variance for which the ratio is 1.0.

Regressions were also performed on the second term in the dispersivity ($\sigma_{xi} \rho_{xiui}$). Observations of these quantities in the network model show dependence on both correlation length, and throat conductivity variance. The resulting empirical equations

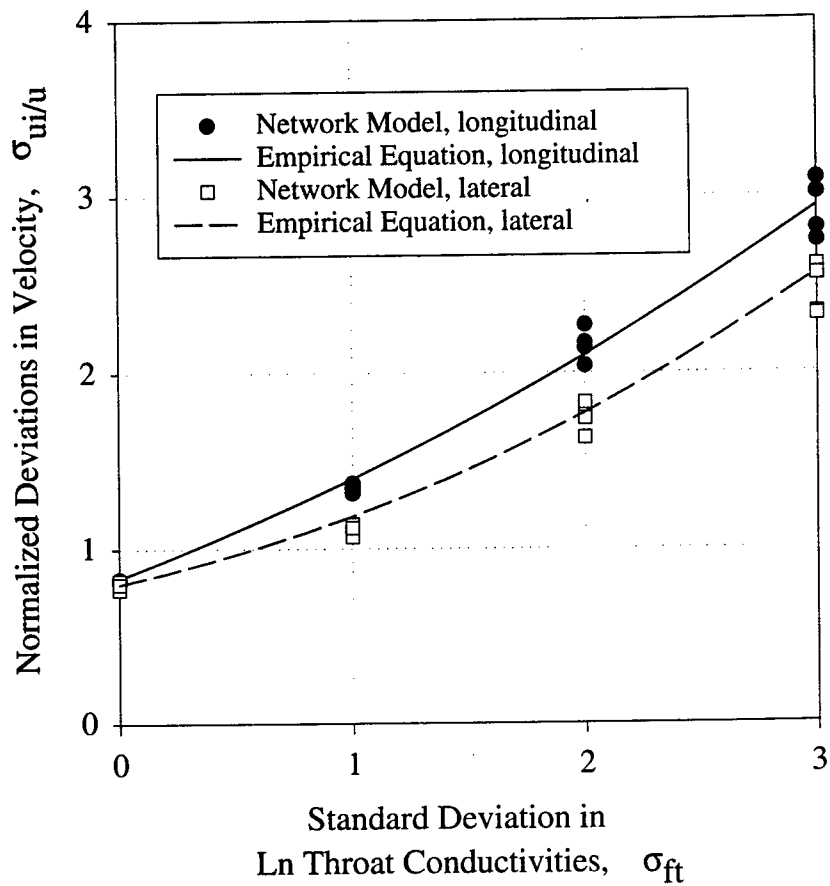


Figure 6.27: Normalized velocity deviations versus standard deviation in throat conductivity for the two-dimensional experiments.

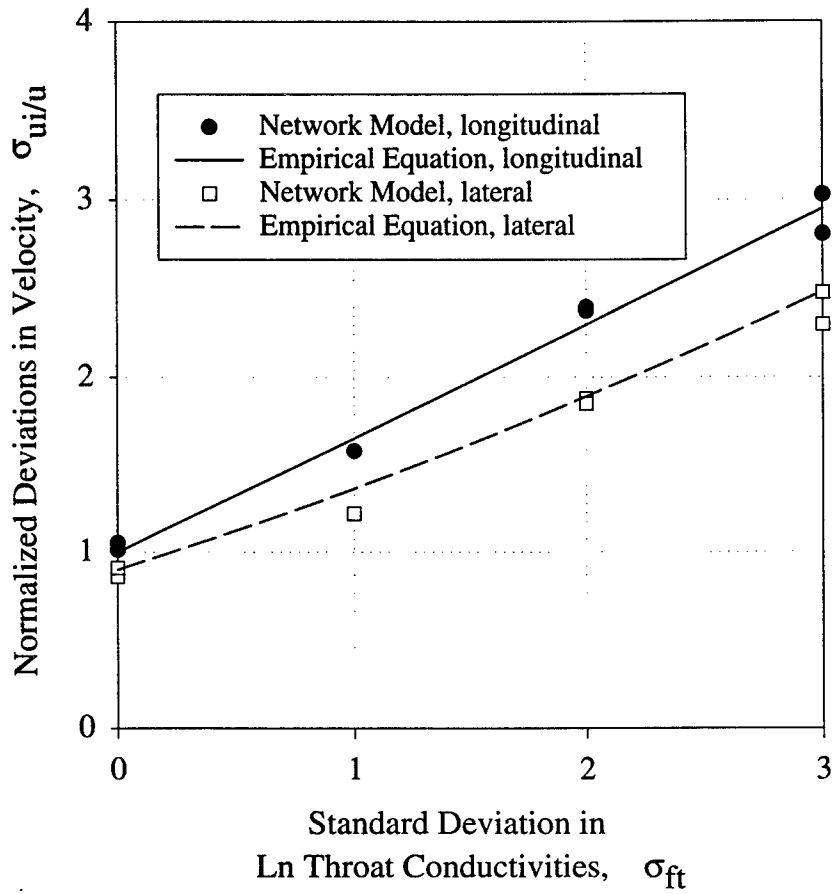


Figure 6.28: Normalized velocity deviations versus standard deviation in throat conductivity for the three-dimensional experiments.

are

$$\sigma_{L\rho Lu_L} = \left(1 + \frac{9}{n}\right) \frac{\lambda}{10} e^{\left(\frac{\sigma_{ft}(n-3)}{2}\right)} + \left(\frac{58}{n^2-1}\sigma_{ft}\right) \quad (6.38)$$

$$\sigma_{T\rho Tu_T} = \frac{\lambda}{2} \left(\frac{1}{2n} + \frac{e^{-\sigma_{ft}}}{9-n}\right). \quad (6.39)$$

In three dimensions, the longitudinal correlation term reduces to a linear function of the correlation length and the conductivity variance. In two dimensions, the longitudinal term's dependence on correlation length diminishes with increasing conductivity variance. In fact, in the limit of infinite conductivity variance ($\sigma_{ft} \rightarrow \infty$) with finite correlation length, the longitudinal correlation term is independent of the correlation length. The lateral correlation term shows the opposite effect. For large conductivity variance, the lateral term approaches a linear function of correlation length. These effects are demonstrated in Figure 6.29 which shows the empirical equations and model observations for a single experiment series.

The empirical equation predictions are compared against the model observations in Figure 6.30. This figure simply demonstrates that the empirical equations in terms of problem dimension, correlation length, and throat conductivity variance capture most of the variability in the observations.

When the two sets of empirical equations (Equations 6.33 and 6.38) are combined, we have an empirical expression to describe apparent asymptotic dispersivity in networks. Figures 6.31 and 6.32 show empirical predictions of dispersivity versus network model observations. Because these data come from 6 different network topologies in two and three dimensions with throat conductivity variances ranging from 0 to 9, there is some confidence in these empirical equations for anticipating apparent dispersivities, given the basic structural elements of the network (dimension, correlation length, and throat conductivity variance).

6.4 Creating Networks to Match Macroscale Observations

The preceding sections have demonstrated an ability to empirically estimate macroscopic effective conductivity and apparent dispersivity of a given network prior to simulating flow and transport. This ability will now be used to create networks having desired macroscopic properties given from field testing at a particular site. The goal is to supplant the actual porous medium with a much coarser medium (the network) having the same flow and transport character. Flow and transport character includes the volumetric fluid content, resistance to fluid flow, and *observable*

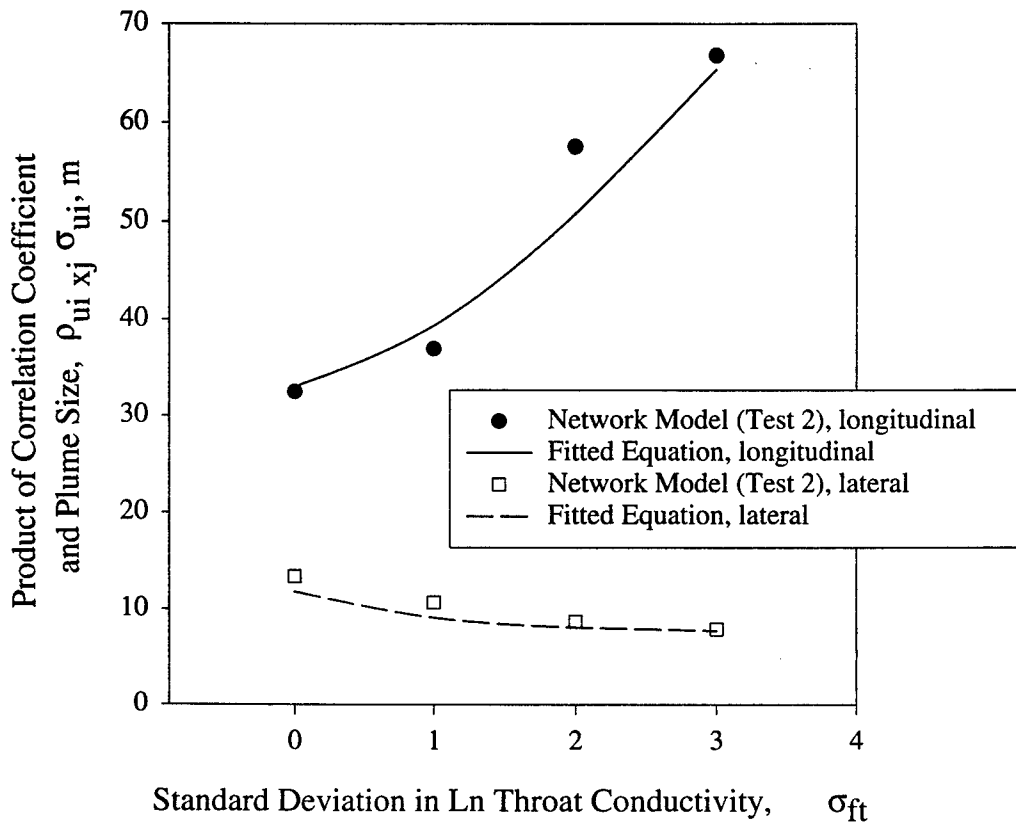


Figure 6.29: Correlation terms versus throat conductivity deviations for a single experiment series (2D2).

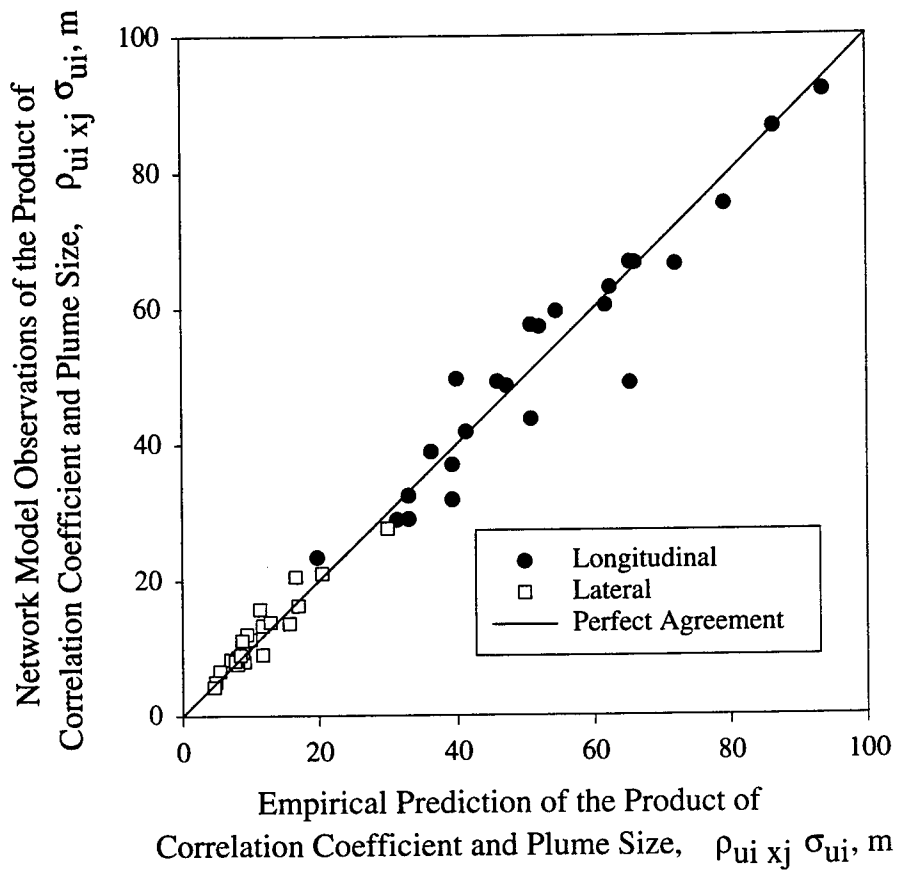


Figure 6.30: Empirical predictions of the correlation term versus network model observations.

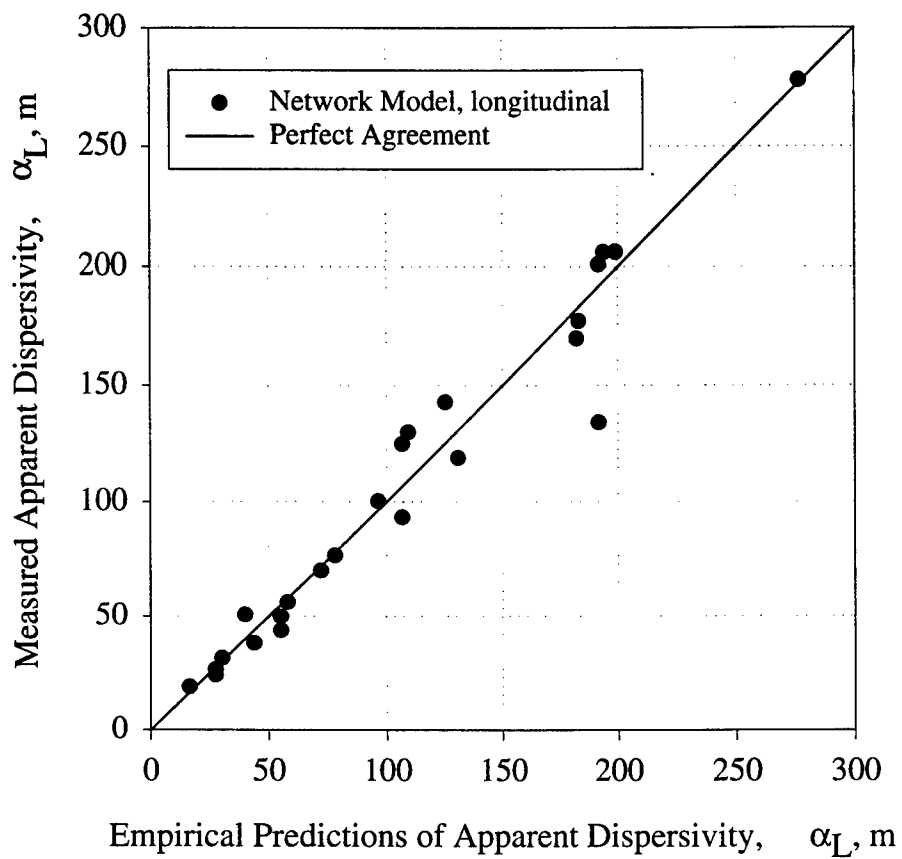


Figure 6.31: Empirical predictions and network observations of apparent longitudinal dispersivity.

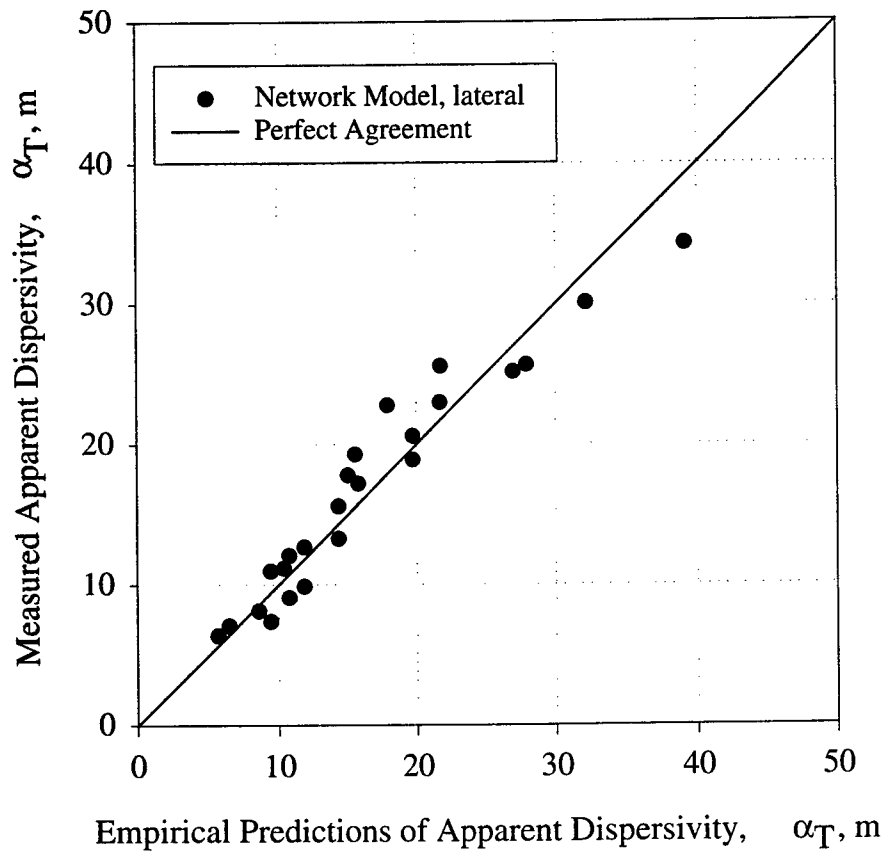


Figure 6.32: Empirical predictions and network observations of apparent lateral dispersivity.

constituent spreading. If these properties are matched for all desired observation scales, the network medium and the actual medium are, for simulation purposes, identical.

6.4.1 Network Parameters.

Parameters that control the network structure and dictate flow and transport behavior are:

- average connection spacing,
- maximum throat length,
- mean \ln throat conductivity,
- variance in \ln throat conductivity, and
- probability decay parameter for throat creation.

Note that no transport properties are assigned when simulating conservative transport. All transport properties are inherent in the network structure itself.

Like other 'inverse' problems, establishing fine scale data (individual throat properties) to match coarse property measurements is not a well-posed problem. The resulting network is not unique. There exists an infinite number of networks that produce the same averaged macroscopic behavior. It seems logical to begin with the most difficult feature to match, dispersivity, and work toward the simplest feature, porosity.

6.4.2 Matching Apparent Dispersivity.

Equations 6.33 and 6.38 are empirical expressions describing apparent dispersivities as functions of dimension of the network, the correlation length, and the throat conductivity variance. These equations may be used to create nomographs showing the interdependence among the parameters and the dispersivities. Figures 6.33 and 6.34 show these nomographs and the data used to create the empirical equations they depict. Far from the cloud of data points, little confidence should be placed in these curves as they represent significant extrapolation. These graphs reinforce the earlier discussion that the longitudinal dispersivity is controlled largely by conductivity variance, while lateral dispersivity is controlled more by correlation length. These tendencies are physically consistent with the ideas presented in Chapter 3. Lateral dispersion is caused primarily by flow division and longitudinal dispersion is caused primarily by travel-time variation. The degree of separation by flow division is

governed by the lengths of the throats. Travel-time variation results from differences in individual throat conductivities.

These relationships mean that, to get very small lateral dispersivities seen in nearly homogeneous materials, the correlation length must be very small. This implies that the average connection spacing must also be small and the resolution must be high. This is true for continuous discretization schemes (such as finite elements or finite volumes) as well. For these schemes, numerical smearing of the plumes may overwhelm small values of physical dispersion unless much resolution is employed.

Longitudinal and lateral dispersivities measured from field tracer tests or interpreted from contaminant plume growth rates are used to select the appropriate conductivity deviations and correlation length from the nomographs. Knowing these, the throat conductivity variation used in network generation is simply the square of the standard deviation.

The average connection spacing must be set to provide adequate spatial resolution in the domain, permit a reasonable number of throats beneath the correlation length, and not exceed a tolerable limit on the number of connections to be simulated for the given computational resources. The average connection spacing, s , defines the number of connections by

$$N_c \approx \frac{V_d}{s^n}. \quad (6.40)$$

where V_d is the volume of the simulation domain in three dimensions, the area of the simulation domain in two dimensions, or the length of the simulation domain in one dimension.

Coordination numbers should be about 8 in two dimensions and 11 in three dimensions to adequately represent the possible throat orientations and approximate isotropy. These requirements increase as the conductivity variance increases. Average coordination number may be estimated

$$\overline{CN} = \frac{2N_t}{N_c}, \quad (6.41)$$

where \overline{CN} is the approximate average coordination number, N_t is the number of throats in the domain, and N_c is the number of connections in the domain. The network model will function with smaller coordination numbers, but our ability to anticipate behavior is lessened. When coordination numbers are small the discreteness of the medium can 'jump' scales. That is, the medium begins to 'see' a minimum discrete scale that is larger than the average connection spacing. It behaves as though it were a coarser network. To ensure these desired coordination numbers,

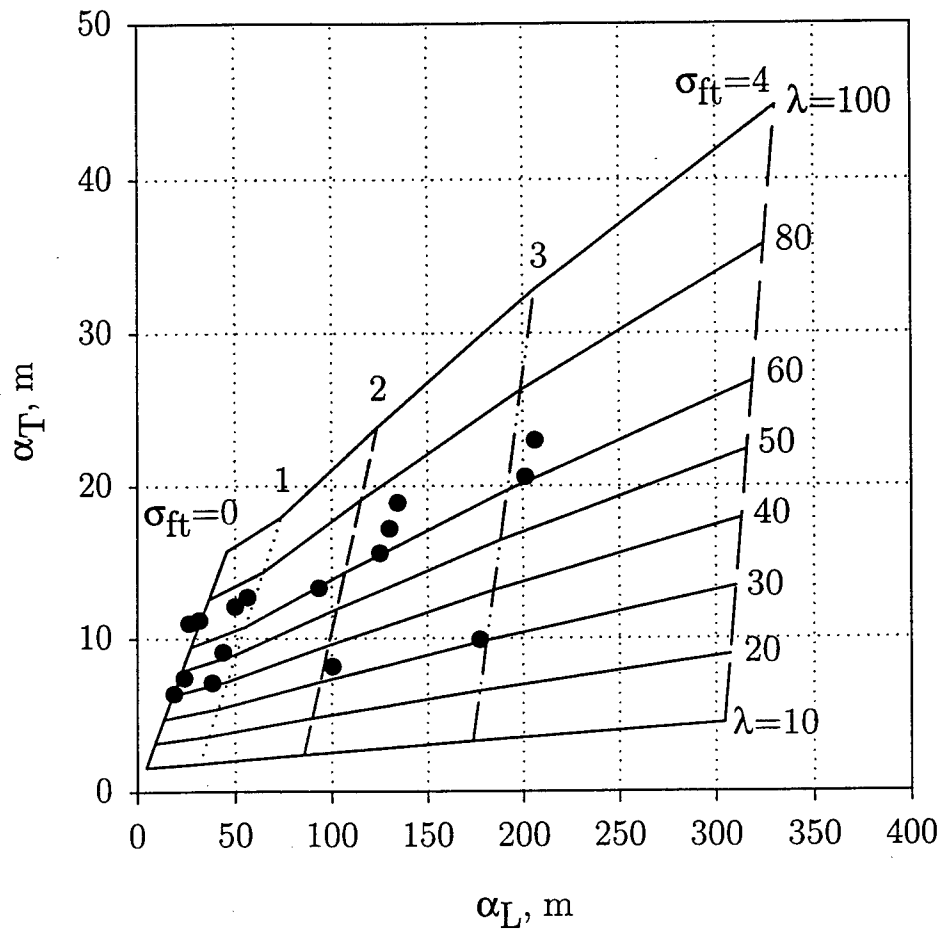


Figure 6.33: A nomograph for asymptotic, apparent dispersivity in two-dimensional networks.

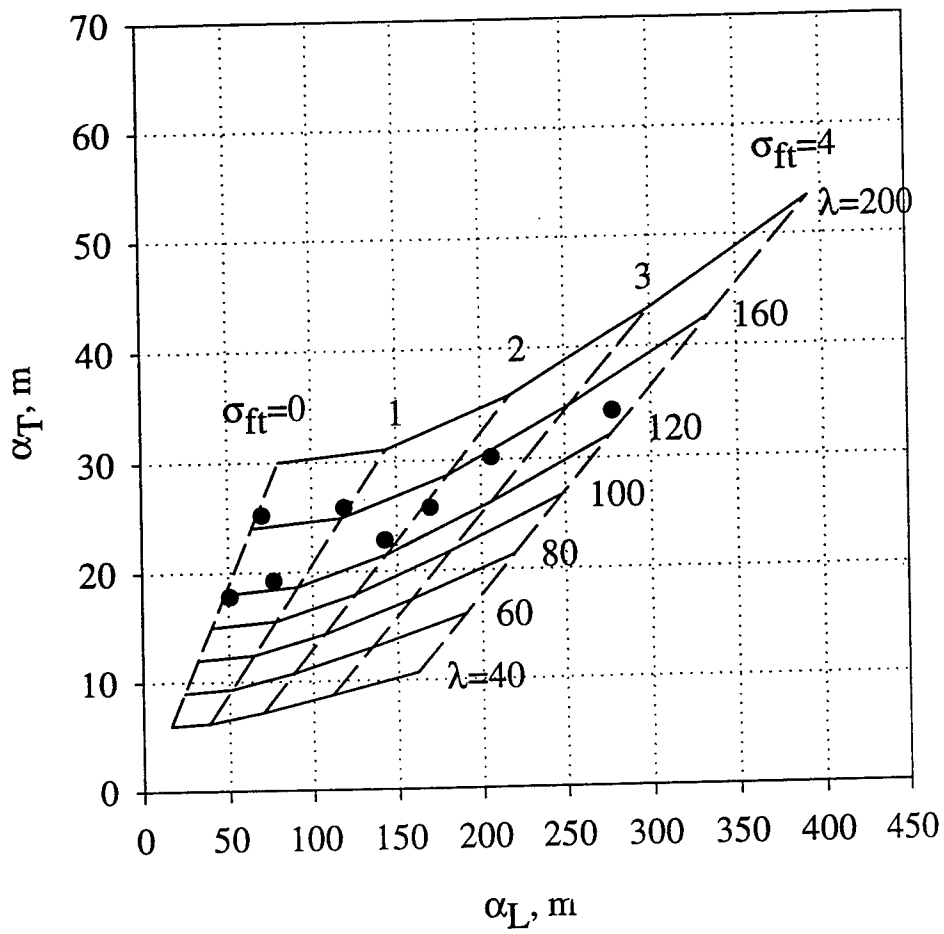


Figure 6.34: A nomograph for asymptotic, apparent dispersivity in three-dimensional networks.

the average connection spacing should not exceed about two-thirds the correlation length. Therefore, the average connection spacing should be the minimum of the spacing needed for resolution or two-thirds the correlation length.

Knowing the average connection spacing, a minimum connection spacing must be provided for random connection placement. A minimum spacing of about 60 percent of the average is usually a good value. This minimum is easy to produce when generating random numbers and does not restrict the time step unduly. As the minimum spacing approaches the average spacing, we must generate very many random numbers before finding a satisfactory connection distribution. If the connections are distributed in a spatially-regular fashion (as with a structured grid), the minimum spacing is not required.

The maximum throat length and probability decay functions must be assigned. If the average connection spacing and the correlation length are separated by a factor of 3 or more, the probability decay function should be used to establish the correlation length. This will encourage better local connectivity with enough longer throats to produce the desired correlation length. In this case, one third the desired correlation length should be used for the probability decay function and the maximum throat length should be set to some value larger than the correlation length (perhaps 1.5 times the correlation length).

If the average connection spacing and correlation length are not separated by a factor of 3, added emphasis on local connectivity is probably not needed. Therefore, the maximum throat length may be set to the correlation length and the decay parameter may be set to some large value (perhaps the correlation length or larger). Finally, the number of throats should be chosen to achieve the desired coordination number using Equation 6.41.

6.4.3 Matching Effective Conductivity.

At this point, the throat topology has been established and the required throat conductivity variance is set. The mean throat conductivity, μ_f , must be computed to produce the desired effective conductivity. Topology and conductivity variance fix the dispersive character of the network. Changing μ_f does not affect apparent dispersivities. Therefore, the network generator uses a reference value for μ_f and the defined network topology to compute the geometric mean of the patch conductivities and the variance in patch conductivities. These quantities are used in Gelhar's small perturbation expression (Equation 6.3) to compute an interim effective conductivity, K_c . A revised μ_f is computed by linear scaling of the computed and desired effective

conductivities,

$$\mu_f = \ln \left(e^{\mu_r} \frac{K_e}{K_c} \right) \quad (6.42)$$

where μ_r is the reference mean ln conductivity (usually 0), and K_e is the desired effective conductivity, [LT^{-1}]

When direct effective-conductivity measurements are not available, a tracer plume's movements may be used to estimate conductivity of the medium. From the tracer motion, the *instantaneous* speed of the plume's centroid is needed. Dividing the total travel distance of the plume by the arrival time of the peak concentration provides an *average* velocity. This velocity may be significantly different than the bulk seepage velocity and the asymptotic plume speed. A plume's speed only approaches the bulk seepage velocity in the asymptotic limit. Therefore, the plume must travel great distances before its composite travel time is similar to that predicted by the asymptotic seepage velocity and the distance traveled. Ideally, two late-time images of the plume could be used to provide a more representative velocity measurement.

With an estimate of the asymptotic plume speed, we may compute a corresponding effective conductivity. Equation 6.29, predicts the effective porosity from the volumetric porosity and throat conductivity variance. This effective porosity relates bulk seepage velocity to a composite Darcy flux. With an estimate of the head gradient from pressure contours, an effective conductivity may be computed using this Darcy flux. Then, mean throat conductivity may be computed as before.

6.4.4 Matching Porosity.

Estimates of volumetric porosity may be extracted from core samples, from tracer experiments, or, lacking other data, from literature values based on classification of material in the boring logs. In its present form, the network model defines porosity as a constant value for the domain. Porosity of the network is controlled by a single value, the cross-sectional area of the throats (A_T). This same value for cross-sectional area is applied to all throats in the domain. The volume of each throat is simply the throat length multiplied by A_T . Therefore, this cross-sectional area may be scaled to match the desired porosity. The network topology must be defined before this scaling can be performed. Throats in the network are created with a nominal cross-sectional area and their volumes are accumulated. A_T is computed as follows.

$$A_T = \frac{A_0 \phi V_d}{\sum_{m=1}^{nthroats} V_m} \quad (6.43)$$

where A_T = modified cross-sectional area i , [L^2],
 A_0 = reference throat cross-sectional area (chosen to be 1), [L^2],
 ϕ = desired volumetric porosity, [-],
 V_d = volume of the simulation domain, [L^3], and
 V_m = original volume of throat m , [L^3].

For spatially variable porosity, a similar scaling could be performed in subregions over which the porosity might be assumed constant. Or, a more realistic representation of porosity may be obtained by assigning porosity to individual throats in a stochastic manner. Hassan and Cushman [59] demonstrate that non-uniform porosity dramatically affects transport behavior.

6.4.5 Application of the Conditioning Procedure.

The following steps summarize the procedure for creating isotropic networks to match macroscopic parameters

- Use the desired longitudinal and lateral dispersivities and Figures 6.33 and 6.34 to estimate correlation length and throat conductivity deviation.
- Set the average connection spacing based on the desired correlation length, desired spatial resolution in the results, and available computational resources.
- Set the decay parameter and maximum throat length to match the choices of correlation length and average connection spacing.
- Select the desired number of throats to ensure an adequate coordination number.
- Obtain the desired effective conductivity in one of two ways,
 - directly from a field test or other measurement, or
 - from an estimate of instantaneous plume speed in the asymptotic regime, a computed effective porosity, and an estimate of the average head gradient.
- Set the volumetric porosity to match observations, modified to account for effective versus total porosity.

This procedure for network generation was followed to create and evaluate a two-dimensional and a three-dimensional network. Table 6.4.5 shows the requested properties, the network parameters, and the measured macroscopic properties after simulating flow and transport.

Table 6.4: Examples of conditioned networks.

	2-D Networks	3-D Networks
Desired Properties		
Apparent Dispersivities (m)	105 / 20	150 / 18 / 18
Asymptotic Plume Speed (m/d)	1.5	1.0
Computed Parameters		
Correlation Length (m)	90.	85.
Standard Deviation in $\ln K_t$	1.8	2.9
Variance in \ln Throat Conductivity	3.2	8.4
Effective / Volumetric Porosity	0.97	0.66
Average Connection Spacing (m)	25.	55.
Maximum Throat Length (m)	100.	85.
Probability Decay Parameter (m)	30.	9,999.
Effective Conductivity (m/d)	1.45	0.66
Resulting Properties		
Average Coordination Number	9.5	8.8
Mean \ln Throat Conductivity	0.587	-0.538
Darcy flux (m/d)	1.61	0.57
Asymptotic Plume Speed (m/d)	1.76	0.81
Asymptotic Dispersivities	95.0 / 15.6	157.7 / 21.4 / 17.7
Number of Connections	5,991	33,555
Number of Throats	28,430	147,799

The resulting media produced dispersivities that were very near the requested values. Observed asymptotic plume speeds were reasonably close to those requested. The speed was overestimated in the two-dimensional case and underestimated in the three-dimensional case. In the three-dimensional case, the coordination number was allowed to dip beneath the recommended value to conserve computation time. This fact is probably responsible for the discrepancy between the desired and observed plume speeds. This three-dimensional network contains almost all possible throats shorter than the prescribed correlation length. Therefore, the coordination number cannot be increased significantly without decreasing the average connection spacing. If, after this process is completed, the resulting macroscopic properties are not close enough to the desired properties, the input parameters may be adjusted.

6.5 Creating Networks From Laboratory-Scale Observations

When asymptotic, macroscopic properties are not available, the network must be created to honor small-scale observations. These observations may consist of many 'point' values of conductivity taken from soil borings. A very different procedure is followed to generate the network. The two basic steps are:

- define large scale stratigraphy or hydrogeologic units, and
- define statistical distributions for use within each distinct hydrogeologic unit.

6.5.1 Hydrogeologic Units.

The medium cannot be known wholly, but the hydrogeologic units that comprise the study area may be delineated with some confidence. The philosophy employed in this modeling approach is that, when possible, large scale structure in the medium is established deterministically. Structure that exists beneath that scale is introduced statistically. At sites with very little information, perhaps no distinct units may be identified and all structure must be entered statistically.

Boring logs or penetrometer tests define contacts that separate hydrogeologic units. The lateral extent and continuity of these strata may be estimated by intelligent interpolation using 'soft' information such as depositional environments. Point measurements may be analyzed statistically to determine distinct populations. The resulting soil type maps are assigned to a material mesh consisting entirely of tetrahedra.

6.5.2 Sub-Unit Statistical Distributions.

Throats will be generated and throat properties will be assigned based on membership in a particular hydrogeologic unit. The statistical pools from which throat properties are chosen are assumed not to change within a unit. The quantities to be determined for each soil type are:

- probability decay parameter for throat creation,
- mean ln throat conductivity, and
- variance in ln throat conductivity.

By design, the probability decay function is similar to an exponential semi-variogram for conductivity. The two functions describe the same physical property, the spatial persistence of a given value of hydraulic conductivity. If ample point measurements are available within a soil type, a semivariogram may be fit to the data [73]. A semivariogram model (Figure 6.35) is used as a measure of spatial persistence of a particular property (e.g., conductivity). The variogram for hydraulic conductivity is given by

$$\gamma(\xi) = \frac{1}{2n} \sum_{i=1}^n [K(x_i + \xi) - K(x_i)] \quad (6.44)$$

An exponential model to describe the semi-variogram is

$$\gamma(\xi) = \zeta + \sigma_k^2(1 - e^{-\xi/a}) \quad (6.45)$$

where ζ is the nugget and the sill or asymptote is the variance of conductivity, σ_k^2 . The range of the semivariogram is the principal correlation length. For the exponential model, the range is approximately $3a$ [35]. Thus, the probability decay parameter is approximately equal to a in the semi-variogram model. Given the correlation length, the average connection spacing may be computed as before.

If all that is known about a medium's structural scales is that they are larger than the measurement of interest, the correlation length may be assigned some large number. Plume growth will follow the appropriate trend in the pre-asymptotic regime and an asymptote will not be reached. The maximum throat length should be selected as some number larger than or equal to the correlation length, permitting the correlation length to be enforced by the decay parameter.

All fluid must pass through the connections. Therefore, the connection or patch conductivities describe the conductance of the network. It follows that point observations of conductivity should be considered equivalent to patch-averaged conductivity in the network. The mean sample conductivity must be converted to estimate

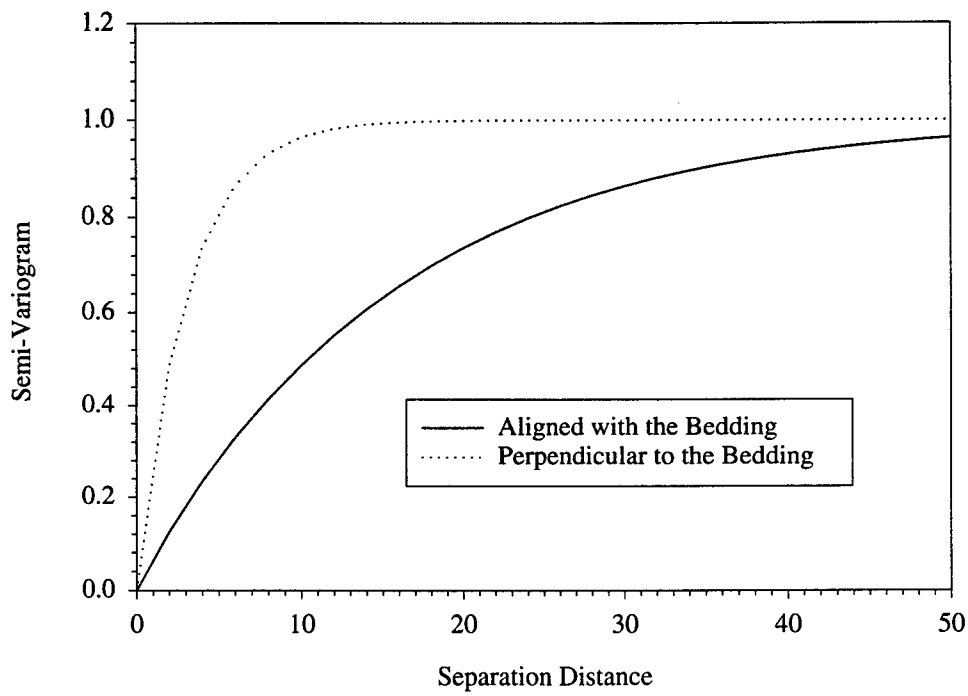


Figure 6.35: An example, exponential semi-variogram for hydraulic conductivity.

the necessary throat mean conductivity. This conversion must account for orientation of the throats. The topological anisotropy in the network is summarized by the 'material tensor'. This tensor is computed by assigning a unit scalar conductivity to each throat and computing the volume average of the orientations. With a unit throat conductivity, Equation 6.6 reduces to

$$N_{ij} = \frac{\sum_{t=1}^{CN} n_i n_j V_t}{\sum_{t=1}^{CN} V_t}. \quad (6.46)$$

As the coordination number increases in an isotropic network, this tensor approaches a diagonal tensor with values of $1/n$ in the diagonal entries, where n is the spatial dimension of the problem. Thus, for an isotropic network, in three dimensions,

$$[N] = \begin{pmatrix} \frac{1}{3} & 0 & 0 \\ 0 & \frac{1}{3} & 0 \\ 0 & 0 & \frac{1}{3} \end{pmatrix},$$

and in two dimensions,

$$[N] = \begin{pmatrix} \frac{1}{2} & 0 \\ 0 & \frac{1}{2} \end{pmatrix},$$

and in one dimension,

$$[N] = 1. \quad (6.47)$$

To impose the effect of orientation, the observed mean may be multiplied by the inverse of the material tensor to estimate the necessary mean throat conductivity,

$$\mu_f = ln \left(\frac{b \mathbf{N}^{-1} e^{\mu_m}}{\phi} \right) \quad (6.48)$$

where μ_m is the mean of the measured conductivities for this soil type, $[LT^{-1}]$ and b is a coefficient that accounts for local anisotropy. For a medium that is globally isotropic (or nearly so), the inverse material tensor is equivalent to multiplying by the dimension of the problem.

$$\mu_f = ln \left(\frac{b n e^{\mu_m}}{\phi} \right) \quad (6.49)$$

In the limit of infinite coordination number, b is 1.0. For the coordination numbers tested here, this coefficient appears to be about 1.15. For example, in an isotropic, two-dimensional network, the mean of the throat conductivities should be

about twice the mean of the patch conductivities divided by the porosity. Throat conductivity variance must be set to provide comparable variability in the velocities between the network and the soil. Thus, the network and the soil should have similar conductivity variances. Perhaps the installed network variance should be reduced slightly to account for velocity variance caused by orientation. This orientation-based velocity variance was observed in these tests to be less than 0.25.

The number of throats and number of connections are set as they were before. Creating these networks similar to unconditional simulation in geostatistics [35]. This process creates equally-probable realizations of the medium, but does not include the ability to enforce conductivity at a particular point in the domain. Monte Carlo simulation is needed to assess risk and estimate uncertainty. Because this network-generation process does not attempt to match effective, macroscopic properties, the approach is not restricted to isotropic networks. This procedure for generating networks from small scale observations is offered as an untested guide based on accumulated experience and observations from the model.

6.6 Conclusions

Existing theory for predicting effective conductivity was shown to provide acceptable results for a wide range of network configurations and conductivity variability. Empirical equations were needed to describe normalized distributions of velocity and velocity-position correlation that comprise an alternative form of the definition of dispersivity. When combined, these empirical expressions predict well the asymptotic longitudinal and lateral dispersivities for the networks tested.

If asymptotic, macroscopic estimates of effective conductivity or apparent dispersivity are available, networks may be created to provide these desired properties with little or no trial-and-error. This process was demonstrated to be reasonably accurate for both two- and three-dimensional networks. Asymptotic conditions cannot be predicted on the basis of correlation length alone. Conductivity variance must also be considered. Correlation length is important for establishing apparent lateral dispersivity and may dictate the minimum resolution required for a simulation.

Chapter 7

Detailed Analysis of Flow and Transport Behavior in A Macroscopic, Discrete Network Model of Porous Media

Abstract

Fluid flow and conservative tracer migration through stochastic, discrete networks are analyzed in detail. Network simulations are compared to known behavior, analytical solutions (where appropriate), experimental observations, and behavior of continuum-based models of groundwater flow and transport. Fluid flux through the network obeys a Darcian relationship in a macroscopic sense. Therefore, network results compare well with analytical solutions and continuum-model solutions for steady and transient Darcian flow through homogeneous media. Further, the network is shown to honor fluid-flux and head-gradient relationships observed in laboratory experiments conducted by the University of Colorado [70, 51].

Transport of a conservative tracer through the network is shown to be consistent with historical evidence of Gaussian concentration distributions in porous media. However, the network results are not fully consistent with advection dispersion theory. Differences between the two theories are discussed. The network demonstrates an ability to model observed transport in laboratory experiments with acceptable accuracy. The network also produces reasonable, but unverified behavior for density-dependent fluid flow.

Chapter 5 presents an alternative approach for simulating flow and transport through porous media that is based on stochastic discrete networks. These networks are created by mapping the volume of porous material into many, interconnected, one-dimensional conduits. These conduits (called throats) should not be confused with individual pores in a porous medium. This representation is intended at a much larger scale. The throats could be imagined as a well-connected system of fractures within an impermeable matrix. Thus, instead of mapping a fracture system to an equivalent porous medium [118], this approach maps a porous medium onto an equivalent fracture network.

Chapter 5 shows the network model's ability to reproduce the apparent scale effect in dispersivity and physically-correct, wholly-downstream tracer migration in the absence of diffusion. Chapter 6 demonstrates a procedure for creating discrete networks to display desired macroscopic properties. Here, we provide a more detailed evaluation of flow and transport behavior in the network and compare network results to observations in real porous media. The comparisons will be grouped into three categories,

- steady and transient saturated fluid flow,
- conservative transport in steady, saturated flow,
- density-dependent and variable viscosity flows.

Comparisons include documented analytical solutions for steady and transient flow through porous media and laboratory observations of fluid flux through homogeneous and heterogeneous experimental packings [70]. Network predictions for conservative transport are assessed for their consistency with known tracer transport behavior and are compared with advection-dispersion-theory predictions. Density-dependent flows are computed with the network model and assessed qualitatively.

7.1 Saturated Fluid Flow

Throats meet and exchange mass at connections that are assumed to contain no volume. Each throat in the network conducts fluid as a homogeneous porous material. Therefore, at low Reynolds' number, flux, q , through each throat is described by a one-dimensional Darcy's law (for example, [33])

$$q \propto \frac{\Delta H}{\Delta l} \quad (7.1)$$

where H is the total head, $[L]$, and l is the position along the throat, $[L]$. The constant of proportionality is the scalar hydraulic conductivity for that throat, $K_t, [LT^{-1}]$.

Adopting a larger view, the network is simply a coarse porous medium consisting of many flow paths (throats), not unlike the pore-scale structure. At this larger scale, bulk fluid flux through this coarse medium may be related to applied gradients in total head. It is not surprising that, when viewed in a spatially-averaged sense, the network also obeys a Darcy-like law for fluid flux. This result is shown analytically by Peters [108].

Because the discrete network produces a macroscopic approximation of Darcy flow, the network and traditional, discretized-continuum models approximating the Darcy flow equation yield similar results. In fact, one could easily construct a network and a finite difference approximation having identical coefficient matrices for solving the global head solution. Obviously, solving the same linear system results in the same total head field for both approaches. Network structures containing longer-range connectivity lead to coefficient matrices with additional entries, but the fundamental behavior of the macroscopic head field is similar. Thus, flow through discrete networks, like flow through discretized continua, should approach macroscopic, analytical solutions for Darcian flow through homogeneous media. To demonstrate the behavior of fluid flow in the network, some example problems are solved for both steady and transient flow.

7.1.1 Analytical Solutions for Steady, Saturated Flow

Steady, Darcy flow equation may be solved analytically for simple boundary conditions and homogeneous media (for example, [46]). For example, steady flow in a confined aquifer bounded by parallel ditches produces a linear distribution of piezometric head between the two, known water levels at the ditches. To examine this case, a network consisting of 1000 randomly positioned connections and 5000 throats lying in an $x - y$ plane was constructed. Constant total heads of 120 m and 100 m were applied at $x = 0$ and $x = L$, respectively. Solid boundaries were installed at $y = 0$ and $y = L$. Because of symmetry in y , the boundaries in y are equivalent to infinite domain and the problem is, effectively, one dimensional. Figure 7.1 shows a plan view of the contours of the piezometric surface from the network simulation and a plot of network results (along a line $y = L/2$) versus the analytical solution. The network results were averaged to a uniform 51- x 51-node visualization mesh for interpretation. Agreement is generally very good. Near the boundaries, a slight effect from averaging can be seen. Averaging becomes one-sided near the boundaries, causing an apparent underprediction at the upper end and an apparent overprediction at the lower end for this planar solution.

Another well-studied analytical solution is steady flow to a well in a confined aquifer [33]. The simplest solution is for a well at the center of circular island. The

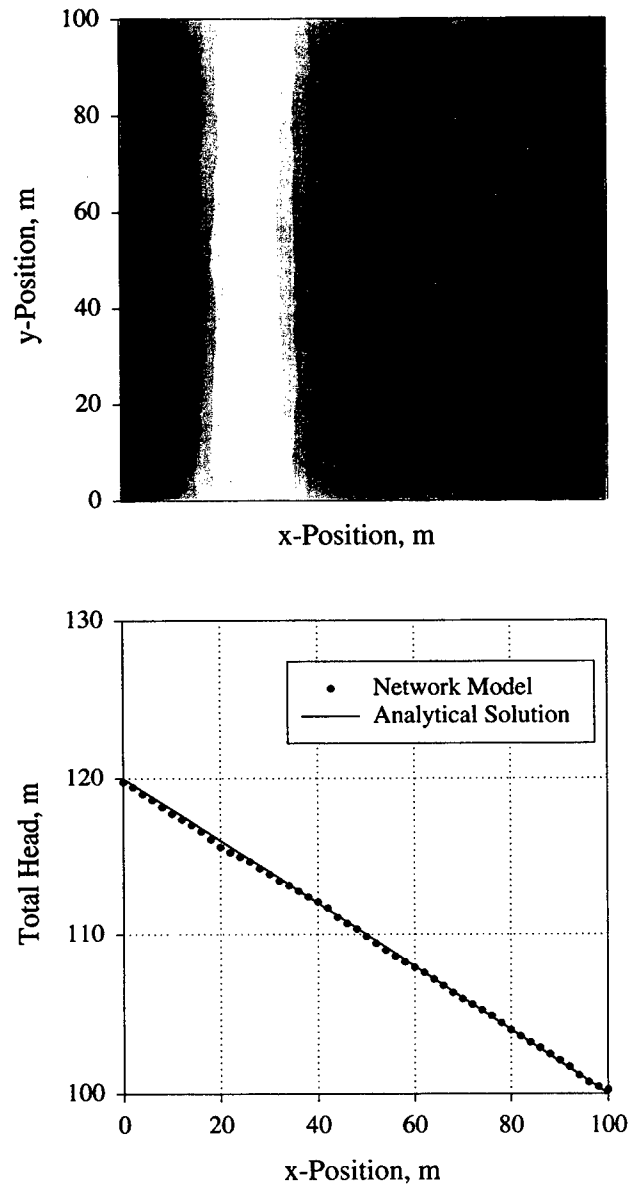


Figure 7.1: Steady flow between two ditches in a confined, homogeneous aquifer. Contours of the piezometric surface (top) and cross-section comparing network results and the analytical solution for Darcy flow (bottom).

well is screened over the entire depth of a constant-thickness, homogeneous, confined aquifer. This solution is Theim's formula,

$$h_0 - h = \frac{Q}{2\pi KB} \ln \frac{r_e}{r} \quad (7.2)$$

where h_0 = fixed head on the boundary, $[L]$,
 h = piezometric head, $[L]$,
 Q = volumetric flow rate through the well, $[L^3T^{-1}]$,
 K = saturated hydraulic conductivity, $[LT^{-1}]$
 B = thickness of the aquifer, $[L]$,
 r_e = distance from the well to the island boundary, $[L]$, and
 r = radial position from the well, $[L]$.

In truth, Theim's formula is only valid when fixed head is applied on the boundary (the well-in-an-island problem). However, in an infinite aquifer, drawdown ($h_0 - h$) would be very small at some large radius because the flow is converging. As radius increases, the area of the face of an imaginary cylinder increases, while the total flow rate through this face remains constant. Therefore, the specific flux and the head gradient diminish with r . We may use this approximate solution in an infinite aquifer to obtain an approximate head distribution in a rectangular domain by employing the method of images or superposition [33]. One simply accumulates the effects of many wells, both real and artificial, to enforce the boundary heads.

Our problem has a single pumping well at the center of a rectangular island. A single image well is needed across each boundary to inject fluid at the same rate the real well withdraws it, thus creating offsetting effects and no drawdown along the boundaries. However, each of these image wells requires another image well to offset its effects on the far boundary. Thus, the series is infinite, but converges. This process was used to create an approximate analytical solution for this problem.

The network created for the two-ditch problem was also used to simulate the well problem. A uniform, constant head was applied to all boundaries. At the center of the domain, $5 \text{ m}^3/d$ were extracted from a single connection. Figure 7.2 shows predicted head values and the analytical solution. The network-produced drawdown curve closely follows the analytical solution. As with other discrete approximations, the accuracy of the network solution near the well is a function of the resolution.

The two solutions presented, steady flow between two ditches and steady flow to a well, are simple test cases that have been used to test continuum models of Darcy flow for many years. They are given here to reaffirm that macroscopic flow in a discrete network is very similar to macroscopic flow in a discretized continuum model for Darcy flow.

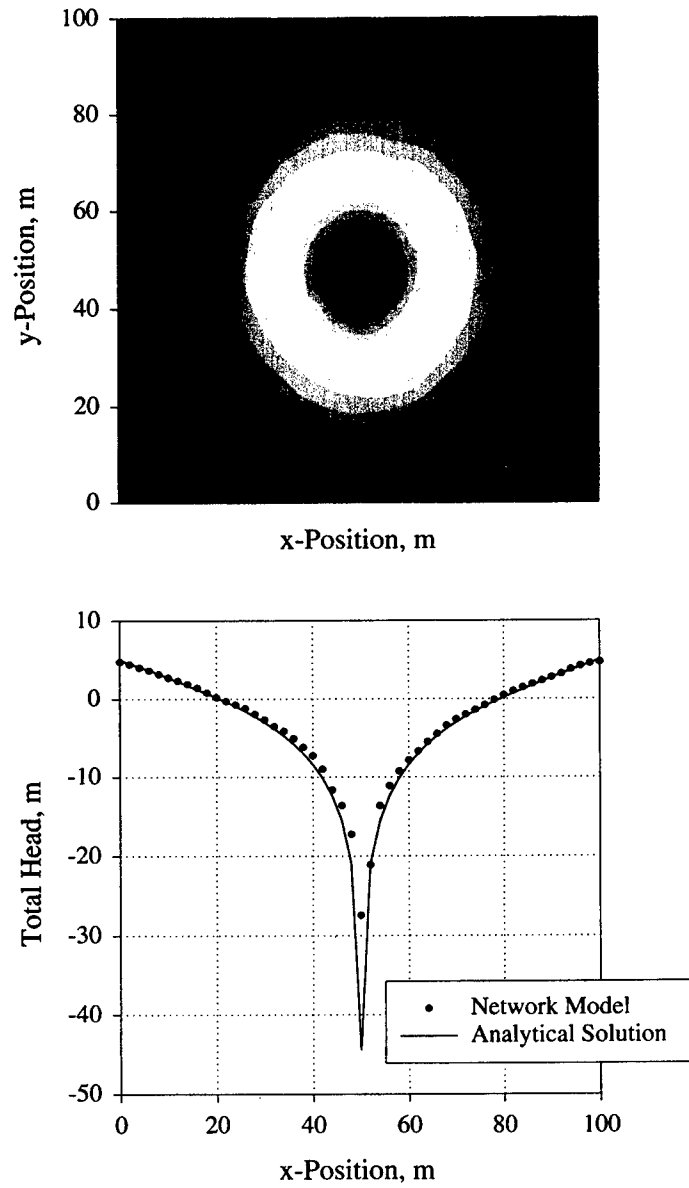


Figure 7.2: Steady flow to a well in a confined, homogeneous aquifer. Contours of the piezometric surface (top) and comparison of network results and analytical solution (bottom).

7.1.2 Comparison to Laboratory Measurements of Steady, Saturated Fluid Flow

To further explore the behavior of the network model, simulation results were compared against laboratory data collect by Illangasekare et al [70]. The testing apparatus is summarized here and is described in more detail by Illangasekare [70] and Garcia [51]. Flow aspects are discussed here. Transport for these same experiements is discussed in the next section of this chapter. The experimental device is a 244 *cm* x 122 *cm* x 6.2 *cm* horizontal tank (Figure 7.3). Fixed heads are applied to the boundaries in the longest dimension. The top and bottom boundaries and the sides are solid walls. Experiments were conducted with homogeneous and heterogeneous packings.

For the homogeneous packings, the tank was filled uniformly with a #30 sand. The saturated hydraulic conductivity and volumetric porosity of this sand were determined in separate testing to be 0.116 *cm/s* and 0.47, respectively [51]. The ends of the tank were packed with gravel to facilitate an even application of the constant head boundary conditions. The gravel, estimated by Garcia [51] to be about 4 *cm* wide, was separated from the sand by a screen and filter material. Therefore, an effective tank length of 236 *cm* was adopted for the remainder of these comparisons.

Fluid flux through the slab was measured under steady flow conditions with fixed, different heads applied at each end of the tank. Heads were measured at 45 internal sampling ports distributed throughout the domain (Figure 7.4). The prevailing hydraulic gradient was estimated using head values measured in the sampling ports nearest the end boundaries. This measured head gradient was considered a more reliable measure than the applied head boundary conditions [70]. This gradient and the sample length were used to create appropriate boundary conditions.

Several pieces of information were needed to construct the network. These include an average interconnection spacing, a maximum throat length, the mean \ln conductivity for the throats, and the variance in \ln throat conductivity. A single material type was used to represent the sand. Because the porous slab is very thin, a two-dimensional network layout was selected.

This medium was a carefully-packed, artificially-homogeneous material. The largest characteristic lengths in this medium were estimated to be on the order of several grain diameters. Therefore, the network that best represents this medium is one that contains only short throats. Interconnection spacing and maximum throat length were set to be 2.0 *cm* and 4.0 *cm*, respectively to provide resolution comparable to a 118- x 61-node regularly-spaced mesh. The flow solution is not sensitive to the choice of these spacings. Virtually the same flow solution could be

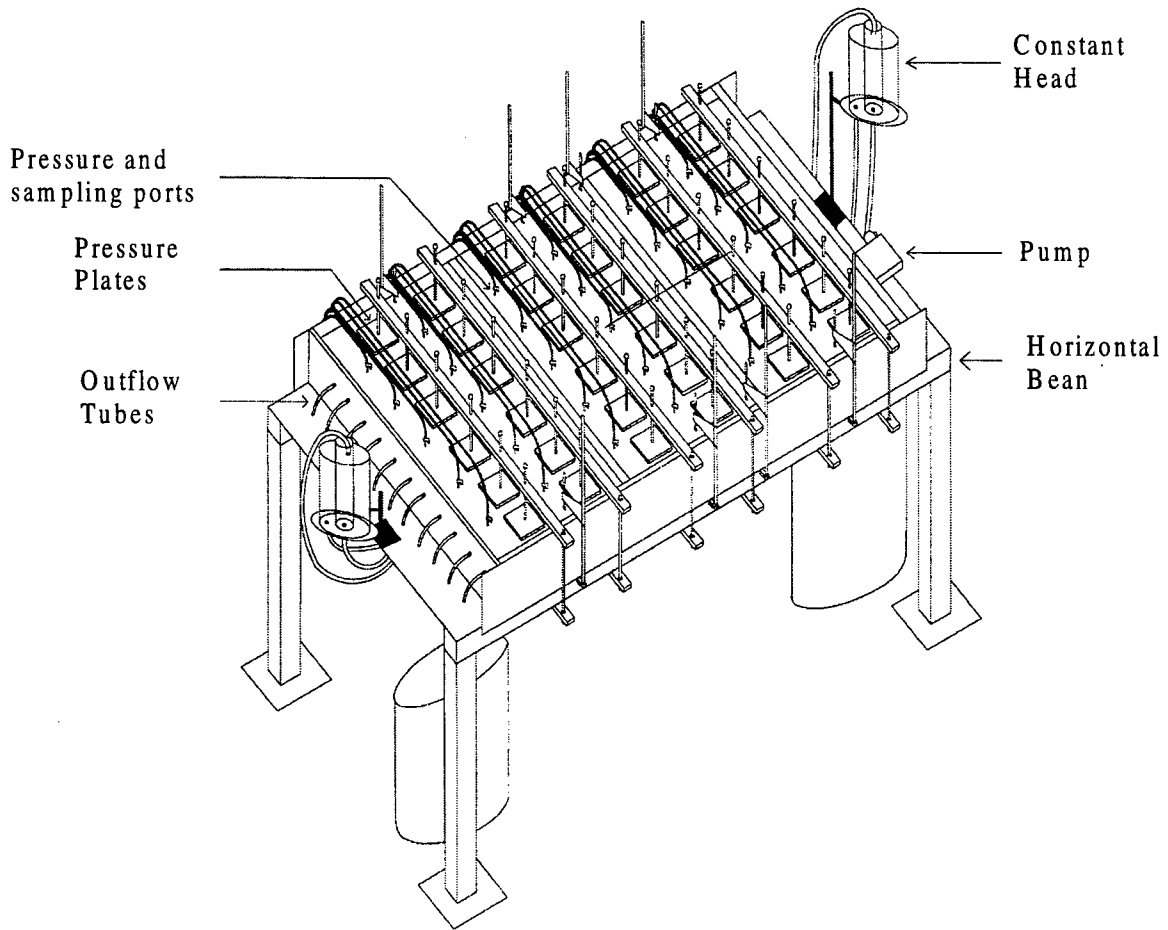


Figure 7.3: Diagram of the experimental tank at the University of Colorado (from Illangasekare [70]).

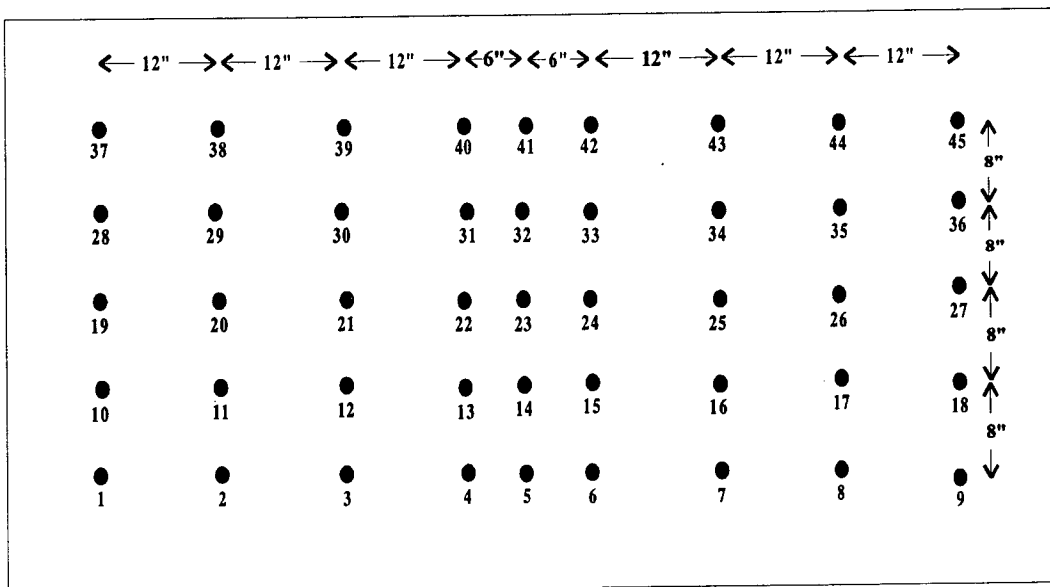


Figure 7.4: Location and numbering of the sampling ports.

obtained on a coarser network. However, transport comparisons to be discussed later reveal that, even this resolution is too coarse to describe multidimensional transport through this homogeneous material. The throat-creation decay parameter was arbitrarily set to some large number to encourage most connections closer than 4 cm to be joined with a throat. These parameter choices provided about 7,500 connections and 37,000 throats.

A small variance in ln throat conductivity (0.5) was installed to approximate local irregularities among the flow paths. Chapter 6 proposed that observed conductivities should be compared to patch conductivity values, not throat values. The following equation was provided to approximately relate mean patch conductivity to mean throat conductivity in isotropic networks

$$\overline{K}_t = \frac{nb}{\phi} \overline{K}_p \quad (7.3)$$

where n = dimension of the problem, [-],
 b = anisotropy coefficient, [-],
 ϕ = porosity, [-], and
 K_p = patch conductivity, [LT^{-1}].

The anisotropy coefficient adjusts the conductivity to account for a finite coordination number. If an infinite number of throats were represented on a patch, the patch would be perfectly isotropic. Small coordination numbers mean that there will be significant anisotropy at the patch level. As the coordination number approaches infinity, the anisotropy coefficient tends to 1. For coordination numbers near 10, this coefficient is about 1.15.

Not all void space in a porous medium is equally accessible to the flowing fluid. There are recirculation zones and local, low-permeability zones. We may separate the mobile and immobile fluids explicitly during the calculation or we may treat the immobile fluid as part of the matrix. For these exercises, the immobile fluid was treated as solid and not included in the throat volumes. Therefore, an effective porosity was needed to create the network. DeMarsily [33] offers a ratio of about 0.8 for effective to total porosity for sands. With a measured volumetric porosity of 0.48, the sand in the experiment should have an effective porosity of about 0.38. Using this porosity and the permeameter-measured conductivity for this sand (.116 *cm/s* or 6.96 *cm/min*), Equation 7.3 suggests a throat conductivity of 42.13 *cm/min*. When tested, the resulting network produced a computed, mean patch conductivity of 8.12 *cm/min* and an estimated effective conductivity of 0.13 *cm/s*.

Illangasekare et al. [70] conducted several fluid flow experiments in this homogeneous packing. Two experiments were selected for comparison to the network model. For this discussion, they will be labeled HMTE1 (homogeneous tracer experiment

1) and HMTE7 (homogeneous tracer experiment 7). The effective conductivities of the material, as packed, were experimentally estimated to be $10.65 \text{ cm}/\text{min}$ for HMTE1 and $8.51 \text{ cm}/\text{min}$ for HMTE7 [51]. Both exceeded the permeameter measurement of $6.96 \text{ cm}/\text{min}$. Observations indicated a measurable decrease in the effective conductivity of the slab with the age of the tank [51].

The constructed network medium was used, without adjustment, to compute fluid conductance. In HMTE1, the applied head boundary conditions were 55.94 cm on the right, and 49.10 cm on the left. These heads are slightly modified from those given by Garcia [51] to account for a 236 cm simulation domain. The resulting flowrate through the network was $171 \text{ cm}^3/\text{min}$. Illangasekare et al. [70] observed a flowrate of $228 \text{ cm}^3/\text{min}$. Similarly, HMTE7 was simulated with boundary heads of 67.33 cm and 65.62 cm . The computed flowrate was $42.75 \text{ cm}^3/\text{min}$ and the observed flowrate was $46.95 \text{ cm}^3/\text{min}$. The desired flux through the network was met by linearly scaling the mean value of the pre-calibration throat conductivity distribution and regenerating the network. Figure 7.5 gives observed contours of total head from Garcia [51] and those computed with the network for HMTE1. The measured and modeled heads are similar and, not surprisingly in this homogeneous medium, nearly planar.

Illangasekare et al [70] also explored flow and transport through controlled heterogeneous media. The heterogeneous packing used five sands for which the hydraulic conductivity ranged from about $6 \text{ m}/\text{d}$ to over $1000 \text{ m}/\text{d}$. The frequency of occurrence of these sands was designed to match a lognormal distribution. The tank was subdivided into 200 compartments, each $12.2 \text{ cm} \times 12.2 \text{ cm}$ and 6.2 cm deep. The cells at the ends of the tank were made smaller to permit the installation of a gravel reservoir for uniform application of boundary heads. Within each compartment, a single sand type was placed. The spatial distribution of sand types was designed by the Waterways Experiment Station and the University of Colorado using a simulated annealing algorithm from Deutsch and Journel [35]. The objective was to create a medium with long-range continuity of material properties. The variogram used to generate the packing was anisotropic with a range of about 90 cm along the tank's long dimension and about 18 cm across the tank. The realization chosen contained higher conductivity paths toward the interior of the domain to minimize the effects of lateral boundaries on transport through the sample. After creating the experimental medium, its properties were analyzed. The resulting mean conductivity in the lognormal distribution was $5.77 \text{ cm}/\text{min}$, the observed variance in lognormal conductivity was 2.86 [51], and the observed longitudinal correlation length (or range) was about 111 cm [51]. Figure 7.6 shows the distribution of sands in the domain. The gray border is a bounding box used only during network

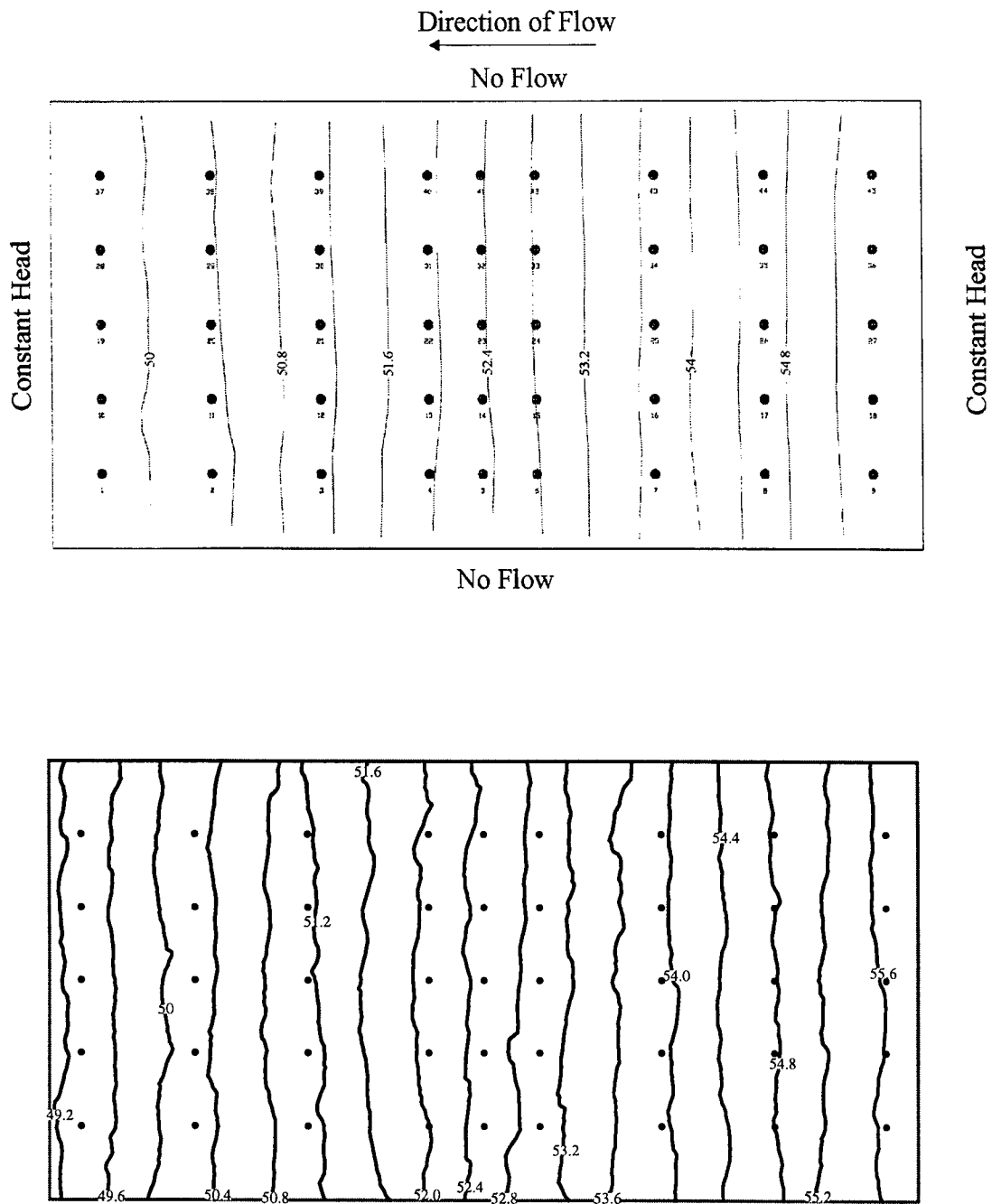


Figure 7.5: Contours of total head for the experimental tank [51] (top) and the network model (bottom) for HMTE1.

construction to avoid boundary effects and is not part of the simulation domain.

The heterogeneous experiment may be simulated by the network in two ways. Because we know the material type at each position in the domain, we may discretize the domain into many, nearly homogeneous regions and assign properties based on spatial position. Or, we may create a network using only the histogram of these material types and a measure of their spatial continuity. Taking the first approach, Figure 7.6 was used as a material mesh, defining the large-scale heterogeneity. This documents the ability to perform conditioned simulation using the network. Elements in a material mesh provide a map for assigning throat properties. Each material type points to a particular statistical distributions used for throats lying in that element. Throats that cross element-type boundaries are assigned the harmonic mean of conductivities drawn from the two conductivity distributions.

The interconnection spacing was set relatively small and maximum throat length was kept short to resolve the conductivity blocks. An average connection spacing of 3 *cm* was chosen to provide about 4 connections across the smallest material element (12 *cm*). The maximum throat length was selected to be 6 *cm* and the throat length distribution was made uniform by selecting a large probability decay parameter. Each material was assigned a small conductivity variance to represent local non-uniformity and a mean throat conductivity for each material type was computed with Equation 7.3.

An alternative method for constructing the network uses only the statistical distributions of conductivity and a measure of the characteristic lengths. Taking this approach, a single material type was chosen to represent the entire domain. Within this material type, the mean throat conductivity was computed by applying the mean from the lognormal distribution of sand conductivities, 5.77 *cm/min*, as the patch value in Equation 7.3. This suggested a distribution with a mean throat conductivity of 34.92 *cm/min*. The variance in \ln throat conductivity was assigned to be the same as the sand-type distribution, 2.86 [51]. The throat-probability-decay parameters were given by Garcia's fitted variogram, 37.2 *cm* in the longitudinal and about 7.2 *cm* in the lateral [70]. The created network was comparatively very coarse, requiring only 370 connections and about 1200 throats. This coarseness was possible because only the statistical distribution of characteristic lengths needed to be resolved. The largest characteristic length in this material is about 1 *m*. Therefore, an interconnection spacing near 10 *cm* was possible. The maximum throat length was set to be about 240 *cm* and the exponential-decay probability function determined which throats to create.

This statistical network medium had the same distribution of properties as the experimental medium, but included no information about the relative position of

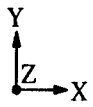
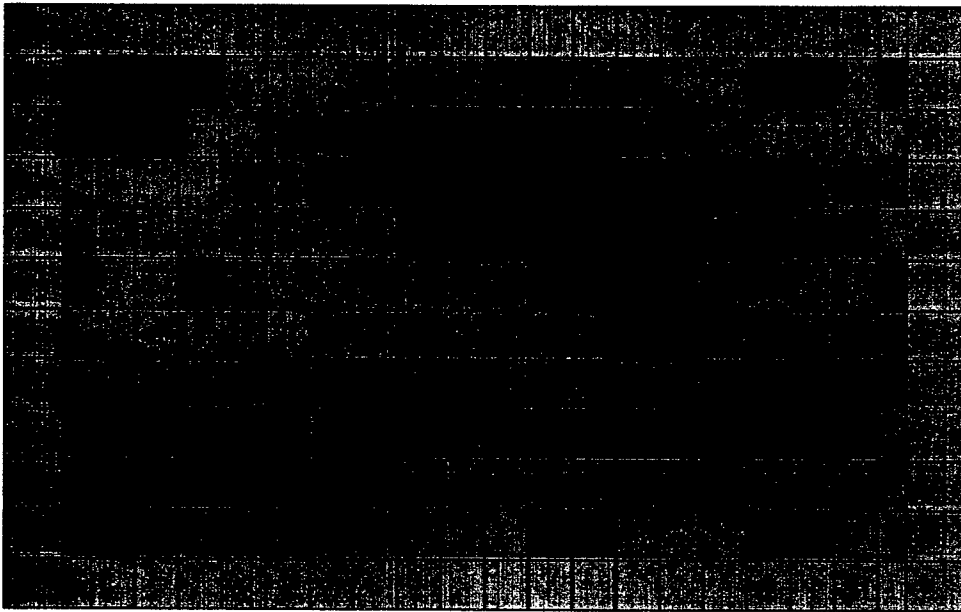


Figure 7.6: Distribution of materials in the experimental tank. Red indicates #8 sand, orange, # 16 sand, green, #30 sand, blue, #70 sand, and navy, #110 sand.

the materials. Taking this strictly statistical approach to network creation forfeits the ability to look at spatial detail inside the domain. This is evident by comparing details of conductivity. Volume-averaged conductivities are shown for the two approaches in Figure 7.7. In the network with only statistical structure, material continuity is ensured by throat lengths. This structure is not apparent when viewing connection-level average conductivities. The head distribution with statistical structure resembles a perturbed linear pressure drop, whereas the head field in Figure 7.8 contains obvious spatial structure.

Boundary heads applied to both networks were 57.03 *cm* on the right and 55.44 *cm* on the left boundaries, assuming the same 236 *cm* medium length. Contours of head for the two networks are given in Figure 7.8. Again, the internal head structure between the two network media are vastly different, but the total head drop is the same. Head values from the experiment were not available.

Observed flow through the network with explicit structure was 51.0 cm^3/min , which is very near the experimental value of 50.2 cm^3/min . Without modification, the measured flowrate through the statistical-structure network was about 100.3 cm^3/min , or nearly twice the observed flowrate of 50.2 cm^3/min . Given the 3 order-of-magnitude range of conductivity values in the individual sands, this factor of 2 seems a reasonably close pre-calibration approximation. The mean of the throat conductivity distribution was scaled to be 17.47 cm/min to match the observed flux.

The alternative network structures presented here represent the extremes. Most applications will fall between these two approaches to network creation. Large-scale stratigraphic structure may be provided by a material mesh and the remaining structure would be added statistically.

7.1.3 Transient, Saturated Flow

Transient fluid flow must account for storage in the matrix-fluid system caused by compression of the fluid and solid and by rearrangement of the matrix [46]. In continuum models, this is normally handled through a storage coefficient multiplying the time derivative in the flow equation. The fluid/matrix system is assumed to compress elastically, permitting fluids to move in and out of storage with no change in material properties (e.g., porosity). A similar approach is adopted in the network. Storage in the matrix/fluid combination is lumped into an apparent compression, greatly simplifying the model's internal accounting. The specific storage may be related to the compressibility by

$$S_s = c_p \rho g \phi \quad (7.4)$$

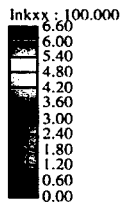
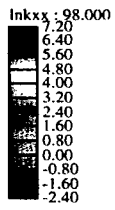


Figure 7.7: Ln-transformed, connection-averaged conductivity contours for the network with explicit structure (top) and the network with statistical structure (bottom).

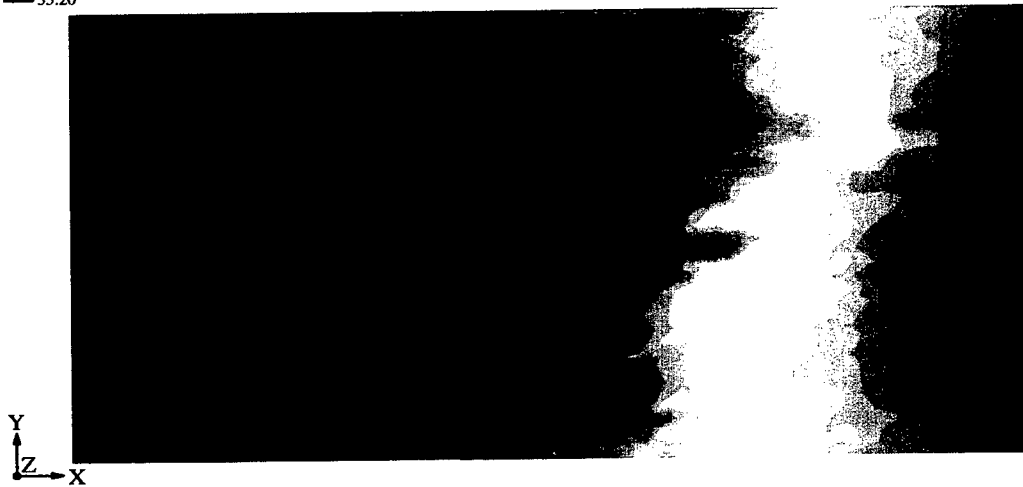
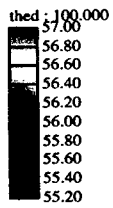
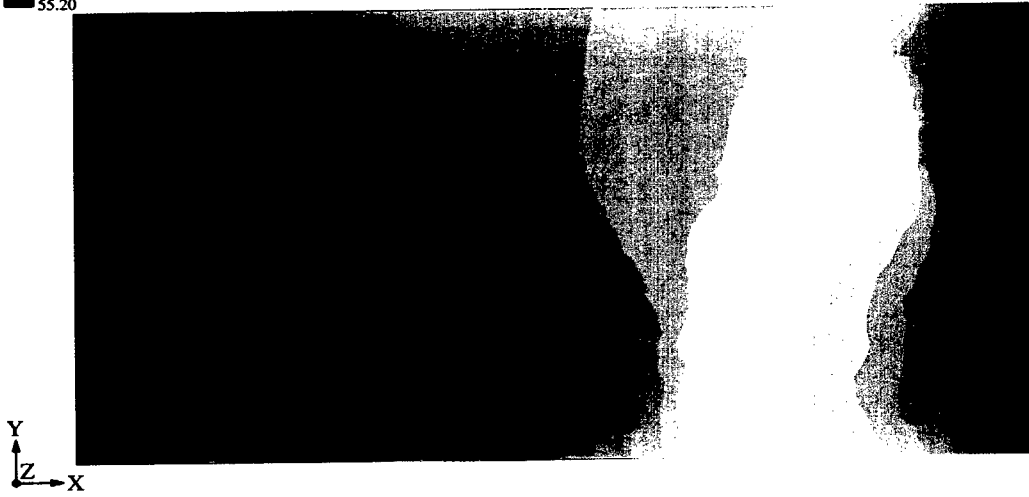
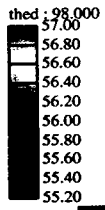


Figure 7.8: Computed head fields with the heterogeneous packing.

where S_s = specific storage, $[L^{-1}]$,
 c_p = apparent compressibility, $[T^2LM^{-1}]$,
 ρ = fluid density, $[ML^{-3}]$, and
 g = gravitational acceleration, $[LT^{-2}]$.

With this knowledge, transient flow through the network may be compared with transient, Darcian flow through saturated porous media. There are several analytical solutions for transient, Darcian flow, including the two problems chosen here, transient flow to a well and a traveling pressure wave. The Theis solution describes transient flow to a well in an infinite domain (for example, [33]).

$$h(r, t) = \frac{Q}{4\pi KB} \int_{1/u}^{\infty} \frac{e^{-\tau}}{\tau} d\tau \quad (7.5)$$

$$u = \frac{4Kt}{r^2 S_s} \quad (7.6)$$

where h = total head, $[L]$,
 Q = pumping rate, $[L^3T^{-1}]$,
 K = hydraulic conductivity, $[LT^{-1}]$,
 B = aquifer thickness, $[LT^{-2}]$,
 t = time, $[LT^{-2}]$, and
 r = radial distance from the well, $[L]$.

The network simulation was performed in a square, bounded domain, and the method of images was used to estimate the analytical solution (Figure 7.9). The network reproduces this snapshot of transient growth of a cone of depression with reasonable accuracy. The transient head at a point 20 m from the well is examined in Figure 7.10. For elapsed time larger than 4 days, the comparison between analytical and network solutions is very good. For elapsed time less than 4 days, the network predicts early arrival of measurable drawdown. The network is a coarse discretization of the medium, while the analytical solution assumes a perfect continuum. The discreteness of the network tends to smear the large spatial gradients in head seen in the first 4 days. Similar effects should be expected with most discrete approximation to diffusion-like equations.

The network model was used to simulate a traveling pressure wave in a confined porous medium of uniform thickness. Initially, total head is uniform throughout the domain. At time 0.0, a step change in the pressure is applied to one boundary. This pressure discontinuity propagates through the domain and degenerates. In a semi-infinite domain, the solution is given by

$$h(x, t) = h_i + h_b \operatorname{erfc} \left(\frac{x S_s^{1/2}}{2(Kt)^{1/2}} \right) \quad (7.7)$$

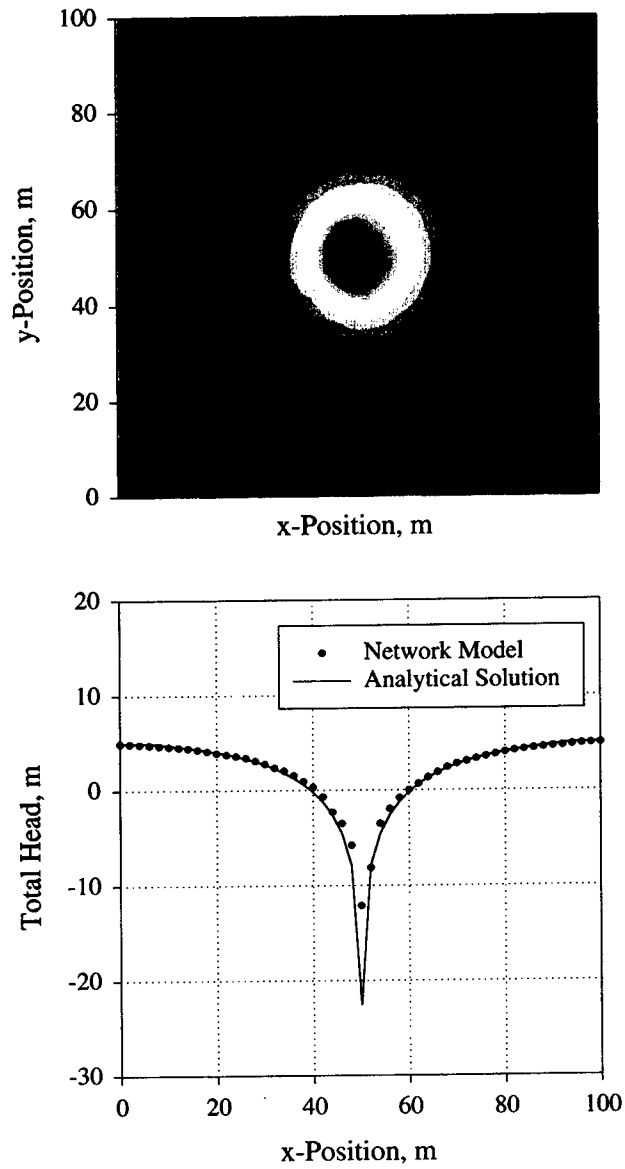


Figure 7.9: Transient flow to a well in a confined, homogeneous aquifer. Contours of the piezometric surface (top) and comparison of network results and analytical solution (bottom) for an elapsed time of 15 days.

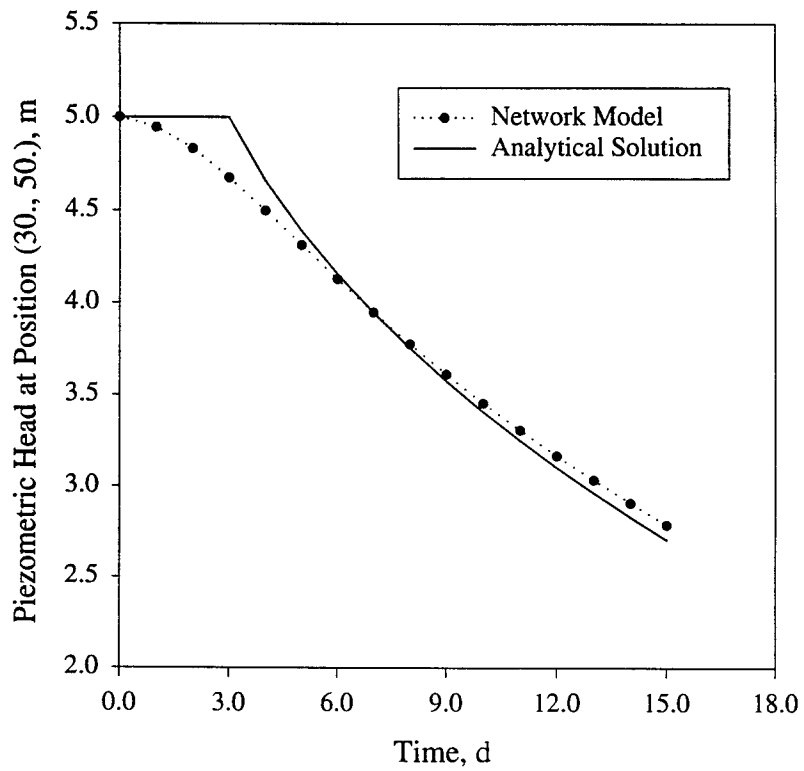


Figure 7.10: Comparison of network simulation and analytical solution at a fixed position for transient flow to a well in a confined, homogeneous aquifer.

where h_i = initial, uniform total head, $[L]$,
 h_b = step increase in total head, $[L]$, and
 x = position from the boundary, $[L]$.

If we examine travelling pressure wave early in its motion, the downstream boundary will see only a small effect, and the semi-infinite solution is an acceptable approximation. Figure 7.11 shows the network results and the analytical solution for the traveling wave at a time of 12 days. The agreement is acceptable, but the numerical simulation consistently lags behind the analytical solution.

These comparisons confirm that the network model matches analytical solutions of Darcy flow, experimental observations, and continuum numerical model descriptions. The computational effort required to solve the network should be comparable to explicit, continuum numerical models with nodal resolution similar to the connection spacing. Thus, there is no significant advantage or disadvantage associated with the network for saturated flow simulation.

7.2 Conservative Transport in Steady, Saturated Flow

Historically, conservative transport through porous media has been represented by the advection-dispersion equation (ADE) that describes a mean translation and a diffusive spreading of tracer

$$\frac{\partial c}{\partial t} = -\nabla \cdot (uc) + \nabla \cdot (D\nabla c) \quad (7.8)$$

where c = concentration of solute, $[M/L^3]$,
 t = time, $[T]$,
 u = seepage velocity from a decoupled flow solution, $[L/T]$, and
 D = dispersion coefficient tensor, $[L^2/T]$.

The dispersion coefficient is composed of a hydrodynamic dispersion term and a molecular diffusion term

$$D_{ij} = D_{ij}^d + D^m \delta_{ij} = (\alpha_L - \alpha_T) \frac{u_i u_j}{u} + \alpha_T u \delta_{ij} + D^m \delta_{ij} \quad (7.9)$$

where D^d = hydrodynamic dispersion coefficient, $[L^2/T]$,
 δ_{ij} = Kronecker delta, $[-]$,
 D^m = molecular diffusion coefficient, $[L^2/T]$,
 α_L = longitudinal dispersivity, $[L]$,
 α_T = transverse dispersivity, $[L]$,
 u_i, u_j = fluid velocity magnitudes in the i and j directions, $[LT^{-1}]$, and
 u = mean fluid velocity magnitude, $[LT^{-1}]$.

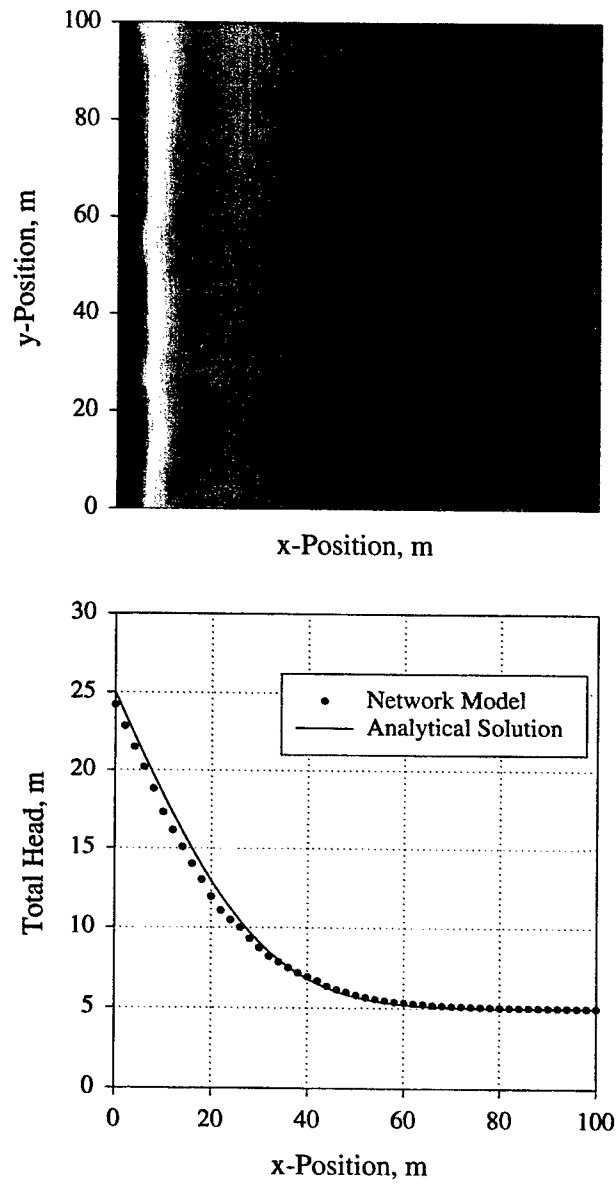


Figure 7.11: A transient pressure wave moving through a homogeneous porous medium. Contours of the piezometric surface (top) and comparison of network results and analytical solution (bottom) for an elapsed time of 12 days.

The dispersion term uses a diffusion coefficient to represent unresolved differential advection about the mean motion. This approach is used in practice because it has been shown to match historical observations, normally from laboratory studies [2]. These observations indicate that, after long travel times, a continuous injection at the boundary of a packed column produces a sigmoidally-shaped concentration profile along the column and an instantaneous source produces a nearly Gaussian concentration profile [30], shapes that are consistent with the ADE. In heterogeneous media, the parameters in the ADE display a dependence on the scale of observation, making the equation difficult to use [2]. If parameters are fitted to match a particular plume state, those parameters are not necessarily valid at any other stage in the plume's development. Further, a large dispersion coefficient may predict artificial, omnidirectional diffusive spreading.

Highly-resolved simulations of heterogeneous media attempt to resolve the velocity field in detail, shifting much of the burden of plume growth to the advection term from the dispersion term. Often, these approaches rely on a diffusion model to describe the effects of 'sub-grid-scale' velocity variation.

The network model simulates conservative transport as pure advection in the throats (no molecular diffusion at present), and perfect mixing at connections. Without a diffusion term, the network produces a directionally-biased, downstream mixing effect. The network model has been shown to produce visually-realistic tracer concentration plumes whose growth matches observed trends. This chapter compares transport in discrete networks to advection-dispersion theory and to observations from homogeneous and heterogeneous laboratory experiments. The purpose here is to examine differences between discrete network simulation and advection-dispersion theory and to evaluate the network's ability to reproduce observed behavior.

The network-model view of transport and the advection-dispersion equation represent the same physical behavior in different ways. Although the parameters in the ADE are unsubstantiated in heterogeneous media, practitioners have been able to fit the ADE to their data satisfactorily for many years [2]. Therefore, for transport through the network to be a credible representation of transport in porous media, it must display some similarity with ADE solutions. The network was compared against three analytical solutions for the ADE,

1. an instantaneous point source in a macroscopically uniform flow field,
2. a continuous point source in a macroscopically uniform flow field, and
3. a continuous boundary source in a macroscopically uniform flow field.

Table 7.1: Network Properties.

Parameter	Value
Domain Length (x)	2,500 m
Domain Width (y)	1,500 m
Domain Height (z)	1,500 m
Interconnection Spacing	60 m
Maximum Throat Length	100 m
Mean Throat Conductivity	1.0 m/d
Variance in ln Throat Conductivity	4.0
Number of Connections	25,000
Number of Throats	150,000

One objective here was to determine whether ADE parameters could be found to approximate concentration profiles produced by the network. To permit these comparisons, a single three-dimensional network was created with the properties listed in Table 7.1

7.2.1 Instantaneous Point Source of Tracer.

Steady flow through the network was computed with constant heads applied to the boundaries in the longest dimension. These heads were designed to produce a unit macroscopic gradient. One thousand grams of tracer per day were injected for 5 days at a position (250, 750, 750) within the domain (Figure 7.12). Plume growth was observed for 1500 days after the injection ceased. A snapshot of the plume was taken at 1205 days. At this time, the leading edge of the plume has reached the downstream boundary and mass was beginning to exit the simulation domain.

The analytical solution for an instantaneous point source in a three-dimensional domain is [128]

$$c(x, y, z, t) = \frac{M}{8\phi(\pi^3 t^3 D_{xx} D_{yy} D_{zz})^{1/2}} \exp \left[-\frac{(x - x_c)^2}{4D_{xx}t} - \frac{(y - y_c)^2}{4D_{yy}t} - \frac{(z - z_c)^2}{4D_{zz}t} \right] \quad (7.10)$$

where c = concentration, $[ML^3]$,
 M = mass of tracer injected at time 0. $[M]$, and
 x_c, y_c, z_c = coordinates of the centroid of the plume, $[L]$.

The apparent seepage velocity is approximated by the plume centroid's distance from the point of injection and the elapsed time. Individual dispersivity values may be isolated by examining the ratio of concentrations along a line in one coordinate

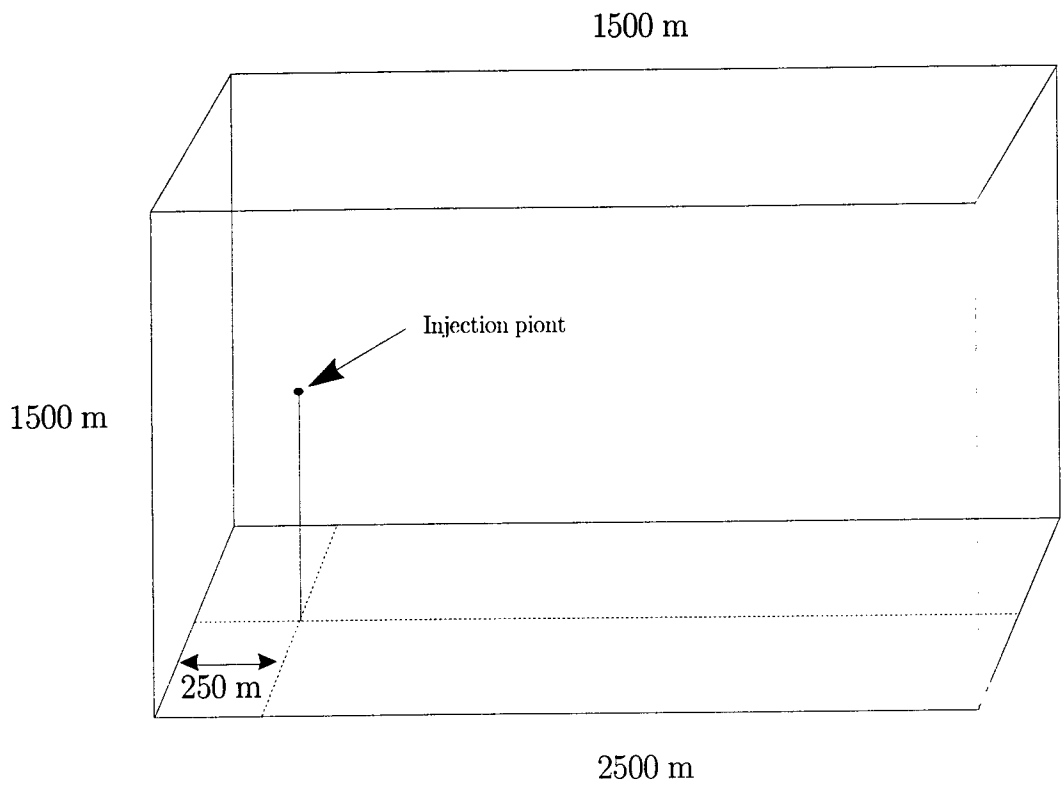


Figure 7.12: A schematic showing dimensions of the domain and the point of injection.

direction. For example, taking two concentration values along a line of constant y and z , we have

$$\frac{c_1}{c_2} = \exp \left[\frac{-(x_1 - x_c)^2 + (x_2 - x_c)^2}{4D_{xx}t} \right]. \quad (7.11)$$

Knowing that D_{xx} is simply the apparent seepage velocity times the apparent dispersivity, $u\alpha_x$, we may compute the appropriate dispersivity to fit the ADE.

Cross-sections through the network plume are compared to analytical solutions to the ADE in Figures 7.13 and 7.14. Concentration profiles were taken near the apparent center of the developing plume at position (1150, 800, 780). It is apparent that ADE parameters may be found that closely match the network plume in the lateral (y) cross section (Figure 7.13). In the longitudinal direction (x), the network plume shows a nearly Gaussian distribution over much of its length (Figure 7.14). The exceptions are for $x < 250$ m for which the network concentrations are identically zero, and several spikes in concentration occurring for x less than 1000 m. ADE predictions of non-zero concentration upstream of the injection location are not physically possible. The spikes correspond to pockets of low permeability material that have delayed some of the tracer migration. When the tracer plume passed that position, plume concentrations were much higher. Tracer delayed in these low conductivity throats retains this high concentration until reaching the ends of these throats, when mixing reduces their values. These spikes will not travel with the developing plume, but will be gradually depleted, providing a source of tracer to the rear of the plume and producing long tails on concentration breakthrough curves.

The ADE solution with longitudinal dispersivity of 140 m and lateral dispersivities of 20 m nearly matched the observed concentration profile for much of its length. These are the constant coefficients needed over the life of the plume to create the Gaussian distribution shown in Figure 7.14. We know that the dispersivities began much smaller than these values and have grown with the plume's size (Chapter 5). Network simulation permits us to compute an instantaneous value of these parameters. The longitudinal and lateral dispersivities are measured by

$$\alpha_L = (\sigma_{x_L} \rho_{x_L u}) \left(\frac{\sigma_u}{\bar{u}} \right) \quad (7.12)$$

$$\alpha_T = (\sigma_{x_T} \rho_{x_T v}) \left(\frac{\sigma_v}{\bar{u}} \right). \quad (7.13)$$

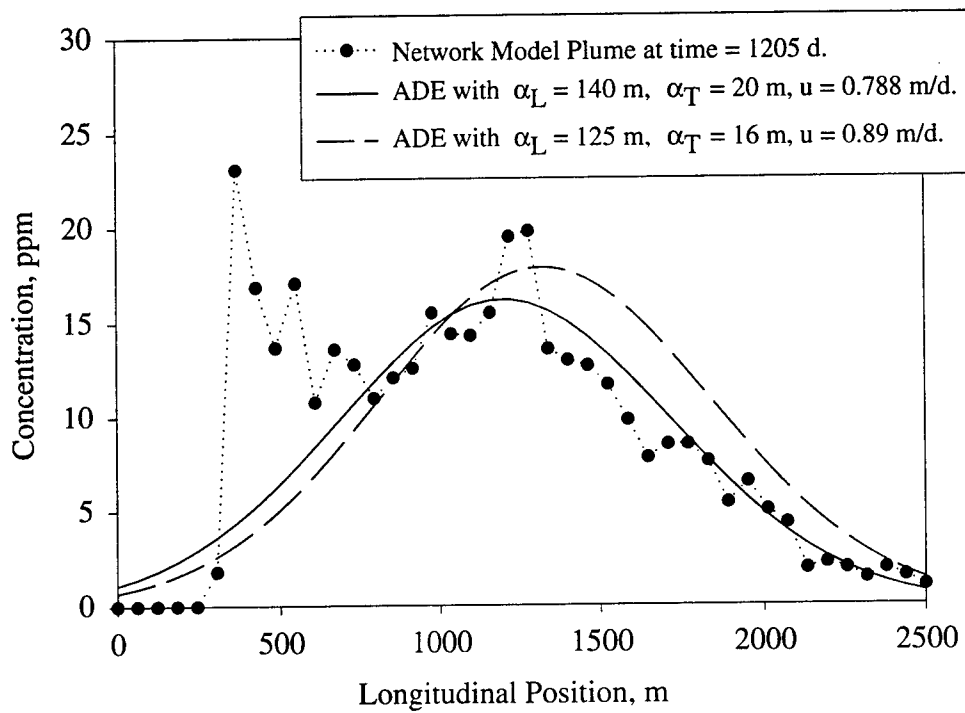


Figure 7.13: Lateral cross-sections through plumes predicted by the advection dispersion equation and the network model for an instantaneous source of contaminant.

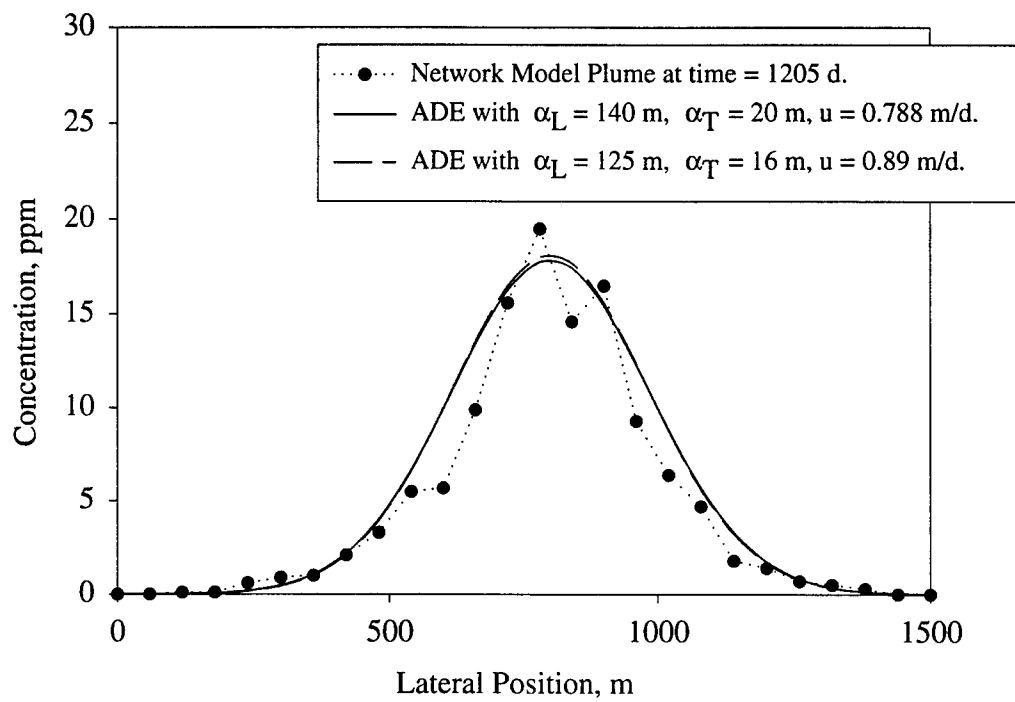


Figure 7.14: Longitudinal cross-sections through plumes predicted by the advection dispersion equation and the network model for an instantaneous source of contaminant.

where

- α_L = longitudinal dispersivity, $[L]$,
- α_T = transverse dispersivity, $[L]$,
- σ_{xL} = standard deviation in longitudinal tracer particle position, $[L]$,
- σ_{xT} = standard deviation in transverse tracer particle position, $[L]$,
- ρ_{xLu} = longitudinal position-velocity correlation coefficient, $[-]$,
- ρ_{xTv} = transverse position-velocity correlation coefficient, $[-]$,
- σ_u = standard deviation in longitudinal velocity, $[LT^{-1}]$,
- σ_v = standard deviation in transverse velocity, $[LT^{-1}]$, and
- \bar{u} = longitudinal speed of the plume centroid, $[LT^{-1}]$.

Figure 7.15 shows a measure of plume size versus travel distance for a scale-dependent dispersivity and a constant dispersivity. The constant dispersivity predicts linear growth with distance while the scale-dependent dispersivity, an empirical fit taken from Arya [4], shows a nearly parabolic shape. Where these two lines intersect, the two theories predict the same, pre-asymptotic plume centroid position and plume size (by this measure). Therefore, we may find a velocity and a constant dispersivity that will produce a plume matching these statistics. The instantaneous dispersivity is prescribed by the slopes of these lines. Using Arya's [4] empirical equation, the ratio of instantaneous dispersivity to the equivalent constant dispersivity may be computed to be a constant at 1.75.

The instantaneous speed of the plume is measured as the tracer-mass-weighted fluid velocity in the domain. The instantaneous velocity is significantly lower than that needed to fit the ADE. When the plume is small, its speed often is much larger than the bulk fluid velocity. A small plume is able to find preferential paths of higher conductivity through which to move. As the plume becomes larger, it encompasses more of the velocity structure and its speed more closely resembles the bulk fluid velocity.

Often, detailed plume images are not available and the ADE parameters are fit to a concentration breakthrough curve at a fixed location. Figure 7.16 shows concentration breakthrough curves for the network plume and two ADE solutions at $x = 1158 \text{ m}$. Note that the spikes seen in the plume cross section never arrive at this observation point. The network plume breakthrough may be fit very well with an ADE. However, the ADE parameters that best fit the breakthrough curve are slightly different than those needed to fit the plume cross-sections.

These comparisons demonstrate a strong similarity between the network model plumes and those predicted by the ADE. However, the network remains fixed, while the ADE parameters (advection velocity and longitudinal and lateral dispersivities) vary depending on when and how the parameters are extracted.

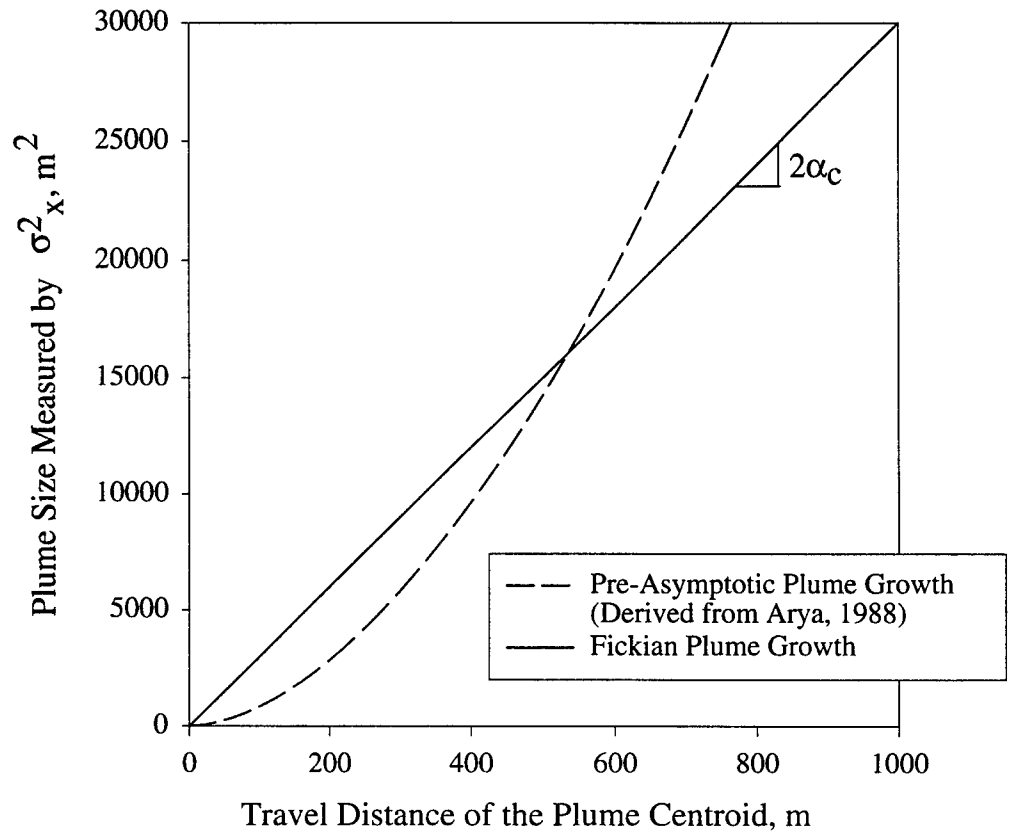


Figure 7.15: Plume characteristics for constant and scale-dependent dispersivities.

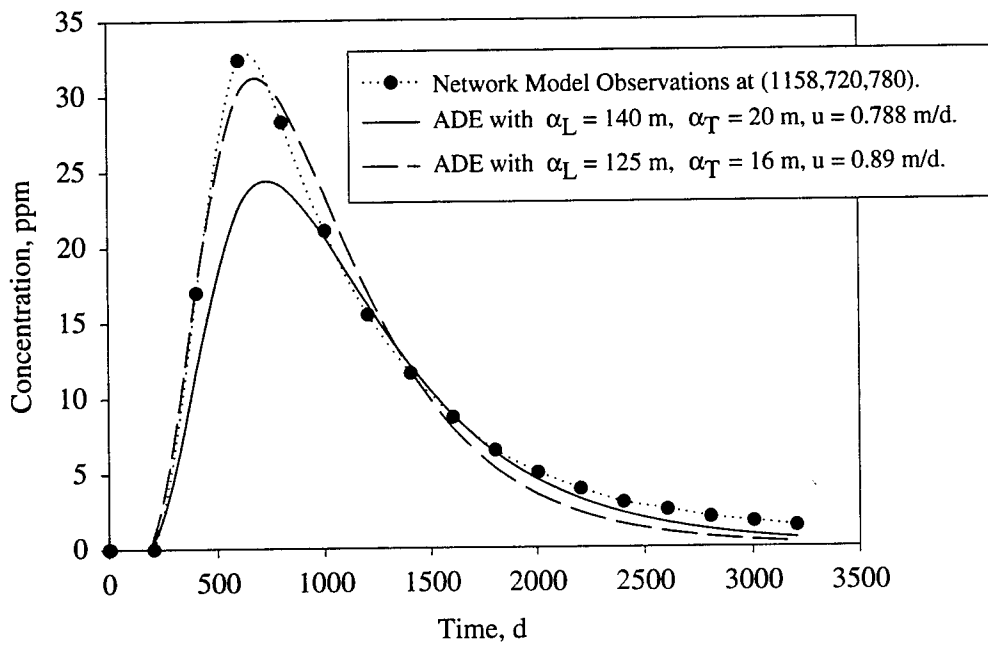


Figure 7.16: Concentration breakthrough curves taken at (1158, 800, 780) for the network plume and two ADE solutions.

7.2.2 Continuous Point Source of Tracer.

Leaking underground storage tanks, slowly-partitioning entrapped NAPLs, and dissolving solid contamination resemble continuous point sources. To examine a continuous point source, mass was injected at a constant rate (1000 g/d), for the entire simulation time (4400 d), at the same position as the instantaneous source. After this amount of simulation time, the concentration field was observed to be virtually steady. Mass entering the injection well was nearly offset by mass exiting the downstream boundary. The analytical solution for the steady-state concentration field with a continuous point source is [128]

$$c(x, y, z, \infty) = \frac{dM/dt}{4\phi\pi r(D_{yy}D_{zz})^{1/2}} \exp\left[\frac{(x-r)v}{2D_{xx}}\right] \quad (7.14)$$

$$r = \left(x^2 + y^2 \frac{D_{xx}}{D_{yy}} + z^2 \frac{D_{xx}}{D_{zz}}\right)^{1/2} \quad (7.15)$$

A longitudinal cross section of concentration was taken near the injection location. This concentration profile and two ADE solutions are given in Figure 7.17. The network plume correctly shows no upstream spreading in the absence of molecular diffusion. In the figure, one ADE curve is given for near-asymptotic properties taken from the instantaneous point source simulation at 1205 d. This curve shows good agreement with the network model downstream of the injection point. However, those parameters incorrectly predict significant upstream migration of tracer. The other ADE curve was created by arbitrarily reducing dispersivities to lessen the effect of the upstream spreading. Substantial upstream motion persisted, even with these smaller coefficients, and the downstream predictions are poor. The shape of these ADE curves depends on the ratio of longitudinal to lateral dispersivity, but, in general, the upstream migration for this problem only becomes negligible at a distance from the source equal to several times the longitudinal dispersivity. In our case, that is several hundred meters.

7.2.3 Continuous Boundary Source of Tracer.

A continuous source of tracer was applied to the upstream boundary of the network described in Table 7.1. This is effectively a one-dimensional problem although, in such a heterogeneous medium, tracer moves through preferential flow paths. By averaging tracer concentrations laterally and vertically, the concentration field becomes a one-dimensional, smooth, spreading front. The ADE may be used to estimate the apparent dispersivity of this medium as one would fit a column test. The analytical

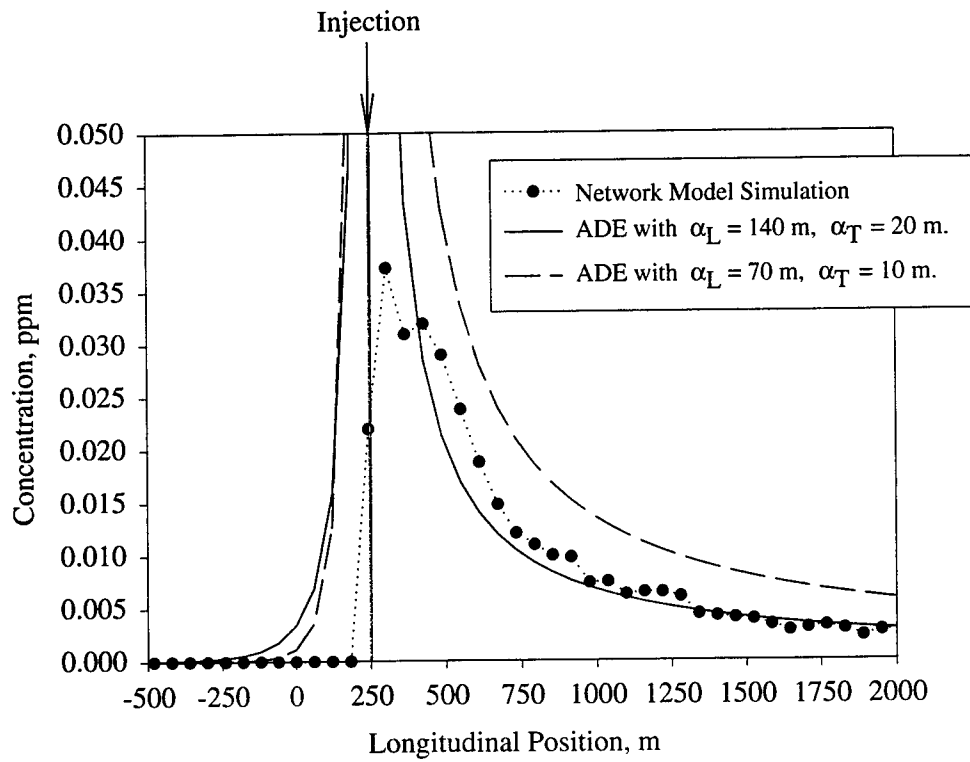


Figure 7.17: ADE and network simulation concentration profiles along the approximate centerline of a plume from a continuous point source injection of tracer.

solution for a diffusing concentration front is [128]

$$c(x, t) = \frac{c_0}{2} \left[\operatorname{erfc} \left(\frac{x - u_s t}{2D_L t^{1/2}} \right) + \exp \left(\frac{u_s x}{D_L} \right) \operatorname{erfc} \left(\frac{x + u_s t}{2D_L t^{1/2}} \right) \right] \quad (7.16)$$

where c_0 is the concentration at the upstream boundary. The $0.25c_0$ and the $0.50c_0$ concentration values were monitored in the network simulation to ‘back-calculate’ the apparent dispersivity. Figure 7.18 shows computed dispersivities for the constant boundary source and for an instantaneous point source in the same network. The two measurement techniques produce similar behavior in apparent dispersivity.

Seepage velocity used in the dispersivity computations was the asymptotic velocity. The speed of the $c_0/2$ concentration value approaches the asymptotic value prescribed by the bulk fluid velocity (Figure 7.19) for long-time simulation. If an instantaneous velocity is used, the apparent dispersivity behavior is much different.

7.2.4 Summary of the Comparisons with Advection-Dispersion Theory.

The ADE may be fitted to well-developed instantaneous-source plumes and to the downstream portion of continuous-source plumes. Unfortunately, the parameters computed are only valid for the conditions of that test. If the concentration state must be predicted for another time or another set of boundary conditions, the ADE may produce inaccurate results. Time-dependent or plume-scale dependent coefficients will not resolve these issues for problems other than instantaneous point sources.

7.2.5 Comparison of the Network Model Against Laboratory Data.

Plumes from the network do not coincide with analytical solutions for the ADE, but seem to match observational evidence that has led to the ADE’s acceptance. Therefore, the network should produce valid predictions of tracer transport. This proposal was tested by comparing the network against transport observations from laboratory experiments conducted at the University of Colorado [70, 51].

The homogeneous experimental packing discussed earlier was examined with a point source and a line source. For HMTE7, five liters of 1.2 g/l potassium bromide solution was introduced at the upstream boundary. Given a measured, constant flux through the boundary ($46.95 \text{ cm}^3/\text{min}$), this injection lasted 106 min. Bromide was measured in samples taken from the tank effluent.

To simulate experiment HMTE7 with the network model, the mean throat conductivity was adjusted from the prior flow testing so that the network and experimental fluxes matched. Tracer was introduced at a constant concentration all along

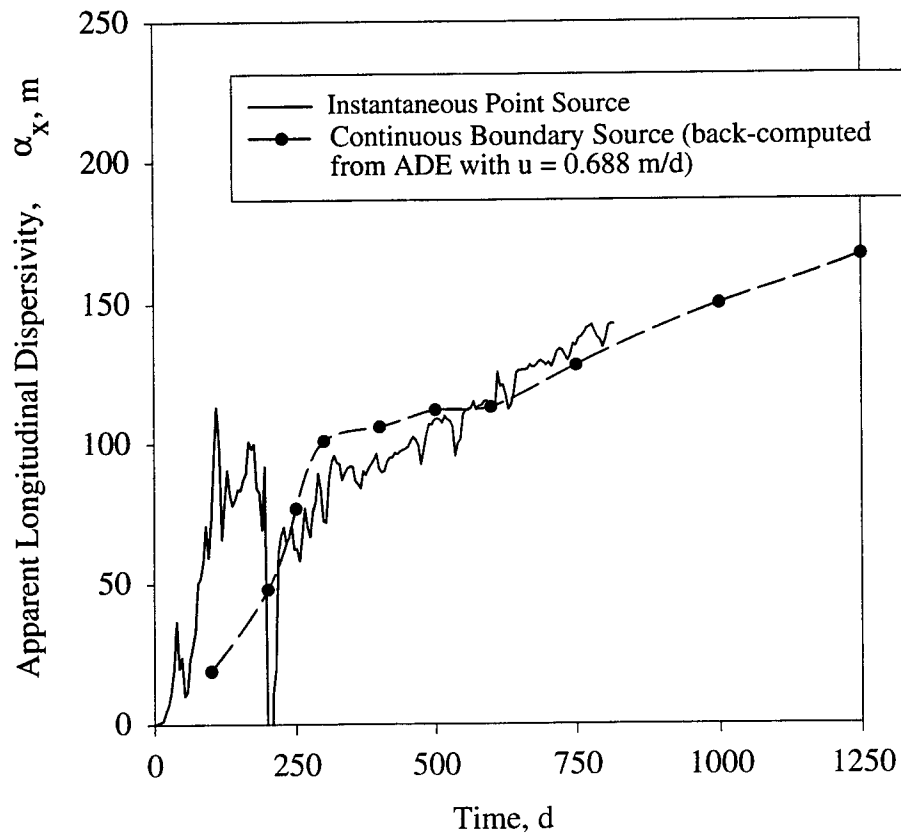


Figure 7.18: Dispersivities computed from a moving concentration front and an instantaneous point source of tracer.

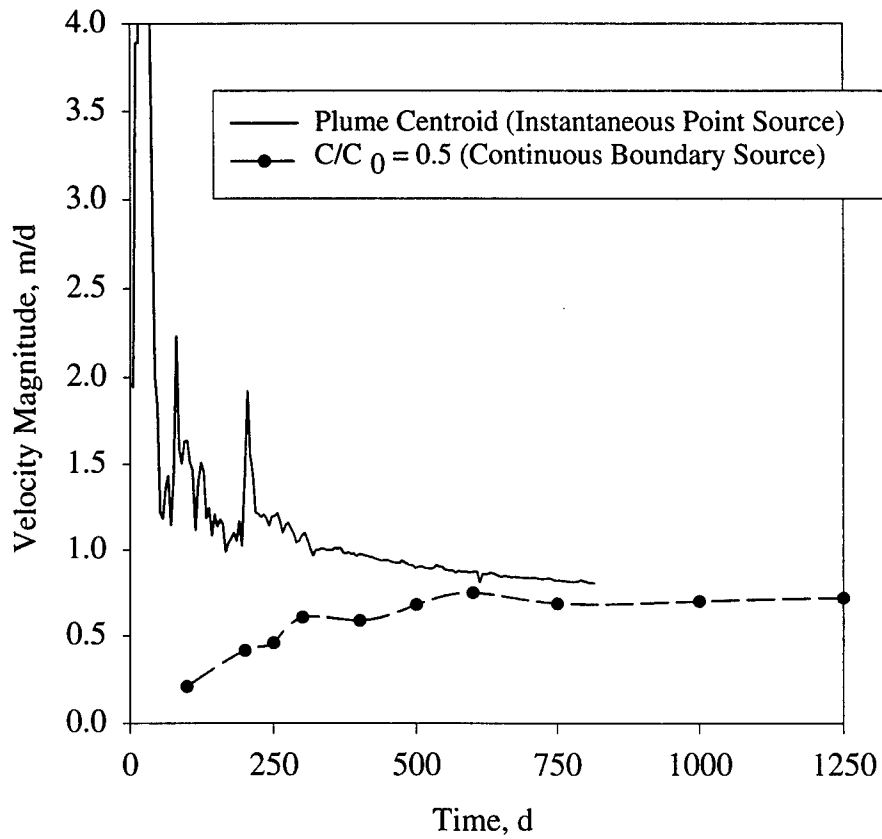


Figure 7.19: Speed of the median concentration for the moving front problem and the speed of the centroid of a plume from an instantaneous injection.

the upstream boundary of the network. The computed and observed concentrations at the end of the tank are shown in Figure 7.20.

The network model contains no dispersion parameters. The only coefficients available for manipulation were the throat lengths, conductivity variance, and the effective porosity. This is a homogeneous medium, suggesting that the throat lengths must remain short (i.e., on the order of the actual pore size). The peak arrival times of the simulated and observed plumes were similar, indicating that the effective porosity is appropriate. Increasing variance in throat conductivity would improve the prediction of first arrival of the plume, but would diminish the peak concentration. Therefore, although a better fit to the data may be possible by modifying these parameters, the values chosen during the flow comparisons were judged acceptable. The very early arrival in the experiment may be due to additional dispersion in the inlet and outlet reservoirs that contain gravel, screening, and fabric, and in the tubing and valves.

The same tank was used to examine a point injection of benzene-saturated water. Five *ml/min* of benzene-saturated water was injected for 4 hours into port 16 (Figure 7.4). Benzene concentrations were monitored in samples taken from ports downstream for an additional 4 hours. To simulate this problem with the network model, a point source of water and a point source of tracer mass were injected at a connection corresponding to the location of port 16. Comparisons were made between the model and the observations at ports 13 and 12, located directly downstream of the injection. The plume profiles revealed comparable shapes with substantial error in the position of the leading and trailing edges of the plumes. Further, amplitudes of the concentration profiles predicted by the model were only a small fraction (about 30 percent) of the observed amplitudes. The network model produced too much lateral spreading of the solute.

Lateral dispersivity is dictated by the correlation length in the network. The longest throats in the original network were 4 *cm*. A much finer network would be needed to reproduce the observed small lateral dispersivity. It was established during the flow comparisons that the head field for this medium is very nearly planar. Further, the tracer is confined to a small portion of the domain for these simulations. Therefore, a subdomain 100 *cm* long and 40 *cm* wide was created. This subdomain extended in longitudinal dimension from the 70 *cm* position to the 170 *cm* position, including the injection location and both observation ports (13 and 12). Laterally, the computational subdomain was positioned to straddle the injection and observation ports. The linear pressure field was interpolated to the ends of the subdomain and no-flow boundaries were assumed on the lateral boundaries. With this smaller domain, an interconnection spacing of 0.4 *cm* and a maximum throat

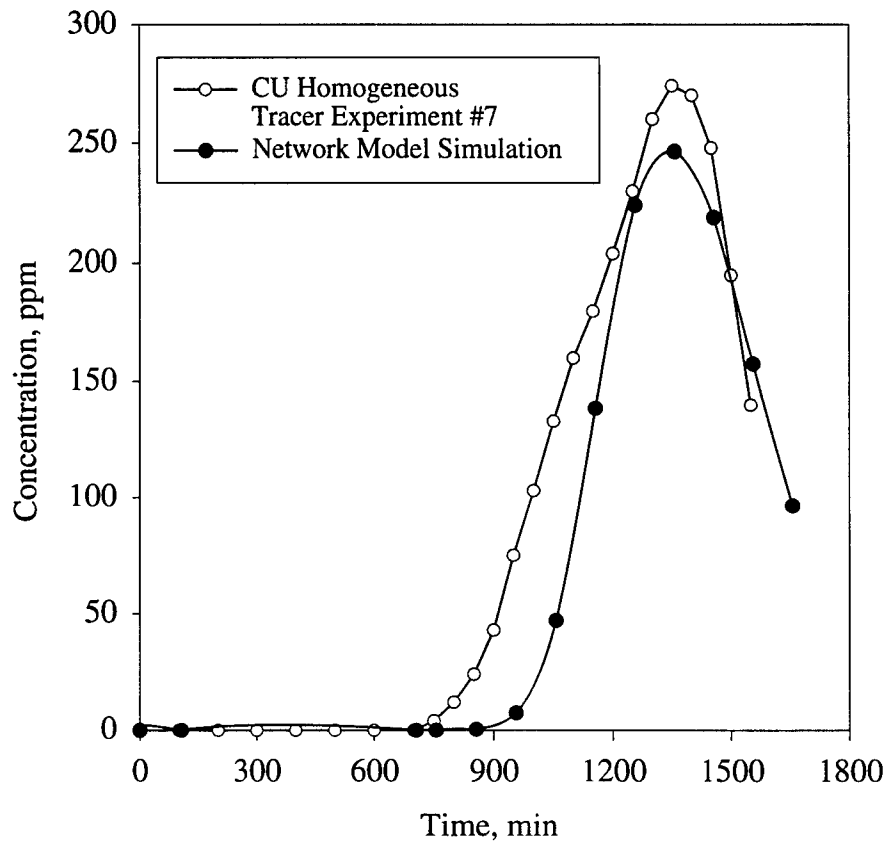


Figure 7.20: Simulated and measured concentration breakthrough curves for HMTE7.

length of 0.8 *cm* were possible. The limitation here is the time step size which is controlled by the minimum travel time for a throat in the domain.

To maintain consistency with longitudinal spreading induced by the network in HMTE7, the throat conductivity variance was increased slightly, further reducing the time step size. That the variance must increase as the resolution increases is logical. With more resolution, less media are represented by each throat, thereby reducing the effects of averaging and increasing variance. The resulting tracer concentration contours are shown in Figure 7.21. Breakthrough curves for this plume are compared to observations in Figures 7.22 and 7.23. Although the amplitudes are improved with increasing resolution, more resolution will be needed to reproduce the very small lateral spreading indicated by the observed data. Garcia [51] suggests a lateral dispersivity of 1 *mm* or less. This value is consistent with the trend in peak concentration versus resolution in Figure 7.24. The observed peak is near 0.45. To achieve this, an interconnection spacing of about 2 *mm* with a maximum throat length near 4 *mm* will be needed. The resolution required for this problem exceeds the computational resources available on the desktop workstation used for this study.

A breakthrough curve was examined with the heterogeneous experiment (HTTE4). Again, 5 *l* of 1.2 *g/l* potassium bromide solution was introduced at the upstream boundary of the tank. Fresh water followed the potassium bromide solution. Comparisons were made for both types of network discretization, explicit structure and statistical structure. Figure 7.25 shows concentration plumes for both networks. Both display preferential paths through the medium. Consequently, breakthrough curves for both networks and the experimental tank are similar (Figures 7.26 and 7.27). To resolve the explicit structure required about 3000 connections and 14000 throats. The network with only statistical structure was created with 370 connections and about 1200 throats.

Asymptotic macrodispersivity was estimated by Garcia [51] to be about 106 *cm* for this material. This parameter is intended only for the asymptotic state. Using such a large dispersivity for this pre-asymptotic problem would produce a severely smeared plume.

The network was designed to represent naturally heterogeneous media. To simulate homogeneous media and examine lateral spreading will require substantial resolution. Most continuum codes will experience similar problems with numerical dispersion. Unless the lateral extent of the plume is resolved in detail, numerical dispersion will dwarf the physical dispersion, artificially spreading the contaminant.

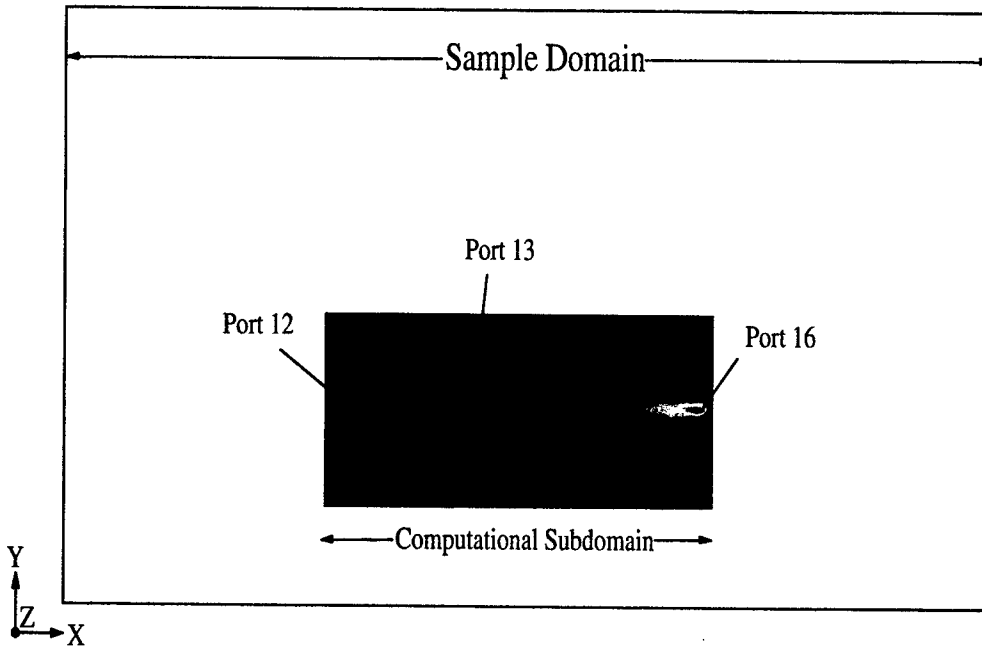
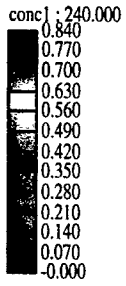


Figure 7.21: The sample domain, the computational subdomain, and contours of concentration for HMTE1.

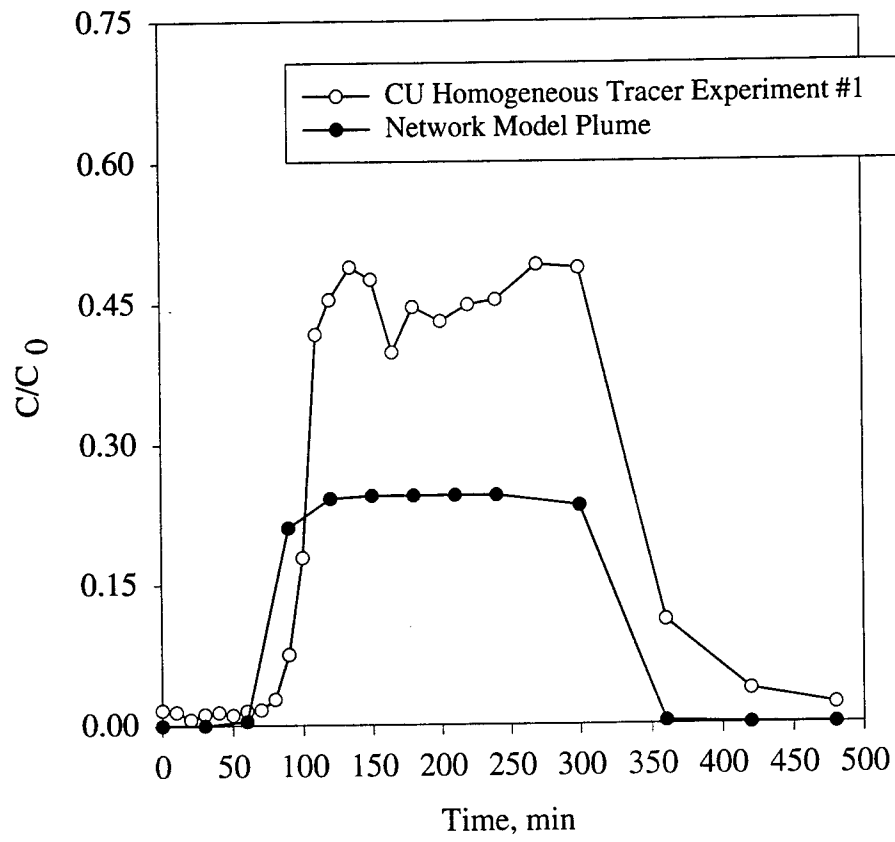


Figure 7.22: Simulated and measured concentration breakthrough curves for HMTE1 (Port 13).

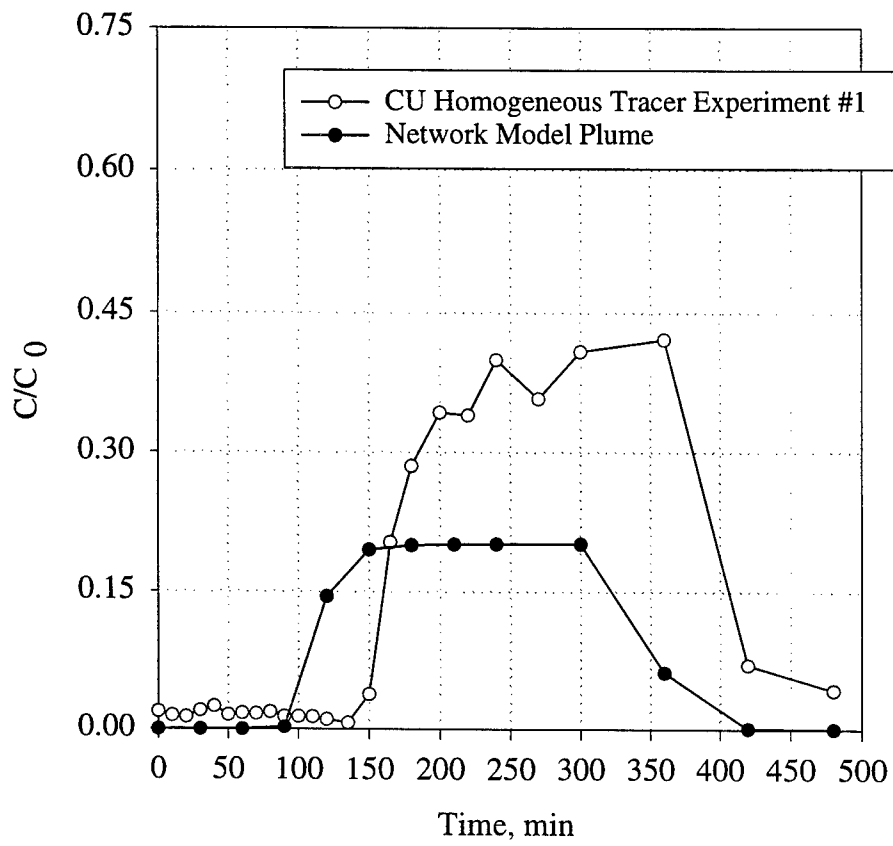


Figure 7.23: Simulated and measured concentration breakthrough curves for HMTE1 (Port 12).

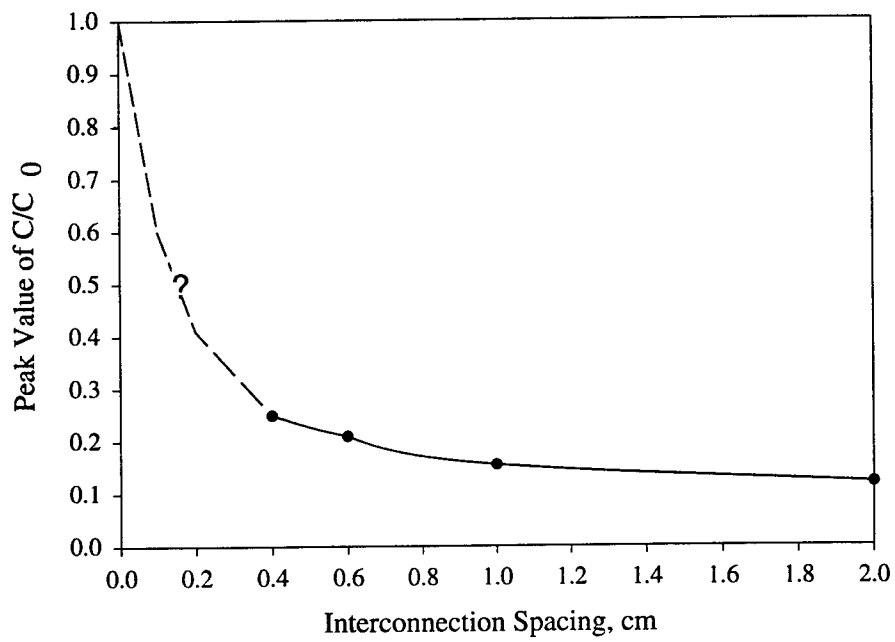


Figure 7.24: Interconnection spacing versus peak concentration at port 13.

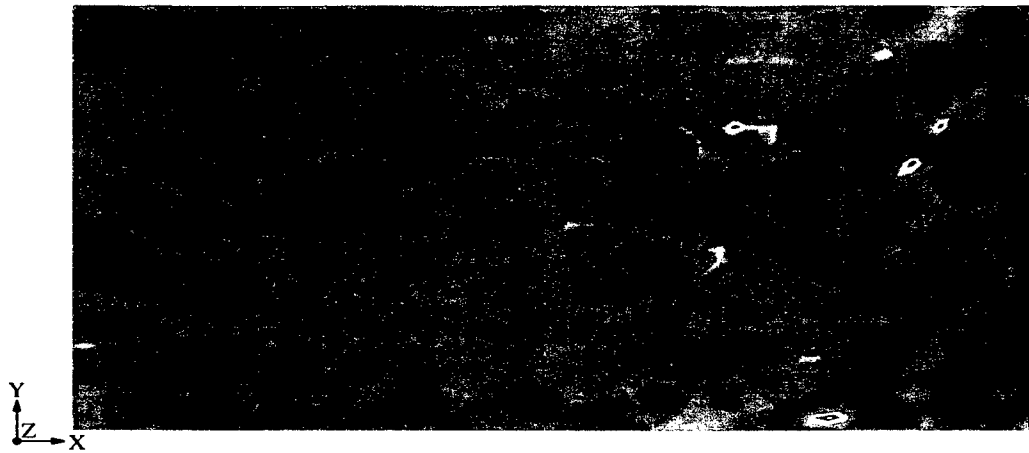
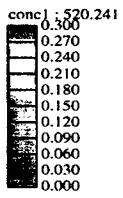
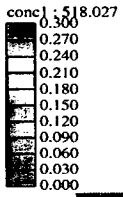


Figure 7.25: Concentration plumes for the network with explicit structure (above) and statistical structure (below) HTTE4.

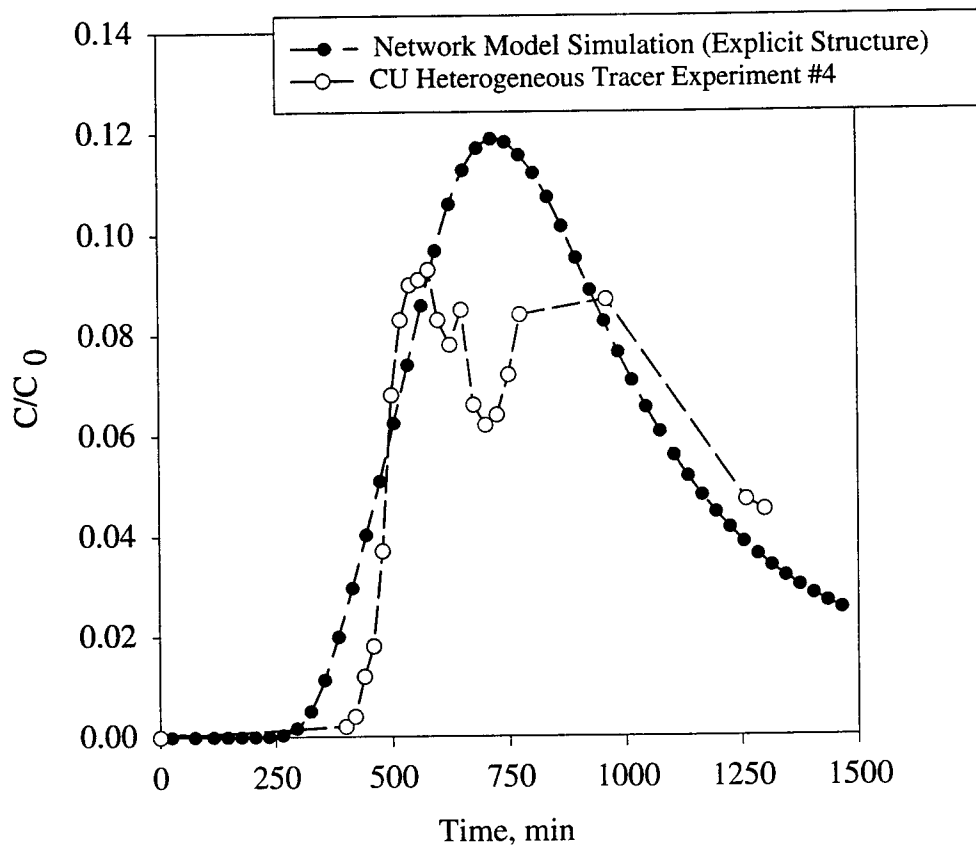


Figure 7.26: Simulated and measured concentration breakthrough curves for HTTE4 with explicit structure.

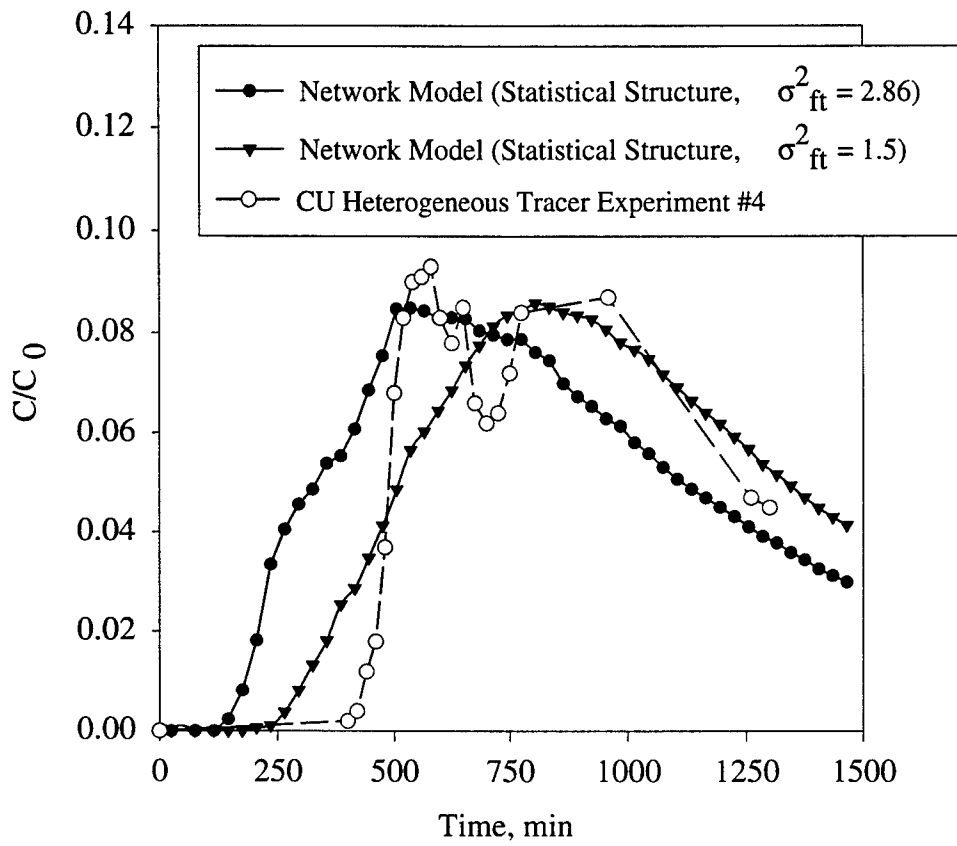


Figure 7.27: Simulated and measured concentration breakthrough curves for HTTE4 with statistical structure.

7.3 Density-Dependent Flows

The network was also used to simulate a few problems in density-dependent flow. A thin, vertical slab that is 100 *cm* on a side by 10 *cm* thick was mapped to a discrete network. All boundaries on the slab were defined as solid. A layer of fluid containing a dense, miscible tracer was placed over a layer of fresh water. The presence of this constituent at a concentration of 1.0 *g/g* produced a fluid/constituent mixture with a specific gravity of 1.5. The dense fluid seeks the bottom of the sample amid much mixing. Figure 7.28 shows four images during this overturning process. Figure 7.29 shows an alternative contouring of the final image from Figure 7.28. All normalized concentrations greater than 0.25 are colored red while concentrations less than 0.25 are colored blue. This permits us to see a miscible fingering phenomenon in the displacement. The finger spacing is approximately 25 *cm* in this coarse system. These simulations simply show potential use of the network for density-dependent flows. Additional work in this area is needed to develop confidence in the quantitative results.

7.4 Conclusions

Discrete network modeling is shown to be an effective approach for simulating saturated fluid flow and conservative transport in macroscopic, heterogeneous porous media. Fluid flow through the networks compares well with macroscopic solutions for Darcy flow and with laboratory observations. Transport through the networks provides acceptably close matches with laboratory data and is compatible with advection-dispersion theory under appropriate conditions. Further, the network permits direct installation of characteristic length distributions, thus simulating pre-asymptotic transport mechanisms very efficiently. In summary, the network approach is an efficient and effective direct simulation tool that avoids the use of dispersion parameters while producing correct flow and transport behavior.

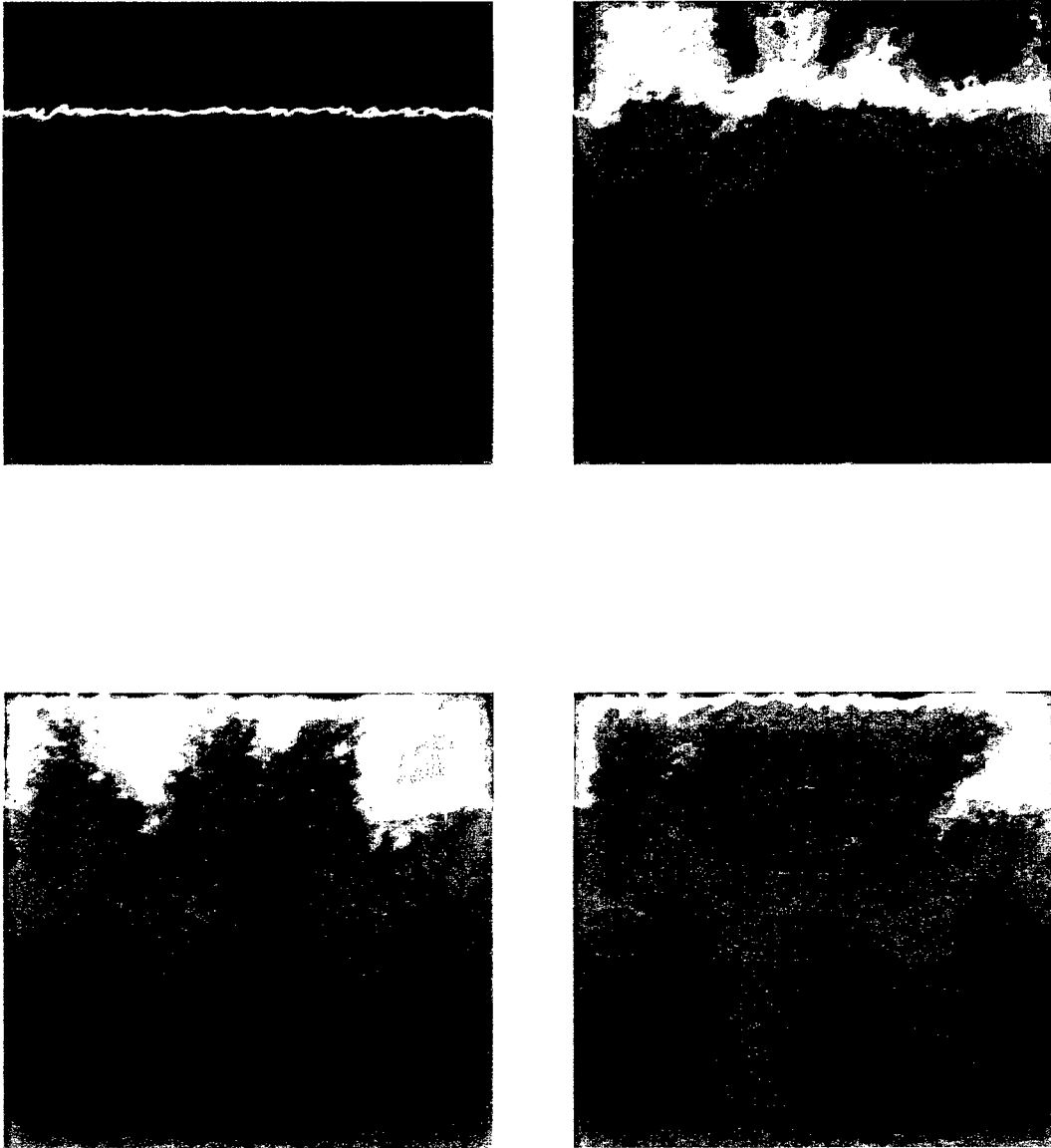


Figure 7.28: Time series of the overturning of an unstable density configuration. Elapsed time increases from upper left (initial condition), to upper right (6000 s), to lower left (14000 s), to lower right (20000 s). Red indicates higher concentration and blue indicates lower concentration.

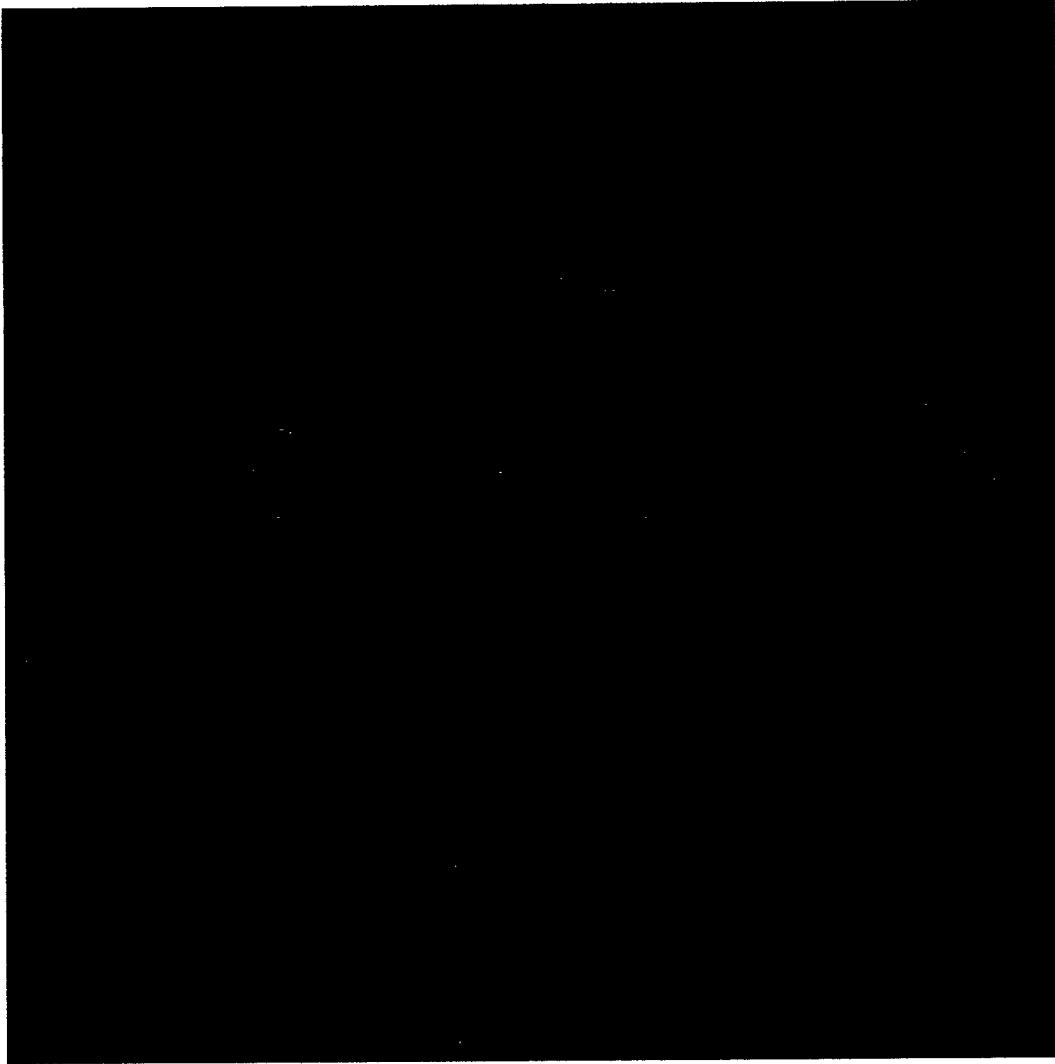


Figure 7.29: Alternative contouring for an elapsed time of 14000 s in the overturning problem. Red indicates relative concentration greater than 0.25 and blue indicates relative concentration smaller than 0.25.

Chapter 8

Discrete Network Modeling of Immiscible Flow Through Porous Media

Abstract

A stochastic, discrete network modeling approach is offered to simulate the movement of immiscible fluids through porous media. Immiscible fluids follow preferential flow paths defined by heterogeneity at many spatial scales. Immiscible displacement often occurs as nonuniform, finger-like flow. Lenses of fine material may act as capillary barriers while lenses of coarse material act as capillary traps. These flow features are difficult to capture with contemporary numerical models of immiscible flow.

Each throat in the network corresponds to a macroscopic path within in the modeled medium. The distribution of throat lengths represents the larger scales of heterogeneity in the medium. Immiscible flow through the each throat in the network is modeled as sharp-front displacement. Like its pore-scale counterparts, this macroscopic network permits no partial saturations. Rather, partial saturations emerge in terms of spatial averages of the network state. Saturated hydraulic conductivities and entry heads are defined randomly for the throats. The model demonstrates reasonable behavior for drainage and imbibition and shows promise for modeling capillary barriers and localized, macroporous-breakthrough phenomena.

This work extends a stochastic discrete network approach for saturated flow and conservative, miscible transport presented in Chapter 5 to simulate immiscible fluid

flow. The hallmark of this approach is keeping model process descriptions simple, but consistent with known behavior at the small scale. When enough resolution is included, complex, macroscopic behavior emerges. Consequently, the discrete network approach often requires substantial spatial resolution, but is less reliant on constitutive models than are traditional modeling techniques. The problem of immiscible fluid flow in porous media, with its complicated, saturation-based constitutive models, seemed an ideal candidate for this approach.

8.1 Immiscible Fluid Flow in Heterogeneous Media

Many liquids do not mix appreciably with each other and move as separate fluid phases through porous media. If the medium is not equally attracted to each of the fluids, a capillary force will exist, greatly complicating flow behavior. Predictive capability for immiscible fluid flow is necessary to evaluate flow in the unsaturated zone and to assess the migration and residual distribution of non-aqueous phase liquid contaminants (NAPLs). Drinking-water standards for these contaminants are usually very stringent, and their solubilities, although small, usually exceed these standards by orders of magnitude. Their relatively low solubilities permit the immiscible fluid to act as long-term, continuous sources of dissolved contaminant to passing groundwater. Hydrodynamic extraction techniques will only rarely be sufficient to remove nonwetting fluid isolated by capillary forces [68].

When describing saturated fluid flow and conservative transport, physical heterogeneity is important. But, for immiscible flow, it is paramount. For example, two media with different pore size distributions may produce similar flow and dispersion characteristics, but remarkably different immiscible flow behavior. Material property changes may arrest advancing fluid interfaces. Several key processes for immiscible flow are dictated by the variability and position of material properties

- capillary barriers,
- capillary entrapment, and
- channeling (fingering).

8.1.1 Capillary Barriers and Capillary Entrapment.

Natural soils often contain dramatic variations in physical properties. When an invading non-wetting fluid encounters a material interface and the pore radii in that material are sufficiently small, the invading fluid front may be arrested (Figure 8.1). The capillary force creates a barrier to the non-wetting fluid.

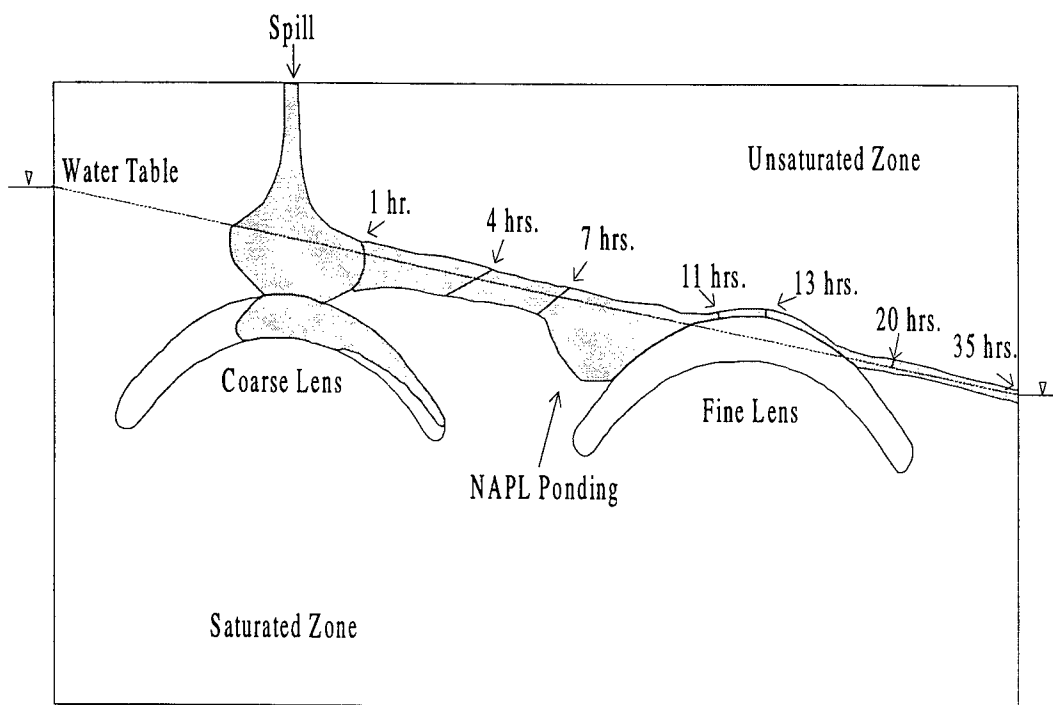


Figure 8.1: Experimental observation of a capillary barrier caused by a fine grain lens and capillary entrapment in a coarse-grain lens (from Illangasekare et al. [71]).

As a non-wetting fluid travels through the medium, bubbles or ganglia (larger, connected blobs) of this fluid may become surrounded by wetting fluid and immobilized as demonstrated by Schwille [127]. Mechanisms for the existence and mobilization of these ganglia are discussed by Hunt et al. [68]. In macroscopically heterogeneous media, entrapment may occur in pockets or layers of coarser material surrounded by fine-grain material (Figure 8.1). The fraction of pore space occupied by this trapped non-aqueous liquid may be as high as 20 to 30 percent [71].

8.1.2 Channeling or Fingering.

When one fluid displaces another, it may do so as a non-uniform front. The term 'fingering' is loosely used to describe such nonuniform displacement. In ideal, homogeneous material, fingering may arise from instability that produces a bifurcation in the solution path. In natural porous media, fingering is attributed to small-scale preferential flow paths rather than instability [83]. Because conductivity of a fluid phase depends strongly on the fraction of pore space occupied by that fluid, there exists a feedback mechanism in finger formation. In fact, experimental observations suggest that, at material interfaces, breakthrough may occur in an extremely limited range, perhaps a single macropore [22]. Fluid escaping from one pocket of coarse material may appear in another coarse lens down gradient with no visible path. The result of this displacement process is shown in Figure 8.2.

8.2 Modeling Approaches

Modeling of immiscible flow through heterogeneous media may be approached in several ways, including,

- traditional, discretized continuum equations,
- streamtubes or streamlines,
- network models.

8.2.1 Continuum-Based Flow Equations.

In this, the traditional approach for modeling macroscopic immiscible flow, the fluids are assumed to coexist in a mixture of partial saturations (S). Each fluid phase is described by local mass balance and local momentum transport (Darcy's law). Without source or sink terms, and assuming an incompressible matrix and fluids, the governing equations take the form

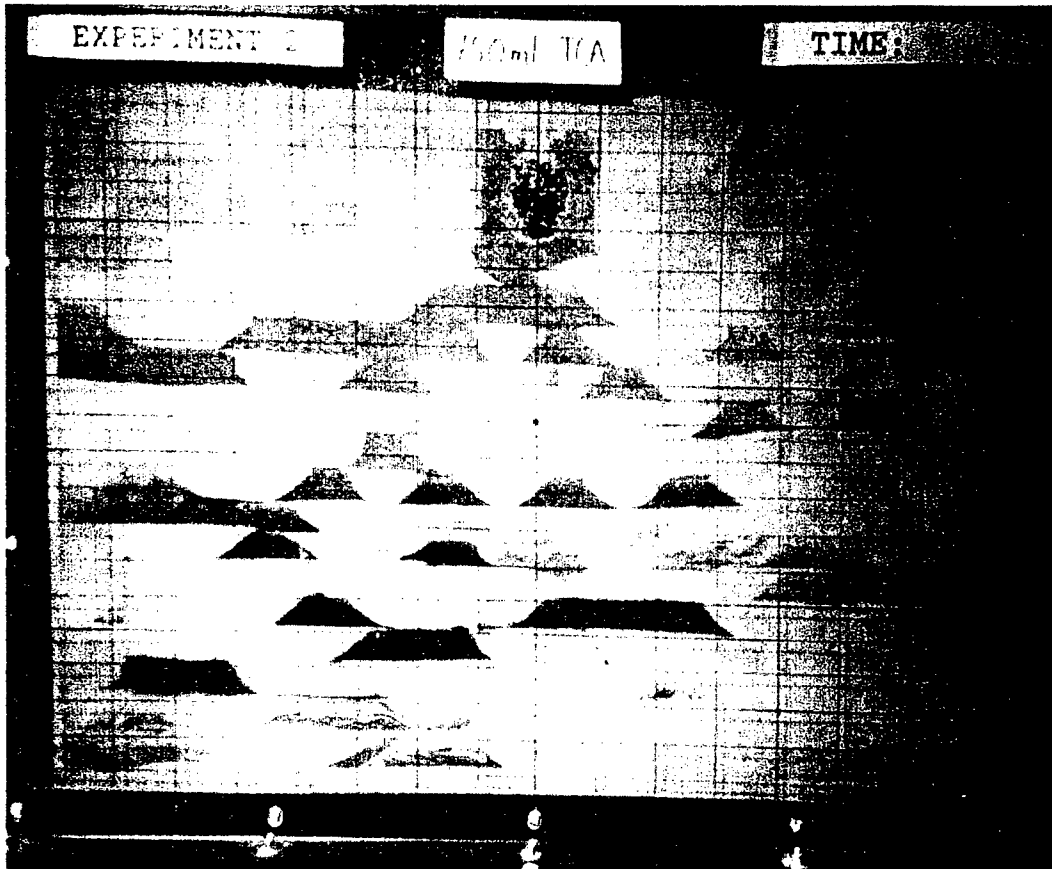


Figure 8.2: Observed distribution of non-aqueous contaminant showing macroscale entrapment and evidence of macroporous breakthrough [22].

$$\phi \frac{\partial}{\partial t} S_w = \nabla_i \cdot \left[\frac{k_{ij} k_{rw}}{\mu_w} \left(\frac{\partial P_w}{\partial x_j} - \rho_w g \frac{\partial z}{\partial x_j} \right) \right] \quad (8.1)$$

$$\phi \frac{\partial}{\partial t} S_{nw} = \nabla_i \cdot \left[\frac{k_{ij} k_{rnw}}{\mu_{nw}} \left(\frac{\partial P_{nw}}{\partial x_j} - \rho_{nw} g \frac{\partial z}{\partial x_j} \right) \right] \quad (8.2)$$

where k_{ij} = intrinsic permeability, $[L^2]$,
 k_{rw}, k_{rnw} = wetting and non-wetting phase relative permeabilities, $[-]$,
 μ_w, μ_{nw} = wetting and non-wetting phase viscosities, $[ML^{-1}T^{-1}]$, and
 P_w, P_{nw} = wetting and non-wetting phase pressures, $[ML^{-1}T^{-2}]$.

Note that repeated indices (i, j) imply summation. Repeated r, w , and nw do not imply summation. These equations are coupled through the capillary pressure which is given by

$$P_c(S_w) = P_{nw} - P_w \quad (8.3)$$

and the sum of saturations

$$S_w + S_{nw} = 1. \quad (8.4)$$

These equation assume that there is no interfacial shear.

Constitutive equations are required to relate the saturation to capillary pressure and to estimate the local permeability of the medium to each fluid phase. The most widely used constitutive equations for immiscible flow are the Brooks and Corey equations [18] and the van Genuchten equations [140] because each of these permits analytical computation of relative permeability. The Brooks and Corey equations are

$$P_C = P_C(S_W) = P_d(S_e)^{\frac{-1}{\lambda}} \quad (8.5)$$

$$k_{rW} = k_{rW}(S_W) = S_e^{\frac{2}{\lambda}+3} \quad (8.6)$$

$$k_{rNW} = k_{rNW}(S_W) = (1 - S_e)^2 \left(1 - S_e^{\frac{2}{\lambda}+1} \right) \quad (8.7)$$

where P_d = displacement pressure, $[ML^{-1}T^{-2}]$,
 S_e = effective saturation, $[-]$, and
 λ = pore index, $[-]$.

Hassanizadeh and Gray [63] concluded that the single-phase Darcy's law cannot be extended directly to apply to multiple fluid phases. Further, they determined that saturation-based, hysteretic relationships for capillary pressure and relative permeability are theoretically 'unsatisfactory' [63] and proposed inclusion of interfacial area in the constitutive relationships to remove hysteresis [62].

Butts and Jensen [19] suggested that it is possible to construct useful macroscopic constitutive parameters for immiscible flow when the immiscible fluid plume is much larger than the characteristic length of heterogeneity. However, they stated that the development of appropriate effective parameters to include the effects of small-scale fingering is unfinished. In summary, the described immiscible fluid flow processes are difficult to capture with traditional, local-continuum-based formulations.

When observed from a distance, spreading of an immiscible fluid can resemble the spreading of a conservative tracer in single-phase flow. For this reason, some have advocated immiscible flow with a Fickian dispersion term to account for nonuniformity of the displacement [111, 85]. This approach compares well with a few, high-resolution numerical simulations of immiscible flow. However, one author acknowledged [111] that a Fickian dispersion model will only be valid for random heterogeneities with limited spatial correlation. Further, a diffusion-based flow model will overpredict mixing of the fluids and capillary barriers will be difficult to represent accurately. Numerical smearing at the capillary barrier causes nonphysical migration of the non-wetting phase (NAPL) across a barrier [71]. Once the barrier is broken, relative permeability across the barrier is finite and the continuum model will predict migration of the non-wetting phase.

8.2.2 Streamtube or Streamline Modeling.

Streamtube or streamline modeling offers an efficient method for simulating immiscible displacement for oil recovery in heterogeneous reservoirs. In the streamline technique of Thiele et al. [135], a two- or three-dimensional, single-fluid pressure solution was computed on a fine grid. Particle paths were traced to determine streamlines. These streamlines were used as one-dimensional paths along which a simplified immiscible displacement was computed. Changes in the flow field required recomputation of the streamlines. Rather than map the old interface position to the new streamlines, they elected to project the solution from known initial condition. Therefore, this method is inappropriate for problems with dramatic changes in flow direction. Further, this approach cannot easily include nonuniform initial conditions or the effects of gravity [135].

8.2.3 Network Modeling.

Many researchers have used network models to represent porous media, e.g., [43, 21, 94, 88]. The vast majority of these were pore-scale models in which the size of network components were approximately the size of a soil grain. These models produced capillary-pressure hysteresis with saturation [74] while using very simple fluid flow models at the pore-level. Pore-scale network models also have shown

the ability to simulate capillary entrapment in media with organized heterogeneity larger than individual pores [44]. Most network models have represented fluid flow as quasi-static. In this model, when the driving pressure overcomes a pore's entry pressure, the pore is invaded completely. There are some network models that simulate dynamic fluid flow, assuming Poiseuille flow in each pore [87]. However, there are very few examples of macroscopic network models for immiscible flow through porous media. Of these, most have focused on the representation of interconnected fractures as a network [99]. Yortsos et al. [148] constructed a network model in which each network pore represented a macroscopic region of the porous medium. They simulated quasi-static drainage to examine percolation issues.

8.3 Discrete Numerical Modeling Philosophy for Immiscible Flow

Within a single pore in a porous medium, immiscible flow is not remarkably complicated. Only when we include many interconnected pores, does behavior become complex. The discrete network approach taken here assumes that the same logic applies at the macroscopic scale. We propose to keep the model physics very simple within small lenses of porous material, and rely on resolution to produce complex macroscopic behavior. A stochastic, discrete network approach was chosen to examine immiscible flow.

8.4 Numerical Approximation for Immiscible Flow

Stochastic discrete networks represent a porous medium as many, interconnected, one-dimensional throats (Chapter 5). Flow properties are assigned randomly to the throats. Flow and transport through this discrete network are approximated numerically, assuming perfect advection in the throats and mixing at the connections.

8.4.1 Assigning Throat Properties.

Following the work for conservative transport in Chapter 5, each throat acts as though filled with homogeneous porous material. Assuming a narrow pore-size distribution, one-dimensional immiscible displacement through this medium will occur as a nearly sharp front. This is equivalent to a discontinuous capillary pressure versus saturation curve in traditional modeling context. For such a curve, the macroscopic capillary pressure is defined entirely by the entry pressure and the residual. Given this, the assumption of distinct fluid phases at the macroscopic scale is not

unreasonable. Presently, the throat-level residual is limited to an immobile wetting fluid.

Each throat in the network is assigned a scalar saturated hydraulic conductivity and a single entry head. Both of these values are selected randomly from given distributions. Observations of real soils have indicated that conductivity and capillary pressure are related [38]. For similar soil types, the Leverett J function has been used to relate permeability, k , capillary pressure, P_c , surface tension σ , and porosity, ϕ

$$J(S_w) = \frac{P_c}{\sigma} \sqrt{\frac{k}{\phi}} \quad (8.8)$$

where S_w is the wetting fluid saturation, [-]. Thus, for comparable saturation states and the same fluids and porosity, the quantity $P_c \sqrt{k}$ is nearly constant for the different materials. For each material, a mean hydraulic conductivity \bar{K} and a mean displacement pressure \bar{P}_d are known from their distributions. A constant J value is computed using these mean values and the throat displacement pressures are defined

$$P_{dt} = \bar{P}_d \sqrt{\frac{\bar{K}}{K_t}}. \quad (8.9)$$

This results in perfect, inverse correlation between conductivity and entry pressure or entry head. The displacement pressure is not allowed to fall beneath a prescribed minimum value.

8.4.2 Flow Solution in Each Throat.

Throats in the network are subdivided as necessary into non-uniform-length segments as described in Chapter 5. Each segment in the throat contains a single, mobile fluid phase. Partial saturations are not simulated. Partial phase saturations are computed only when averaging for observation or computation of body forces. Flow through the throats is dynamic. An immobile wetting-phase fluid fraction accounts for residual due to adsorbed water or recirculation in the crevices.

Each discrete segment within a throat contains one mobile fluid mass and m conservative constituent masses. As with saturated flow, flow through the throats is one dimensional. Segments move intact along the throat. The flux profile along the throat is linear for compressible fluids and constant for incompressible fluids. Flux is computed along the throat,

$$q_T = -K_0 \frac{\mu_0}{\mu} \left(\frac{\partial H_0}{\partial l} + \frac{H_c}{L} + \left(\frac{\rho_C}{\rho_0} - 1 \right) g \frac{\partial z}{\partial l} \right) + c_p \rho_0 g \frac{\partial H_0}{\partial t} \quad (8.10)$$

where $q_T =$ flux, $[LT^{-1}]$,
 $K_0 =$ saturated hydraulic conductivity of the throat, $[LT^{-1}]$,
 $\mu_0 =$ dynamic viscosity of fresh water, $[ML^{-1}T^{-1}]$,
 $\mu =$ local dynamic viscosity, $[ML^{-1}T^{-1}]$,
 $H_0 =$ total head expressed in fresh water, $[L]$,
 $H_c =$ capillary head expressed in fresh water, $[L]$,
 $\rho_C =$ density of the fluid/constituent mixture, $[ML^{-3}]$, and
 $g =$ gravitational acceleration, $[LT^{-2}]$.

The differences between saturated flow through a network and immiscible fluid flow through the network are the addition of a capillary force and a more complex fluid distribution scheme at the connections. Capillary force is computed using apparent saturation state of the individual throat taken from the previous time step. This saturation-based capillary force was found to be more stable one based on individual interfaces.

8.4.3 Conservation of Fluid Mass at the Connections.

Total fluid mass is conserved at the connections. This conservation statement permits computation of total head at the connections required to enforce mass conservation over the time step. This process is identical to that given in Chapter 5 with the solution variable being the local total head.

During a time step, each connection accumulates and distributes fluid mass and constituent mass. On the first of two passes, voids are created in 'outbound' throats consistent with the velocities implied by the global head solution. Fluids entering the connection must be distributed logically to fill these voids. Logically, the most non-wetting fluid would seek out the throat with the smallest entry pressure. Therefore, 'outbound' throats at a connection are filled in order of decreasing entry pressure (the throst with the highest entry head is filled first). Reservoirs of accumulated fluid at each connection are depleted in order of decreasing wettability (Figure 8.3). Constituents are fully mixed within each phase at the connections. Presently, no interphase constituent mass transfer is permitted, although it would be straightforward to do so.

8.5 Results of Network Model Simulation

Immiscible flow was examined in several network model media. The network model is three dimensional. To save computation time, these simulations were made in a quasi-two-dimensional domain.

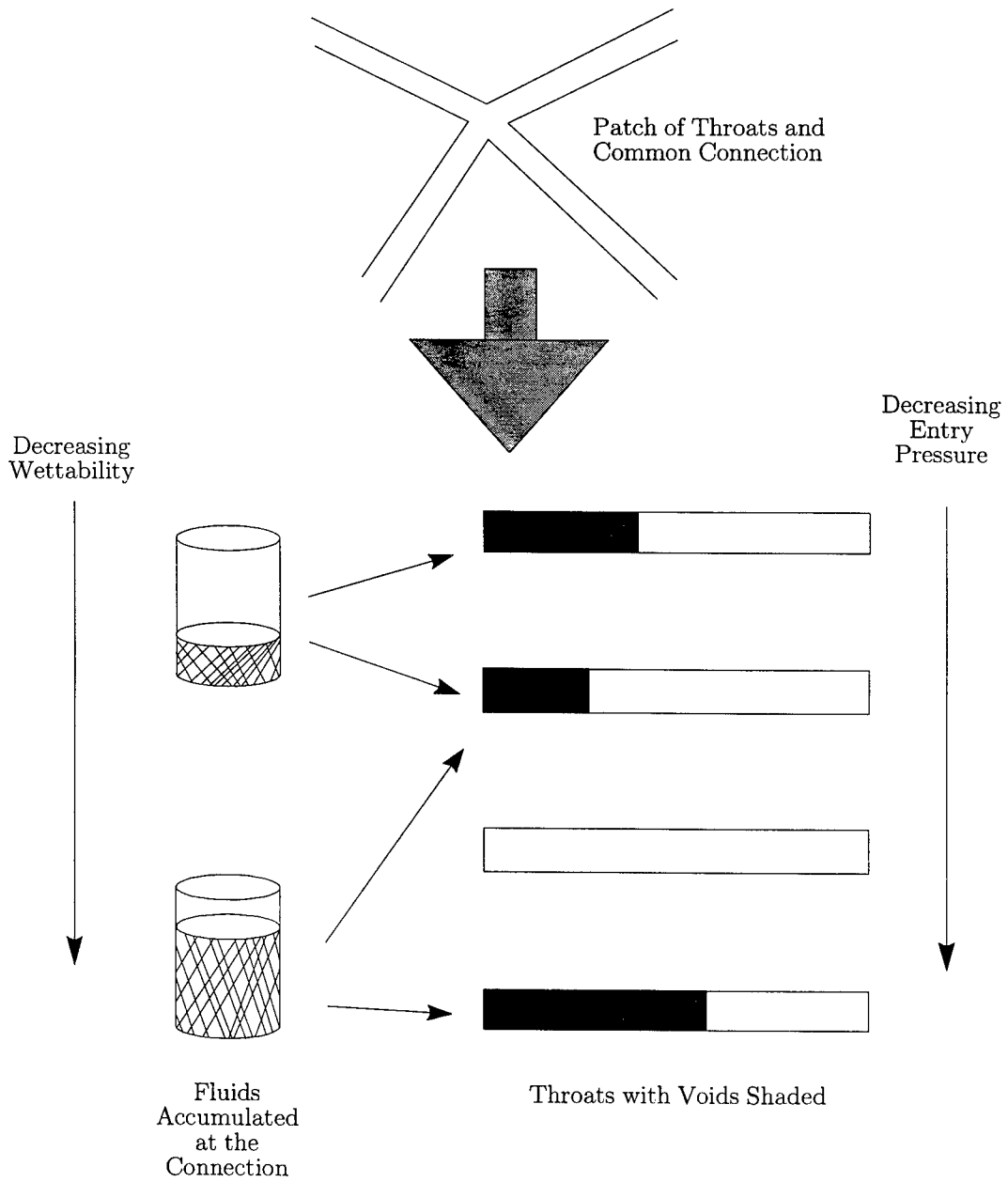


Figure 8.3: Procedure for filling voids in the throats.

8.5.1 Immiscible Displacement.

A network was created in the $x-y$ plane to represent a porous slab 100 *cm* by 100 *cm* and 10 *cm* thick. The network was filled initially with wetting fluid. The downstream boundary was assigned a constant total head of wetting fluid equal to 100 *cm*. The upstream boundary was assigned a constant non-wetting-fluid head of 150 *cm*. The remaining boundaries were defined solid. A very small variance in conductivity (0.1) was assigned isotropically. The mean and minimum entry heads were set to 5.0 *cm*. The fluids were assumed incompressible, with identical specific gravities and specific viscosities. Figure 8.4 shows the apparent saturations of the displacement upon averaging to the observation mesh. At this observation resolution, the displacement front looks non-uniform with obvious small-scale channeling. By averaging the same network simulation to a coarser observation mesh, the displacement front appears much smoother and more uniform (Figure 8.5).

8.5.2 Spontaneous Imbibition.

A network with similar dimensions was created in the $x-z$ plane to explore gravity drainage and imbibition. Throat conductivities were assigned from a lognormal distribution with a variance of 1.0. Entry heads were assigned with Equation 8.9 using a mean entry head of 10 *cm* and a minimum entry head of 10 *cm* (Figure 8.6). Initially, the network throats were filled completely with non-wetting fluid (no residual wetting fluid). The specific gravities of the wetting and non-wetting fluids were set to 1.0 (water) and 0.00123 (air), respectively. The bottom boundary of the network was established as a reservoir of wetting fluid with a head equal to the static head of the non-wetting fluid (0.123 *cm*). The top boundary was attached to a reservoir of non-wetting fluid with a total head of 100 *cm*, implying a pressure head of zero (gage). Spontaneous imbibition pulled the wetting fluid into the network. Imbibition ceased when the capillary force was offset by the self-weight of the wetting fluid (Figure 8.7). Behind the imbibition front, the medium contains very little residual non-wetting fluid. The height of capillary rise is only slightly larger than the minimum entry head of 10 *cm*. Although many throats with larger entry heads exist in the network, the height of capillary rise is restricted to continuous paths of high entry pressure.

8.5.3 Primary Drainage.

The same network and boundary conditions used for imbibition were used to investigate drainage. The network was initially filled with wetting fluid. The heavier wetting fluid was displaced through the bottom boundary by the lighter non-wetting

sat2 : 600,171
1.000
0.900
0.800
0.700
0.600
0.500
0.400
0.300
0.200
0.100
0.000

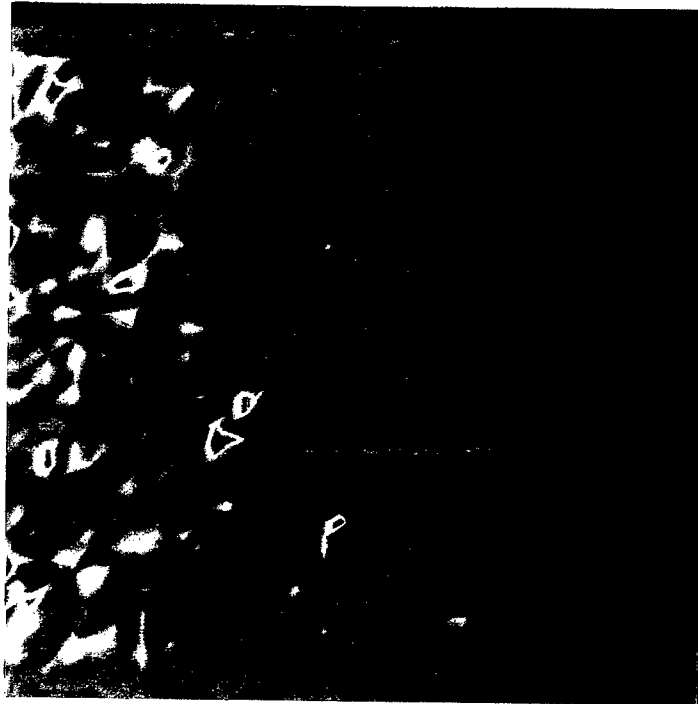


Figure 8.4: Contours of apparent saturation for fine observation of immiscible displacement.

sat2 : 600,171
0.720
0.660
0.600
0.540
0.480
0.420
0.360
0.300
0.240
0.180
0.120
0.060
-0.000



Figure 8.5: Contours of apparent saturation for coarse observation of immiscible displacement.

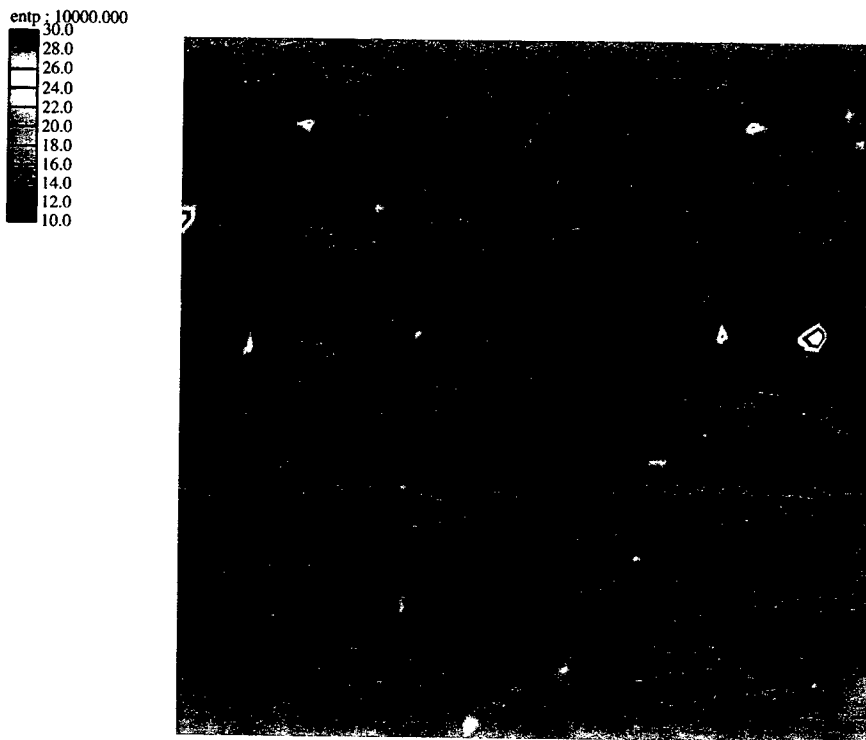


Figure 8.6: Contours of spatially-averaged entry head for the two-dimensional porous slab.

sat1 : 800.024
1.00
0.90
0.80
0.70
0.60
0.50
0.40
0.30
0.20
0.10
0.00

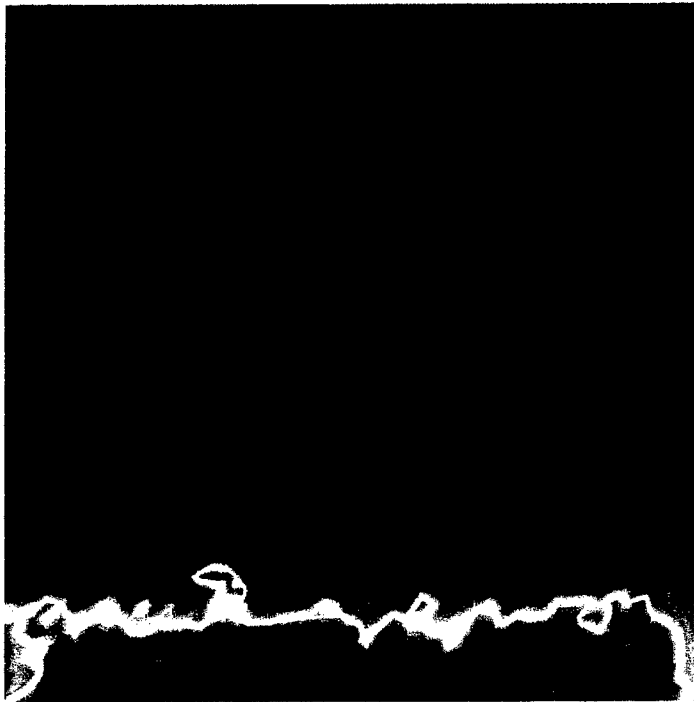


Figure 8.7: Contours of apparent saturation for imbibition in the network.

fluid entering at the top. Contours of the apparent saturation of non-wetting fluid near equilibrium are shown in Figure 8.8. Substantial entrapment of wetting fluid is observed throughout the domain. The magnitude of wetting-phase residuals seem physically unrealistic, but are appropriate for the physics represented in the network. Each throat drains when the weight of fluid overcomes the capillary resistance. The weight of fluid is controlled by the orientation of the throat while capillary force is independent of orientation. Thus, nearly horizontal throats experience very little drainage of the wetting phase. This saturation profile confirms that the network behaves differently than a one-dimensional bundle of capillaries [75]. In the network, we must consider interconnectivity and orientation of the throats.

8.5.4 Capillary Hysteresis.

If the entire simulation network is treated as a single porous medium sample, we may determine composite capillary pressure versus saturation ($P_c - S$) curves. A capillary pressure versus saturation curve may be developed by applying known wetting and non-wetting phase pressures to the boundaries of the network and observing average saturations. These experiments have been performed with quasi-static, pore-scale network models for several years [131]. Because the macroscopic network is functionally similar to these pore scale networks, one expects similar behavior, although at a different scale. Non-wetting residual at the throat level is not modeled explicitly. Thus, non-wetting residual occurs by larger-scale bypassing of throats containing non-wetting fluid.

Figure 8.9 shows drainage followed by imbibition. For these tests, both fluids have the same specific gravity. The medium is filled initially with wetting fluid. The non-wetting fluid head is increased incrementally until the medium ceases to drain with increasing non-wetting fluid head. The medium was allowed to equilibrate for each combination of boundary pressures. For these medium and fluid properties, drainage stops at an average wetting-fluid saturation near 0.3. The non-wetting fluid head is then gradually decreased, permitting the wetting fluid to displace the non-wetting fluid. Some of the non-wetting fluid remains in the medium, causing hysteresis in the capillary pressure versus saturation curves.

8.5.5 Capillary Barrier.

A vertical porous slab was created with two types of material (Figure 8.10). Throats lying in the upper material were assigned a uniform entry head of 10 *cm*. Throats in the lower material were assigned entry heads from a one-sided distribution with a mean of 45 *cm* and a minimum of 45 *cm* with variance assigned through the Leverett scaling process. Figure 8.11 shows contours of the entry head for the

sat1 : 10000.000
1.000
0.900
0.800
0.700
0.600
0.500
0.400
0.300
0.200
0.100
0.000



Figure 8.8: Contours of apparent saturation for gravity drainage in the network.

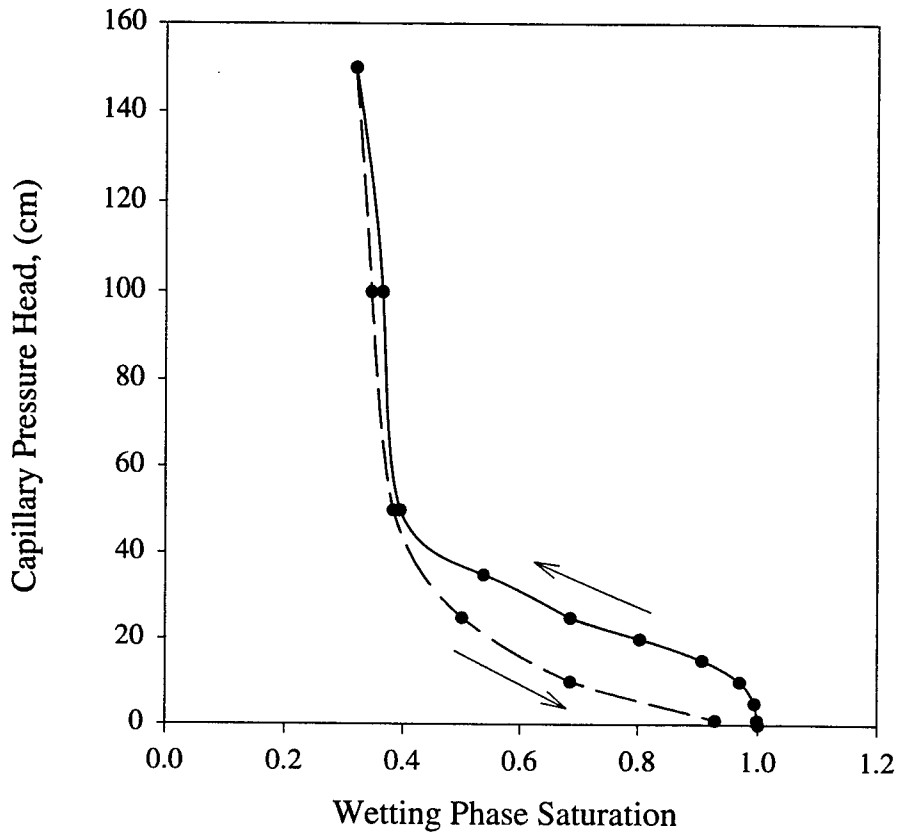


Figure 8.9: Capillary pressure versus wetting-fluid saturation for drainage and imbibition.

capillary barrier problem. An immiscible, non-wetting fluid with a specific gravity of 2.0 was injected at a point above the material discontinuity. The non-wetting fluid proceeded downward and spread. As the dense, immiscible fluid came in contact with the capillary barrier, it spread laterally and began to pond. Non-wetting fluid saturations in the plume remained much less than 1.0. Flow in the throats crossing the boundary ceased at the first appearance of the non-wetting fluid. Therefore, any wetting fluid that is bypassed during the initial invasion has no path to escape. As the head above the material interface increased, the capillary barrier was overcome. Displacement occurs only at a few, localized 'weak' points rather than a large front. Further, the displacement appeared to be discontinuous in time. This is physically similar to the breakthrough processes observed in the laboratory [22]. To produce this behavior with traditional, discretized continuum models would require a more complex, two- or three-dimensional computation on a very highly resolved mesh.

8.6 Conclusions and Additional Work

At the pore scale, immiscible fluids remain distinct. When these fluids are described as a continuous mixture, constitutive parameters must be concocted to describe the macroscopic effects of the fluid-fluid interfaces. These constitutive parameters are complex to implement numerically, difficult to measure, and incapable of predicting some observed physics.

This discrete network modeling approach for immiscible flow retains distinct fluid phases in a macroscopic representation of the medium. The network model produces reasonable, macroscopic immiscible flow behavior without relying on complex constitutive models. Capillary hysteresis emerges from simulation with the network. The network simulates the correct physical phenomena behind capillary barriers and non-wetting phase residuals. However, because flow solutions in the throats are one-dimensional, it tends to overestimate wetting phase residuals for the gravity drainage problem. The present computational scheme is acceptable for small gradients in entry head. However, because the applied capillary force is determined from the prior time step, the time step may become quite small when a moving interface encounters a material discontinuity. An improved scheme for applying capillary force should be derived.

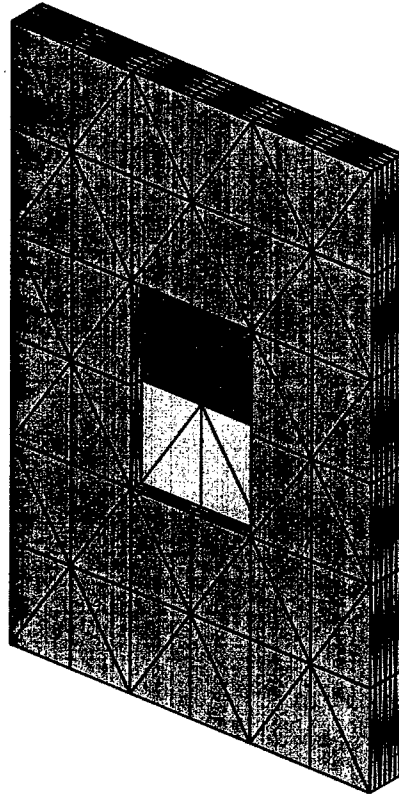


Figure 8.10: Diagram of the material types used to simulate a capillary barrier. The green material around the exterior defines a bounding box used only for network generation.

entp: 1800.010
56.0
52.0
48.0
44.0
40.0
36.0
32.0
28.0
24.0
20.0
16.0
12.0
8.0

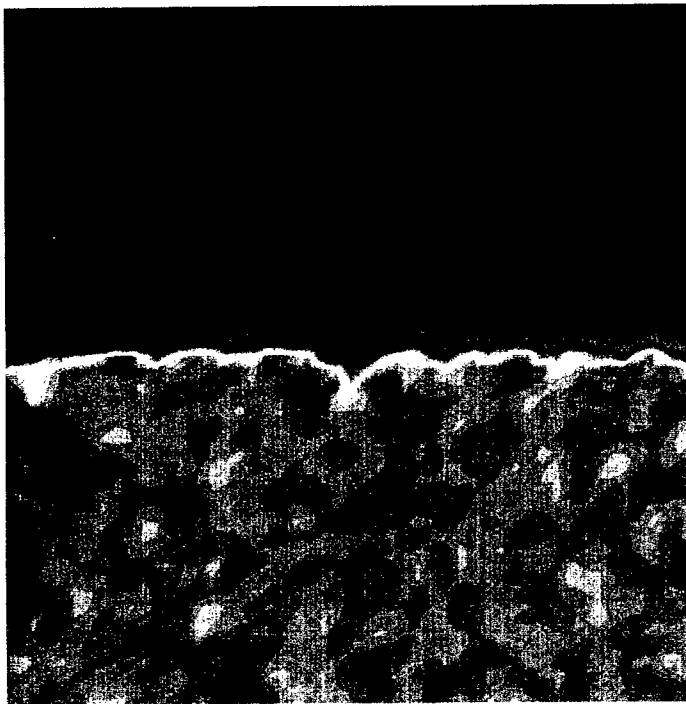


Figure 8.11: Contours of entry head for the capillary barrier problem.

sat2 : 600.019

1.00
0.90
0.80
0.70
0.60
0.50
0.40
0.30
0.20
0.10
0.00



Figure 8.12: Contours of apparent saturation for the capillary barrier problem.

sat2 : 1800.010
1.00
0.90
0.80
0.70
0.60
0.50
0.40
0.30
0.20
0.10
0.00

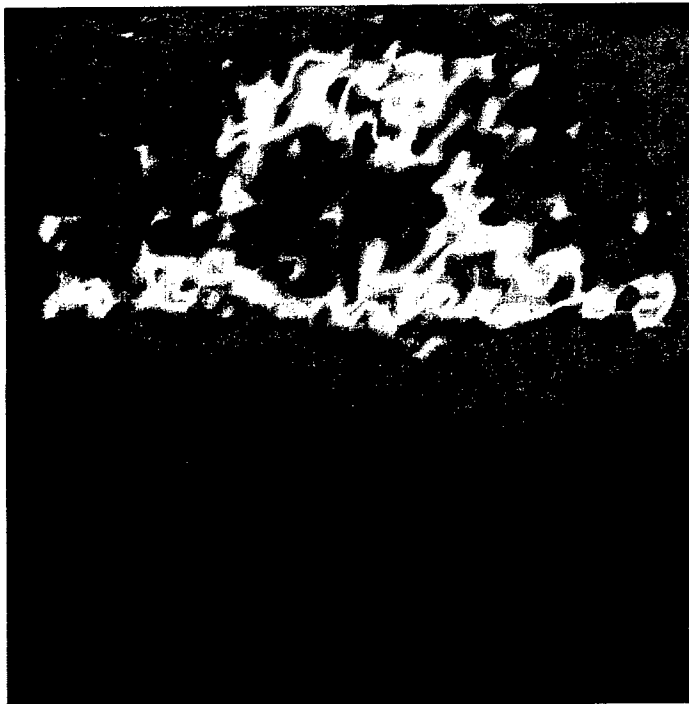


Figure 8.13: Contours of apparent saturation showing localized breakdown of the capillary barrier problem.

Chapter 9

Conclusions and Future Directions

Our drinking water supply is priceless. However, in the near future, the depth of our society's pockets will be tested by the cost of environmental remediation. To minimize these costs, effective groundwater remediation schemes must be designed and operated using field and laboratory testing and credible numerical simulation of fluid flow and contaminant fate and transport. Natural heterogeneity compromises our ability to use laboratory and field measurements in concert with field-scale numerical simulation.

9.1 Brief Summary of Findings

This study concludes that the best approach for simulating fluid flow and contaminant transport in heterogeneous media is to resolve as much detail (even statistical detail) as possible, relying on constitutive parameters only at the finest scale resolvable. Measurements of macroscopic, effective flow and transport parameters may depend strongly on the measurement scale and technique. Time-dependent or tracer-plume-scale dependent equation coefficients are valid only for particular situations (an instantaneous point source in a macroscopically-uniform flow field). Rather than extend these effective parameters, this effort focused on the efficient representation of discrete structure to reproduce macroscopic behavior.

Highly-resolved discrete structure may be achieved in several ways,

- finely-discretized continuum modeling with random conductivity fields,
- stochastic discrete network modeling presented here, and
- particle-based transport modeling.

Present computing resources are considerable, but not infinite. Therefore, resolution must be included intelligently. Discretized continuum models normally require the number of pressure and velocity unknowns to be approximately equal. Network modeling permits some decoupling of the pressure and velocity resolutions because pressure is computed at the network connections and velocity in the throats. Thus, the coordination number controls the ratio of velocity to pressure unknowns. Particle-based transport schemes permit almost complete separation of the flow and transport resolution, but detailed velocity structure is needed to produce the proper dispersive behavior. Coarse resolution in the velocity fields might be coupled with a correlated-random walk approach to simulate dispersion [123, 122, 108].

Simulating saturated fluid flow with a discrete network and with a comparably-discretized continuum model produces similar answers with similar computational cost. However, the network structure offers a potentially more efficient way to model transport. It allows direct inclusion of characteristic length and conductivity distributions in the model medium. This permits us to reproduce the velocity structure and variability that dictate dispersion. For this reason, the network reproduces observed plume growth behavior, physically-correct, wholly-downstream dispersion (in the absence of molecular diffusion), and reasonable matches to laboratory scale observations. Further, this nearly direct connection with the velocity statistics makes it possible to condition networks to model large-scale heterogeneity explicitly. For isotropic media, networks may be created with approximately the correct effective conductivity and asymptotic dispersivity. In the pre-asymptotic regime, plumes in the network grow nearly linearly with plume size. Thus, network structure dictates transport behavior and is not invalidated by changes in hydrologic conditions or contaminant configurations.

Because the philosophy here is to model, discretely, the distribution of characteristic lengths, the resolution required increases substantially with the degree of homogeneity. The network has a tendency to overpredict dispersion in a homogeneous material. This resolution requirement also exists with discretized continuum models that suffer from numerical dissipation of large gradients.

9.2 Ideas for Future Work

Much remains to be explored in the use of stochastic discrete networks for modeling flow and transport through porous media. Specific work may be grouped into the following categories:

- exploring behavior and correctness of the existing model.
- conditioning networks to honor site-specific data.

- improving numerical accuracy and speed,
- incorporating additional processes.

The network model is a non-traditional, unstructured, n -phase, m -component, locally-adaptive numerical model for simulating steady or transient flows with variable density and viscosity and conservative transport with mobile and immobile fluid fractions. Many aspects of this model remain unverified. For example, the model contains the framework for three-phase flow, but throat-scale constitutive rules for applying a capillary force with three or more phases are missing. Because the macroscopic, discrete network is a non-traditional modeling technique, additional confirmation is needed to support the network's credibility as a valid alternative. The network should be applied to additional laboratory data sets and to documented field data. Density-dependent and multi-phase flow behavior in the network appears reasonable, but should be explored thoroughly and compared to observations. The network demonstrated an ability to produce miscible fingering. Finger spacing should be checked against stability theory [56] and compared to laboratory observations.

We must also extend our ability to create networks that honor field observations. The procedure for network creation (Chapter 6) has a theoretical foundation, but requires empirical equations to establish a few parameters. The range of validity of these equations must be determined. Further, conditioning networks in anisotropic media must be examined.

To this point, more attention has been paid to process descriptions than computational speed and efficiency. Explicit transport computations often require a small time step size. The step size is limited by a Courant condition that is the shortest time to evacuate a throat. This restrictive time step size might be relaxed by adopting a reasonable transport step size for accuracy, and using a semi-implicit scheme to compute direct mass transfer from the upstream to the downstream connection during the step. This would sacrifice some time accuracy by permitting a numerical smearing for the sake of increased speed.

Immiscible flow in the network is computationally inefficient because velocities resulting from the application of large capillary forces cause severe time-step restrictions. Improved schemes for damping oscillations near a discontinuity in capillary pressure are needed.

This work has demonstrated that pressure solutions are much less sensitive to the underlying network structure than are transport computations. This suggests that the network structure itself might be adapted in time to be coarse in regions without constituent transport and more detailed in regions with transport. This

might be accomplished by imbedding simple structures for which the flow solution is known without computation (e.g., a Wheatstone bridge). This structure would provide the same fluid flux for the equivalent structures, but a variety of velocities to cause dispersion. Further, transport computations might easily be limited to those throats containing constituent mass.

Other network generation ideas may be explored. Presently, distribution of connections randomly in the domain is a time-consuming process because a minimum interconnection spacing is enforced. Perhaps nodes from an automatically-generated tetrahedral mesh might define connection locations for the network. This approach would control interconnection spacing and build on years of previous research. Instead of assigning throat properties from a material mesh, geostatistics might be used to assign patch-level statistics. Throats leaving a connection would be given attributes to honor patch-level statistics.

The network model's capabilities should be expanded to include additional processes needed to simulate remediation. Molecular diffusion, simple sorption, and reaction should be added. The network should be able to discriminate between diffusion-limited retardation and actual sorption. At present, porosity is assigned to be a constant value globally. Porosity should be assigned randomly from distributions keyed to material type.

An intriguing feature of the network model is the distribution of concentrations it produces within an observational-averaging volume. In the network, throats are subdivided into segments, each containing fluid masses and constituent masses. Because each throat knows nothing about its position relative to the other throats, network results must be averaged to an observation mesh for interpretation and comparison to observations. Therefore, each observation-mesh average value may contain contributions from tens of throats and hundreds of segments, each with a potentially different concentration. Observation in real soils is a similar process. A sample of fluid is withdrawn and fully mixed. Fluids contributing to the sample may have had different concentrations, even though they were very near each other. For some reactions, knowing the average concentration in a region is adequate. However, some reactions require certain critical conditions (e.g., a threshold concentration) to proceed. An average value may suggest that no reaction is occurring, but locally, the necessary conditions may exist.

To demonstrate local variability in concentration, a quasi-two-dimensional network with about 11,000 connections and 50,000 throats was used to simulate growth of an instantaneous point source. The network domain was 2,500 *m* long and 1,500 *m* wide and 10 *m* thick. An observation mesh of 81 x 51 x 2 was used to view the plume. A single node was selected at the center of the observation mesh. For

a single snapshot in time, all segment concentrations contributing to that node's average concentration were tabulated. A frequency histogram of these 987 individual segment concentrations was created (Figure 9.1). The volume-averaged nodal concentration in the observation mesh is 0.97 g/m^3 , but many segment values were nearly twice the average value. Further, over 40 percent of the segments contained no constituent mass. There is no evidence to suggest that the distribution of concentrations found in the network resembles the distribution in real soils, but it is an interesting area for study.

The discrete network reaffirms that highly-resolved models with simple model physics can simulate flow and transport processes in both the early-time and late-time regimes. Compared to other high-resolution models, the discrete network offers a more efficient and direct means of representing spatially-uncertain discrete structure. The model also shows promise for modeling elusive multi-fluid flow processes.

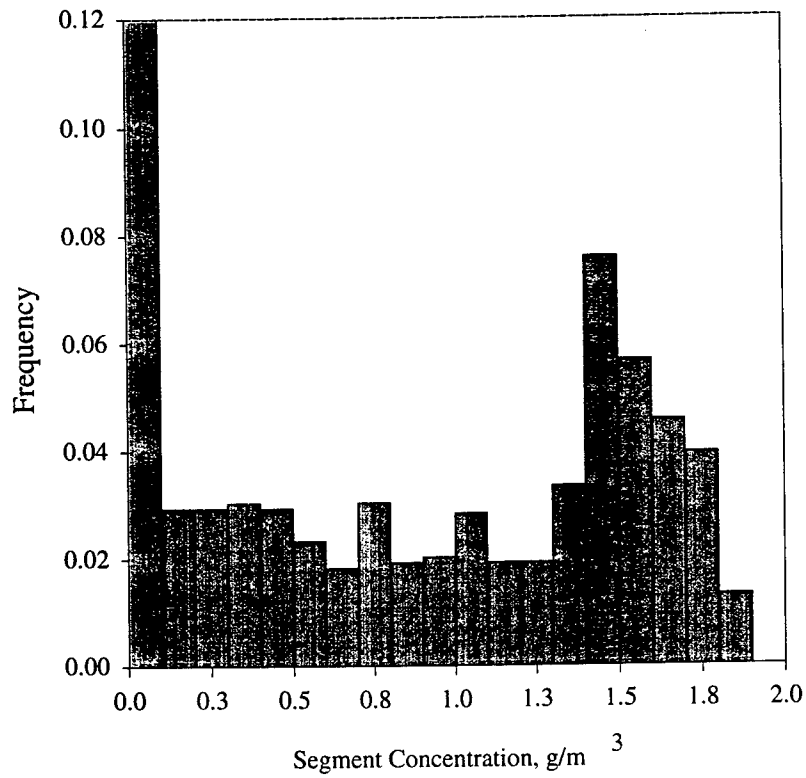


Figure 9.1: Histogram of concentration within a single observational-averaging volume.

Bibliography

- [1] M. P. Allen and D. J. Tildesley. *Computer Simulation of Liquids*. Oxford University Press, Oxford, 1989.
- [2] M. P. Anderson. "Movement of Contaminants in Groundwater: Groundwater Transport - Advection and Dispersion". In *Groundwater Contamination*, pages 37–45. National Academy Press, Washington, DC, 1984.
- [3] R. Aris. "On the Dispersion of a Solute in a Fluid Flowing Through a Tube". *Proceedings of the Royal Society of London*, A235:67–77, 1956.
- [4] A. Arya, T. A. Hewett, R. G. Larson, and L. W. Lake. "Dispersion and Reservoir Heterogeneity". *Society of Petroleum Engineers Reservoir Engineering*, pages 110–119, 1988.
- [5] Y. Bachmat and J. Bear. "Macroscopic Modeling of Transport Phenomena I: The Continuum Approach". *Transport in Porous Media*, 1:213–240, 1986.
- [6] G. K. Batchelor. *Fluid Dynamics*. Cambridge University Press, Cambridge, 1967.
- [7] P. Baveye and G. Sposito. "The Operational Significance of the Continuum Hypothesis in the Theory of Water Movement Through Soils and Aquifers". *Water Resources Research*, 20(5):521–530, 1984.
- [8] J. Bear. *The Transition Zone Between Fresh and Salt Waters in Coastal Aquifers*. PhD thesis, University of California, Berkeley, CA, 1960.
- [9] J. Bear. "Some Experiments in Dispersion". *Journal of Geophysical Research*, 66(8):2455–2467, 1961.
- [10] J. Bear. *Dynamics of Flow in Porous Media*. American Elsevier, New York, 1972.

- [11] J. Bear and Y. Bachmat. "Transport Phenomena in Porous Media - Basic Equations". In *Fundamentals of Transport Phenomena in Porous Media*, pages 3-61. Martinus Nijhoff Publishers, Dordrecht, 1984.
- [12] J. Bear and C. Braester. "On the Flow of Two Immiscible Fluids in Fractured Porous Media". In *Proceedings of the First Symposium on Fundamentals of Transport Phenomena in Porous Media*, pages 177-202, New York, 1972. Elsevier.
- [13] R. B. Bird, W. E. Stewart, and E. N. Lightfoot. *Transport Phenomena*. John Wiley and Sons, New York, 1960.
- [14] N. Bjerrum and E. Manegold. *Kolloid Z.(USSR)*, 43(5), 1927.
- [15] J. P. Boon and S. Yip. *Molecular Hydrodynamics*. Dover, New York, 1980.
- [16] J. Bredehoeft. "Much Contaminated Ground Water Can't Be Cleaned Up". *Groundwater*, 30(6):834-835, 1992.
- [17] H. Brenner. *Macrotransport Processes*. Butterworth-Heinemann, Boston, 1993.
- [18] R. H. Brooks and A. T. Corey. "Hydraulic Properties of Porous Media". Technical Report 3, Colorado State University, Fort Collins, CO, 1964.
- [19] M. B. Butts and K. H. Jensen. "Effective Parameters for Multiphase Flow in Layered Soils". *Journal of Hydrology*, 183:101-116, 1996.
- [20] G. F. Carey and J. T. Oden. *Finite Elements: Computational Aspects: Volume III*. Prentice-Hall, Englewood Cliffs, NJ, 1984.
- [21] I. Chatzis and F. A. L. Dullien. "Modeling Pore Structure by 2-D and 3-D Networks with Application to Sandstones". *Journal of Canadian Petroleum Technology*, January-March:97-108, 1977.
- [22] R. Compos. "Spatial Analysis of Non-Aqueous Phase Liquid Entrapment Distribution in Heterogeneous Soil". Master's thesis, University of Colorado, 1997.
- [23] J. H. Cushman. "Volume Averaging, Probabilistic Averaging, and Ergodicity". *Advances in Water Resources*, 6:182-184, 1983.
- [24] J. H. Cushman. "On Unifying Concepts of Scale, Instrumentation, and Stochastics in the Development of Multiphase Transport Theory". *Water Resources Research*, 20(11):1668-1676, 1984.

- [25] J. H. Cushman and T. R. Ginn. "Nonlocal Dispersion in Media with Continuously Evolving Scales of Heterogeneity". *Transport in Porous Media*, 13:123-138, 1993.
- [26] J. H. Cushman and T. R. Ginn. "On Dispersion in Fractal Porous Media". *Water Resources Research*, 29(10):3513-3515, 1993.
- [27] J. H. Cushman and B. X. Hu. "A Resume of Nonlocal Transport Theories". *Stochastic Hydrology and Hydraulics*, 9:105-116, 1995.
- [28] G. Dagan. "Models of Groundwater Flow in Statistically Homogeneous Porous Formations". *Water Resources Research*, 15(1):47-63, 1979.
- [29] G. Dagan. "Statistical Theory of Groundwater Flow and Transport: Pore to Laboratory, Laboratory to Formation, and Formation to Regional Scale". *Water Resources Research*, 22(9):120S-134S, 1986.
- [30] G. Dagan. *Flow and Transport in Porous Formations*. Springer-Verlag, Berlin, Germany, 1989.
- [31] G. Dagan. "Higher Order Correction of Effective Permeability of Heterogeneous Isotropic Formations of Lognormal Conductivity Distribution". *Transport in Porous Media*, 12:279-290, 1993.
- [32] G. de Josselin de Jong. "Longitudinal and Transverse Diffusion in Granular Deposits". *Transactions of the American Geophysical Union*, 39(1):67-74, 1958.
- [33] G. de Marsily. *Quantitative Hydrogeology: Groundwater Hydrology for Engineers*. Academic Press, Orlando, FL, 1986.
- [34] A. J. Desbarats. "Spatial Averaging of Hydraulic Conductivity in Three-dimensional Heterogeneous Porous Media". *Mathematical Geology*, 24:273-286, 1992.
- [35] C. V. Deutsch and A. G. Journel. *GSLIB: Geostatistical Software Library and User's Guide*. Oxford University Press, New York, 1992.
- [36] P. Döll and W. Schneider. "Lab and Field Measurements of the Hydraulic Conductivity of Clayey Silts". *Groundwater*, 33(6):884-891, 1995.
- [37] J. C. I. Dooge. "Looking for Hydrologic Laws". *Water Resources Research*, 22(9):46S-58S, 1986.

- [38] F. A. L. Dullien. *Porous Media: Fluid Flow and Pore Structure*. Academic Press, San Diego, CA, second edition, 1991.
- [39] D. Edelin. "Part II: Nonlocal Field Theories". In A. C. Eringen, editor, *Continuum Physics, Volume IV: Polar and Non-Local Field Theories*, pages 75–204. Academic Press, New York, 1976.
- [40] A. C. Eringen. *Mechanics of Continua*. John Wiley and Sons, New York, 1976.
- [41] A. C. Eringen. "Part III: Nonlocal Polar Field Theories". In A. C. Eringen, editor, *Continuum Physics, Volume IV: Polar and Nonlocal Field Theories*, pages 205–267. Academic Press, New York, 1976.
- [42] R. P. Ewing and S. C. Gupta. "Modeling Percolation Properties of Random Media Using a Domain Network". *Water Resources Research*, 29(9):3169–3178, 1993.
- [43] I. Fatt. "The Network Model of Porous Media I. Capillary Pressure Characteristics". *Transactions of the American Institute of Mechanical Engineering*, 207:144–159, 1956.
- [44] L. A. Ferrand and M. A. Celia. "The Effect of Heterogeneity on the Drainage Capillary Pressure-Saturation Relation". *Water Resources Research*, 28(3):859–870, 1992.
- [45] S. Follin. *Numerical Calculations of Heterogeneity of Groundwater Flow*. PhD thesis, Royal Institute of Technology, Stockholm, 1992.
- [46] R. A. Freeze and J. A. Cherry. *Groundwater*. Prentice-Hall, Englewood Cliffs, NJ, 1979.
- [47] J. J. Fried. *Groundwater Pollution*. Elsevier, Amsterdam, 1975.
- [48] U. Frisch. *Probabilistic Methods in Applied Mathematics*. Academic Press, New York, 1968.
- [49] U. Frisch, B. Hasslacher, and Y. Pomeau. "Lattice-Gas Automata for the Navier-Stokes Equation". *Physical Review Letters*, 56(14):1505–1508, 1986.
- [50] H. M. Gaber, S. D. Comport, W. P. Inskeep, and H. A. El-Attar. "A Test of the Local Equilibrium for Adsorption and Transport of Picloram". *Journal of Soil Science Society of America*, 56:1392–1400, 1992.

- [51] J. E. Garcia. An experimental investigation of upscaling of water flow and solute transport in saturated porous media. Master's thesis, University of Colorado, 1995.
- [52] L. W. Gelhar. "Stochastic Subsurface Hydrology From Theory to Applications". *Water Resources Research*, 22(9):129-139, 1986.
- [53] L. W. Gelhar. *Stochastic Subsurface Hydrology*. Prentice-Hall, Englewood Cliffs, NJ, 1993.
- [54] L. W. Gelhar and C. L. Axness. "Three-Dimensional Stochastic Analysis of Macrodispersion in Aquifers". *Water Resources Research*, 19(1):161-180, 1983.
- [55] L. W. Gelhar, C. Welty, and K. R. Rehfeldt. "A Critical Review of Data on Field-Scale Dispersion in Aquifers". *Water Resources Research*, 28(7):1955-1974, 1992.
- [56] R. J. Glass, J-Y. Parlange, and T. S. Steenhuis. "Wetting Front Instability 1. Theoretical Discussion and Dimensional Analysis". *Water Resources Research*, 25(6):1187-1194, 1989.
- [57] A. L. Gutjahr, L. W. Gelhar, A. A. Bakr, and J. R. Macmillan. "Stochastic Analysis of Spatial Variability in in Subsurface Flows, 2: Evaluation and Applications". *Water Resources Research*, 14(5):953-959, 1978.
- [58] C. A. Hall, A. Porsching, and G. L. Messina. "On a Network Method for Unsteady Incompressible Fluid Flow on Triangular Grids". *International Journal for Numerical Methods in Fluids*, 15:1383-1406, 1992.
- [59] A. E. Hassan, J. H. Cushman, and J. W. Delleur. "The Significance of Porosity Variability to Flow and Transport in Randomly Heterogeneous Porous Media". in review.
- [60] M. Hassanizadeh and W. G. Gray. "General Conservation Equations for Multi Phase Systems: 1. Averaging Procedure". *Advances in Water Resources*, 2:131-141, 1979.
- [61] S. M. Hassanizadeh. "On the Transient Non-Fickian Dispersion Theory". *Transport in Porous Media*, 23:107-124, 1996.
- [62] S. M. Hassanizadeh and W. G. Gray. "Mechanics and Thermodynamics of Multiphase Flow in Porous Media Including Interphase Boundaries". *Advances in Water Resources*, 13(4):169-185, 1990.

- [63] S. M. Hassanizadeh and W. G. Gray. "Toward an Improved Description of the Physics of Two-Phase Flow". *Advances in Water Resources*, 16:53-67, 1993.
- [64] J. P. Heller. In D. E. Elrick, editor, "*Proceedings of the Second International Conference on Fundamentals of Transport Phenomena in Porous Media*", page 1, Guelph, Canada, 1972. International Association of Hydraulic Research.
- [65] R. Herrmann, P. Hubert, and H. Kobus. "The sub-systems: Groundwater". *Journal of Hydraulic Research*, 9:49-56, 1991. Extra issue.
- [66] J. Horno, C. F. Gonzàles-Fernàndez, and A. Hayas. "The Network Method for Solutions of Oscillating Reaction-Diffusion Systems". *Journal of Computational Physics*, 118:310-319, 1995.
- [67] M. K. Hubbert. "Darcy's Law and the Field Equations of the Flow of Underground Fluids". *American Institute of Mining, Metallurgical, and Petroleum Engineers, Transactions*, 207:222-239, 1956.
- [68] J. R. Hunt, N. Sitar, and K. S. Udell. "Nonaqueous Phase Liquid Transport and Cleanup 1. Analysis of Mechanisms". *Water Resources Research*, 24(8):1247-1258, 1988.
- [69] C. W. Rovey III and D. S. Cherkauer. "Scale Dependency of Hydraulic Conductivity Measurements". *Groundwater*, 33(5):769-780, 1995.
- [70] T. H. Illangasekare. "Upscaling of Water and Solute Transport in Porous Media: Final Report". Technical report, University of Colorado at Boulder, 1995.
- [71] T. H. Illangasekare, D. N. Yates, E. Armbruster, J. Wald, and D. D. Reible. "Laboratory Evaluation of Limitations of Conventional Numerical Multiphase Flow Models in Porous Media". In T. F. Russell et al, editor, *Computational Methods in Water Resources IX, Vol. 2*, pages 289-296, Southampton, U. K., 1992. Computational Mechanics Publications.
- [72] N. C. Irwin, M. M. Botz, and R. A. Greenkorn. "Experimental Investigation of Characteristic Length Scale in Periodic Heterogeneous Porous Media". *Transport in Porous Media*, 25:235-246, 1996.
- [73] E. H. Isaaks and R. M. Srivastava. *An Introduction to Applied Geostatistics*. Oxford University Press, New York, 1989.

- [74] G. R. Jerould and S. J. Salter. "The Effect of Pore-Structure on Hysteresis in Relative Permeability and Capillary Pressure: Pore-Level Modeling". *Transport in Porous Media*, 5:103–151, 1990.
- [75] W. A. Jury. *Soil Physics*. John Wiley, New York, 1991.
- [76] G. Karypis and V. Kumar. "Parallel Multilevel Graph Partitioning". Technical Report TR 95-036, Univeristy of Minnesota, 1995.
- [77] J. B. Keller. "Wave Propagation in Random Media". *Proceedings of Symposia in Applied Mathematics*, 13:227–246, 1962.
- [78] P. R. King. "Upscaling Permeability: Error Analysis for Renormalization". *Transport in Porous Media*, 23:337–354, 1995.
- [79] P. R. King, A. H. Muggeridge, and W. G. Price. "Renormalization Calculations of Immiscible Flow". *Transport in Porous Media*, 12:237–260, 1993.
- [80] D. L. Koch and J. F. Brady. "A Non-Local Description of Advection-Diffusion with Application to Dispersion in Porous Media". *Journal of Fluid Mechanics*, 180:387–403, 1987.
- [81] D. L. Koch and J. F. Brady. "Nonlocal Dispersion in Porous Media: Nonmechanical Effects". *Chemical Engineering Science*, 42(6):1377–1392, 1987.
- [82] W. B. Krantz. "Scaling Initial and Boundary Value Problems as a Teaching Tool for a Course in Transport Phenomena". *Chemical Engineering Education*, pages 145–152, 1970.
- [83] B. H. Kueper and E. O. Frind. "An Overview of Immiscible Fingering in Porous Media". *Journal of Contaminant Hydrology*, 2:95–110, 1988.
- [84] Lawrence Livermore National Laboratory. "www.llnl.gov/casc/parflow". Technical Report UCRL-TB-118581 Rev. 1, University of California, October 1996.
- [85] P. Langlo and M. S. Espedal. "Macrodispersion for Two-Phase, Immiscible Flow in Porous Media". *Advances in Water Resources*, 17:297–316, 1994.
- [86] R. Lenormand. "Use of Fractional Derivative for Fluid Flow in Heterogeneous Media". In *Proceedings of the 3rd European Conference on Mathematics of Oil Recovery*, Delft, 1992.

- [87] R. Lenormand, E. Toulboul, and C. Zarcone. "Numerical Models and Experiments on Immiscible Displacements in Porous Media". *Journal of Fluid Mechanics*, 189:165-187, 1988.
- [88] C. Lin and J. C. Slattery. "Three-Dimensional, Randomized, Network Model for Two-Phase Flow Through Porous Media". *AIChE Journal*, 28:311-324, 1982.
- [89] B. B. Mandelbrot. *The Fractal Geometry of Nature*. W. H. Freeman, New York, 1982.
- [90] C. M. Marle. "Ecoulements Monophasiques en Milieu Poreux". *Rev. Inst. Fr. Petrole*, XXII:1471, 1967.
- [91] G. Matheron. *Les Variables Regionalisees et Leur Estimation*. Masson, Paris, 1965.
- [92] G. Matheron and G. de Marsily. "Is Transport in Porous Media Always Diffusive? A Counterexample". *Water Resources Research*, 16(5):901-917, 1980.
- [93] W. D. McComb. *The Physics of Fluid Turbulence*. Oxford Engineering Science Series No. 25. Clarendon Press, Oxford, 1990.
- [94] K. K. Mohanty. *Fluids in Porous Media: Two-Phase Distribution and Flow*. PhD thesis, University of Minnesota, Minneapolis, 1981.
- [95] F. J. Molz, O. Güven, and J. G. Melville. "An Examination of Scale-Dependent Dispersion Coefficients". *Groundwater*, 21(6):715-725, 1983.
- [96] F. J. Molz, O. Güven, J. G. Melville, and C. Cardone. "Hydraulic Conductivity Measurements at Different Scales and Contaminant Transport Modeling". In J. H. Cushman, editor, *Dynamics of Fluids in Hierarchical Porous Media*, pages 37-60. Academic Press, London, 1990.
- [97] H. J. Morel-Seytoux and M. Nachabe. "An Effective Scale-Dependent Dispersivity Deduced from a Purely Convective Flow Field". *Journal of Hydrological Sciences*, 37(2):93-104, 1992.
- [98] S. Mukhopadhyay. *The Effect of Correlations and Large-Scale Heterogeneities on Flow and Transport in Porous Media and Fractured Rocks*. PhD thesis, University of Southern California, Los Angeles, 1995.

- [99] S. Mukhopadhyay and M. Sahimi. "Heat Transfer and Two-Phase Flow in Fractured Reservoirs". *Society of Petroleum Engineers Journal*, 24043:207-219, 1992.
- [100] S. P. Neuman. "Universal Scaling of Hydraulic Conductivities and Dispersivities in Geologic Media". *Water Resources Research*, 26(8):1749-1758, 1990.
- [101] S. P. Neuman. "Generalized Scaling of Permeabilities: Validation and Effect of Support Scale". *Geophysical Research Letters*, 21(5):349-352, 1994.
- [102] S. P. Neuman and S. Orr. "Prediction of Steady State Flow in Nonuniform Geologic Media by Conditional Moments: Exact Nonlocal Formalism, Effective Conductivities, and Weak Approximation". *Water Resources Research*, 29(2):341-364, 1993.
- [103] S. P. Neuman, C. L. Winter, and C. M. Newman. "Stochastic Theory of Field Scale Dispersion in Anisotropic Porous Media". *Water Resources Research*. 23(3):453-466, 1987.
- [104] Department of Defense. "Defense Environmental Restoration Program Annual Report to Congress for Fiscal Year 1995", May 1996. Volume 2.
- [105] R. L. Olsen and M. C. Kavanaugh. "Can Groundwater Remediation Be Achieved". *Water Environment and Technology*, March:42-47, 1993.
- [106] G. Oster, A. Perelson, and A. Katchalsky. "Network Thermodynamics". *Nature*, 234:393-399, 1971.
- [107] J. Peraire, J. Peiro, and K. Morgan. "A 3D Finite Element Multigrid Solver for the Euler Equations". In *Proceedings of the 30th Aerospace Sciences meeting and Exhibit, January 6-9, Reno, NV*. American Institute of Aeronautics and Astronautics, 1992.
- [108] J. F. Peters. personal communication.
- [109] J. F. Peters and S. E. Howington. "Pre-Asymptotic Transport Through Porous Media". In G. Delic and M. F. Wheeler, editors, *Next Generation Environmental Models: Computational Methods*. pages 271-280. SIAM, Philadelphia. 1997.
- [110] O. A. Plumb and S. Whitaker. "Dispersion in Heterogeneous Porous Media 1. Local Volume Averaging and Large-Scale Averaging". *Water Resources Research*, 24(7):913-926, 1988.

- [111] K. Pruess. "A Fickian Diffusion Model for the Spreading of Liquid Plumes Infiltrating Heterogeneous Media". *Transport in Porous Media*, 24:1-33, 1996.
- [112] H. Rajaram and L. W. Gelhar. "Three-Dimensional Spatial Moments Analysis of the Borden Tracer Test". *Water Resources Research*, 27(6):1239-1251, 1991.
- [113] H. Rajaram and L. W. Gelhar. "Plume-Scale Dependent Dispersion in Aquifers With a Wide Range of Scales of Heterogeneity". *Water Resources Research*, 31(10):2469-2482, 1995.
- [114] X. Sánchez-Vila, J. Carrera, and J. P. Girardi. "Scale Effects in Transmissivity". *Journal of Hydrology*, 183:1-22, 1996.
- [115] P. G. Saffman. "Dispersion Due to Molecular Diffusion and macroscopic Mixing in Flow Through a Network of Capillaries". *Journal of Fluid Mechanics*, 7:194-208, 1960.
- [116] M. Sahimi. "Flow Phenomena in Rocks: From Continuum Models to Fractals, Percolation, Cellular Automata, and Simulated Annealing". *Reviews of Modern Physics*, 65(4):1393-1534, 1993.
- [117] M. Sahimi. "Fractal and Superdiffusive Transport and Hydrodynamic Dispersion in Heterogeneous Porous Media". *Transport in Porous Media*, 13:3-40, 1993.
- [118] M. Sahimi. *Flow and Transport in Porous Media and Fractured Rock: From Classical Methods to Modern Approaches*. VCH, Weinheim, Germany, 1995.
- [119] M. Sahimi, A. A. Heiba, B. D. Hughes, H. T. Davis, and L. E. Scriven. Dispersion in flow through porous media, 1982. Society of Petroleum Engineers Paper Number 10969.
- [120] M. Sahimi, B. D. Hughes, L. E. Scriven, and H. T. Davis. "Dispersion in Flow Through Porous Media — I. One-Phase Flow". *Chemical Engineering Science*, 41(8):2103-2122, 1986.
- [121] M. Sahimi and A. O. Imdakm. "The Effect of Morphological Disorder on Hydrodynamic Dispersion in Flow Through Porous Media". *Journal of Physics A*, 21:3822-3870, 1988.
- [122] T. D. Scheibe and C. R. Cole. "Non-Gaussian Particle Tracking: Application to Scaling of Transport Processes in Heterogeneous Porous Media". *Water Resources Research*, 30(7):2027-2039, 1994.

- [123] A. E. Scheidegger. *The Physics of Flow Through Porous Media*. University of Toronto Press, Toronto, 1960.
- [124] D. Schulze-Makuch and R. S. Cherkauer. "Method Developed for Extrapolating Scale Behavior". *EOS*, 78(1):3, 1997.
- [125] F. W. Schwartz. "Macroscopic Dispersion in Porous Media: The Controlling Factors". *Water Resources Research*, 13(4):743-752, 1977.
- [126] F. W. Schwartz, L. Smith, and A. S. Crowe. "A Stochastic Analysis of Macrodispersion in Fractured Media". *Water Resources Research*, 19(5):1253-1265, 1983.
- [127] F. Schuille. *Dense Chlorinated Solvents in Porous and Fractured Media: Model Experiments*. Lewis Publishers, Chelsea, Michigan, 1988. English edition translated by J. F. Pankow.
- [128] G. Segol. "*Classic Groundwater Simulations: Proving and Improving Numerical Models*". PTR Prentice Hall, Engewood Cliffs, NJ, 1993.
- [129] L. Smith and R. A. Freeze. "Stochastic Analysis of Steady State Groundwater Flow in a Bounded Domain 2. Two-Dimensional Simulations". *Water Resources Research*, 15(6):1543-1559, 1979.
- [130] L. Smith and F. W. Schwartz. "Mass Transport, 2, Analysis of Uncertainty in Prediction". *Water Resources Research*, 17(2):351, 1981.
- [131] W. E. Soll and M. A. Celia. "A Modified Percolation Approach to Simulating Three-Fluid Capillary Pressure-Saturation Relationships". *Advances in Water Resources*, 16:107-126, 1993.
- [132] G. Sposito, W. A. Jury, and V. K. Gupta. "Fundamental Problems in the Stochastic Convection-Dispersion Model of Solute Transport in Aquifers and Field Soils". *Water Resources Research*, 22(1):77-88, 1986.
- [133] G. I. Taylor. "Diffusion by Continuous Movements". *Proceedings of the London Mathematical Society*, 20:196-212, 1922.
- [134] G. I. Taylor. "Dispersion of Soluble Matter in Solvent Flowing Slowly Through a Tube". *Proceedings of the Royal Society of London*, A219:186-203, 1953.
- [135] M. R. Thiele, R. P. Batycky, M. J. Blunt, and Jr. F. M. Orr. "Simulating Flow in Heterogeneous Systems Using Streamtubes and Streamlines". *Society of Petroleum Engineers Reservoir Engineering*, pages 5-12, 1996.

- [136] A. F. B. Tompson, S. F. Ashby, R. D. Falgout, S. G. Smith, T. W. Fogwell, and G. A. Loosmore. "Use of High Performance Computing to Examine the Effectiveness of Aquifer Remediation". In *Proceedings of the X International Conference on Computational Methods in Water Resources*, volume 2, Dordrecht, 1994. Kluwer Academic Publishers.
- [137] A. F. B. Tompson and L. W. Gelhar. "Numerical Simulation of Solute Transport in Three-Dimensional, Randomly Heterogeneous Porous Media". *Water Resources Research*, 26(10):2541-2562, 1990.
- [138] A. F. B. Tompson and W. G. Gray. "A Second-Order Approach for the Modeling of Dispersive Transport in Porous Media: 1. Theoretical Development". *Water Resources Research*, 22(5):591-599, 1986.
- [139] C. F. Tsang, Y. W. Tsang, and F. V. Hale. "Tracer Transport in Fractures: Analysis of Field Data Based on a Variable-Aperture Channel Model". *Water Resources Research*, 27(12):3095-3106, 1991.
- [140] M. Th. van Genuchten. "A Closed-Form Equation for Predicting the Hydraulic Conductivity of Unsaturated Soils". *Soil Science Society of America Journal*, 44:892-898, 1980.
- [141] J. E. Warren and F. F. Skiba. "Macroscopic Dispersion". *Society of Petroleum Engineers Journal*, pages 215-230, 1964.
- [142] S. W. Wheatcraft and J. H. Cushman. "Hierarchical Approaches to Transport in Heterogeneous Porous Media". *Water Resources Research*, pages 263-269, 1991.
- [143] S. W. Wheatcraft and S. W. Tyler. "An Explanation of Scale-Dependent Dispersivity in Heterogeneous Aquifers Using Concepts of Fractal Geometry". *Water Resources Research*, 24(4):566-578, 1988.
- [144] S. Whitaker. "Advances in the Theory of Fluid Flow Through Porous Media". *American Institute of Chemical Engineering Journal*, 61(12):14-28, 1969.
- [145] E. F. Wilkins. "Prelude; Groundwater for the Future". *Water Environment and Technology*, 5(3):4, 1993.
- [146] K. G. Wilson. "Problems in Physics with Many Scales of Length". *Scientific American*, 241:158, 1979.
- [147] W. W. Wood. "Diffusion: The Source of Confusion?". *Groundwater*, 34(2):193, 1996.

-
- [148] Y. C. Yortsos, C. Satik, J.-C. Bacri, and D. Salin. "Large-Scale Percolation Theory of Drainage". *Transport in Porous Media*, 10:171–195, 1993.

Appendix A

Computation of Effective Conductivity

Gelhar [53] begins with an expression for Darcy's law

$$Q_i = -K \frac{\partial \phi}{\partial x_i} \quad (\text{A.1})$$

where q_i is the flux in direction i , $[LT^{-1}]$, K is hydraulic conductivity, $[LT^{-1}]$, ϕ is the potential, $[L]$. The potential and the logarithm of conductivity are decomposed into their mean and zero-mean random components

$$\phi = H + h, \quad E[\phi] = H, \quad E[h] = 0, \quad (\text{A.2})$$

$$\ln K = F + f, \quad E[\ln K] = F, \quad E[f] = 0, \quad (\text{A.3})$$

where E indicates an expectation. By taking the expectation of both sides of the Darcy equation

$$E[Q_i] = -E \left[K \frac{\partial \phi}{\partial x_i} \right] = -E \left[e^F e^f \frac{\partial (H + h)}{\partial x_i} \right] = -e^F E \left[e^f \left(\frac{\partial H}{\partial x_i} + \frac{\partial h}{\partial x_i} \right) \right]. \quad (\text{A.4})$$

Beacuse the conductivity distribution is lognormal,

$$e^F = K_g \quad (\text{A.5})$$

where K_g is the geometric mean of the conductivity distribution, $[LT^{-1}]$. Further, the exponential for conductivity variation, f , may be approximated by a Taylor series

$$e^f \approx \left(1 + f + f^2/2 + f^3/3 + \dots \right), \quad (\text{A.6})$$

leaving

$$E[Q_i] = -K_g E \left[\left(\left(1 + f + f^2/2 + f^3/3 + \dots \right) \frac{\partial H}{\partial x_i} + \frac{\partial h}{\partial x_i} \right) \right]. \quad (\text{A.7})$$

At this point, terms that are third-order perturbation and higher are assumed negligible. Given that

$$E \left[\frac{f^2}{2} \right] = \frac{\sigma_f^2}{2}, \quad (\text{A.8})$$

with σ_f^2 being the variance in the perturbations of $\ln K$, the equation becomes

$$E[Q_i] = K_g \left[J_i \left(1 + \frac{\sigma_f^2}{2} \right) - E \left[\frac{\partial h}{\partial x_i} f \right] \right]. \quad (\text{A.9})$$

where J_i is the large scale gradient in head [-].

To evaluate the remaining expectation term, begin with the head distribution for an isotropic, heterogeneous medium

$$\frac{\partial}{\partial x_i} \left(K \frac{\partial h}{\partial x_i} \right) = 0, \quad i = 1, 2, 3. \quad (\text{A.10})$$

Differentiating and dividing through by $\ln K$ gives

$$\frac{\partial^2 \phi}{\partial x_i^2} + \frac{\partial \ln K}{\partial x_i} \frac{\partial \phi}{\partial x_i} = 0, \quad K \neq 0 \quad (\text{A.11})$$

Decomposing K and ϕ into their mean and perturbed components, expanding, and taking the expectations yields the following equation for the mean head distribution

$$\frac{\partial^2 H}{\partial x_i^2} + \frac{\partial F}{\partial x_i} \frac{\partial H}{\partial x_i} + E \left[\frac{\partial f}{\partial x_i} \frac{\partial h}{\partial x_i} \right] = 0. \quad (\text{A.12})$$

By subtracting this mean equation from the original, we are left with the random component or mean-removed equation

$$\frac{\partial^2 h}{\partial x_i^2} + \frac{\partial F}{\partial x_i} \frac{\partial h}{\partial x_i} + \frac{\partial f}{\partial x_i} \frac{\partial H}{\partial x_i} = E \left[\frac{\partial f}{\partial x_i} \frac{\partial h}{\partial x_i} \right] - \frac{\partial f}{\partial x_i} \frac{\partial h}{\partial x_i}. \quad (\text{A.13})$$

Assuming the second order perturbation terms to the right of the equal sign are small, we are left with

$$\begin{aligned} \frac{\partial^2 h}{\partial x_i^2} + A_i x_i \frac{\partial h}{\partial x_i} - J_i \frac{\partial f}{\partial x_i} &= 0, \\ A_i &= \frac{\partial F}{\partial x_i}, \\ J_i &= \frac{\partial H}{\partial x_i}. \end{aligned} \quad (\text{A.14})$$

A solution to this problem is possible using spectral representations for h and f .

$$\begin{aligned} h(x_i) &= \int_{k_i} e^{ik_i x_i} dZ_h(k_i) \\ f(x_i) &= \int_{k_i} e^{ik_i x_i} dZ_f(k_i) \end{aligned} \quad (\text{A.15})$$

where Z is a stochastic process with the following properties

$$E[dZ] = 0 \quad (\text{A.16})$$

$$E[dZ(\omega_1)dZ^*(\omega_2)] = 0, \omega_1 \neq \omega_2 \quad (\text{A.17})$$

$$E[dZ(\omega)dZ^*(\omega)] = S(\omega)d\omega \quad (\text{A.18})$$

and S is the spectral density function. Using these representations for h and f in the random component equation and integrating over the wave number produces

$$dZ_h = -\frac{ik_i J_i dZ_f}{k^2 - ik_i A_i}; k^2 = k_1^2 + k_2^2 + k_3^2 \quad (\text{A.19})$$

Finally,

$$E \left[\frac{\partial h}{\partial x_i} f \right] = \int_k ik_i E[dZ_h dZ_f^*] = J_i \int_k \frac{k_i k_j}{k^2 - iA_j k_j} S_{ff}(k) dk = J_i F_{ij} \quad (\text{A.20})$$

where

$$F_{ij} = \int_k \frac{k_i k_j}{k^2 - iA_j k_j} S_{ff}(k) dk. \quad (\text{A.21})$$

If the gradient in the mean conductivity and the gradient in the head are assumed slowly varying in space, and thus locally constant, we get

$$E[q_i] = K_g J_j \left(\left(1 + \frac{\sigma_f^2}{2} \right) \delta_{ij} - F_{ij} \right) = \hat{K}_{ij} J_j \quad (\text{A.22})$$

in which \hat{K}_{ij} represents the effective conductivity.

For a two dimensional, statistically isotropic system with no trend in the mean conductivity ($A_i = 0$), F_{ij} may be evaluated to show that the effective conductivity is the geometric mean,

$$\hat{K}_{ij} = K_g \delta_{ij} \quad (\text{A.23})$$

In a three dimensional, perfectly layered system with statistical isotropy in the plan view,

$$\begin{aligned} \hat{K}_{11} = \hat{K}_{22} &= K_g \left(1 + \frac{1}{2} \sigma_f^2 \right) \\ \hat{K}_{33} &= K_g \left(1 - \frac{1}{2} \sigma_f^2 \right). \end{aligned} \quad (\text{A.24})$$

For the more general case in three dimensions with statistical anisotropy, the result is

$$\hat{K}_{ii} = K_g \left[1 + \sigma_f^2 \left(\frac{1}{2} - g_{ii} \right) \right], \quad i = 1, 2, 3 \text{ (no sum on } i) \quad (\text{A.25})$$

but g_{ii} could only be evaluated numerically [53].

Appendix B

Relating σ_f to σ_q

To relate the variance in conductivity to the variance in specific flux, Gelhar [53] begins with the expanded version of Equation A.9.

$$E[Q_i] = K_g \left[J_i \left(1 + \frac{\sigma^2 f}{2} \right) - E \left[\frac{\partial h}{\partial x_i} f \right] + \dots \right]. \quad (\text{B.1})$$

To get the flux perturbation equation, this mean equation is subtracted from a Darcy expression for total head (mean plus perturbation),

$$q_i = Q_i - E[Q_i] = -K \frac{\partial(H + h)}{\partial x_i} - E[Q_i]. \quad (\text{B.2})$$

The resulting equation for the perturbation of flux is

$$q_i = -K \frac{\partial(H + h)}{\partial x_i} - K_g \left[J_i \left(1 + \frac{\sigma^2 f}{2} \right) - E \left[\frac{\partial h}{\partial x_i} f \right] + \dots \right]. \quad (\text{B.3})$$

At this point, only the first order perturbation terms are retained, leaving

$$q_i = K_g (J_i e^f - 1). \quad (\text{B.4})$$

Using a two term approximation for the exponential, the equation for the perturbation in flux becomes

$$q_i = K_g \left(J_i - \frac{\partial h}{\partial x_i} \right). \quad (\text{B.5})$$

Rearranging and taking the gradient of both sides produces

$$\frac{\partial^2 h}{\partial x_i^2} = \frac{\partial}{\partial x_i} (J_i f) - \frac{1}{K_g} \frac{\partial q_i}{\partial x_i}. \quad (\text{B.6})$$

Substituting this expression for the Laplacian of head perturbation into Equation A.14 yields

$$\frac{\partial}{\partial x_i}(J_i f) - \frac{1}{K_g} \frac{\partial q_i}{\partial x_i} - J_i \frac{\partial f}{\partial x_i} + A_i \frac{\partial h}{\partial x_i} = 0. \quad (\text{B.7})$$

Here, Gelhar uses the spectral representations for h and f as before to solve this equation. For $A_i = 0$, the spectrum of fluxes may be related to the spectrum of conductivities as follows

$$S_{q_i q_j}(k) = K_g^2 J_m J_n \left(\delta_{im} - \frac{k_i k_m}{k^2} \right) \left(\delta_{jn} - \frac{k_j k_n}{k^2} \right) S_{ff}(k) \quad (\text{B.8})$$

For a three-dimensional statistically-isotropic medium, this leaves

$$\begin{aligned} \sigma_{q_1}^2 &= \frac{8}{15} \frac{\sigma_f^2 q^2}{\gamma^2} \\ \sigma_{q_2}^2 = \sigma_{q_3}^2 &= \frac{1}{15} \frac{\sigma_f^2 q^2}{\gamma^2} \end{aligned} \quad (\text{B.9})$$

with

$$\gamma = \frac{q}{K_g J} \quad (\text{B.10})$$

In two dimensions,

$$\begin{aligned} \sigma_{q_1}^2 &= \frac{3}{8} \sigma_f^2 q^2 \\ \sigma_{q_2}^2 &= \frac{1}{8} \sigma_f^2 q^2 \end{aligned} \quad (\text{B.11})$$

Appendix C

Macrodispersion Coefficients

Beginning with the macrodispersivity equation that is valid after large displacement time[53]

$$A_{ij} = \int_k \frac{S_{q_i q_j}(k) dk}{q^2 [i k_1 + \alpha_L k_1^2 + \alpha_T (k_2^2 + k_3^2)]} \quad (\text{C.1})$$

For a two-dimensional, isotropic medium, the macrodispersivity tensor becomes

$$A_{ij} = 0, \quad i \neq j \quad (\text{C.2})$$

$$A_{11} = \sigma_f^2 \lambda \quad (\text{C.3})$$

$$A_{22} = -\frac{\sigma_f^2}{8} (\alpha_L + 3\alpha_T) \quad (\text{C.4})$$

For a three-dimensional, isotropic medium with an exponential covariance model for conductivity

$$A_{ij} = 0, \quad i \neq j \quad (\text{C.5})$$

$$A_{11} = \frac{\sigma_f^2 \lambda}{\gamma^2} \quad (\text{C.6})$$

$$A_{22} = A_{33} = \frac{\sigma_f^2 \alpha_L}{15\gamma} \left(1 + \frac{4\alpha_T}{\alpha_L} \right) \quad (\text{C.7})$$

REPORT DOCUMENTATION PAGE

Form Approved
OMB No. 0704-0188

Public reporting burden for this collection of information is estimated to average 1 hour per response, including the time for reviewing instructions, searching existing data sources, gathering and maintaining the data needed, and completing and reviewing the collection of information. Send comments regarding this burden estimate or any other aspect of this collection of information, including suggestions for reducing this burden, to Washington Headquarters Services, Directorate for Information Operations and Reports, 1215 Jefferson Davis Highway, Suite 1204, Arlington, VA 22202-4302, and to the Office of Management and Budget, Paperwork Reduction Project (0704-0188), Washington, DC 20503.

1. AGENCY USE ONLY (Leave blank)		2. REPORT DATE September 1997	3. REPORT TYPE AND DATES COVERED Final report	
4. TITLE AND SUBTITLE Discrete Network Modeling for Field-Scale Flow and Transport Through Porous Media			5. FUNDING NUMBERS	
6. AUTHOR(S) Stacy E. Howington, John F. Peters, Tissa H. Illangasekare				
7. PERFORMING ORGANIZATION NAME(S) AND ADDRESS(ES) U.S. Army Engineer Waterways Experiment Station 3909 Halls Ferry Road, Vicksburg, MS 39180-6199; University of Colorado, Boulder, CO 80309			8. PERFORMING ORGANIZATION REPORT NUMBER Technical Report CHL-97-21	
9. SPONSORING/MONITORING AGENCY NAME(S) AND ADDRESS(ES) Discretionary Research Program U.S. Army Engineer Waterways Experiment Station 3909 Halls Ferry Road, Vicksburg, MS 39180-6199; Army Environmental Center, Aberdeen Proving Ground, MD 21010			10. SPONSORING/MONITORING AGENCY REPORT NUMBER	
11. SUPPLEMENTARY NOTES Available from National Technical Information Service, 5285 Port Royal Road, Springfield, VA 22161.				
12a. DISTRIBUTION/AVAILABILITY STATEMENT Approved for public release; distribution is unlimited.			12b. DISTRIBUTION CODE	
13. ABSTRACT (Maximum 200 words) <p>Natural soil is a discrete, heterogeneous porous material with many sizes of physical structure. These multi-scale discrete media resist description by differential equations with macroscopic parameters. Constitutive parameters may display an apparent scale dependence or the governing equations may exhibit non-physical behavior. To address these issues, a discrete-medium modeling philosophy is adopted that relies less on complex constitutive theory and more on computational resolution. Specifically, a stochastic, high-resolution, discrete network model is developed and explored for simulating macroscopic flow and conservative transport through macroscopic porous media.</p> <p>Networks can be created to honor macroscopic porosity, effective conductivity, and apparent dispersivity estimates or to honor statistical distributions of small scale conductivities. Flow through a discrete network compares well with analytical solutions for macroscopic, Darcian fluid flow. Transport through a discrete network differs fundamentally from advection-dispersion theory. However, network-predicted concentration profiles and breakthrough curves are consistent with historical observations of nearly-Gaussian concentration distributions. Dispersion in the network is a natural consequence of its discrete structure. For immiscible flow, network models offer the potential to simulate capillary barriers and macroporous breakthrough phenomena.</p>				
14. SUBJECT TERMS Dispersivity Groundwater modeling			15. NUMBER OF PAGES 315	
Network modeling Scale-dependence			16. PRICE CODE	
17. SECURITY CLASSIFICATION OF REPORT UNCLASSIFIED	18. SECURITY CLASSIFICATION OF THIS PAGE UNCLASSIFIED	19. SECURITY CLASSIFICATION OF ABSTRACT	20. LIMITATION OF ABSTRACT	